USE OF LAGRANGIAN METHODS TO SIMULATE HEAVY STORM-INDUCED RIVER PLUME DYNAMICS AND RECREATIONAL WATER QUALITY IMPACTS IN THE NEARSHORE REGION OF SOUTHWESTERN LAKE MICHIGAN

By

Chelsea Weiskerger

A DISSERTATION

Submitted to
Michigan State University
in partial fulfillment of the requirements
for the degree of

Environmental Engineering – Doctor of Philosophy
Environmental Science and Policy – Dual Major

2022

ABSTRACT

USE OF LAGRANGIAN METHODS TO SIMULATE HEAVY STORM-INDUCED RIVER PLUME DYNAMICS AND RECREATIONAL WATER QUALITY IMPACTS IN THE NEARSHORE REGION OF SOUTHWESTERN LAKE MICHIGAN

By

Chelsea Weiskerger

The Great Lakes are the primary source of drinking water for nearly 30 million people in the region. During storm events runoff from upstream watersheds and (combined) sewer overflows delivers pathogens to the Lakes. The pathogens are then transported to beaches and water intakes by the lake circulation, posing risks to human health. Fecal indicator organisms such as *Escherichia coli* are used to track pollution levels and to take proactive measures to manage coastal resources and to safeguard public health by closing beaches to the public, issuing swimming advisories, etc. Predictive modeling of coastal water quality continues to be an attractive approach to generate water quality forecasts and to gain insights into key processes. Although progress has been made in understanding and quantifying the impacts of tributary loading and river plumes on microbial pollution at beaches, the impacts of extreme storm events on coastal water quality are not well-understood. As the frequency and intensity of storm events increase, the pollution footprint of extreme storm events has not been quantified in a way that can be used to inform policy. Complex nearshore features, including irregular coastlines and coastal structures calls for high-resolution modeling that is computationally demanding. While traditional Eulerian approaches to plume modeling have been previously used, comparisons with available observed plume data indicated that Lagrangian particle tracking improves prediction of plume dimensions (and hence risks) in southwestern Lake Michigan. Therefore, coupled hydrodynamic and reactive particle tracking models were developed and tested to simulate the complex dynamics of multiple river plumes induced by extreme storm events in the Chicago area in southwestern Lake Michigan. The present-day Chicago River normally flows to the Mississippi River and discharges into Lake Michigan only during "backflow" events triggered by these storms. Simulations of extreme storm-induced river plumes during years 2008, 2010, 2011, 2013 and 2017 were reported and models tested using available data on currents, water temperatures, concentrations of indicator bacteria (*E. coli*) and the spatial extent of turbidity plumes using MODIS Terra satellite imagery. Results suggest that plumes associated with the extreme storms persist along the Chicago shoreline for up to 24 days after the commencement of backflow release and that plume areas of influence range from 7.9 to 291 km^2 in the nearshore. Plume spatiotemporal dynamics were largely related to the volume of water released via backflow events and the duration of the backflow releases. Empirical relations were proposed to allow beach and stormwater managers to predict plume spatiotemporal dynamics in real time. Model results from a Lagrangian *E. coli* fate and transport model were compared against monitoring data collected at 16-18 beaches during and after backflow events in 2010 and 2011. Results indicate that all Chicago Park District beaches are susceptible to *E. coli* concentrations that exceed USEPA thresholds for safe recreation after extreme storms. Therefore, the current approach to beach management, which involves closing all beaches during and immediately after backflow events, is likely prudent. However, results also suggest that beaches are probably being reopened prematurely after storm events, as beaches may be at risk for degraded water quality for multiple days, post backflow event. To address data gaps, we recommend that future research focus on the collection of additional *in situ* hydrometeorological and water quality data during and after extreme storms and backflow events. These data may be collected using unmanned aerial vehicles or autonomous sensor systems.

To the giants whose shoulders I have been fortunate to stand on

ACKNOWLEDGEMENTS

This work was partially supported by United States Geological Survey project #RC108429, titled "Evaluate the Fate and Transport of Historic Backflows from the Chicago Area Waterway System to Lake Michigan". Additional financial support was provided via a Cooperative Institute for Great Lakes Research (CIGLR) Graduate Research Fellowship and a 2019-2020 Clifford Humphrys Fellowship for Preservation of Water Quality in the Great Lakes.

The guidance and mentorship of my PhD committee chairman, Dr. Mantha Phanikumar, was integral to the planning, preparation and completion of the research described herein. I would like to acknowledge my deepest thanks to Professor Mantha for his patience and assistance throughout the research and dissertation processes. Collaborators, including Dr. Mark Rowe, Dr. P. Ryan Jackson and Dr. James Duncker also provided guidance, data and technical assistance during the development of models and interpretation of results. I especially want to thank Dr. Rowe for introducing me to the Lagrangian particle tracking model used for the majority of simulations presented. My doctoral committee – Dr. Jade Mitchell, Dr. Joan Rose and Dr. Irene Xagoraraki – were crucial to keeping my dissertation research focused, and applicable to the fields of engineering, public health, environmental health and policy. I am incredibly grateful for their perspective and advice regarding my research. My lab and departmental colleagues provided a close network that I could always rely on. I specifically want to thank Ammar Safaie and Saeed Memari for providing guidance as I familiarized myself with the FVCOM modeling procedure. Finally, I want to thank my family, particularly my father, late mother and brother, for making sure that I have always had their support and any resources that I needed to be successful.

TABLE OF CONTENTS

LIST OF TABLES

LIST OF FIGURES

KEY TO SYMBOLS

A_1	Stability function constant, unitless, referenced in Chapter 3
A_2	Stability function constant, unitless, referenced in Chapter 3
A_m	Horizontal eddy viscosity coefficient ($m^2\ s^{-1}$), referenced in Chapter 3
A_h	Thermal horizontal eddy diffusion coefficient ($m^2\ s^{-1}$), referenced in Chapter 3
AntePrec	24-hour antecedent rainfall amounts at Chicago O'Hare International Airport (inches), referenced in Chapter 5
AvgEC	Average *E. coli* concentration at a beach after a backflow event (MPN 100 mL^{-1}), referenced in Chapter 6
B_1	Stability function constant, unitless, referenced in Chapter 3
B_2	Stability function constant, unitless, referenced in Chapter 3
C	Microbial concentration (CFU 100 mL^{-1} or MPN 100 mL^{-1}), referenced in Chapters 2, 3, and 6
C_1	Stability function constant, unitless, referenced in Chapter 3
D	Brownian diffusivity ($m^2\ s^{-1}$), referenced in Chapter 4
DurationC	Backflow duration at the CRCW outlet (hr), referenced in Chapter 5
DuractionW	Backflow duration at the Wilmette outlet (hr), referenced in Chapter 5
E_1	Mellor-Yamada 2.5-level turbulence model constant, unitless, referenced in Chapter 3
E_2	Wall proximity function constant, unitless, referenced in Chapter 3
err_j	Absolute error between model derived and MODIS-Terra derived variable *j* (km or km^2), referenced in Chapter 4
F_u	Horizontal diffusion in the x-direction ($m^2\ s^{-1}$), referenced in Chapters 1, 2 and 3
F_v	Horizontal diffusion in the y-direction ($m^2\ s^{-1}$), referenced in Chapters 1, 2 and 3
F_w	Vertical diffusion ($m^2\ s^{-1}$), referenced in Chapters 1, 2 and 3
F_q	Horizontal diffusion of turbulent kinetic energy ($m^2\ s^{-1}$), referenced in Chapter 3

F_l	Horizontal diffusion of the turbulent macroscale ($m^2\ s^{-1}$), referenced in Chapter 3
footprint	Maximum plume footprint in the nearshore zone (km^2), referenced in Chapter 5
f_p	Fraction of contaminant particles attached to suspended solids, unitless, referenced in Chapters 2 and 6
f_u	Coriolis force in the x-direction (s^{-1}), referenced in Chapters 1, 2 and 3
f_u	Coriolis force in the y-direction (s^{-1}), referenced in Chapters 1, 2 and 3
G_H	Model coefficient for stability, unitless, referenced in Chapter 3
g	Acceleration due to gravity ($m^2\ s^{-1}$), referenced in Chapter 3
H	Water depth (m), referenced in Chapters 2 and 3
I_t	Solar irradiance at the surface of the water at time t ($W\ M^{-1}$), referenced in Chapter 2
K_m	Vertical eddy viscosity coefficient ($m^2\ s^{-1}$), referenced in Chapters 1, 2 and 3
K_h	Thermal vertical eddy diffusion coefficient ($m^2\ s^{-1}$), referenced in Chapters 1, 2 and 3
K_H	Horizontal mixing coefficient ($m^2\ s^{-1}$), referenced in Chapter 2
K_V	Vertical mixing coefficient ($m^2\ s^{-1}$), referenced in Chapter 2
k	Overall microbial decay rate (d^{-1}), referenced in Chapter 2
k_{b1}	Microbial base mortality rate (d^{-1}), referenced in Chapter 2
k_{bi}	Microbial decay rate due to solar inactivation (d^{-1}), referenced in Chapter 2
k_{bs}	Microbial decay rate due to sedimentation (d^{-1}), referenced in Chapter 2
k_d	Microbial dark mortality rate (d^{-1}), referenced in Chapters 2, 3 and 6
k_I	Contaminant inactivation rate with solar radiation ($m^2\ W^{-1}\ d^{-1}$), referenced in Chapters 2 and 6
k_e	Solar radiation extinction rate (m^{-1}), referenced in Chapters 2 and 6
L	Wall proximity function input (m^{-1}), referenced in Chapter 3
l	Turbulence macroscale ($m^3\ s^{-2}$), referenced in Chapter 3
M	Shear frequency (s^{-1}), referenced in Chapter 3

N	Brunt-Väisälä frequency (s^{-1}), referenced in Chapter 3
O_i	Observed value of a variable at time *i* (units of observed variable), referenced in Chapter 3
O_j	Value of variable *j* determined from MODIS-Terra data (units of variable *j*, km or km^2), referenced in Chapter 4
P_b	Buoyancy production of turbulent kinetic energy (m s^{-1} kg^{-1}), referenced in Chapter 3
P_i	Model predicted value of a variable at time *i* (units of predicted variable), referenced in Chapter 3
P_j	Value of variable *j* from modeled plume data (units of variable *j*, km or km^2), referenced in Chapter 4
P_{sea}	Percent sea water (percentage), referenced in Chapter 2
P_s	Shear production of turbulent kinetic energy (m s^{-1} kg^{-1}), referenced in Chapter 3
p_a	Air pressure at the water surface (Pa), referenced in Chapters 1, 2 and 3
p_H	Hydrostatic pressure (Pa), referenced in Chapters 1, 2 and 3
Pr	Molecular Prandtl number, unitless, referenced in Chapter 3
Pr_t	Turbulent Prandtl number, unitless, referenced in Chapter 3
Pr_H	Horizontal Prandtl number, unitless, referenced in Chapter 3
Pr_V	Vertical Prandtl number, unitless, referenced in Chapter 3
ProxC	Proximity of a beach to the CRCW outlet (km), referenced in Chapter 6
ProxW	Proximity of a beach to the Wilmette outlet (km), referenced in Chapter 6
Q	River discharge (m^3 s^{-1}), referenced in Chapters 4, 5 and 6
q	Non-hydrostatic pressure (Pa), referenced in Chapters 1, 2 and 3
q^2	Turbulent kinetic energy (m^2 s^{-2}), referenced in Chapter 3
S	Salinity (PSU), referenced in Chapters 1 and 2
S_C	Source term for contaminants, referenced in Chapter 4
S_m	Stability function for vertical eddy viscosity, unitless, referenced in Chapter 3

S_h	Stability function for vertical thermal eddy diffusion, unitless, referenced in Chapter 3
T	Water temperature (°C), referenced in Chapters 1, 2, 3 and 6
TimeEC	Time until an initial increase in *E. coli* at a beach is seen (hr after backflow begins), referenced in Chapter 6
TimeExceed	Time of last exceedance of 2.37 $\log_{10}$MPN 100 ml^{-1} at beach (hr after backflow begins), referenced in Chapter 6
TimeScale	Time until plume dissipation into Lake Michigan (hr), referenced in Chapter 5
t_n	Current time step in explicit Runge-Kutta scheme (s), referenced in Chapter 4
t_{n+1}	Future time step in explicit Runge-Kutta scheme (s), referenced in Chapter 4
t_{90}	Time to inactivate 90% of contaminant concentration (d^{-1}), referenced in Chapter 2
u	Velocity component in the *x*-direction (m s^{-1}), referenced in Chapters 1, 2 and 3
$\bar{u}$	Mean velocity component in the *x*-direction (m s^{-1}), referenced in Chapter 3
$\|V\|$	Prevailing current velocity (m s^{-1}), referenced in Chapter 3
v	Velocity component in the *y*-direction (m s^{-1}), referenced in Chapters 1, 2 and 3
$\bar{v}$	Mean velocity component in the *y*-direction (m s^{-1}), referenced in Chapter 3
$\vec{v}(\vec{x}, t_n)$	Three-dimensional velocity field at time t_n (m s^{-1}), referenced in Chapter 4
ν_C	Turbulent diffusion coefficient of a contaminant (m^2 s^{-1}), referenced in Chapter 4
v_s	Settling velocity (m d^{-1}), referenced in Chapters 2 and 6
$\widetilde{W}$	Wall proximity function, unitless, referenced in Chapter 3
w	Velocity component in the *z*-direction (m s^{-1}), referenced in Chapters 1, 2 and 3
$\overline{w}$	Mean velocity component in the *z*-direction (m s^{-1}), referenced in Chapter 3
x	East-west directional plane, unitless, referenced in Chapters 1, 2 and 3
$\vec{x}$	Particle position at time t_n (m), referenced in Chapter 4
x_n	Particle *x*-position at time t_n in the explicit Runge-Kutta scheme (m), referenced in Chapter 4

x_{n+1} Particle x-position at time t_{n+1} in explicit Runge Kutta scheme (m), referenced in Chapter 4

y North-south directional plane, unitless, referenced in Chapters 1, 2 and 3

y_n Particle y-position at time t_n in the explicit Runge-Kutta scheme (m), referenced in Chapter 4

y_{n+1} Particle y-position at time t_{n+1} in explicit Runge Kutta scheme (m), referenced in Chapter 4

z Vertical directional plane, unitless, referenced in Chapters 1, 2 and 3

$\boldsymbol{z}$ Vertical coordinate of particle location (m), referenced in Chapters 2 and 6

Γ Contaminant diffusivity ($m^2 s^{-1}$), referenced in Chapter 4

ζ Free surface elevation (m), referenced in Chapter 3

ξ_n Current particle position in x-plane at time n (m), referenced in Chapter 4

ξ_1 x term in the explicit Runge-Kutta scheme (m), referenced in Chapter 4

ξ_2 x term in the explicit Runge-Kutta scheme (m), referenced in Chapter 4

ξ_3 x term in the explicit Runge-Kutta scheme (m), referenced in Chapter 4

ξ_4 x term in the explicit Runge-Kutta scheme (m), referenced in Chapter 4

θ Temperature correction factor, unitless, referenced in Chapters 2 and 6

Ω^u Momentum control element area (m^2), referenced in Chapter 3

Ω^ζ Tracer control element area (m^2), referenced in Chapter 3

γ_n Current particle position in σ-plane at time n (m), referenced in Chapter 4

γ_1 σ term in explicit Runge Kutta scheme (m), referenced in Chapter 4

γ_2 σ term in explicit Runge Kutta scheme (m), referenced in Chapter 4

γ_3 σ term in explicit Runge Kutta scheme (m), referenced in Chapter 4

γ_4 σ term in explicit Runge Kutta scheme (m), referenced in Chapter 4

ε Dissipation rate of turbulent kinetic energy ($m^2 s^3$), referenced in Chapter 3

η_n Current particle position in y-plane at time n (m), referenced in Chapter 4

η_1 y term in explicit Runge Kutta scheme (m), referenced in Chapter 4

η_2 — y term in explicit Runge Kutta scheme (m), referenced in Chapter 4

η_3 — y term in explicit Runge Kutta scheme (m), referenced in Chapter 4

η_4 — y term in explicit Runge Kutta scheme (m), referenced in Chapter 4

κ — von Karman constant, unitless, referenced in Chapter 3

ρ_0 — Density of water (kg m^{-3}), referenced in Chapters 1, 2, 3 and 4

σ — Sigma coordinate in the vertical plane (m), referenced in Chapter 4

σ_n — Particle σ-position at time t_n in explicit Runge Kutta scheme (m), referenced in Chapter 4

σ_{n+1} — Particle σ-position at time t_{n+1} in explicit Runge Kutta scheme (m), referenced in Chapter 4

τ — Bed shear stress (m^2 s^{-2}), referenced in Chapters 1, 2 and 3

$\boldsymbol{\tau}$ — Time in explicit Runge-Kutta scheme (s), referenced in Chapter 4

ϖ — Vertical velocity component in the context of sigma coordinates (m s^{-1}), referenced in Chapter 4

$\hat{\varpi}$ — Vertical velocity component in the context of sigma coordinates, normalized to water depth and free surface elevation (m s^{-1}), referenced in Chapter 4

1. Introduction and Context:

1.1. Ensuring Public Health at Great Lakes Recreational Beaches

With over 17,000 km of shoreline, the Laurentian Great Lakes provide ample recreational and tourism opportunities for local municipalities and visitors alike (USEPA, 2019). Beach tourism alone brings 14–31 million people to the Chicago's shoreline per year (Nevers and Whitman, 2011). Many beachgoers engage in activities such as swimming, sunbathing and playing in sand at beach areas, frequently leading to exposure to any contaminants that may be entrained in the sand or water at the beach (Heaney et al., 2009).

At beaches, contaminants of human health concern are most frequently microbiological in nature and may include bacteria, viruses and protozoa, as well as emerging contaminants like antimicrobial resistant microorganisms and fungi (Corsi et al., 2016; da Costa Andrade et al., 2015; Sabino et al., 2011; Turgeon et al., 2012). These contaminants can come from both point (i.e., sewage outfalls) and nonpoint (i.e., runoff and wave deposition) sources, and their public health implications can vary widely, from gastrointestinal illness, to respiratory, skin or eye infections (Harwood et al., 2014).

Beginning in 2000, the *Beaches Environmental Assessment and Coastal Health (BEACH) Act* mandated the monitoring and management of recreational beaches across the USA for the benefit of public and environmental health (Beaches Environmental Assessment and Coastal Health Act (BEACH) Act, 2000). As a result of this mandate, management agencies have been sampling beach water to track contamination, water quality, and overall beach health for decades. However, this contaminant tracking frequently involves culturing indicator bacteria or amplifying contaminant genetic material via quantitative Polymerase Chain Reaction (qPCR) (Griffith and Weisberg, 2011; Lavender and Kinzelman, 2009). These processes can take three to 48 hours to yield water quality information and results, leading to a lag between water contamination events and beach actions such as swimming advisories or closures (USEPA, 2014a, 2013). Consequently, beachgoers may be exposed to contaminants of public health concern before water quality degradation has been discovered. Even with daily *in situ* beach water quality monitoring, public health in recreational areas is thus not always guaranteed.

Statistical, data-based and mechanistic models have been developed in recent years, to aid in the prediction and "nowcast" simulation of water quality at beaches. Statistical models such as multiple linear regression and partial least squares regression, and data-based (e.g., artificial neural network) models have shown promise in predicting recreational water quality using hydrometeorological conditions as input (Francy et al., 2013; He and He, 2008; Nevers and Whitman, 2005; USEPA, 2012; Zhang et al., 2018). Mechanistic models of hydrodynamics and water quality have also been able to simulate contaminant fate and transport in coastal areas with reasonable precision (Liu and Huang, 2012; Safaie et al., 2016; Thupaki et al., 2010). While these modeling approaches leave room for continued improvement and do not always capture nearshore water quality, they are becoming an intriguing option to supplement *in situ* monitoring for the purposes of beach management and public health decision making.

1.2. Southwestern Lake Michigan Beaches and Water Quality

With hundreds of beaches along its shore (EGLE, 2016; IDEM, 2016; IDPH, 2018; WDNR, 2000), Lake Michigan is a popular destination for local and visiting beachgoers alike. Water quality at these beaches can vary widely, both spatially and temporally. Jeorse Park beach, near the Illinois – Indiana border (Figure 1-1) has been regularly cited as one of the most polluted beaches in the US, exceeding the EPA–mandated contamination exceedance threshold of 2.37 $\log_{10}$(MPN 100 ml^{-1}) on more than 40% of the days that it is monitored. Meanwhile, only 13.5 km southeast of

Jeorse Park (Figure 1-1 *inset*), Marquette Park beach samples exceed 2.37 $\log_{10}$(MPN 100 ml^{-1}) on only 5% of days that it is monitored (Dorfman and Haren, 2014). Likewise, beach indicator bacteria concentrations can change by up to 4 orders of magnitude over the course of hours to days, especially during turbulent weather patterns, including storms (IDPH, 2018).

Figure 1-1: Google Earth imagery showing Lake Michigan, with inset focused on the highly contaminated Jeorse Park beach and the nearby but much less contaminated Marquette Park beach

Southwestern Lake Michigan beaches extend from Wilmette, Illinois to the Illinois–Indiana border. Water quality at these beaches, like at many others across the USA, is often impacted by point- and non-point contamination sources as well as meteorological, sunlight, seasonal and beach morphological influences (Byappanahalli et al., 2015; Heaney et al., 2014; Whitman et al., 2008). Southwestern Lake Michigan beaches are somewhat unique, though, in that they can also be impacted by the intense urbanization of the Chicago region as well as the heavy industrialization of oil refineries and steel mills in northwest Indiana.

1.3. Water Management and Heavy Storm Effects in Chicago

The city of Chicago, situated on the southwestern shore of Lake Michigan, has a population of 2.7 million (US Census Bureau, 2019). This highly urbanized area is impacted by the lake to the east as well as three river channels: the North Shore Channel in Wilmette, the Chicago River in downtown Chicago and the Calumet River near the Illinois–Indiana border (Figure 1-2). The water in the city, rivers and lake has been managed by the Metropolitan Water Reclamation District of Greater Chicago (MWRD; originally called the Chicago Sanitary District) since 1889 (MWRD, n.d.). From a recreational standpoint, the Chicago Park District (CPD) is responsible for beach water quality monitoring and management at Chicago's 24 public recreational beaches, determining when to advise against beach usage due to water quality degradation (CPD, 2020).

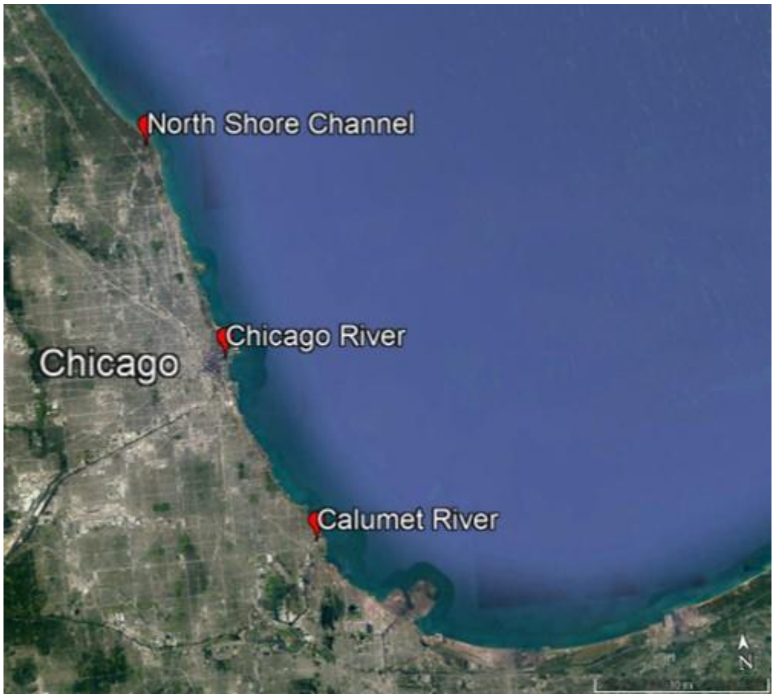

Figure 1-2: Google Earth imagery of the Chicago region, showing the three major river outlets affecting the city

1.3.1. The Unique River Conditions in Chicago

The Chicago area has presented a unique river flow regime since the early 1900's. Historically, there were only two rivers in the Chicago region (the Chicago River and the Calumet River), and both flowed eastward from upstream in their watersheds and toward Lake Michigan (Figure 1-3a) (ASCE, 2020; Hansen, 2009; Hill, 2019). By the mid-1800's, Chicago was growing rapidly, releasing sewage and stormwater into the Chicago River. As a result, highly contaminated water from the Chicago River was flowing into Lake Michigan, the primary drinking water source for residents of the city. Such contamination caused public health concerns and outbreaks of waterborne infections such as typhoid, cholera and dysentery within the city (ASCE, 2020; Hansen, 2009; Hill, 2019). In 1889, Chicago created the Chicago Sanitary District and between 1892 and 1900, a large-scale effort to dredge the riverbed and reverse the flow of the Chicago River was undertaken (ASCE, 2020; Hansen, 2009; Hill, 2019). A system of sluice gates and lock infrastructure was built at the mouth of the Chicago River. This system, called the Chicago River Controlling Works (CRCW) was used to help divert flows when necessary while supporting portage between the river and Lake Michigan (USACE, 2014). In the following decades, infrastructure for the North Shore Channel and Wilmette Pumping station (completed in 1910) and Thomas J. O'Brien lock and dam (completed in 1960) was implemented to further prevent the flow of water from the rivers into Lake Michigan (Figure 1-3b) (USACE, 2014).

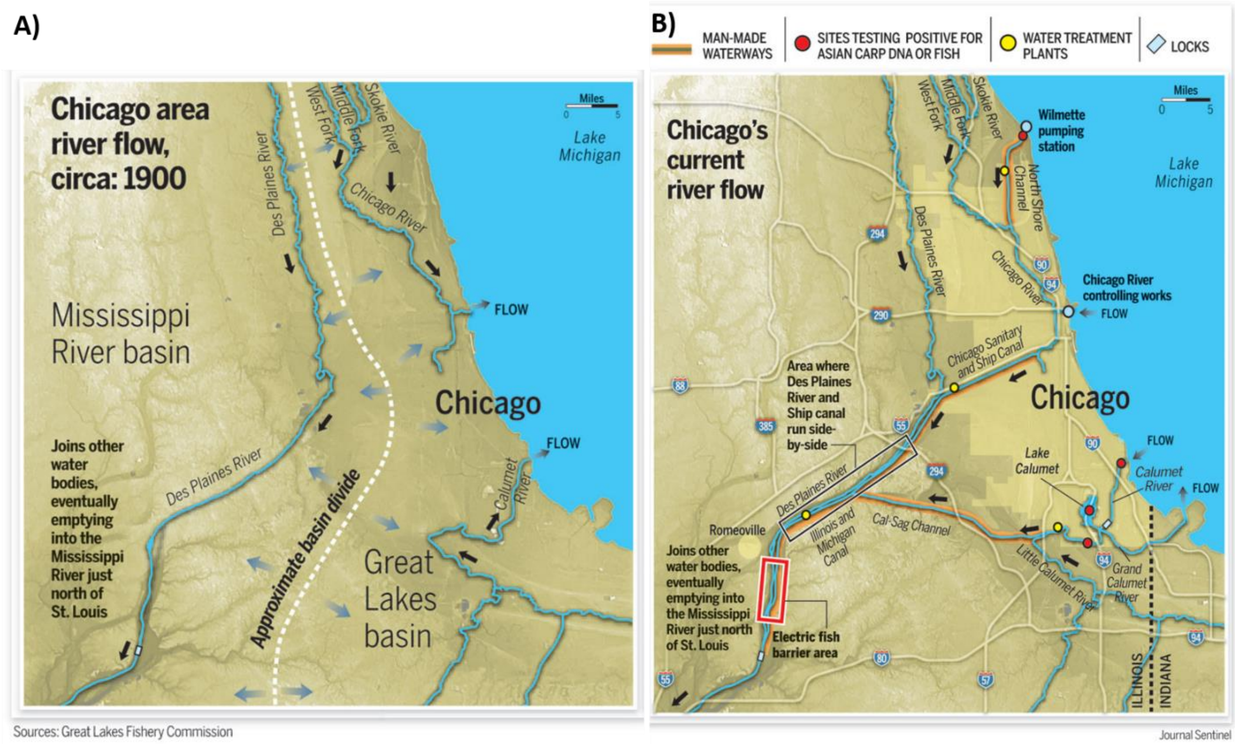

Figure 1-3: Schematics showing the difference in river flow regime in the Chicago area before (A, left) and after (B, right) the completion of the Chicago River flow reversal (1892 - 1900), Wilmette Pumping Station (1910) and O'Brien Lock and Dam (1960). Image adapted from the Great Lake Fishery Commission and the Milwaukee Journal Sentinel

Since 1960, the North Shore Channel, Chicago River and Calumet River have flowed westward to the Mississippi River under normal flow conditions (i.e., when there is low risk of flooding for Chicago or western downstream areas). However, the infrastructure at the Wilmette pumping station, CRCW and O'Brien lock and dam were put into place so that river flows can be directed back into the lake during heavy storm events. This combination of river flow reversals (also known as backflow events) and flow control structures allows for a balance between preserving Lake Michigan water quality and preventing flooding within Chicago during storms (USACE, 2014). Herein, any storm that threatens flooding in the Chicago area and thus necessitates a backflow to Lake Michigan will be deemed a "heavy storm" or "extreme storm".

1.3.2. Backflow Events and Their Impact on Beach Management

During heavy storms that precipitate backflow events in Chicago, the infrastructure at Wilmette pumping station and the CRCW and O'Brien locks and dams are engaged to send stormwater back into Lake Michigan in the form of river plumes.

Backflow events are relatively uncommon, occurring an average of 1.0 times per year, for 1.51 days annually, on average, since 1985 (USACE, 2014, MWRD, 2019). There is no single threshold for amount of rainfall or storm return period to trigger a backflow event in Chicago. Initiation of backflow involves assessment of factors such as the timing and duration of the storm, the area over which the rain falls, and status of the stormwater management system and reservoir capacity (Duncker and Johnson, 2016). As a result, storms with return periods ranging from two months to 100 years (NOAA National Weather Service, 2020) have precipitated backflow events in Chicago. Between 1985 and 2017, the Chicago region experienced 32 storms that resulted in backflow events. These storms produced 3.91 (August 1985) to 23.75 (August 1987) cm of precipitation at Chicago O'Hare Airport (NOAA National Weather Service, 2020). While there were no backflows in 1988, 1991 – 1995, 1998, 2000, 2003 – 2006 and 2012, other years such as 1985, 1987, 1990, 1997, 2001, 2008, 2009, 2011 and 2017 yielded multiple backflow-inducing storms (Figure 1-4). These backflow events often have a duration of 24 hours or less, but on occasion, extreme storms will facilitate multiple-day backflows (e.g., 13 – 16 September 2008). The volume of water released during backflow events is dependent upon the amount of rain that the city receives, with total volumes for the 32 events ranging from 35,961.41 m^3 (17 – 18 August 1990) to 41,825,393.30 m^3 (13 – 16 September 2008) (Table 1-1, Figure 1-5) (USACE, 2014).

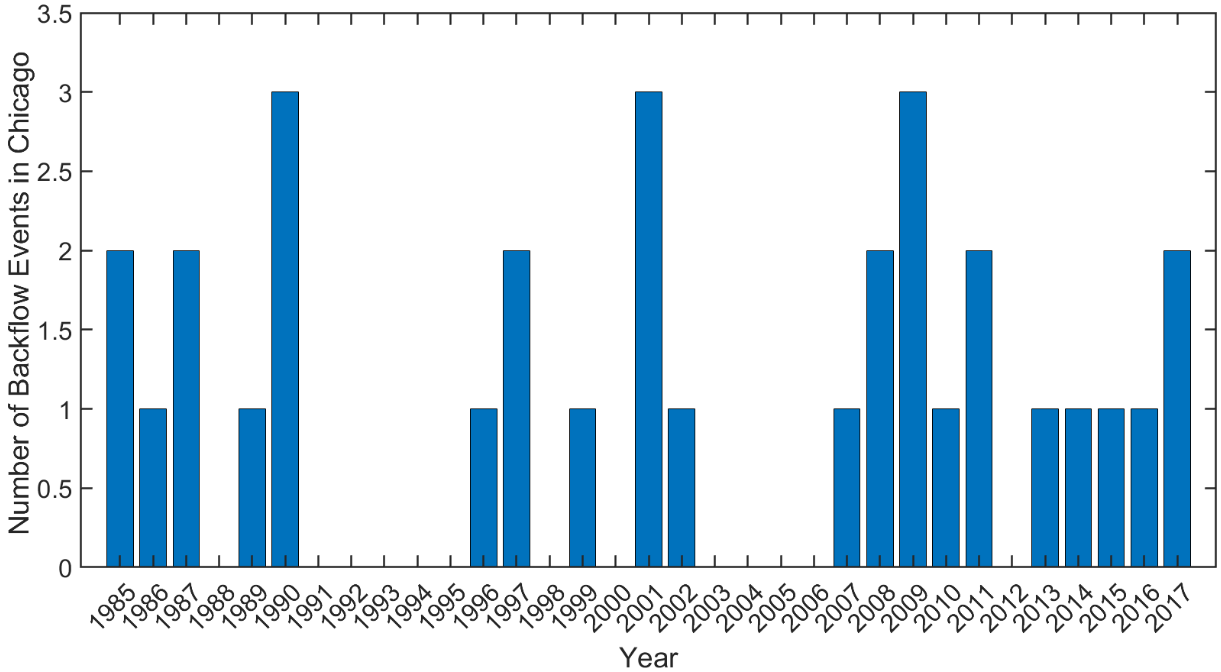

Figure 1-4: Bar plot showing the annual frequency of backflow events in the Chicago area, 1985 - 2017

Table 1-1: Annual number of backflow events, number of days under backflow conditions and total volume of stormwater released during backflows, 1985 – 2017

Year	Number of Backflow Events	Number of Days Under Backflow Conditions	Annual Total Volume of Water Released During Backflows (m^3)
1985	2	2	799857.51
1986	1	1	200626.82
1987	2	4	7476188.27
1988	0	0	0
1989	1	2	196841.41
1990	3	6	3673742.14
1991	0	0	0
1992	0	0	0
1993	0	0	0
1994	0	0	0
1995	0	0	0
1996	1	2	5871173.68
1997	2	5	17935281.03
1998	0	0	0
1999	1	1	36718.49
2000	0	0	0
2001	3	3	4500854.61

Table 1-1 (cont'd)

2002	1	1	6631284.36
2003	0	0	0
2004	0	0	0
2005	0	0	0
2006	0	0	0
2007	1	2	874932.24
2008	2	6	43569711.09
2009	3	4	1565646.31
2010	1	1	24737287.47
2011	2	2	8810545.93
2012	0	0	0
2013	1	2	40577721.62
2014	1	2	1987341.19
2015	1	2	4408869.11
2016	1	1	128741.85
2017	2	4	10468556.29

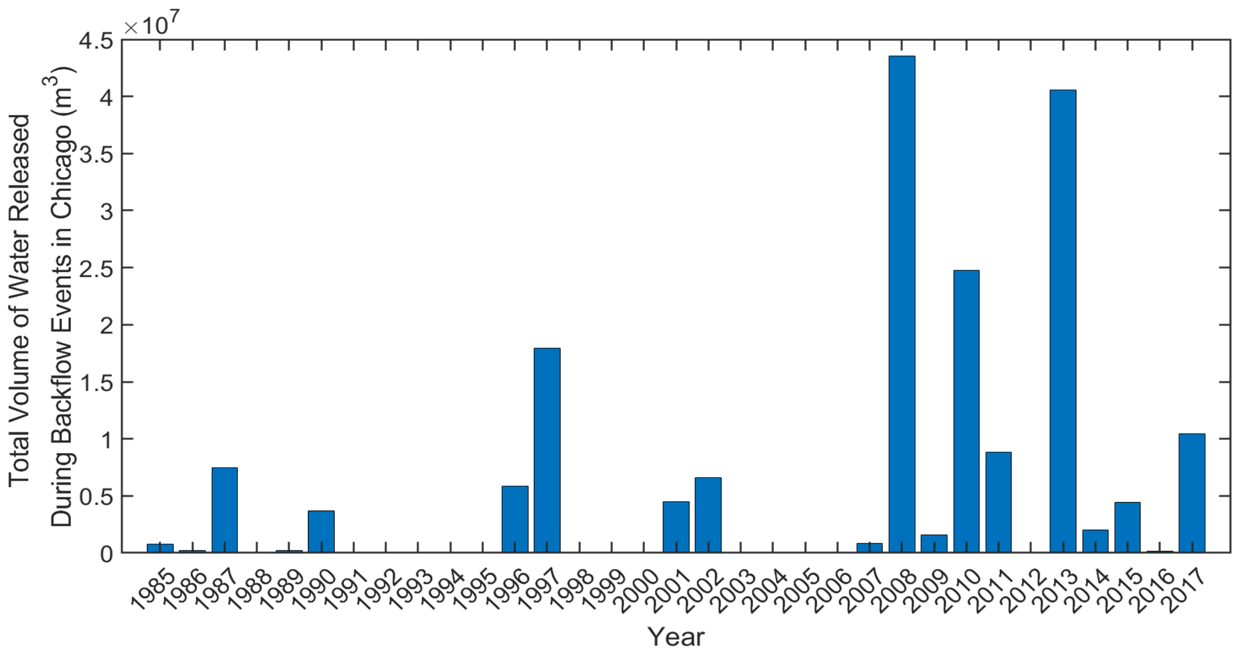

Figure 1-5: Bar plot showing the total volume of water released during backflow events each year, 1985-2017

While observational data regarding the water quality in the stormwater released during backflow events are scarce, it is likely that the water carried through the rivers and out to Lake Michigan during these events is composed of runoff from upstream watersheds. This runoff may contain biological and chemical contaminants associated with the urban Chicago area, industrial region of northwest Indiana and the agricultural land west of the city. In the resulting plumes, these contaminants may move from the river outlets and to the nearshore areas of Lake Michigan, potentially degrading beach water quality and fostering swimming advisories at local beaches (City of Chicago, 2014).

1.4. Brief Introduction to Water Quality Numerical Modeling with the Finite Volume Community Ocean Model (FVCOM)

In the absence of observational data to track water quality within backflow-induced river plumes in Lake Michigan, modeling can be valuable in characterizing the dynamics and water quality impacts of backflow events. There is a wide range of numerical and mechanistic models available for application to natural waters (Blumberg and Mellor, 1987; Bravo et al., 2017; Hamrick et al., 1992; Lesser et al., 2004; Madani et al., 2020), and these models can be powerful tools for simulating nearshore hydrodynamics and their resulting impacts on water quality. One example of such models is the Finite Volume Community Ocean Model (FVCOM) (Chen et al., 2006).

FVCOM is an unstructured-grid, finite-volume, fully three-dimensional model that can couple hydrodynamics with ice, sediment, ecosystem, water quality, or wave functions to simulate conditions in coastal aquatic ecosystems (Chen et al., 2006, 2003). This framework utilizes the primitive momentum (Eq. 1-1a-c), continuity (Eq. 1-2), temperature (Eq. 1-3), salinity (Eq. 1-4) and density (Eq. 1-5) equations.

$$\frac{\partial u}{\partial t} + u\frac{\partial u}{\partial x} + v\frac{\partial u}{\partial y} + w\frac{\partial u}{\partial z} - fv = -\frac{1}{\rho_o}\frac{\partial(p_H + p_a)}{\partial x} - \frac{1}{\rho_o}\frac{\partial q}{\partial x} + \frac{\partial}{\partial z}\left(K_m\frac{\partial u}{\partial z}\right) + F_u \quad \text{(1-1a)}$$

$$\frac{\partial v}{\partial t} + u\frac{\partial v}{\partial x} + v\frac{\partial v}{\partial y} + w\frac{\partial v}{\partial z} + fu = -\frac{1}{\rho_o}\frac{\partial(p_H + p_a)}{\partial y} - \frac{1}{\rho_o}\frac{\partial q}{\partial y} + \frac{\partial}{\partial z}\left(K_m\frac{\partial v}{\partial z}\right) + F_v \quad \text{(1-1b)}$$

$$\frac{\partial w}{\partial t} + u\frac{\partial w}{\partial x} + v\frac{\partial w}{\partial y} + w\frac{\partial w}{\partial z} = -\frac{1}{\rho_o}\frac{\partial q}{\partial z} + \frac{\partial}{\partial z}\left(K_m\frac{\partial w}{\partial z}\right) + F_w \quad \text{(1-1c)}$$

$$\frac{\partial u}{\partial x} + \frac{\partial v}{\partial y} + \frac{\partial w}{\partial z} = 0 \quad \text{(1-2)}$$

$$\frac{\partial T}{\partial t} + u\frac{\partial T}{\partial x} + v\frac{\partial T}{\partial y} + w\frac{\partial T}{\partial z} = \frac{\partial}{\partial z}\left(K_h\frac{\partial T}{\partial z}\right) + F_T \quad \text{(1-3)}$$

$$\frac{\partial S}{\partial t} + u\frac{\partial S}{\partial x} + v\frac{\partial S}{\partial y} + w\frac{\partial S}{\partial z} = \frac{\partial}{\partial z}\left(K_h\frac{\partial S}{\partial z}\right) + F_S \quad \text{(1-4)}$$

$$\rho = \rho(T, S, p) \quad \text{(1-5)}$$

In these equations, (u, v, w) are the velocity components of water currents in the east-west (x), north-south (y), and vertical (z) directions, respectively (m s^{-1}), while t is time. fu and fv are Coriolis terms for the x and y directions, F_u, F_v are horizontal diffusion terms in the x and y directions, respectively and F_w represents a vertical diffusion term (m^2 s^{-1}). K_m is a vertical eddy viscosity coefficient (m^2 s^{-1}), ρ_0 is the density of water (kg m^{-3}), p_a is air pressure (Pa), p_H represents hydrostatic pressure (Pa) and q is non-hydrostatic pressure (Pa). In Eq. 1-3, T denotes temperature (°C), while S in Eq. 1-4 is salinity (PSU) and p in Eq. 1-5 is a generalized pressure term (Pa) (Chen et al., 2006). These equations are solved over a computational mesh of the model domain (Figure 1-6) between time steps to simulate hydrodynamics within FVCOM.

Figure 1-6: Sample model domain mesh grid for Lake Michigan, showing triangular grid elements joined by nodes, where FVCOM calculations for meteorology, hydrodynamics and water quality variables are interpolated

Inputs to FVCOM include the bathymetry of the water body to be modeled, data from meteorological stations and buoys surrounding the model domain, as well as stream gauge data corresponding to the river flows that can impact nearshore circulation. Meteorological data inputs include air temperature, water temperature, air pressure, precipitation, relative humidity, wind speed and wind direction observations over the model temporal domain, while river input data include discharge time series and, optionally, salinity and water temperature in rivers over time. Bathymetry of the water body, and in turn, depth of the water column, are interpolated to the model domain's mesh as an input.

As the model runs, it uses Eq. 1-1 – 1-5 to calculate hydrodynamics as a function of meteorological forcing (wind, precipitation, solar radiation) and the Coriolis effect due to Earth's rotation. Important model parameters include turbulent vertical and horizontal eddy viscosities, horizontal and vertical diffusivities, and parameters associated with bed shear stress (τ, m^2 s^{-2}). Model results for the computational domain are exported over hourly timesteps. This allows for the model to simulate these conditions spatiotemporally (Chen et al., 2006, 2003).

FVCOM is a fully three-dimensional model that uses a terrain-following (sigma-) coordinate system in the vertical direction (Figure 1-7). The sigma layers ensure that the water column is uniformly discretized, regardless of the local depth, ensuring that vertical processes are adequately resolved. Thus, model results can vertically-integrated for subsequent analysis (Chen et al., 2006, 2003).

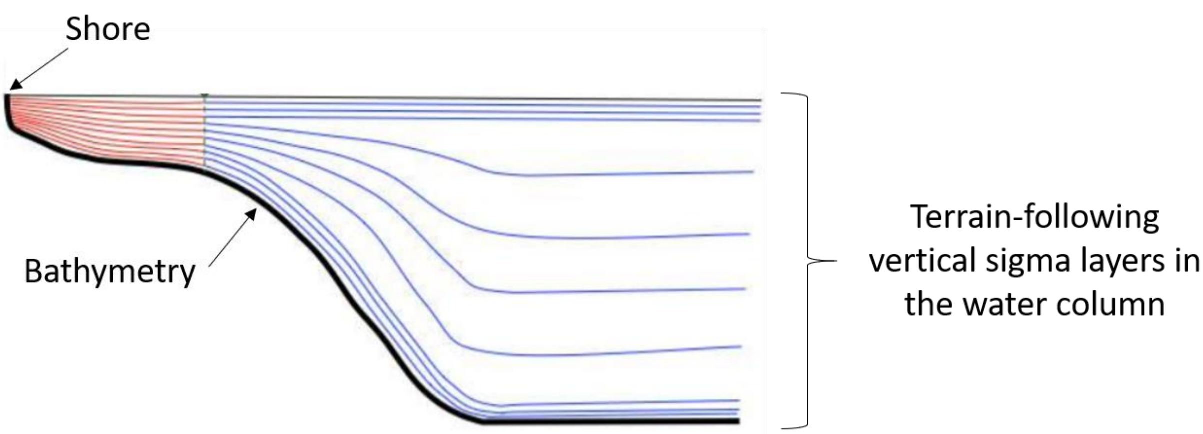

Figure 1-7: Schematic showing how terrain-following sigma layers are utilized within the FVCOM framework, to discretize vertically-variable conditions and make the resulting models fully three-dimensional. Image adapted from Chen et al. (2006)

In addition to the base hydrodynamics modeled by FVCOM, Eulerian modules such as the water quality model, specific contaminant models and the offline Lagrangian Particle Tracking model can be activated to track contamination in the water across space and time. The Eulerian models take contaminant concentration values and locations as initial conditions and use the hydrodynamics of the water body to calculate subsequent contaminant concentrations in the water body over time (Ge et al., 2012a; Ji et al., 2008; Rowe et al., 2019; Safaie et al., 2016; Thupaki et al., 2013, 2010). In contrast, the Lagrangian approach utilizes input of discrete particle locations within the model domain as initial conditions, using hydrodynamics to track the locations of individual particles within the water over time (Anderson and Phanikumar, 2011; Huang et al., 2019; Nekouee et al., 2015; Rowe et al., 2016). Each of these modeling approaches is slightly different from the others, and there are tradeoffs in the use of any of them, depending upon the modeling context and research questions. All three have been used previously to track contaminants, but the Lagrangian approach is used less frequently than Eulerian approaches like FVCOM's built-in water quality and general ecological models (Bravo et al., 2017; Huang et al., 2019; Nekouee et al., 2015).

1.5. Research Objectives

Extreme precipitation events (i.e., those that facilitate backflows of the Chicago River, North Shore Channel and Calumet River) create conditions that make *in situ* sampling and observation of water quality and river plumes difficult. For this reason, beach managers at the CPD take a conservative approach to the protection of public health, closing large swathes of the shoreline during backflow events (USACE, 1996). For example, if a backflow event occurs at the Wilmette Pumping Station, all beaches from Evanston, IL to Ohio St. Beach in downtown Chicago are closed. If either CRCW or O'Brien Lock release stormwater to Lake Michigan, all beaches in Illinois that are south of Ohio St. close (USACE, 1996). Only within 24 hours of the end of a backflow event does MWRD sample beaches near the river outlets to determine bacterial and chemical water quality, to make decisions regarding the re-opening of beaches (MWRD, 2019). While it stands to reason that stormwater plumes associated with backflow events can rapidly degrade recreational water quality and impact public health (City of Chicago, 2014), there is a lack of observational data to support or refute this idea. Modeling can help visualize and characterize the effects of backflow events on recreational water quality in Chicago, potentially allowing for more targeted management of beaches during and after storms. With this in mind, the overarching research goal of this dissertation is to use numerical modeling techniques to characterize backflow-induced river plumes in the Chicago area, to describe the spatial and temporal scales of their impacts on the nearshore zone and local beach water quality.

There are two classes of potential approaches to characterizing contaminant plumes in natural waters: Eulerian and Lagrangian. Each of these approaches has advantages and drawbacks, depending on model context and research questions. The first objective of the research is to test the predictive capacity of each, to optimize the prediction of backflow-associated contaminant plumes in Lake Michigan against the limited observational data available for the plumes. The Eulerian approach to modeling river plumes has known limitations including excessive numerical diffusion that tends to smear plumes while overestimating their spatial extent. This approach is also inherently unable to resolve plume details at scales smaller than the mesh size. Due to these limitations, the Lagrangian approach is expected to lead to tighter plumes relative to those produced by the Eulerian method. For this reason, it is predicted that a Lagrangian approach will better simulate backflow-associated contaminant plumes, compared to Eulerian methods.

Once an optimal modeling framework is determined for reliable simulation of backflow-associated contaminant plumes from the three Chicago-area river outlets, that optimal model approach will be used to simulate the impacts of multiple backflow events in the area. Five backflow events in Chicago, between 2008 and 2017, will be simulated using the optimal model approach, to determine the spatiotemporal scales of the contaminant plumes along the Chicago shoreline. These five events occurred in September 2008, July 2010, July 2011, April 2013 and October 2017, and released 8,405,507 to 41,825,393 m^3 of stormwater to Lake Michigan (USACE, 2014). Due to differential volumes of water released between the backflow events, it is predicted that the spatiotemporal scales of plumes will also vary. Plumes of higher volumes can be expected to have larger areas of influence, impacting more of the shoreline for longer periods than plumes of smaller volumes. However, storms leading to backflow events are expected to lead to volatile wind and wave conditions within the lake, potentially fostering mixing and rapid dispersion of the plumes in the lake. Based on assessment of satellite imagery (Vermote, 2015), backflow-associated plumes are hypothesized to impact beaches and nearshore areas within 5 – 10 km of the three river outlets in the Chicago area, depending upon wind conditions, before dispersing into the lake. Likewise, plumes are expected to impact the nearshore areas in Chicago for 1 – 5 days after the end of the backflow releases.

To link the backflow plume dynamics and scales to public health in Chicago, the plume simulations for backflow events in 2010 and 2011 will be adjusted to simulate the microbial water quality dynamics associated with the plumes. Extending the research to public health and water quality will require the simulation of fecal indicator bacteria contamination and the factors influencing its fate and transport (Ge et al., 2012b; Safaie et al., 2016; Thupaki et al., 2010). Using a calibrated Lagrangian particle tracking model that incorporates these fate and transport factors, a novel coupled hydrodynamic and particle tracking model will simulate backflow-induced river plumes and the fate and transport of *E. coli* within them. By including factors associated with solar inactivation, base mortality, settling, and/or biological interactions, models may predict how beach water quality is impacted by these storm-associated contaminant plumes. Due to these additional factors influencing microbial decay in the plumes, it is expected that plumes of microbial contamination will reach nearby Chicago beaches but may be limited in their spatial and temporal impacts on recreational water quality. Beaches nearer to the river outlets will likely be more greatly affected by the plumes than those farther away, and the impacts on beaches will likely decline over time, as the plumes disperse into the lake. Generally, it is hypothesized that microbial water quality degradation associated with backflow plumes may not impact all beaches along the shore in the same way. Consequently, the CPD and MWRD approach to broadly closing beaches during backflow events may be overly conservative. Some beaches – especially those farther from river outlets – may be able to safely stay open to recreation during and after backflow events. Similarly, some beaches may be at increased risk due to storm-associated plumes and may require additional management during and after storms.

2. Numerical Modeling of Microbial Fate and Transport in Natural Waters: Review and Implications for Normal and Extreme Storm Events

2.1. Introduction

Water systems and the recreational opportunities that they afford bring millions of people outside each year, especially during warm weather. Over 75% of people traveling in the summer visit beaches, and in Chicago alone, 20 million people go to Lake Michigan beaches annually, on average (Klein et al., 2004; Nevers and Whitman, 2011). To protect public health and the safety of beachgoers, the *Beaches Environmental Assessment and Coastal Health* (BEACH) Act of 2000 requires routine monitoring of coastal water quality at both marine and freshwater beaches across the USA (*Beaches Environmental Assessment and Coastal Health Act (BEACH Act)*, 2000). This monitoring, however, often involves obtaining samples and either culturing for fecal indicator organisms (FIO) such as *E. coli* or enterococci or using quantitative Polymerase Chain Reactions (qPCR) to determine FIO concentrations in the water. These approaches take time, leading to a delay of up to 24 hours before obtaining water quality information to effectively manage beach usage for public health. This delay can be the difference between keeping beachgoers safe by advising against beach access and putting them in danger by keeping a contaminated beach open for recreation.

To avoid the lag time associated with water sample analyses, mechanistic, statistical and other data-based models have emerged as potentially feasible alternatives to daily water quality monitoring. These models incorporate parameters associated with meteorology, hydrodynamics, human and wildlife usage, water turbidity, and settling of suspended sediments to predict microbial concentrations (Abu-Bakar et al., 2017; Bravo et al., 2017; Eregno et al., 2018; Francy et al., 2009; Garcia-Alba et al., 2019; Ge et al., 2012b; Liu et al., 2006; Madani et al., 2020; Nevers et al., 2020;

Nevers and Whitman, 2005; Safaie et al., 2016; Shively et al., 2016; Thupaki et al., 2010; Wong et al., 2009; Zhang et al., 2018, 2015, 2012).

Numerical mechanistic models have shown variable success in predicting microbial concentrations in coastal and beach systems across space and time. As knowledge of aquatic systems and their various influences on waterborne microorganisms has progressed in recent years, predictive capacity of models has increased as well (Hipsey et al., 2008; Liu et al., 2006; Madani et al., 2020; Safaie et al., 2016). However, with a still incomplete knowledge of how components of the aquatic environment interact to influence microbial fate and transport, improving the representation of processes as well as source behavior, parameter identification and model evaluation remains an evolving process.

This process is further complicated by the often rapidly-changing conditions within aquatic environments. For example, Lakes Michigan and Huron in the Laurentian Great Lakes, USA, have become significantly clearer since the 1990's. in response to an invasion by dreissenid mussels (Binding et al., 2015; Fahnenstiel et al., 2010; Yousef et al., 2017). This clarification likely impacts microbial survival in the water, due to the subsequent changes in sunlight extinction and solar microbial inactivation rates in the water (Weiskerger and Whitman, 2018). Similarly, changes to microbial sources and hydrodynamics associated with climate change (Curriero et al., 2001; Delpla and Rodriguez, 2014; Patz et al., 2008; Xu et al., 2019) may lead to changes in how microbial fate and transport can be effectively modeled. Not only is sea level predicted to rise due to climate change, frequency and intensity of storm events are projected to increase for many regions as well (IPCC, 2014). Sea level rise will undoubtedly change the layout of beach areas, leading to phenomena like shoreline erosion and increased foreshore areas that are susceptible to microbial transfer between water and sand (Dvorak et al., 2018). At the same time, a predicted increase in the frequency and intensity of storm events will likely lead to increased runoff of urban and agricultural contaminants to rivers, which will in turn flow to coastal areas and potentially impact beach water quality (Dwight et al., 2002).

Herein, we aim to compare the various approaches to modeling microbial (i.e., FIO) fate and transport in coastal aquatic environments using coupled mechanistic hydrodynamic and transport modeling approaches, to determine how these approaches impact model predictive capability. Examples of such models include the Finite Volume Community Ocean Model (FVCOM) (Chen et al., 2006), the Princeton Ocean Model (POM) (Blumberg and Mellor, 1987; Bravo et al., 2017; Thupaki et al., 2013, 2010), the Aquatic Ecosystem Model 3D (AEM3D) (Madani et al., 2020), Delft3D (Lesser et al., 2004), and the Environmental Fluid Dynamics Code (EFDC) (Hamrick, 1992) to name only a few. For the purposes of this review, we will concentrate on these mechanistic and process-based models of FIO fate and transport, but statistical and data-based modeling approaches are briefly discussed to the extent that they can support mechanistic modeling efforts. We then discuss the application of such approaches to emerging modeling questions surrounding the simulation of storm-associated river plumes and microbial exchange between beach sand and water. While nearshore environments harbor a variety of microorganisms, including bacteria, viruses and fungi, this work will focus on modeling of FIO such as *E. coli*, enterococci, and coliforms. Understanding how numerical models predict water quality will lend insight into which approaches may be most appropriate for modeling recreational water quality to ensure public health in the face of climatic and environmental changes.

2.2. Modeling Hydrodynamics and Microbial Fate & Transport

Numerical modeling of hydrodynamics in coastal environments depends heavily on the physics of the water body, meteorological conditions over time and the impacts of river/estuary inputs. Water moves in three spatial dimensions and over time, so utilizing a 3-Dimensional hydrodynamic model is key to adequately simulating water movement in coastal areas. Unstructured grid models (e.g., FVCOM) may have advantages in simulating coastal water quality due to their ability to accurately represent nearshore features such as irregular coastlines, barrier islands and sandbars, harbors, breakwaters etc.

Generally, coastal hydrodynamics are governed by 3-Dimensional, unsteady forms of the Navier-Stokes momentum equations (Eq. 2-1 – 2-3) and the assumption of the continuity equation (Eq. 2-4) (Chen et al., 2006, 2003; Liu, 2018).

$$\frac{\partial u}{\partial t} + u\frac{\partial u}{\partial x} + v\frac{\partial u}{\partial y} + w\frac{\partial u}{\partial z} - fv = -\frac{1}{\rho_o}\frac{\partial(p_H + p_a)}{\partial x} - \frac{1}{\rho_o}\frac{\partial q}{\partial x} + \frac{\partial}{\partial z}\left(K_m\frac{\partial u}{\partial z}\right) + F_u \qquad (2\text{-}1)$$

$$\frac{\partial v}{\partial t} + u\frac{\partial v}{\partial x} + v\frac{\partial v}{\partial y} + w\frac{\partial v}{\partial z} + fu = -\frac{1}{\rho_o}\frac{\partial(p_H + p_a)}{\partial y} - \frac{1}{\rho_o}\frac{\partial q}{\partial y} + \frac{\partial}{\partial z}\left(K_m\frac{\partial v}{\partial z}\right) + F_v \qquad (2\text{-}2)$$

$$\frac{\partial w}{\partial t} + u\frac{\partial w}{\partial x} + v\frac{\partial w}{\partial y} + w\frac{\partial w}{\partial z} = -\frac{1}{\rho_o}\frac{\partial q}{\partial z} + \frac{\partial}{\partial z}\left(K_m\frac{\partial w}{\partial z}\right) + F_w \qquad (2\text{-}3)$$

$$\frac{\partial u}{\partial x} + \frac{\partial v}{\partial y} + \frac{\partial w}{\partial z} = 0 \qquad (2\text{-}4)$$

In these equations, *x*, *y*, and *z* represent the east, north and vertical directions, while *u*, *v*, and *w* denote the velocity components in the *x*, *y*, and *z* directions, respectively (m s^{-1}). *fu*, *fv* are the Coriolis terms, F_u, F_v are the horizontal diffusion terms in the x and y directions, respectively and F_w is a vertical diffusion term (m^2 s^{-1}). K_m denotes a vertical eddy viscosity coefficient (m^2 s^{-1}) and ρ_o represents the density of water (kg m^{-3}). Air pressure at the water surface is denoted by p_a, hydrostatic pressure is represented by p_H and *q* is the non-hydrostatic pressure (all in Pa) (Chen et al., 2006). Using these equations, models can effectively account for the effects of temperature, density, and Coriolis force on water movement over time. The effects of waves in the nearshore environment (e.g., wave-current interactions, bottom shear stress) can be simulated using coupled hydrodynamic and spectral wave models such as the FVCOM-Surface Wave (FVCOM-SWAVE) model (Qi et al., 2009).

Building on the general hydrodynamic model, microbial fate and transport associated with diffusion, dispersion, advection, and mortality within an aquatic system can be simulated (Abu-Bakar et al., 2017; Bravo et al., 2017; Chapra, 2008; Eregno et al., 2018; Hipsey et al., 2008; Liu et al., 2006; Madani et al., 2020; Safaie et al., 2016; Thupaki et al., 2010). The governing equation for microbial fate and transport is based on the advection-dispersion-reaction (ADR) equation, formulated in terms of FIO concentration (Eq. 2-5). This equation includes terms for advection, diffusion/dispersion in the water column, and microbial decay (Chen et al., 2006; Safaie et al., 2016).

$$\frac{\partial C}{\partial t} + u\frac{\partial C}{\partial x} + v\frac{\partial C}{\partial y} + w\frac{\partial C}{\partial z} = \frac{\partial}{\partial x}\left(K_H\frac{\partial C}{\partial x}\right) + \frac{\partial}{\partial y}\left(K_H\frac{\partial C}{\partial y}\right) + \frac{\partial}{\partial z}\left(K_V\frac{\partial C}{\partial z}\right) - kC \tag{2-5}$$

In the equation, C corresponds to the microbial concentration (Colony Forming Units (CFU) 100 ml^{-1}), k represents the overall microbial decay rate (d^{-1}), and K_V and K_H are the vertical and horizontal mixing coefficients, respectively ($m^2 s^{-1}$). Horizontal and vertical mixing are described using the Smagorinsky and Mellor-Yamada 2.5 level turbulence parameterizations (Chen et al., 2006, 2003). Microbial decay can depend on factors such as microbial taxon and base mortality, water temperature and chemistry, attachment to and detachment from suspended solids, settling after attachment to suspended solids, sunlight inactivation, and interactions with other biota in the aquatic environment (Hipsey et al., 2008). Because of its dependence on these factors, the decay term in mechanistic models has taken on many forms within the literature and is often a combination of multiple terms.

2.3. Boundary and Initial Conditions

Key drivers of hydrodynamics in the nearshore region include winds and/or tides (Nguyen et al., 2017, 2014) and riverine/estuarine flows (Abu-Bakar et al., 2017; Gao et al., 2015, 2011; Kashefipour et al., 2006). These are often governed by local conditions such as bathymetry, wind stress, Coriolis force, and water temperature, which can vary spatiotemporally. For example, seasonality of thermal or density stratification in large lakes such as Lake Michigan can impact circulation as well as buoyancy of contaminant plumes, leading to differential impacts on water quality and hydrodynamics throughout the year (Beletsky and Schwab, 2001; Nekouee et al., 2015a). Similarly, estuarine exchange flows and the corresponding changes in vertical density stratification (and hence vertical mixing) are controlled by the along-channel wind component which changes seasonally (Scully et al., 2015). In addition to seasonal-temporal variability in fluid properties, there are spatial influences that control hydrodynamics. The impacts of Coriolis force can vary by latitude as well as water body size, with effects becoming significant for large (> 5 km width) lakes and at high latitudes (Mortimer, 1974). Because these effects can vary spatiotemporally while also influencing large-scale hydrodynamics by influencing stratification, it is important to specify related model boundary conditions as realistically as possible.

Boundary conditions for the momentum equations are well-known and include wind stress on the surface of the water column and bed friction on the lake/seabed; additional details are available in Chen et al. (2006, 2003). For the FIO transport model, the nature of the source(s) dictates the type of boundary conditions used. For beaches impacted by riverine sources, monitoring data collected at the river mouth can be used to provide boundary forcing for the FIO transport model. However, most mechanistic models use small time steps (on the order of seconds to minutes) while monitoring data are collected less frequently (e.g., weekly or bi-weekly), introducing significant uncertainty into the modeling due to a mismatch between the model time steps and forcing data. In addition, model inputs are generally specified at regular intervals while monitoring data may be irregular and with gaps (e.g., missing data during weekends).

One way to address this limitation is to use calibrated watershed models (Bedri et al., 2014; Mohammed et al., 2019; Niu and Phanikumar, 2015) or statistical models to generate high-resolution boundary forcing data at the river mouth when high-resolution discharge data are available (e.g., at a United States Geological Survey (USGS) gauging station in the USA). Several researchers have exploited a potential correlation between river discharge (Q) and FIO (e.g., *E. coli*) concentrations (C) and have used statistical relations between Q and C to generate high-resolution tributary loading data for nearshore FIO models (Bravo et al., 2017; Madani et al., 2020; Safaie et al., 2016). Compared to the use of sparse monitoring data to represent tributary loading in FIO models, these approaches have promise as they can better describe rapid changes in loading and may be suitable for simulating the impacts of extreme storm events on microbial water quality in coastal areas. For beaches with no known riverine sources, observed FIO dynamics may be driven by local sources including birds (Converse et al., 2012; Eregno et al., 2018; Nevers et al., 2018), resuspension of bottom sediment-bound FIO (Gao et al., 2015, 2011) and shoreline sand (Nevers et al., 2020; Weiskerger et al., 2019). A comprehensive analysis of the relative importance of the different sources calls for detailed modeling of hydrodynamics including currents and waves, sediment transport, sediment-FIO interactions and relatively fine computational grids to capture the impact of shoreline birds and sand. Because initial conditions for hydrodynamic models of lakes and reservoirs may specify a waterbody that is initially at rest (zero velocity components), a spin-up period is often used to allow models to catch up with observed data. For FIO models, the initial concentration of FIO may include a small non-zero background value and model spin-up time may allow for increased water quality predictability over the model simulation period.

2.4. Components of the Microbial Decay Function

One generic form of the microbial decay function from Eq. 2-5 is represented by Eq. 2-6, where total microbial loss (k) is characterized by the combination of a base mortality rate (k_{b1}), light inactivation rate (k_{bi}) and settling rate (k_{bs}) (Chapra, 2008; Sokolova et al., 2013). All of the decay terms in the equation are daily decay rates (units of d^{-1}).

$$k = k_{b1} + k_{bi} + k_{bs} \tag{2-6}$$

The factors that influence these three terms, though, can be variable and specific to the model domain, context, and aims.

Liu et al. (2006) further separated this basic decay function for Lake Michigan, yielding a function that accounted for bacterial loss due to settling and light inactivation, with a temperature correction factor to justify changes due to temperature variations from 20°C (Eq. 2-7). In this model, f_p is the fraction of FIO particles attached to suspended solids (unitless), v_s represents settling velocity (m d^{-1}), H is the depth of the water column (m), k_I is the inactivation rate associated with solar radiation (m^2 W^{-1} d^{-1}), I_t denotes the solar irradiance at the surface of the water at time t (W m^{-2}), θ is the temperature correction factor (unitless), and T is the water temperature (°C).

$$k = \left[\frac{f_p v_s}{H} + k_I I_t\right] \theta^{T-20} \tag{2-7}$$

The right-hand side of this equation is composed of a sedimentation/settling term, a light inactivation term, and a temperature correction factor, when read from left to right. Though it incorporates terms for temperature, settling, and sunlight impacts on FIO, this form of the decay function fails to account for other potentially important influences.

Microbial survival in aquatic systems can be subject to impacts due to temperature, salinity, light penetration and inactivation, predation, competition for resources, nutrient availability and other natural (or base) mortality. Similarly, conditions such as the presence of aquatic vegetation and dreissenid mussels in a water body can impact bottom shear stress, thereby influencing sedimentation and resuspension of FIO. These factors can be difficult to characterize, especially when they vary between systems. In marine or brackish ecosystems where salinity may vary over time and space, it can have a substantial impact on the survival and persistence of several microorganisms (Anderson, 1979; Carlucci and Pramer, 1960; Evison, 1988; Hanes and Fragala, 1967; Hipsey et al., 2008; Johnson et al., 1997; Kaspar and Tamplin, 1993; Mancini, 1978; Sinton et al., 2002; Solic and Krstulovic, 1992). Similarly, in systems with high levels of mixing or turbidity, FIO may not settle out of the water column as much as they would for less well-mixed systems that would foster settling (Li and Gregory, 1991). Finally, light inactivation has been shown to play a significant role in FIO decay via inactivation in natural waters (Boehm et al., 2009; Whitman et al., 2004). This is especially true for oligotrophic or low-turbidity waters that do not have high levels of suspended solids that can serve as refugia for FIO (Weiskerger and Whitman, 2018).

Impacts can also vary between different microorganisms. Cabelli (1977), Colford et al. (2007), and Schang et al. (2016) document differential sensitivities to environmental pressures between *E. coli*, *Cryptosporidium parvum*, *Giardia lamblia*, *and Campylobacter* spp. in natural waters. Sanders et al. (2005) tested the impact of organism-dependent sensitivities to environmental survival influences on model predictive ability. They found that a model with the same environmental influences underpredicted *E. coli* concentrations, but overpredicted concentrations of both total coliforms and enterococci, compared to observations.

2.4.1. Dark Mortality, Base Mortality and Temperature/Salinity Dependence

Base mortality (k_{b1}) and dark mortality (k_d) terms are often used in models to account for the natural decay that microbes undergo, independent of sunlight effects. The value of k_d can be highly variable, depending on the geographic location and the microorganism of focus (Hipsey et al., 2008; Jin et al., 2003; Liu et al., 2015; Liu and Huang, 2012; Rodrigues et al., 2011; Safaie et al., 2016; Thupaki et al., 2010). Models have been presented using k_d values as low as $8.6*10^{-5}$ d^{-1} (Thupaki et al., 2010) and *in vitro* experiments have yielded k_d rates of up to 2.2 d^{-1} (Jin et al., 2003). Once k_d is established, it is then possible to correct for other factors affecting k_{b1}, like temperature, salinity, or pH of the water.

While salinity and its impacts on microbial persistence are frequently negligible in freshwater systems, marine and estuarine systems often have dynamic salinity conditions, and microbial decay rates are proportional to salinity levels (Anderson, 1979; Carlucci and Pramer, 1960; Evison, 1988; Hanes and Fragala, 1967; Hipsey et al., 2008; Johnson et al., 1997; Kaspar and Tamplin, 1993; Mancini, 1978; Sinton et al., 2002; Solic and Krstulovic, 1992). As a result, models in the context of marine or estuarine systems calculate k_{b1} in terms of salinity, using either percent sea water (P_{sea}) (Mancini, 1978) or salinity (S, PSU) terms (Eq. 2-8 and 2-9).

$$k_{b1} = (k_d + 0.006P_{sea}) \tag{2-8}$$

$$k_{b1} = (k_d + 0.02S) \tag{2-9}$$

Dark mortality rates are developed for a reference water temperature of 20°C, so an adjustment to account for variability in temperature is also needed. Microorganism base mortality terms are adjusted for temperature using the Arrhenius equation (Garcia-Alba et al., 2019; Rehmann and Soupir, 2009; Thupaki et al., 2010). Resulting temperature correction factor values can range from 1.04 to 1.11 (Rehmann and Soupir, 2009), but frequently are assumed to be 1.07 (Thomann and Mueller, 1987). This adjustment indicates a strong temperature dependence, with a doubling of the mortality rate for every 10°C increase in temperature (Chapra, 2008). The resulting full formulation of the base mortality term is thus represented by Eq. 2-10 and 2-11, where θ represents the temperature correction factor.

$$k_{b1} = (k_d + 0.006P_s)\theta^{T-20} \tag{2-10}$$

$$k_{b1} = (k_d + 0.02S)\theta^{T-20} \tag{2-11}$$

A majority of existing models use some version of this formulation to determine base mortality rate of microorganisms in natural waters (Table 2-1). Notable exceptions were found in models from Liu et al. (2014), McCorquodale et al. (2004), Hipsey et al. (2008), Rehmann and Soupir (2009), Servais et al. (2007a, 2007b), and de Brauwere et al. (2011). Rather than using a dark mortality rate to calculate base mortality, Liu et al. (2014) use the time to inactivate 90% of microorganisms in the dark (t_{90}). McCorquodale et al. (2004) use a curve-fitting procedure on field-collected data to determine the impact of salinity on base mortality. Hipsey et al. (2008) and Rehmann and Soupir (2009) incorporate the effects of salinity and pH on mortality (c_{S_M} and c_{pH_M}, respectively), sensitivity of the microorganism to salinity and pH (β and $K^{\delta}_{pH_M}$, respectively), nutrient limitation (f^{LIM}) and dissolved organic carbon concentration (DOC_L) when calculating base mortality. Following Servais et al. (2007a, 2007b), de Brauwere et al. (2011) uses a logistic relationship between microbial decay and temperature to determine k_{b1}.

Table 2-1: Base mortality terms used in contaminant fate and transport models

Aquatic Environment Type	Simulated Microorganism	Base Mortality Term	Reference
Freshwater/Marine	*E. coli*	$k_d\theta^{T-20}$	Mancini (1978)
Freshwater Lake/River	Coliform	$k_d\theta^{T-20}$	Auer and Niehaus (1993)
Freshwater Lake/River	Fecal Coliform	k_d	Canale et al. (1993)
Freshwater Lake	*E. coli*, enterococci, Fecal Coliform	k_d	Jin et al. (2003)
Freshwater Lake/River	*E. coli*	k	Jamieson (2004)
Brackish Lake	Fecal Coliform	$(0.00014S^2 + 0.0024S + 0.0253)\theta^{T-20}$	McCorquodale et al. (2004)
Estuary/Coastal	Total Coliform, Fecal Coliform	$k_d\theta^{T-20}$	Kashefipour et al. (2006)
Generic Coastal Model	Generic Bacteria, Viruses, Protozoa	$\left[k_d \frac{c_{S_M} S^\alpha}{35}[1 - f^{LIM}(DOC_L)]^\beta\right] \cdot \left[1 + c_{pH_M}\left[\frac{pH^\delta}{K_{pH_M}^\delta + pH^\delta}\right]\right]\theta^{T-20}$	Hipsey et al. (2008)
Freshwater Stream	*E. coli*	$\left[k_d \frac{c_{S_M} S^\alpha}{35}[1 - f^{LIM}(DOC_L)]^\beta\right] \cdot \left[1 + c_{pH_M}\left[\frac{pH^\delta}{K_{pH_M}^\delta + pH^\delta}\right]\right]\theta^{T-20}$	Rehmann and Soupir (2009)
Freshwater Lake	*E. coli*	$k_d\theta^{T-20}$	Thupaki et al. (2010)
Estuary/Coastal	*E. coli*	$k_d \frac{e^{\left(\frac{-(T-25)^2}{400}\right)}}{e^{\left(\frac{-25}{400}\right)}}$	Servais et al. (2007a, 2007b); de Brauwere et al. (2011)
Estuary/Coastal	*E. coli*	k_d	Bedri et al. (2011)
Estuary/Coastal	Fecal Coliform	$k_d\theta^{T-20}$	Liu et al. (2012)
Freshwater Lake	*E. coli*	$k_d\theta^{T-20}$	Thupaki et al. (2013)

Table 2-1 (cont'd)

Estuary/Coastal	*Vibrio* spp.	$k_d\theta^{T-20}$	Froelich et al. (2013)
River/Estuary	Fecal Coliform	$k_d\theta^{T-20}$	Boye et al. (2015)
Freshwater Lake	*E. coli*	$\frac{2.3}{t_{90}}\theta^{T-20}$	Liu et al. (2014)
Freshwater Stream	Fecal Coliform	$k_d\theta^{T-20}$	Reder et al. (2015)
Estuary/Coastal	Fecal Coliform	$k_d\theta^{T-20}$	Gao et al. (2015)
Estuary/Coastal	Fecal Coliform	$k_d\theta^{T-20}$	Liu et al. (2015)
Freshwater Lake	*E. coli*	$k_d\theta^{T-20}$	Safaie et al. (2016)
Freshwater Lake	Fecal Coliform	$k_d\theta^{T-20}$	Bravo et al. (2017)
Estuary/Coastal	*E. coli*	$(k_d + k_{salinity})\theta^{T-20}$	Garcia-Alba et al. (2019)
Freshwater Stream	*E. coli*	$k_d\theta^{T-20}$	Mohammed et al. (2019)

2.4.2. Solar Inactivation Terms

It is generally accepted that incoming solar radiation affects the survival of microbes in water systems (Auer and Niehaus, 1993; McCambridge and McMeekin, 1981; Rhodes and Kator, 1990; Whitman et al., 2004). This is especially true in clear, oligotrophic waters, where solar inactivation can be a predominant influence on microbial survival (Boehm et al., 2009; Weiskerger and Whitman, 2018). Many mechanistic fate and transport modelers recognize the impacts of solar inactivation on microbial survival in water and include inactivation parameters in their models.

Accounting for solar irradiation in natural waters inherently involves the calculation of the light extinction rate within the water column. The amount of light penetrating the water column declines exponentially with depth and is influenced by the turbidity or clarity of the water, such that clearer water yields a lower light extinction rate than turbid water. Lower light extinction rates, in turn, yield more intense solar radiation at deeper depths in the water, leading to higher microbial solar inactivation rates (Chapra, 2008).

Nearly all of the models which account for solar inactivation use some variation of Eq. 2-7 in which the Beer-Lambert Law (Eq. 2-12) (Kocsis et al., 2006) is used to model the variation of solar radiation with depth. In the Beer-Lambert equation, $\boldsymbol{z}$ is vertical coordinate of depth (m) and $I_{\boldsymbol{z}}$ represents the amount of solar radiation at vertical coordinate $\boldsymbol{z}$ (W m^{-2}). I_0 is solar radiation at the water surface (W m^{-2}), and k_e is the light extinction rate (m^{-1}) (Weiskerger et al., 2018).It is important to distinguish between k_I from Eq. 2-7 and k_e in Eq. 2-12. In Eq. 2-7, the k_I term is an inactivation rate for FIO as a result of solar radiation (Liu et al., 2014; Safaie et al., 2016; Sanders et al., 2005), whereas k_e in Eq. 2-12 is the rate of light extinction with depth in the water column (Chapra, 2008; Hipsey et al., 2008; Weiskerger et al., 2018).

$$I_z = I_0 e^{-k_e \boldsymbol{z}} \tag{2-12}$$

Model type can have a significant impact on the variables used in parameterization of solar inactivation effects on FIO. Models may employ either total depth (H) or the vertical coordinate (z) within their solar radiation parameterizations, depending on the model context. In 2-dimensional model frameworks, conditions within the water column are often vertically-integrated. For these cases, fate and transport models use a single depth variable (H) and a single solar radiation variable (I_t) to account for potential variability in the vertical dimension (Chapra, 2008; Gao et al., 2015; Liu et al., 2006; Rehmann and Soupir, 2009). Fully 3-dimensional models, in contrast, explicitly define conditions at different depths in the water column via their incorporation of the vertical coordinate variable $\boldsymbol{z}$ within their parameters. For example, fully 3-dimensional models will often incorporate variables for solar radiation at the water surface (I_0) and solar radiation at depth $\boldsymbol{z}$ ($I_{\boldsymbol{z}}$) to capture differences with depth in the water column (Auer and

Niehaus, 1993; Boye et al., 2015; Canale et al., 1993; Hipsey et al., 2008; Jin et al., 2003; Mancini, 1978; Nekouee et al., 2015b; Reder et al., 2015; Safaie et al., 2016; Thupaki et al., 2010, 2013).

A variety of approaches have been used for characterizing the effects of solar inactivation on FIO fate and transport. In some cases, models do not include solar inactivation terms at all (Bedri et al., 2011; De Brauwere et al., 2011; Liu et al., 2015; Liu and Huang, 2012; Madani et al., 2020; Mohammed et al., 2019), often because the water is so turbid that solar effects are assumed negligible compared to other environmental influences. Others use either a microbial decay rate solely as a function of incoming solar radiation (Eq. 2-7) or as a function of the light extinction rate and depth in the water (Eq. 2-12, Table 2-2). Hipsey et al. (2008) expanded the description of solar inactivation effects on FIO in their generic modeling framework, including specific terms for dissolved oxygen (*DO*), pH, salinity (*S*), and solar bandwidth (*b*). Garcia-Alba et al. (2019) included terms corresponding to day length (*DL*) and fraction of solar irradiance that is in the UV spectrum (f_{UV}) as well as the typical light extinction rate, solar inactivation rate, solar irradiance and depth terms seen in other models.

Table 2-2: Solar inactivation terms used in contaminant fate and transport models

Aquatic Environment Type	**Simulated Microorganism**	**Solar Inactivation Term**	**Reference**
Freshwater/ Marine	*E. coli*	$k_I \frac{I_0}{k_e H}(1 - e^{-k_e H})$	Mancini (1978)
Freshwater Lake/River	Coliform	$k_I \frac{I_0}{k_e z}(1 - e^{-k_e z})$	Auer and Niehaus (1993)
Freshwater Lake/River	Fecal Coliform	$k_I \frac{I_0}{k_e z}(1 - e^{-k_e z})$	Canale et al. (1993)
Freshwater Lake	*E. coli*, enterococci, Fecal Coliform	$\frac{\alpha I_0}{k_e H}(1 - e^{-k_e H})$	Jin et al. (2003)

Table 2-2 (cont'd)

Brackish Lake	Fecal Coliform	$k_L\theta^{T-20}$	McCorquodale et al. (2004)
Estuary/ Coastal	*E. coli*	$k_I I_t$	Sanders et al. (2005)
Freshwater Lake	*E. coli*	$(k_I I_t)\theta^{T-20}$	Liu et al. (2006)
Estuary/ Coastal	Total Coliform, Fecal Coliform	$k_I I_t$	Kashefipour et al. (2006)
Generic Coastal Model	Generic Bacteria, Viruses, Protozoa	$\sum_{b=1}^{N_b}\left[\begin{array}{c}\varphi(k_I + c_s S)f_b I_0\left(\frac{1-e^{-k_e z}}{-k_e z}\right)\\ \cdot\left(\frac{DO}{k_{DO}+DO}\right)\\ \cdot\left(1 + c_{pH}\frac{pH^\delta}{\left(k_{pH}\right)^\delta + (pH)^\delta}\right)\end{array}\right]$	Hipsey et al. (2008)
Freshwater Stream	*E. coli*	$k_I\frac{I_t}{k_e H}(1-e^{-k_e H})$	Rehmann and Soupir (2009)
Freshwater Stream	*E. coli*, enterococci	$k_I I_t$	Cho et al. (2010)
Freshwater Lake	*E. coli*	$(k_I I_0 e^{-k_e z})\theta^{T-20}$	Thupaki et al. (2010)
Freshwater Lake	*E. coli*	$(k_I I_0 e^{-k_e z})\theta^{T-20}$	Thupaki et al. (2013)
Marine Coastal	Enterococci	$k_I I_t$	Feng et al. (2013)
River/Estuary	Fecal Coliform	$k_I I_t\frac{1.0-e^{-k_e H}}{k_e H}$	Boye et al. (2015)
Freshwater Lake	*E. coli*	$(k_I I_t)\theta^{T-20}$	Liu et al. (2014)
Freshwater Stream	Fecal Coliform	$k_I\frac{I_0}{k_e H}(1-e^{-k_e H})$	Reder et al. (2015)
Estuary/ Coastal	Fecal Coliform	$(k_I I_t)\theta^{T-20}$	Gao et al. (2015)
Marine Coastal	Enterococci	$k_I I_t$	Feng et al. (2015)
Freshwater Lake	*E. coli*	$(k_I I_0 e^{-k_e z})\theta^{T-20}$	Nekouee et al. (2015b, 2015a)
Freshwater Lake	*E. coli*	$(k_I I_0 e^{-k_e z})\theta^{T-20}$	Safaie et al. (2016)
Freshwater Lake	Fecal Coliform	$(k_I I_0 e^{-k_e z})\theta^{T-20}$	Bravo et al. (2017)
Estuary/ Coastal	*E. coli*	$k_I * DL * f_{UV} * I_0\left(\frac{1-e^{-k_e H}}{k_e H}\right)$	Garcia-Alba et al. (2019)

2.4.3. Sedimentation Terms

In addition to solar inactivation, attachment to suspended solids and settling out of the water column is another significant driver of FIO losses in aquatic environments. 80-100% of total coliforms and *E. coli* have been shown to readily attach to suspended particles in the water column (Hipsey et al., 2006), and viruses have also been shown to easily attach to particulate matter and settle out of suspension (Gerba, 2005).

Similar to the solar inactivation term, several published models do not incorporate sedimentation effects on microbial fate and transport (Bedri et al., 2011; Boye et al., 2015; Feng et al., 2013, 2015; Jamieson et al., 2004; Kashefipour et al., 2006; Sanders et al., 2005; Sinton et al., 1999; Zhu et al., 2011). In models that do incorporate sedimentation losses, settling terms most frequently use parameters representing settling velocity (v_s, as calculated using Stokes' Law), vertical coordinate (z) or the total water column depth (H), and the fraction of the FIO that is attached to particles (f_p, Table 2-3). In many cases, sedimentation terms are also subject to temperature correction, in the same manner that base mortality and solar inactivation terms utilize temperature correction factors (Liu et al., 2006, 2015; Liu and Huang, 2012; Safaie et al., 2016), to acknowledge the fact that overall loss of FIO increases with temperature.

In their generalized sedimentation term, Hipsey et al. (2008) expanded upon the simplified sedimentation terms used in most other models. This expansion accounts for various particle size classes (N_s), particle and attachment surface areas (A_p and A_s, respectively), and settling velocities for attached (v_s) and unattached (v_c) FIO.

Table 2-3: Sedimentation loss terms used in contaminant fate and transport models

Aquatic Environment Type	Simulated Microorganism	Sedimentation Loss Term	Reference
Freshwater Lake/River	Coliform	$\frac{v_s}{z_e}$	Auer and Niehaus (1993)
Freshwater Lake/River	Fecal Coliform	$\frac{v_s}{z}$	Canale et al. (1993)
Freshwater Lake	*E. coli*, enterococci, Fecal Coliform	$f_p \frac{v_s}{H}$	Jin et al. (2003)
Brackish Lake	Fecal Coliform	$f_p \frac{v_s}{H} \theta^{T-20}$	McCorquodale et al. (2004)
Freshwater Lake	*E. coli*	$f_p \frac{v_s}{H} \theta^{T-20}$	Liu et al. (2006)
Generic Coastal Model	Generic Bacteria, Viruses, Protozoa	$\left(1 - f_p\right) \frac{v_c}{z} + f_p \sum_{s=1}^{N_s} \left[\frac{v_s}{z} \left(\frac{A_s}{\sum_{s=1}^{N_s} A_p} \right) \right]$	Hipsey et al. (2008)
Freshwater Stream	*E. coli*	$\frac{v_s C}{H}$	Rehmann and Soupir (2009)
Freshwater Stream	*E. coli*, enterococci	$f_p \frac{v_s}{H}$	Cho et al. (2010)
Freshwater Lake	*E. coli*	$\frac{\partial \left(f_p v_s C\right)}{\partial z}$	Thupaki et al. (2010)
Estuary/Coastal	*E. coli*	$\frac{v_s}{H}$	de Brauwere et al. (2011)
Estuary/Coastal	Fecal Coliform	$f_p \frac{v_s}{H} \theta^{T-20}$	Liu et al. (2012)
Freshwater Lake	*E. coli*	$\frac{\partial \left(f_p v_s C\right)}{\partial z} \theta^{T-20}$	Thupaki et al. (2013)
Freshwater Lake	*E. coli*	$f_p \frac{v_s}{H} \theta^{T-20}$	Liu et al. (2014)
Freshwater Stream	Fecal Coliform	$\frac{v_s}{H}$	Reder et al. (2015)
Estuary/Coastal	Fecal Coliform	$f_p \frac{v_s}{H} \theta^{T-20}$	Liu et al. (2014)
Freshwater Lake	*E. coli*	$\frac{\partial \left(f_p v_s C\right)}{\partial z} \theta^{T-20}$	Safaie et al. (2016)
Freshwater Lake/River	*E. coli*	$f_p \frac{v_s}{H} \theta^{T-20}$	Liu (2018)

Bravo et al. (2017) and Thupaki et al. (2013) incorporated sedimentation effects by including them in the vertical advection term of the 3D ADR equation (Eq. 2-5). As a result, the ADR presented is Eq. 2-13 and the microbial decay function (*kC)* only includes terms for base mortality and solar inactivation in these models.

$$\frac{\partial C}{\partial t} + u\frac{\partial C}{\partial x} + v\frac{\partial C}{\partial y} + \frac{\partial\left(\left(w - f_p v_s\right)C\right)}{\partial z} = \frac{\partial}{\partial x}\left(K_H\frac{\partial C}{\partial x}\right) + \frac{\partial}{\partial y}\left(K_H\frac{\partial C}{\partial y}\right) + \frac{\partial}{\partial z}\left(K_V\frac{\partial C}{\partial z}\right) - kC \qquad (2\text{-}13)$$

2.5. Model Testing and Evaluation

There is a large number of processes influencing FIO fate and transport and it can be difficult to identify a correct conceptual model that acknowledges process interdependencies over wide ranges of environmental variables of interest. Therefore, it is difficult to fully test FIO models across environments, and within the same environment, across different time periods (e.g., dry vs. wet weather events, “normal” vs. extreme events). While calibrated FIO fate and transport models have the potential to aid management by providing near real-time predictions, a majority of the published papers report results of model back-testing (or history matching, see Bredehoeft and Konikow (1993)).

To evaluate the goodness of fit between models and observational data as well as to identify superior model formulations (by comparing different models), the use of multiple model evaluation metrics may be more beneficial (Bredehoeft and Konikow, 1993; Legates and McCabe, 1999) than the use of a single metric such as the coefficient of determination (R^2) or root mean squared error (RMSE). This is due to the fact that no single model performance metric captures all aspects of the data and simulation results, and all metrics have known limitations. In the context of FIO and beach management, evaluating models using the confusion matrix and concepts of sensitivity and specificity (Altman and Bland, 1994; Loong, 2003; Zhang et al., 2018) have proven to be useful, especially from the practical application of issuing beach advisories and closings.

Existing, published models have been tested in a number of ways. Most model testing protocols, particularly those in more recent modeling studies, involve statistical analysis of comparability of model results to observed data. A majority of published models have used RMSE or R^2 as model performance metrics (Table 2-4). Other statistics such as Normalized RMSE (NRMSE), Mean Absolute Error (MAE), Nash-Sutcliffe Efficiency (NSE) (Nash and Sutcliffe, 1970), Percent Bias (PBIAS) (Moriasi et al., 2007) or the Refined Willmott Index of Agreement (Willmott et al., 2012) have also been used by Boye et al. (2015), Liu et al. (2015) and Feng et al. (2013). A subset of the published models were qualitatively assessed, often with comparisons to other models replacing the more quantitative RMSE, R^2, MAE, NSE and Wilmott index statistics (Auer and Niehaus, 1993; Bedri et al., 2011; De Brauwere et al., 2011; Hipsey et al., 2008; Jamieson et al., 2004; Liu, 2018; Liu and Huang, 2012; Mancini, 1978; Rehmann and Soupir, 2009). In all applicable cases, the RMSE or MAE values have units of $\log_{10}$ FIO CFU 100 ml^{-1}, while NRMSE units are percentages and NSE values are unitless.

Table 2-4: Skill statistics and validation data for published numerical models of microbial water quality and FIO fate and transport

Aquatic Environment Type	**Simulated Microorganism**	**Validation Type/Statistic**	**Skill Statistic Value/Qualitative Observations**	**Reference**
Freshwater/ Marine	*E. coli*	Qualitative Evaluation	Good agreement with coliform mortality rates.	Mancini (1978)
Freshwater Lake/River	Coliform	Qualitative Evaluation	Model was based on empirical relationships from lab/field data.	Auer and Niehaus (1993)

Table 2-4 (cont'd)

Freshwater Lake/River	Fecal Coliform	Qualitative Evaluation	Model output is comparable and consistent with observed bacterial loads during wet and dry weather events.	Canale et al. (1993)
Freshwater Lake	*E. coli*, enterococci, Fecal Coliforms	Qualitative Evaluation	Fairly good prediction of observed microbial concentrations, but a general underestimation by the model.	Jin et al. (2003)
Freshwater Lake/River	*E. coli*	Qualitative Evaluation	Modeled results generally simulate observations well. Empirical data should be used to calibrate models for nutrient-rich streams.	Jamieson (2004)
Brackish Lake	Fecal Coliforms	Qualitative Evaluation	Fecal coliform dilution-decay is well-represented in the model, but predictions are susceptible to high levels of uncertainty associated with observed values.	McCorquodale et al. (2004)
Estuary/ Coastal	*E. coli*	R^2	0.19 – 0.70	Sanders et al. (2005)
Freshwater Lake	*E. coli*	RMSE	0.71 – 0.84	Liu et al. (2006)
Estuary/Coastal	Total Coliform	R^2	0.715	Kashefipour et al. (2006)
Estuary/Coastal	Fecal Coliform	R^2	0.686	Kashefipour et al. (2006)
Generic Coastal Model	Generic Bacteria, Viruses, Protozoa	Qualitative Evaluation	The generic model did not outperform other models significantly.	Hipsey et al. (2008)

Table 2-4 (cont'd)

Freshwater Stream	*E. coli*	Qualitative Evaluation	Predictive capacity changes over time. Model underpredicts *E. coli* at shorter time scales but reproduces measurements at longer time scales after storms.	Rehmann and Soupir (2009)
Freshwater Stream	*E. coli*, enterococci	NSE	-0.02 – 0.81	Cho et al. (2010)
Freshwater Lake	*E. coli*	RMSE	0.41	Thupaki et al. (2010)
Estuary/Coastal	*E. coli*	Qualitative Evaluation	Reference model overpredicted median observations by 7 and 3% at Temse and Uitbergen locations, respectively, but the variability of modeled results is much higher (3% for Uitbergen, 50% for Temse) than the observed data.	de Brauwere et al. (2011)
Estuary/Coastal	*E. coli*	Qualitative Evaluation	Model significantly underestimates *E. coli* in a bay.	Bedri et al. (2011)
Estuary/Coastal	Fecal Coliform	R^2	0.71 – 0.83	Liu et al. (2012)
Freshwater Lake	*E. coli*	RMSE	0.52 – 1.36	Thupaki et al. (2013)
Estuary/Coastal	*Vibrio* spp.	RMSE	0.80	Froelich et al. (2013)
Marine Coastal	Enterococci	Willmott Index of Agreement	0.47 – 0.60	Feng et al. (2013)
Freshwater Lake	*E. coli*	NRMSE	5 – 23	Nekouee et al. (2015b, 2015a)
River/Estuary	Fecal Coliform	MAE	0.348	Boye et al. (2015)
Freshwater Lake	*E. coli*	RMSE	2.24 – 3.00	Liu et al. (2014)

Table 2-4 (cont'd)

Freshwater Stream	Fecal Coliform	RMSE	0.44 – 0.70	Reder et al. (2015)
Estuary/Coastal	Fecal Coliform	RMSE	4.42 – 4.80	Gao et al. (2015)
Estuary/Coastal	Fecal Coliform	RMSE	3.62 – 5.37	Liu et al. (2015)
Marine Coastal	Enterococci	RMSE MAE	0.67 – 0.92 0.47 – 0.72	Feng et al. (2015)
Freshwater Lake	*E. coli*	R^2 RMSE NSE	0.60 – 0.72 0.52 – 0.60 0.13 – 0.30	Safaie et al. (2016)
Freshwater Lake	Fecal Coliform	RMSE	0.66	Bravo et al. (2017)
Freshwater Lake/River	*E. coli*	RMSE/ Qualitative Evaluation	Model was optimized for RMSE, given various Manning roughness coefficients. Optimized model used Manning roughness coefficient = 0.035.	Liu (2018)
Estuary/Coastal	*E. coli*	R^2	0.87	Garcia-Alba et al. (2019)
Freshwater Stream	*E. coli*	R^2	0.26 – 0.31	Mohammed et al. (2019)

Based on R^2 to evaluate model performance, the model of Garcia-Alba et al. (2019) produced one of the best descriptions of observed data among the models considered here (R^2 = 0.87). Their model incorporated temperature- and salinity-dependent base mortality ($k_{b1} = \left(k_d + k_{salinity}\right)\theta^{T-20}$) and solar inactivation terms accounting for day length and fraction of irradiance composed of UV radiation ($k_{bi} = k_I * DL * f_{UV} * I_0\left(\frac{1-e^{-k_eH}}{k_eH}\right)$). Based on RMSE alone, one of the published models that best approximates observed microbial concentrations is detailed in

Thupaki et al. (2010) (RMSE = 0.41 $\log_{10}$ CFU 100 ml^{-1}). Within this model, $k_{b1} = k_d\theta^{T-20}$, $k_{bi} = (k_I I_t)\theta^{T-20}$, and $k_{bs} = \frac{\partial(f_p v_s C)}{\partial z}\theta^{T-20}$.

Although comparison of these model frameworks can lend insight into which ones may best simulate microbial water quality, it is important to note that the models were developed under varying contexts. One published approach attempted to develop a generic water quality model, to be used across environments and target microorganisms (Hipsey et al., 2008). This model framework led to complex terms within the decay function, often including parameterization for salinity, pH, dissolved organic carbon concentration, varying particle sizes and settling velocities, and variable sensitivity of the microorganism to such environmental changes. The resulting validation of the model indicated that the generic model did not outperform other existing models in its prediction of contaminant fate and transport. Despite this lack of substantial model improvement over existing models, the generality of this model may be attractive to researchers looking for a single model to predict water quality under various conditions.

A lack of ancillary data may provide a confounding factor in the use of generic models such as the one described in Hipsey et al. (2008). In many cases, models are developed without the use of DOC, pH, temperature and salinity data, instead relying on hydrodynamics and meteorology to model FIO fate and transport. Likewise, additional water quality data such as DOC, pH, temperature and salinity are often not collected or available for model development, potentially hindering the usage and applicability of such a generic model. This could, however, indicate not that generic models may be less useful than specific and localized models, but rather that *in situ* DOC, pH, temperature and salinity data should be collected as part of the water quality monitoring process. For example, while the focus of most FIO modeling efforts is to reproduce the observed FIO concentrations, if no temperature data are collected in the nearshore region, the ability of the coupled FIO-temperature-hydrodynamic model to accurately represent FIO decay is questionable as base mortality, solar inactivation, and sedimentation are often functions of temperature. A majority of the models reported in the literature use microbial decay formulations with a solar inactivation term and use FIO data collected during the daytime. Previous research shows that the highest levels of FIO are typically observed during the early morning hours (e.g., 6:00 AM) (Lušić et al., 2017) due to the absence of solar radiation the previous night. Therefore, modeling the nighttime variation of FIO is important to correctly describe FIO levels in the morning (Ge et al., 2012a); however, since monitoring data are not collected at night, this aspect has not received much attention in the modeling literature.

In the absence of the specific data needed for the generic water quality model described above, selection of an appropriate modeling framework should be based on the target FIO as well as the environmental and hydrological context of the model.

2.6. Applying Microbial Fate and Transport Models to Extreme Storm Events

Numerical simulation of microbial water quality has evolved in recent years, as the dynamics of processes such as solar inactivation have become clearer. Even so, the incomplete knowledge of influences within aquatic systems on water quality indicates that there is still room for model improvement. Likewise, climate and land use/urbanization changes provide additional contexts for the prediction of microbial water quality (Xu et al., 2019). Although the link between extreme precipitation and waterborne disease outbreaks is well-known (Curriero et al., 2001; Thomas et al., 2006), the current generation of FIO models can be further refined and tested for their ability to reproduce observed dynamics during extreme storm events. Major areas of research impacting coastal water quality from the perspective of extreme storm events may include the exchange of FIO between water and sand at beaches, the fate and transport of FIO in storm-associated river plumes and the expansion of water quality monitoring research into microbial source tracking and environmental DNA (eDNA) for use in public health contexts.

The interaction between water and sand at the beach, and its impacts on recreational safety and water quality, has been an active area of discussion in recent years (Alm et al., 2003; Beversdorf et al., 2007; Boehm et al., 2014; Ishii et al., 2007; Solo-Gabriele et al., 2015; Weiskerger et al., 2019; Whitman et al., 2014; Yamahara et al., 2007). Microorganisms in beach sands have been cited as potential sources of contamination and swimmer infection as early as 2003 (Alm et al., 2003). The microbial community within beach sands is unique (Thupaki et al., 2010) in that it can serve as either a sink or a source of FIO to the adjacent recreational water, depending upon wave energies, currents and the movement of the water. When wave energy is low, FIO often get deposited from the water and into shoreline sand where they can form biofilm communities, while higher wave energy frequently leads to the release and re-suspension of FIO from the shoreline sand into the water (Ishii et al., 2007; Weiskerger et al., 2019). These sand-based sources and sinks can heavily impact spatial and temporal trends in FIO concentrations at beaches. Further, the Intergovernmental Panel on Climate Change (IPCC) has predicted increases in wind speeds and wave heights/energies in mid- and upper latitudes as a result of climate change (Pachauri et al., 2014). Similarly, the IPCC has predicted sea level rise in coming decades, a phenomenon already being observed, leading to changes in the beach face and the intertidal zone that is impacted by wave deposition/resuspension of FIO (Nerem et al., 2018; Weiskerger et al., 2019). This will likely lead to increases in wave-induced FIO release from sands and into recreational water. Because of the potential for climate change to significantly impact sand-water exchange of FIO at beaches, it will be integral for numerical models to include sand-sediment-water interactions when predicting microbial water quality. Currently there are gaps in our understanding of these sand-sediment-FIO related processes and there is a need to further refine our mechanistic modeling approaches based on high-quality field observations and datasets which are often lacking. This will be especially important in substantially wave-impacted beach areas, to improve upon model predictions that exclude sand/sediment parameters (Gao et al., 2011; Thupaki et al., 2013).

Such models accounting for sand-sediment-water interactions at the beach may take inspiration from modeling frameworks that incorporate sedimentation. For instance, the modeling approach developed by Hipsey et al. (2008) includes terms for various particle size classes, accounting for differential resuspension effects on “fine” and “coarse” particles. Fine particles require lower bed shear stress values for resuspension, compared to coarse particles, so it may be important to differentiate between the readily resuspended particles and those that are less likely to resuspend after deposition (Brown et al., 2013; Feng et al., 2013; Hipsey et al., 2006). After simulating sediment transport as a function of particle size, sediment-FIO interactions can be modeled using attachment-detachment kinetics following those established for subsurface transport models (Brown and Boehm, 2016).

An additional concern related to how climate change will impact recreational water quality involves storm- and runoff-associated FIO at coastal areas. For many regions, including mid-latitudinal coastal areas, climate change is expected to lead to increasingly frequent and intense storms (Pachauri et al., 2014). Not only will these intense storms make recreating at beaches dangerous via rip tides, rip currents and strong waves, they will also send increased volumes of potentially contaminated runoff and river water downstream, to be released to coastal areas (Barlage et al., 2002). As a result, recreational beaches may be expected to experience the impacts of more frequent and larger storm-associated river FIO plumes.

Effective prediction of the coastal water quality impacts from river FIO plumes will be helpful in not only understanding an additional source of contamination to recreational areas but will also aid in the management of beach resources for public and environmental health. This simulation will require extension of existing numerical modeling approaches to include the determination of FIO concentrations in dynamic river plumes as well as reliable estimation of plume dynamics.

A number of studies have reported a "first-flush" effect for FIO (Brown et al., 2013; Nerem et al., 2018), in which elevated FIO levels were observed following storm events with levels declining in later portions of the storm event and in subsequent events over a season. However, other researchers did not report such an effect (McCarthy et al., 2012). These differences can be attributed to different runoff characteristics of watershed areas, so linking coastal water quality models with well-tested watershed models of FIO is expected to help address current limitations of nearshore FIO models (Brito et al., 2015). For example, microbial composition and concentrations in runoff depend on upstream land uses; runoff from rural/agricultural watersheds is likely to have different water quality concerns than runoff from urbanized or forested catchments (Goonetilleke et al., 2005; Liang et al., 2013; Tong and Chen, 2002). These differences are magnified during first flush phenomena and heavy storm events, where FIO can be released from soils and into the water, leading to high FIO loads in rivers that can then degrade coastal water quality. Therefore, calibrated upstream watershed models can be beneficial for modeling of coastal water quality in response to storm-associated river plume releases, simply because of the differential impacts resulting from different upstream watershed conditions that send FIO loads downstream to the coast.

In addition to the enteric pathogens of human health concern that can be indicated using FIO, microorganisms that cause other health problems, such as respiratory and skin infections, are also often present at beaches, and may be tracked to upstream sources (Fewtrell and Kay, 2015). This is especially true in the context of extreme storm events when beaches are heavily impacted by upstream river flows and plumes. Methods such as microbial source tracking (MST) and the monitoring of eDNA have shown value in their ability to improve predictive modeling of extreme storm events by offering insights into sources and transport pathways for FIO (Brownell et al., 2007; Nevers et al., 2020). Differences in MST and eDNA monitoring results between "normal" and heavy storm conditions can be helpful in determining the types of microorganisms that become active within the aquatic environment in response to storm conditions (Staley et al., 2018). Similarly, they can be informative in characterizing upstream impacts on coastal areas, by revealing potential catchment sources of microorganisms. Integrating well-calibrated watershed FIO models with nearshore water quality models (e.g., Bedri et al. (2014)) or statistical and data-based approaches that describe FIO loading to coastal areas (Bravo et al., 2017) may further improve the performance of nearshore FIO models during extreme events.

Conditions surrounding FIO sedimentation, attachment to suspended solids, and resuspension in riverbeds and coastal areas can vary greatly between storm events. However, there is a notable lack of observational data on water quality during and immediately following different storm conditions. High-resolution FIO data both within and between storm events will be critical to effective simulation of FIO loading, attachment dynamics, sedimentation and resuspension kinetics, and overall water quality in river plumes associated with heavy rain events. It can be difficult to collect these data, due to safety considerations, but the use of sensor networks and small unmanned aerial vehicles has emerged as a potential alternative to field data collection. Morgan et al. (2020) demonstrated the use of unmanned aerial vehicles to photograph and document inland irrigation ponds and used image analysis to characterize water quality from the images collected.

Many existing sensors on water bodies (e.g., select USGS gauging stations) collect ancillary water quality data such as turbidity and electrical conductivity as well. These easy-to-collect data have the potential to help further constrain and evaluate FIO models because of their correlations to microbial water quality (Safaie et al., 2016; Schimmelpfennig et al., 2012; Zhang et al., 2015, 2012). High-resolution water quality data collection is ideal for effective fate and transport modeling, but this data collection can take many forms, including remote sensing and proxy data collection.

In the coastal environment, there are multiple ways to simulate river plumes in numerical water quality models. Along with the river flow inputs, plumes may be characterized by tracking specific FIO within a water quality or FIO-specific model. In these models, FIO concentrations associated with the river inputs and decay function parameters can be specified to reflect local conditions. To assess the relative contributions of FIO from riverine sources to a beach site, constant FIO concentrations or arbitrary FIO masses can be input into the model over a release period (Chatzichristos et al., 2000; Li et al., 2019) and breakthrough curves can be generated over time for specific locations. In contrast, FIO concentrations that are associated with riverine flows may be calculated using empirical relationships between river flowrate and FIO concentration (Bravo et al., 2017; Madani et al., 2020; Safaie et al., 2016). For beaches impacted by multiple river plumes (e.g., Liu et al. (2006); Kim et al. (2009)), the plume dynamics and hence nearshore water quality can be significantly more complex (Figure 2-1). Using realistic boundary conditions/forcing, models can track the FIO within the plumes spatiotemporally. Another attractive option for simulating FIO plumes involves the use of particle tracking (Anderson and Phanikumar, 2011; Byrnes et al., 2011; Huang et al., 2019; Nekouee et al., 2015b; Rowe et al., 2016), especially "reactive" particle tracking models that can account for FIO losses (Xue et al., 2018). In this case, FIO are released to the model domain (i.e., river outlets) as discrete particles. Upon their release, the particles' movements are tracked over time based on the simulated velocity field in three dimensions. This approach, using a Lagrangian formulation for dispersion, has the advantage that it does not suffer from excessive numerical dispersion inherent to Eulerian approaches. All of these approaches have their merits and drawbacks, so it is likely that selection of an optimal framework for plume modeling will require evaluation of the approaches within the context of the research questions and local conditions.

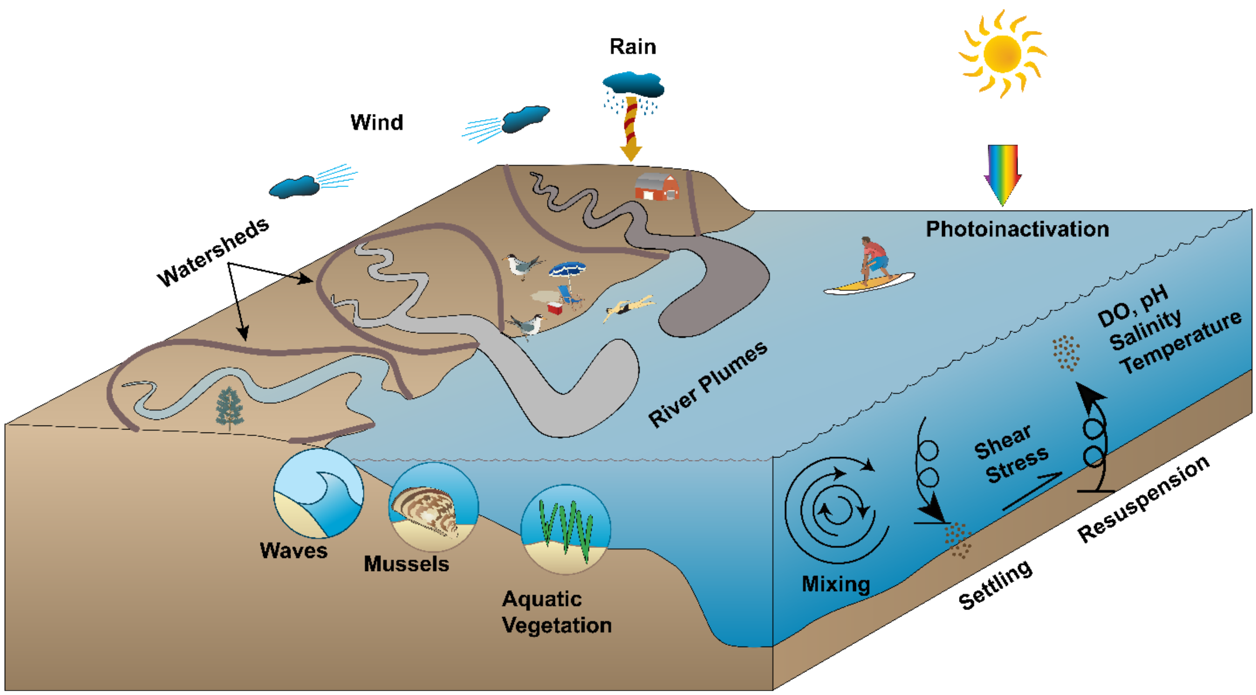

Figure 2-1: Complex factors influencing FIO fate and transport at river-impacted nearshore areas

Emerging issues such as water quality degradation associated with FIO exchange between water and sand, river plumes, upstream watershed impacts, and heavy storm runoff are key to effective modeling of microbial fate and transport in coastal areas. As such, future research and modeling in these areas will be beneficial to the water quality modeling community and knowledge base into the future.

2.7. Conclusions

Numerical models of water quality in nearshore regions can be useful tools for management of recreational water resources. Water quality and FIO fate and transport models within larger coastal ocean modeling frameworks have the potential to predict the fate and transport of FIO and pathogens of human health concern over time and across space. However, these models are only useful if they are refined and validated against observations.

In recent years, development of reliable FIO fate and transport models for aquatic and coastal systems has been an active area of research. As a result, modeling approaches frequently include decay terms associated with base mortality, solar inactivation, and sedimentation, though the specific parameterization of those terms can vary between models (Chapra, 2008). Highly generalized fate and transport models expand upon those terms to account for the effects of salinity, water temperature, pH, dissolved organic carbon, and differential settling rates due to varying particle sizes (Hipsey et al., 2008). Model optimization in terms of FIO tracking has led to frameworks with RMSE values as low as 0.41 $\log_{10}$ FIO CFU 100 ml^{-1} of water (Thupaki et al., 2010). Some models have also been shown to predict up to 87% of variation in FIO concentrations from observed data (Garcia-Alba et al., 2019). While these validation statistics indicate that model frameworks are improving in their prediction of water quality, there is still room to optimize further. It is also important to note that many of these model parameterizations are specific to their local model domains. Generic models of FIO fate and transport can be developed but without extensive datasets to test and constrain processes, generic model formulations may not offer superior performance compared to simpler models (Hipsey et al., 2008). Therefore, it will likely continue to be imperative that models be developed for their specific contexts, in order to maximize their predictive capacity.

FIO fate and transport modeling frameworks linked to watershed models in the contexts of water-sand exchange at the beach and release of FIO during storms can help us prepare for the potential impacts of extreme events on coastal areas. High quality intra- and inter-event data as well as modeling studies are needed to push the predictive capability of the current generation of FIO models. By refining established FIO decay functions to maximize predictive ability of models and combining those with the diffuse point and non-point FIO sources like plumes and sand-water exchange, prediction and tracking of pollutants in nearshore water and sand can be optimized. Confidence in modeling results can be maximized, allowing for more effective management for public health at nearshore and recreational beach areas in the face of climate and land use change.

3. Effect of Turbulent Prandtl Number on Nearshore Water Quality in a Large Lake System

3.1. Introduction

The movement and quality of water in natural settings can be influenced by a range of factors, from meteorological (e.g., surface heat fluxes and wind stress at the top of the water column) to physical basin characteristics including lake morphometry and bed roughness (Silva et al., 2014). Thus, it can be difficult to reliably model hydrodynamics and solute transport, particularly in systems where these factors can change over time and space. Understanding the linkages between the rates of momentum, heat and mass transfer is key to improving the predictive ability of numerical models of hydrodynamics and water quality.

Although the governing equations for fluid flow (the Navier-Stokes equations) contain information at all spatiotemporal scales including molecular scales, direct numerical simulation (DNS) of these equations is computationally demanding and it is impractical to apply DNS models to large lake systems. Therefore, the equations governing turbulent flows are averaged around a mean state (e.g., $\bar{u}$ where u denotes the velocity component in the *x*-direction) and turbulent fluctuations around the mean (denoted by primes, e.g., u') are treated separately. Eddy viscosity A_m (for momentum), eddy diffusivity A_h (for heat) and eddy diffusivity for solute or contaminant mass A_c are additional variables that are often introduced to express the unknown product terms involving turbulent fluctuations resulting from the averaging process in terms of the known variables for the mean state. For example, turbulent fluctuations in momentum and heat in the horizontal (*x* and *y*) directions are expressed using the following equations:

$$-\overline{u'v'} = A_m \frac{\partial \bar{u}}{\partial x} \tag{3-1}$$

$$-\overline{u'T'} = A_h \frac{\partial \bar{T}}{\partial x} \quad (3\text{-}2)$$

where *u* and *v* are the *x*- and *y*-direction velocity components and *T* denotes temperature (similar equations can be written in the vertical direction). The turbulent Prandtl number is a direct consequence of the above parameterization and is defined as the ratio of the eddy viscosity for momentum transfer to the eddy diffusivity for heat (Eq. 3-3) (Chen et al., 2006; Kays, 1994; Ye et al., 2019)

$$Pr_{t,H} = \frac{A_m}{A_h} \quad (3\text{-}3)$$

where the suffix *H* denotes horizontal mixing and a similar Prandtl number is defined in the vertical direction ($Pr_{t,V}$). In water quality simulations, the eddy diffusivity for heat should be replaced with the eddy diffusivity for contaminant mass (Eq. 3-4). Similar to the way momentum and heat transfer rates are related using the turbulent Prandtl number, momentum and contaminant mass transfer rates are linked using the turbulent Schmidt number (Sc_t, Eq. 3-5) (Donzis et al., 2014; Graf and Cellino, 2002; Gualtieri et al., 2017; Rauen et al., 2012).

$$-\overline{u'C'} = A_c \frac{\partial \bar{C}}{\partial x} \quad (3\text{-}4)$$

$$Sc_t = \frac{A_m}{A_c} \quad (3\text{-}5)$$

where *C* denotes the dissolved or suspended contaminant concentration. If the turbulent Schmidt number is known, then the above equation can be used to compute the eddy diffusivity coefficient used in the advection-dispersion-reaction equation for concentration. The FVCOM manual uses the same symbol A_h (used for heat) for the eddy diffusion coefficient for solute transport as well (that is, $A_c = A_h$). Although this maybe a reasonable assumption for the transport of dissolved substances (e.g., DO), significant differences can be expected if the interest is in modeling the transport of suspended material such as sediment or bacteria. Therefore, it is important to make a distinction between A_h and A_c (or alternatively, between the turbulent Prandtl number and the turbulent Schmidt number).

Turbulent Prandtl number (Pr_t) can help characterize the influences of momentum and heat flux on hydrodynamics in the horizontal and vertical directions. Pr_t can be related to the fluid's molecular Prandtl number (Pr) via Eq. 3-6 (Malhotra and Kang, 1984)

$$Pr_t = 1.01 - 0.09Pr^{0.36} \tag{3-6}$$

where $Pr = \upsilon/\alpha$ is the ratio of the kinematic viscosity to the thermal diffusivity of the fluid and is therefore a property of the fluid (Malhotra and Kang, 1984). The turbulent Prandtl number, on the other hand, is a property of the flow field and can change in a complex manner depending on conditions within the water column (Kays, 1994; Ye et al., 2019). Conceptually, Pr_t helps describe the additional shear stress and heat flux that are present in turbulent flows but absent from laminar flows, and how the resulting impacts relate to one another. Eddy diffusivity models have proven to be useful, and continue to be useful, for modeling large natural systems such as lakes and oceans. Recent advances in the field of turbulence modeling have led to models that can simulate hydrodynamics and temperature without the need for a turbulent Prandtl number. These advances, thus, render the concept of a turbulent Prandtl number meaningless for turbulent flows within many fully 3-dimensional unsteady models (Kays, 1994; Launder, 1989; Nagano and Kim, 1988). However, the thermal eddy diffusivities and momentum eddy viscosities remain important for characterizing hydrodynamics and mixing in large bodies of water that are prone to stable stratification (Elliott and Venayagamoorthy, 2011; Noh et al., 2005; Ye et al., 2019). Therefore, turbulent Prandtl numbers in eddy diffusivity models influence the ability of models to predict hydrodynamics (directly) and water quality (indirectly via hydrodynamics) while the turbulent Schmidt number directly influences the ability to predict contaminant concentrations in such large systems.

A simplification of Pr_t is the Reynolds analogy, where momentum and heat transfer rates are identical such that Pr_t is unity (Crimaldi et al., 2006). However, experimental data have suggested that this simplification may not be realistic for environmental turbulent flows, particularly in stably stratified conditions (Crimaldi et al., 2006; Ye et al., 2019). Beginning in the 1990's, research suggested that Pr_t values should realistically be approximately 0.85 for natural waters (Kays, 1994). More recent experimental data, however, have shown that Pr_t values can be location-dependent, varying from 1.5 to 4.2 in Antarctica's Ross Sea (Muench et al., 2009) and from 2 to 8 in Narragansett Bay, Rhode Island USA (Goodman and Levine, 2003).

Values of turbulent Schmidt numbers reported in the literature for environmental flows varied considerably but the best-fitting Sc_t values were found to be in the range 0.1 – 1.0 with values greater than 1.0 (but less than 2.1) representing sediment-laden open channels flows of sand particles (Gualtieri et al., 2017). Although a separate sensitivity analysis can be carried out by varying Sc_t in the range 0.1 – 2.1 after identifying the best Prandtl number for hydrodynamic simulations, the assumption $Sc_t = Pr_t$ is made, following the same assumption in the FVCOM modeling framework and considering that the particle sizes that *E. coli* are known to associate with are significantly smaller than sand particles.

Since molecular and turbulent Prandtl numbers can inherently impact hydrodynamics in a lake setting, they are also important for describing the fate and (especially) transport of contaminants suspended in the water. Therefore, Prandtl numbers may substantially affect the ability of models to characterize water quality in large bodies of water, because of their effects on vertical mixing schemes (Elliott and Venayagamoorthy, 2011; Noh et al., 2005). Further, because contaminants in the water have different molecular properties than the water itself, they may get transported at different rates compared to the rates of momentum and heat transport. Similar to the molecular Prandtl number, the molecular Schmidt number ($Sc = \upsilon/D$) is a property of water and represents the ratio of viscosity (υ) to the binary diffusion coefficient (D) of the contaminant in water. The turbulent Schmidt number is a property of the flow, like the turbulent Prandtl number.

Despite the potential for influence on water quality models, systematic efforts to quantify the effects of turbulent Prandtl and Schmidt numbers on hydrodynamics, thermal structure and concentrations of dissolved and suspended material (e.g., sediment, bacteria) within coastal regions are limited. Because Pr_t values are often assumed to be close to one (Kays, 1994), it seems that there is little discussion of how they can affect hydrodynamics and water quality simulation. However, looking at the effects of different Prandtl numbers on contaminant fate and transport models can shed light on physical drivers of contaminant transport in the nearshore zone. With this in mind, our research objectives were to assess the sensitivity of coupled numerical hydrodynamics and water quality models for southern Lake Michigan to changes in Pr_t inputs. We conducted a sensitivity analysis for models using horizontal and vertical Pr_t values ranging from 0.1 to 10.0 to evaluate the model predictive ability in the context of hydrodynamics and water quality. The results of the sensitivity analysis provided insight into optimal Pr value combinations for simulating lake surface temperature (LST), lake currents and water quality for southwestern Lake Michigan. Further, the results allowed for inferences regarding a theoretical case for using different Pr_t values for bulk water and water quality variables.

3.2. Methods

3.2.1. Numerical Modeling Framework

The Finite Volume Community Ocean Model (FVCOM) numerical modeling framework was used to assess the impacts of turbulent Prandtl number on simulation of hydrodynamics and water quality. This is an unstructured-grid, finite-volume, fully three-dimensional model approach to the simulation of hydrodynamics in nearshore environments, using primitive Navier-Stokes equations governing momentum (Eq. 3-7a-c), continuity (Eq. 3-8), salinity (Eq. 3-9), density (Eq. 3-10) and temperature (Eq. 3-11) (Chen et al., 2003). Equations are solved for nodes and cells across a spatial mesh grid, and over multiple timesteps to create the base hydrodynamics model.

$$\frac{\partial u}{\partial t} + u\frac{\partial u}{\partial x} + v\frac{\partial u}{\partial y} + w\frac{\partial u}{\partial z} - fv = -\frac{1}{\rho_o}\frac{\partial(p_H+p_a)}{\partial x} - \frac{1}{\rho_o}\frac{\partial q}{\partial x} + \frac{\partial}{\partial z}\left(K_m\frac{\partial u}{\partial z}\right) + A_m\left(\frac{\partial^2 u}{\partial x^2} + \frac{\partial^2 u}{\partial y^2}\right) \tag{3-7a}$$

$$\frac{\partial v}{\partial t} + u\frac{\partial v}{\partial x} + v\frac{\partial v}{\partial y} + w\frac{\partial v}{\partial z} + fu = -\frac{1}{\rho_o}\frac{\partial(p_H+p_a)}{\partial y} - \frac{1}{\rho_o}\frac{\partial q}{\partial y} + \frac{\partial}{\partial z}\left(K_m\frac{\partial v}{\partial z}\right) + A_m\left(\frac{\partial^2 v}{\partial x^2} + \frac{\partial^2 v}{\partial y^2}\right) \tag{3-7b}$$

$$\frac{\partial w}{\partial t} + u\frac{\partial w}{\partial x} + v\frac{\partial w}{\partial y} + w\frac{\partial w}{\partial z} = -\frac{1}{\rho_o}\frac{\partial q}{\partial z} + \frac{\partial}{\partial z}\left(K_m\frac{\partial w}{\partial z}\right) + A_m\left(\frac{\partial^2 w}{\partial x^2} + \frac{\partial^2 w}{\partial y^2}\right) \tag{3-7c}$$

$$\frac{\partial u}{\partial x} + \frac{\partial v}{\partial y} + \frac{\partial w}{\partial z} = 0 \tag{3-8}$$

$$\frac{\partial S}{\partial t} + u\frac{\partial S}{\partial x} + v\frac{\partial S}{\partial y} + w\frac{\partial S}{\partial z} = \frac{\partial}{\partial z}\left(K_h\frac{\partial S}{\partial z}\right) + A_h\left(\frac{\partial^2 S}{\partial x^2} + \frac{\partial^2 S}{\partial y^2}\right) \tag{3-9}$$

$$\rho = \rho(T, S, p) \tag{3-10}$$

$$\frac{\partial T}{\partial t} + u\frac{\partial T}{\partial x} + v\frac{\partial T}{\partial y} + w\frac{\partial T}{\partial z} = \frac{\partial}{\partial z}\left(K_h\frac{\partial T}{\partial z}\right) + A_h\left(\frac{\partial^2 T}{\partial x^2} + \frac{\partial^2 T}{\partial y^2}\right) \tag{3-11}$$

In these equations, u, v and w are the velocity components in the x, y and z directions, respectively (m s^{-1}). S and T represent salinity and water temperature. fu and fv are Coriolis terms (m^2 s^{-1}). Horizontal eddy viscosity and eddy diffusivity (m^2 s^{-1}) are represented by A_m and A_h, respectively. Likewise, vertical eddy viscosity is denoted by K_m (m^2 s^{-1}) and thermal vertical eddy diffusion coefficient is K_h (m^2 s^{-1}). ρ_o is the density of water (kg m^{-3}). Pressure terms include air pressure (p_a), hydrostatic pressure (p_H) and non-hydrostatic pressure (q), all in units of Pa.

This base model of hydrodynamics can be expanded to include water quality impacts at nearshore regions, via the use of a Water Quality Model (FVCOM-WQM). This allows the model to simulate localized contamination at beaches (Ge et al., 2012; Thupaki et al., 2010). By including source and sink terms and contaminant decay functions (Eq. 3-12) to the advection-dispersion-reaction (ADR) equation (Eq. 3-13), these models can effectively simulate the flux of microbial water quality contaminants like Fecal Indicator Organisms (FIO) (Liu et al., 2006; Safaie et al., 2016; Thupaki et al., 2010).

$$k = \left[\frac{f_p v_s}{H} + k_I I_t + k_d\right] \theta^{T-20} \tag{3-12}$$

$$\frac{\partial C}{\partial t} + u\frac{\partial C}{\partial x} + v\frac{\partial C}{\partial y} + w\frac{\partial C}{\partial z} = \frac{\partial}{\partial x}\left(A_c\frac{\partial C}{\partial x}\right) + \frac{\partial}{\partial y}\left(A_c\frac{\partial C}{\partial y}\right) + \frac{\partial}{\partial z}\left(K_c\frac{\partial C}{\partial z}\right) - kC \tag{3-13}$$

In the ADR (Eq. 3-13), k is the contaminant decay function, C is the contaminant concentration in the water (commonly MPN 100 mL^{-1}) and A_c and K_c are horizontal and vertical mixing coefficients, respectively (m^2 s^{-1}). Within the contaminant decay function itself (Eq. 3-12), f_p is the fraction of contaminant concentration that is attached to suspended particles in the water (unitless), v_s is the settling velocity of the suspended particles (m d^{-1}) and H is the depth of the water column (m). I_t represents the solar irradiance at the water surface at time t (W m^{-2}), k_I is the contaminant solar inactivation rate (m^2 W^{-1} d^{-1}), k_d denotes base mortality (d^{-1}) and θ^{T-20} is a temperature (T, °C) correction factor (unitless).

Eddy viscosity and diffusivity within FVCOM can be calculated using multiple approaches but are commonly computed using the Smagorinsky formulation in the x and y directions (Smagorinsky, 1963) and the Mellor-Yamada Level 2.5 Turbulent Closure Model in the vertical direction (Mellor and Yamada, 1982).

Utilizing the Smagorinsky formulation, horizontal diffusion of momentum (A_m) and thermal diffusion (A_h) coefficients are calculated using Eq. 3-14 and 3-15, respectively.

$$A_m = 0.5C\Omega^u \sqrt{\left(\frac{\partial u}{\partial x}\right)^2 + 0.5\left(\frac{\partial v}{\partial x} + \frac{\partial u}{\partial y}\right)^2 + \left(\frac{\partial v}{\partial y}\right)^2} \tag{3-14}$$

$$A_h = \frac{0.5C\Omega^\zeta}{Pr_{t,H}} \sqrt{\left(\frac{\partial u}{\partial x}\right)^2 + 0.5\left(\frac{\partial v}{\partial x} + \frac{\partial u}{\partial y}\right)^2 + \left(\frac{\partial v}{\partial y}\right)^2} \tag{3-15}$$

In these calculations, C is a constant parameter, Ω^u and Ω^ζ represent the area of individual momentum and tracer control elements (i.e., cells) in the model domain's mesh grid, respectively. Pr_H is the horizontal Prandtl number. Similar to the overall momentum equations used in FVCOM, u and v here are the velocity components of currents in the x and y horizontal directions.

In the vertical plane, the Mellor-Yamada 2.5 level turbulence model (MY2.5) (Chen et al., 2006; Mellor and Yamada, 1982) solves equations for turbulent kinetic energy (q^2) and q^2l, a combination of turbulent kinetic energy and turbulence length scale (l) (Eq. 3-16 and 3-17).

$$\frac{\partial q^2}{\partial t} + u\frac{\partial q^2}{\partial x} + v\frac{\partial q^2}{\partial y} + w\frac{\partial q^2}{\partial z} = 2(P_s + P_b - \varepsilon) + \frac{\partial}{\partial z}\left(K_q \frac{\partial q^2}{\partial z}\right) + F_q \tag{3-16}$$

$$\frac{\partial q^2 l}{\partial t} + u\frac{\partial q^2 l}{\partial x} + v\frac{\partial q^2 l}{\partial y} + w\frac{\partial q^2 l}{\partial z} = lE_1\left(P_s + P_b - \frac{\widetilde{W}}{E_1}\varepsilon\right) + \frac{\partial}{\partial z}\left(K_q \frac{\partial q^2 l}{\partial z}\right) + F_l \tag{3-17}$$

In these equations, u, v, and w are components of velocity in the x, y, and z directions, following the parameterization in Eq. 3-3 – 3-7. F_q is the horizontal diffusion of turbulent kinetic energy, F_l is the horizontal diffusion of the turbulence macroscale, K_q is the vertical eddy diffusion coefficient and E_1 is a model constant of value 1.8. ε is the dissipation rate of turbulent kinetic energy (Eq. 3-18), where B_1 is a model constant.

$$\varepsilon = \frac{q^3}{B_1 l} \tag{3-18}$$

P_s and P_b in Eq. 3-16 and 3-17 represent shear and buoyancy production, in terms of turbulent kinetic energy, water density (ρ), a reference density (ρ_0), acceleration due to gravity (g), vertical eddy viscosity coefficient (K_m, Eq. 3-19), vertical thermal eddy diffusion (K_h, Eq. 3-20), the Brunt-Väisälä frequency for the calculation of vertical direction of water movement (N) (Kundu et al., 2016), and shear frequency (M).

$$K_m = lqS_m \tag{3-19}$$

$$K_h = lqS_h = \frac{K_m}{Pr_{t,V}} \tag{3-20}$$

where S_m and S_h are stability functions in terms of constants A_1 = 0.92, B_1 = 16.6, C_1 = 0.08, A_2 = 0.74 and B_2 = 10.10 (Eq. 3-21 – 3-22) (Allen et al., 1995; Galperin et al., 1988; Mellor and Yamada, 1982). G_H in the equations below is represented by Eq. 3-23 and must fall between -0.28 for stably stratified conditions and 0.02 for unstable conditions.

$$S_m = A_1 \frac{(1-3C_1-6A_1B_1^{-1})+9(2A_1+A_2)S_H G_H}{1-9A_1A_1G_H} \tag{3-21}$$

$$S_h = A_2 \frac{1-6A_1B_1^{-1}}{1-3A_2(6A_1+B_2)G_H} \tag{3-22}$$

$$G_H = \frac{-l^2N^2}{q^2} \tag{3-23}$$

To calculate the wall proximity function $\widetilde{W}$ from Eq. 3-17, free surface elevation (ζ), mean water depth (H), the von Karman constant κ and a constant of E_2 = 1.33 are incorporated into Eq. 3-24.

$$\widetilde{W} = 1 + \frac{E_2 l^2}{(\kappa L)^2} \tag{3-24}$$

Here, $L^{-1} = (\zeta - z)^{-1} + (H + z)^{-1}$.

By adjusting model inputs to these equations, it is possible to evaluate the impacts of such conditions on model predictive ability, leading to model optimization for applications like beach water quality management and engineering for public health. In this case, Pr_H and Pr_V values were adjusted and assessed for resulting model predictive ability.

3.2.2. Input Data and Boundary Conditions

Hydrodynamic and water quality models were run over a model domain mesh encompassing the entirety of Lake Michigan. Mesh grid resolution was variable, ranging from 50 m near the shore in southwestern Lake Michigan to 2 km offshore and in the northern part of the lake (Figure 3-1), to balance computational requirements with resolution of shoreline features in the lake's southern basin. The mesh was created using Surface-water Modeling System (SMS) 12.2 (Aquaveo, Provo, UT USA). Lake bathymetry data from the National Oceanic and Atmospheric Administration's (NOAA) National Centers for Environmental Information (NCEI) (NOAA, 2018a) were interpolated across the mesh to create the model's three-dimensional spatial domain for FVCOM (Figure 3-2).

Figure 3-1: Google Earth image of Lake Michigan with FVCOM model domain mesh grid overlaid. Mesh grid shows smaller triangular mesh elements (indicating higher mesh resolution) in southwestern Lake Michigan, compared to northern and offshore areas

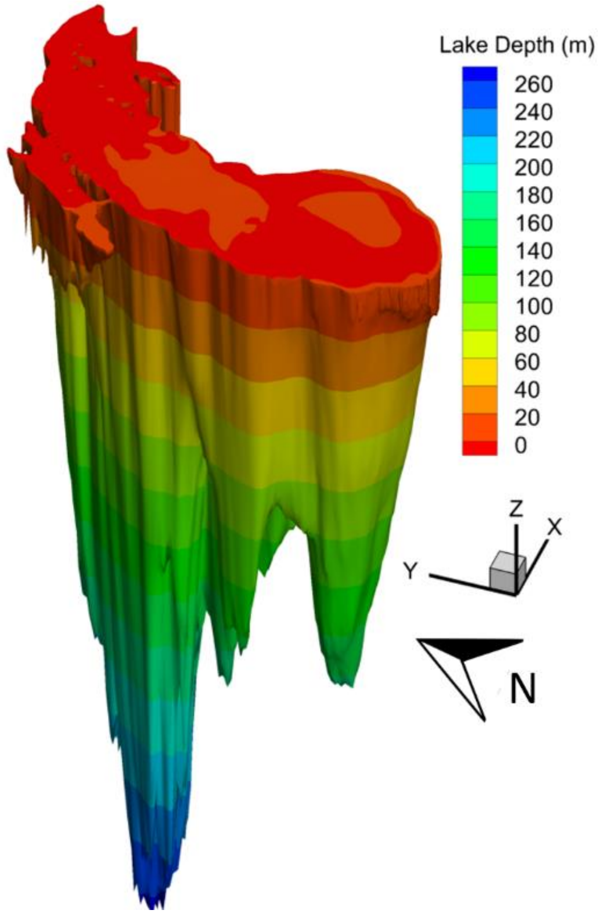

Figure 3-2: Three-dimensional representation of Lake Michigan bathymetry used in FVCOM simulations

When not using a restart file, FVCOM models begin simulations with conditions of zero currents and a lakewide constant temperature. As the models work through calculations and simulation timesteps, they become increasingly robust at simulating spatiotemporally varying conditions in a process called “spin up”. Often, these models require weeks to months of model spin up time before adequately simulating conditions across a lake. Herein, a validated base hydrodynamic model simulating January 1st to June 9th, 2008 was used as a restart file for the model. This allowed for immediate reliable representation of hydrodynamic conditions within Lake Michigan and avoided the need for model “spin up”. Using the restart file, models were initialized to simulate conditions between June 9th and August 27th, 2008 for the sensitivity analysis. Meteorological forcing data corresponding to times throughout the models' temporal domain came from up to 118 buoy and weather station locations, from NOAA's NCEI and National Data Buoy Center (NDBC) (NOAA, 2018a, 2018b) and were interpolated to the model mesh.

Surface winds and heat fluxes in the models were calculated using the COARE 26Z bulk air-sea flux formulation (Fairall et al., 2003, 1996). Mixing was simulated using the turbulent closure models from Smagorinsky (Smagorinsky, 1963) and Mellor & Yamada (Mellor and Yamada, 1982) with horizontal diffusion coefficient (A_m) and vertical eddy viscosity (K_m) values of 0.1 and $1.0*10^{-6}$, respectively. River flow inputs to the model were simulated for the period of June 9th to August 17th, 2008 from USGS stream gauge data from gauge 04095090 in northwest Indiana (41.634° N, 87.178° W).

The Water Quality Model (WQM) within FVCOM used input *E. coli* concentrations at the outlet of the Burns waterway, collected *in situ* between June 8th and August 16th, 2008. The subsequent microbial decay function used to model *E. coli* fate and transport in the lake utilized terms for solar inactivation, sedimentation, and base mortality (Eq. 3-12, above), as presented by Liu et al. (Liu et al., 2006) and Safaie et al. (Safaie et al., 2016). Following Safaie et al. (Safaie et al., 2016), f_p = 0.05, v_s = 1 m d^{-1}, k_I = 0.003 m^2 W^{-1} d^{-1}, k_e = 0.55 m^{-1} and k_d = 0.777 d^{-1} for the models presented.

3.2.3. Sensitivity Analysis

The impacts of changing input turbulent Prandtl numbers on water quality were assessed through the systematic adjustment of both vertical and horizontal turbulent Prandtl numbers within the FVCOM framework. FVCOM allows for the input of horizontal and vertical turbulent Prandtl numbers ranging from 0.1 to 10.0 (Chen et al., 2006). Thirteen different combinations of vertical and horizontal turbulent Prandtl numbers were specified in the FVCOM input file (Table 3-1), resulting in 13 separate model simulations for June – August 2008.

Table 3-1: Names of 13 models used in sensitivity analysis and corresponding horizontal and vertical turbulent Prandtl numbers used

Model Name	Horizontal Prandtl Number ($Pr_{t,H}$)	Vertical Prandtl Number ($Pr_{t,V}$)
mich08-1	0.1	0.1
mich08-2	0.1	0.14
mich08-3	0.14	0.1
mich08-4	0.2	0.2
mich08-5	0.5	0.5
mich08-6	0.85	0.85
mich08-7	1	1
mich08-8	1.18	1.18
mich08-9	2	2
mich08-10	5	5
mich08-11	7	10
mich08-12	10	7
mich08-13	10	10

These combinations of horizontal and vertical turbulent Prandtl numbers span the range of applicable values that can be used in FVCOM and represent ratios that signify higher relative influences of both thermal diffusivity and eddy viscosity as well as a balance between their relative impacts on hydrodynamics. Some of the combinations come from previous published model frameworks (e.g., mich08-2, mich08-8) (Kays, 1994; Safaie et al., 2016), while others were chosen to encapsulate the range of potential value combinations in the models. Within the models, mixing coefficients such as the eddy diffusivity and eddy viscosity remained the same for both hydrodynamics and water quality models. This allowed for the assumption that the resulting Pr_t value in the hydrodynamic model would be equal to the value of the corresponding Sc_t number for the *E. coli* model. This, in turn, meant that the models for hydrodynamics and *E. coli* could both be assessed, in terms of the optimization of Pr_t and Sc_t.

3.2.4. Model Validation

The 13 WQM simulations of southern Lake Michigan in 2008 were comparatively evaluated in terms of their ability to reproduce observational data in the model spatiotemporal domain. Modeled LST was plotted against observed LST at NDBC buoy 45007 (42.674° N, 87.026° W) (NOAA 2018b). Modeled water temperatures at depth over time were plotted and visually compared to observations from a thermistor chain mooring deployed at buoy 45007 (NOAA National Centers for Environmental Information, Accession 0190726). Additionally, root mean squared error (RMSE) values were calculated for the comparisons of the model results (P_i) to observations (O_i) of LST, following Eq. 3-25. Currents within the lake were assessed similarly. Model results for each of the 13 simulations were plotted against currents observed in the *u* and *v* directions at a nearshore Acoustic Doppler Current Profiler (ADCP) location (MADCP: 41.711 °N, 87.210 °W, Figure 3-3) for qualitative evaluation. RMSE values for *u*- and *v*-components of current and the resulting prevailing currents ($|V|$, Eq. 3-26) were calculated as a quantitative assessment.

$$RMSE = \sqrt{\frac{\sum_{i=1}^{n}(P_i - O_i)^2}{n}} \tag{3-25}$$

$$|V| = \sqrt{u^2 + v^2} \tag{3-26}$$

E. coli concentration results were validated against daily sample observations from Ogden Dunes beach in northwest Indiana (41.630° N, 87.197° W) (Figure 3-3). In similar fashion to temperature and current validation for model results, modeled *E. coli* concentration results over time were plotted against observed *E. coli* concentrations at the beach. Multiple validation metrics were used to evaluate the model simulations in the context of *E. coli* because no single metric can capture all aspects of model predictive ability (Legates and McCabe, 1999). As a result, the common coefficient of determination (R^2) and RMSE metrics were used during evaluation and were supplemented by percent bias (PBIAS, Eq. 3-27), Nash-Sutcliffe efficiency (NSE, Eq. 3-28), RMSE-observation standard deviation ratio (RSR, Eq. 3-29) and normalized Fourier norm (F_n, Eq. 3-30) calculations to assess model predictive ability (Fry et al., 2013; Moriasi et al., 2007; Ritter and Munoz-Carpena, 2013; Thupaki et al., 2013). All validation statistics for the prediction of *E. coli* concentrations at Ogden Dunes beach utilized $\log_{10}$-transformations of observed and simulated concentrations (Oudin et al., 2006).

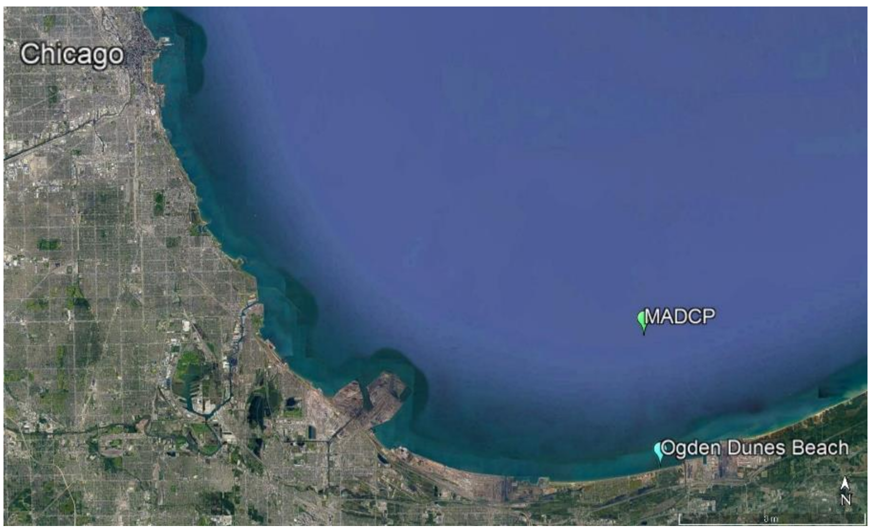

Figure 3-3: Google Earth image showing locations of MADCP and Ogden Dunes beach in southern Lake Michigan, relative to Chicago

$$PBIAS = \frac{\sum_{i=1}^{n}(O_i - P_i)\times 100}{\sum_{i=1}^{n} O_i} \tag{3-27}$$

$$NSE = 1 - \frac{\sum_{i=1}^{n}(O_i - P_i)^2}{\sum_{i=1}^{n}(O_i - \bar{O})^2} \tag{3-28}$$

$$RSR = \frac{\sqrt{\sum_{i=1}^{n}(O_i - P_i)^2}}{\sqrt{\sum_{i=1}^{n}(O_i - \bar{O})^2}} \tag{3-29}$$

$$F_n = \frac{\sqrt{\frac{\sum_{i=1}^{n}(|O_i - P_i|)^2}{n}}}{\sqrt{\frac{\sum_{i=1}^{n}(O_i)^2}{n}}} \qquad (3\text{-}30)$$

Models which maximized R^2 values, minimized RMSE and RSR, and produced NSE, PBIAS and F_n values closest to 1, 0 and 0, respectively, were deemed optimal for simulation of water quality at Ogden Dunes beach. This analysis created a hierarchy of model turbulent Prandtl number options recommended for use in hydrodynamic and water quality modeling for water bodies like southwestern Lake Michigan.

3.3. Results and Discussion

3.3.1. Model Comparisons with Observed Temperature at Buoy 45007

Temperature observations at both the water surface and over the water column depth were recorded in the middle of Lake Michigan's southern basin, at the location of the NOAA NDBC buoy 45007 (NOAA 2018b). These observations were compared to predicted water temperatures at this location for each of the 13 FVCOM models, for the time period of June 9th to August 27th, 2008.

Plotted comparisons of surface water temperatures at buoy 45007 (Figure 3-4) indicate that, overall, the FVCOM models simulate the observed water temperatures reasonably well. During the warming period of late spring to early summer, the models tended to predict more rapid warming of the water than was observed. This is a known limitation within the FVCOM framework and highlights a need for continued model refinement and improvement, particularly in the context of spring and fall seasons, when the water column mixes, changing water temperatures. The models were able to simulate LST especially well toward the middle and end of the summer, with many of the simulated temperatures matching observations very well during August of 2008. Despite the general predictive ability of all models for the summer of 2008 in the context of surface water temperature, there are some discrepancies between the models, suggesting that adjustment of the turbulent Prandtl numbers within the models can impact resulting water temperature predictions.

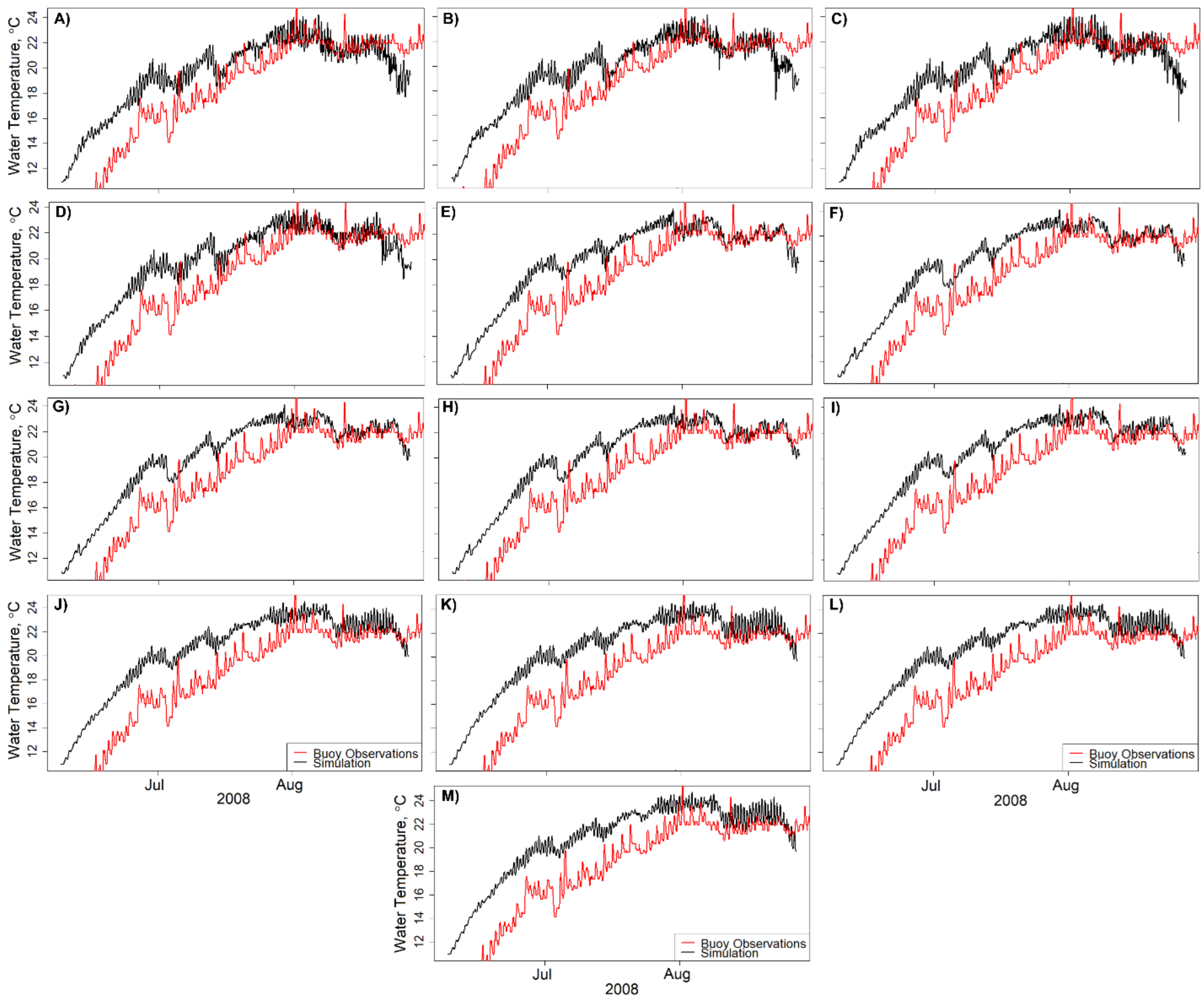

Figure 3-4: Plots comparing simulated (black lines) and observed (red lines) surface water temperatures over time in 2008 at Buoy 45007. Plots A-M correspond to results from models mich08-1 to mich08-13, respectively

As seen in Figure 3-4, models mich08-1, mich08-2, mich08-3, and mich08-4 show a better correlation between observed and simulated surface water temperature than models mich08-9, mich08-10, mich08-11, mich08-12 and mich08-13. These trends are supported by the quantitative analysis of simulated surface water temperatures at the buoy. Models mich08-6 and mich08-7 show the lowest LST RMSE values, when simulations were compared to buoy observations (RMSE range = 2.53 and 2.55 °C, respectively). Generally, models using $Pr_{t,H}$ values ≤ 1 yielded lower RMSE values than those utilizing $Pr_{t,H}$ values > 1. Models mich08-8 through mich08-11 all yielded RMSE values above 3.00 °C (RMSE range = 3.00 – 3.21 °C, Table 3-2). This further indicates that $Pr_{t,H}$ values ≤ 1 may lead to better FVCOM simulations of LST for southwestern Lake Michigan than $Pr_{t,H}$ values > 1. However, it seems that the optimal horizontal and $Pr_{t,V}$ values for prediction of surface water temperature are close to 1, with the optimal model using $Pr_{t,H}$ and $Pr_{t,V}$ values of 0.85.

Table 3-2: Lake surface water temperature RMSE values for 13 FVCOM models with varying Prandtl number combinations

Model Name	**Lake Surface Temperature RMSE (°C)**
mich08-1	2.63
mich08-2	2.63
mich08-3	2.66
mich08-4	2.61
mich08-5	2.57
mich08-6	2.53
mich08-7	2.55
mich08-8	2.59
mich08-9	2.74
mich08-10	3.00
mich08-11	3.17
mich08-12	3.14
mich08-13	3.21

Similar results are seen in visual comparison of water temperature at depth and over time at buoy 45007. Thermistor chain data show that water near the surface of the basin (< 80 m depth) gradually warms to 22.36°C over the course of the summer and particularly in July and August 2008. Meanwhile, water temperatures at depths greater than 80 m remain near 4 °C throughout the summer (Figure 3-5). FVCOM model water temperature results, across the board, did not simulate the depth of the warming over the summer in the middle of the southern basin of Lake Michigan. The FVCOM models also indicated earlier surface water warming at the thermistor chain location than the observational data showed. Model results suggested surface water temperatures of 10°C in June while observations remained near 5°C at the surface until mid-July 2008. While the models do simulate a gradual warming of the surface layers of the lake over the summer, the depth and timing of that warming are not fully captured in any of the model results (Figure 3-5), suggesting that FVCOM models of water temperature would benefit from additional optimization, across the board. However, assessment of the plots can lend some insight into which FVCOM models can better simulate the warming of the basin at depth over time. Mich08-11 through mich08-13 results suggest that water only warmed during the season at depths < ~30 m. Other models indicate that the water warmed at depths less than 40 – 50 m, potentially signifying improved prediction of water temperature at depth for models mich08-1 through mich08-10 over models mich08-11 through mich08-13. Models mich08-5 through mich08-8 show that the water warmed to 20 – 25 °C at depths greater than 10 m, better reflecting the observed warming to that level at depths of up to 30 m compared to other model simulations.

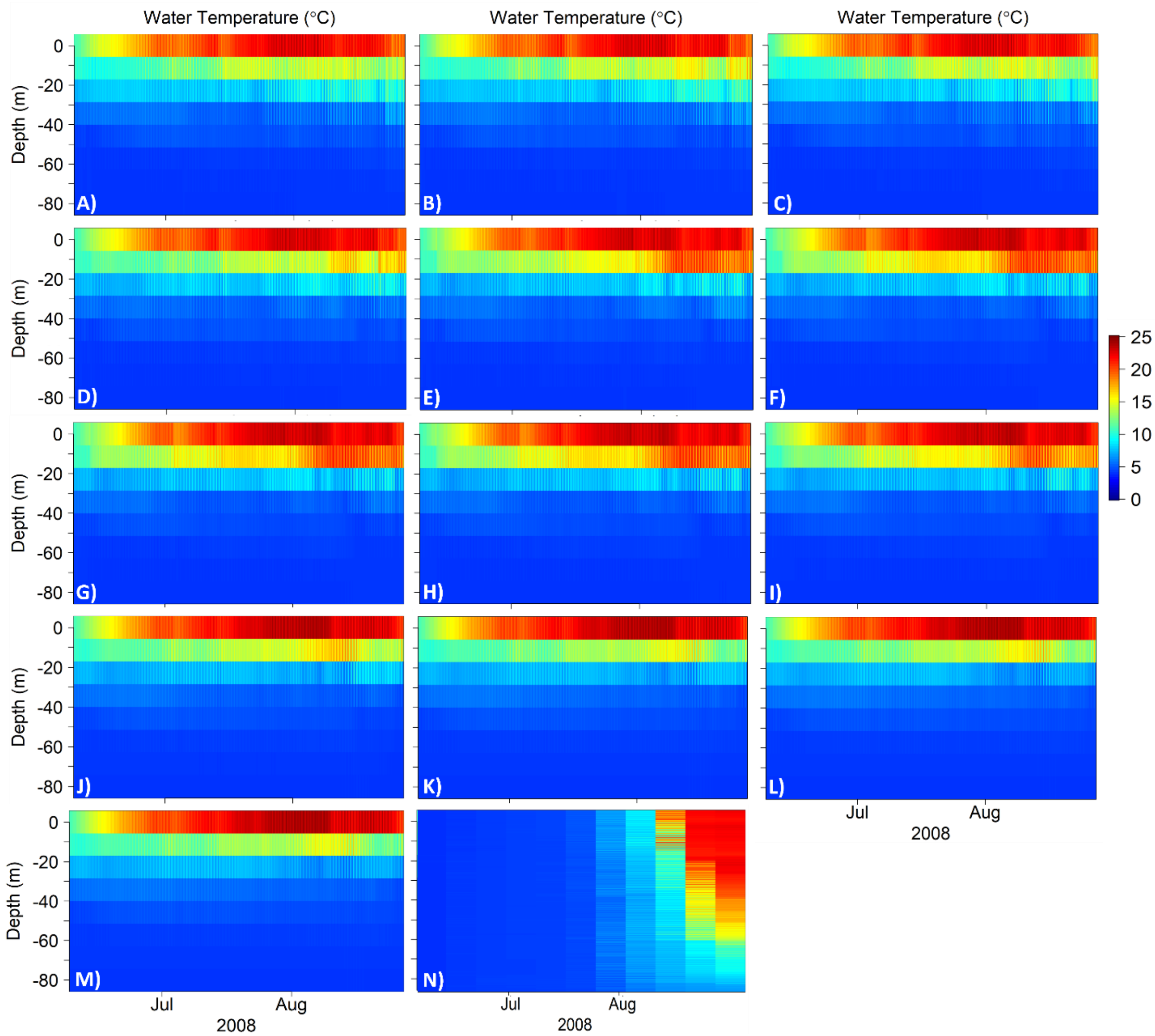

Figure 3-5: Heat map plots comparing simulated water temperatures at depth and over time in 2008, at the location of Buoy 45007. Plots A - M correspond to results from models mich08-1 to mich08-13, respectively and were compared to thermistor chain observations depicted in plot N. Depths were truncated to -80 meters to highlight temperature changes near the water surface

3.3.2. Model Comparisons with Observed Currents at Acoustic Doppler Current Profiler Locations

Additionally, *u* and *v* current component results for the 13 models were compared to *u* and *v* current component observations obtained at the MADCP location near the northwest Indiana shoreline. Plotted comparisons of currents for simulated and observed data show that the 13 models have simulated currents in southern Lake Michigan with reasonable reliability, capturing the majority of maximum and minimum values for both *u*- and *v*-components of current (Figure 3-6). Qualitatively, none of the 13 models is substantially better or worse than the others, in terms of comparison to observed current values.

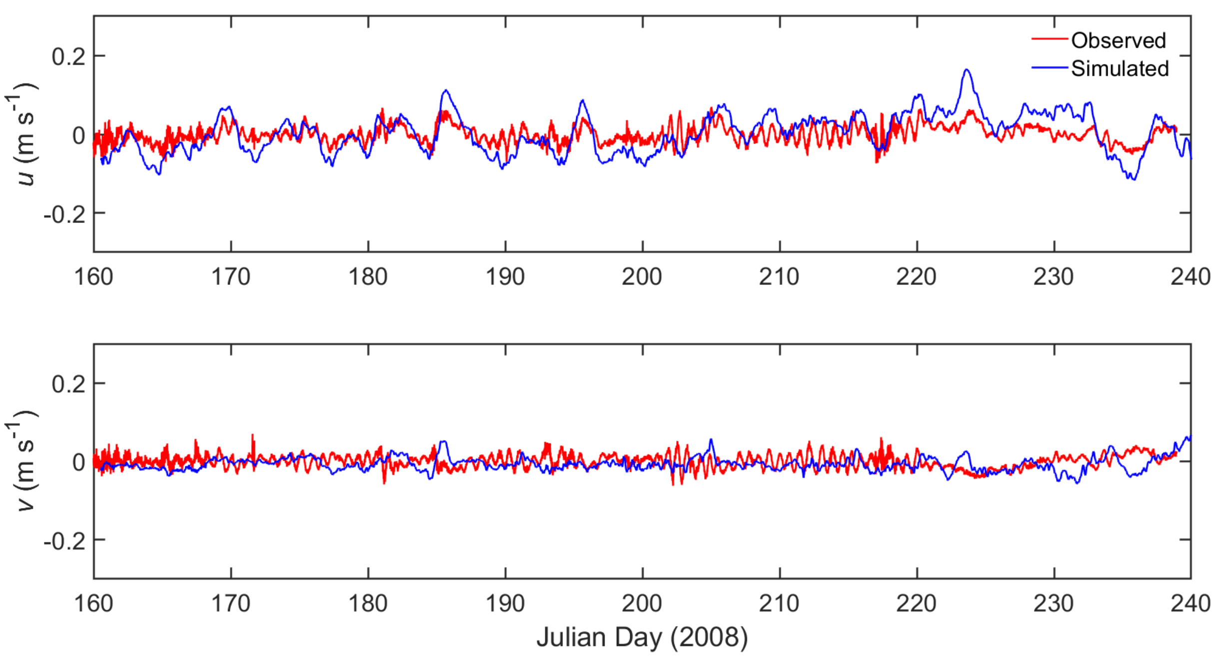

Figure 3-6: Comparison of simulated and observed u- and v-components of current at the MADCP location in Lake Michigan for model mich08-1. Additional comparison plots for other model simulations can be found in Appendices A-1 – A-12

Quantitatively, RMSE values for current comparisons are all in the range of 0.025 to 0.054 m s^{-1} (Table 3-3). RMSE values for *u* current components at both BBADCP and MADCP are larger in magnitude than RMSE values for *v* components, which is common and to be expected. At the

MADCP location, *u* RMSE values are 0.0076 to 0.019 m s^{-1} greater than *v* RMSE values. All RMSE values for *u* and *v* current components are at least an order of magnitude smaller than the values of the current components, further suggesting reasonable predictive ability of the models. These RMSE values are comparable to previously published RMSE values for models of currents in the same area of Lake Michigan (Safaie et al., 2016; Thupaki et al., 2013).

In terms of comparing current predictive ability between models at the MADCP location, RMSE for *u* current component is minimized in models mich08-1, mich08-2 and mich08-3 and maximized for models mich08-11, mich08-12 and mich08-13 (Table 3-3, Figure 3-7). Interestingly, comparison of RMSE values for the *v*-components of current between models shows a different and more varied trend. RMSE for *v*-component of current is minimized under models mich08-12, mich08-13 and mich08-4 and maximized under models mich08-10, mich08-11 and mich08-5 (Table 3-3, Figure 3-7).

Table 3-3: RMSE values for 13 models, comparing modeled and observed u-components, v-components and overall currents at BBADCP and MADCP locations

Model Name	MADCP *u*-Component RMSE	MADCP *v*-Component RMSE	MADCP Overall Current RMSE
mich08-1	0.040	0.026	0.034
mich08-2	0.040	0.026	0.033
mich08-3	0.040	0.026	0.033
mich08-4	0.041	0.025	0.034
mich08-5	0.042	0.026	0.035
mich08-6	0.043	0.026	0.036
mich08-7	0.043	0.026	0.036
mich08-8	0.044	0.026	0.037
mich08-9	0.046	0.026	0.038
mich08-10	0.049	0.041	0.026
mich08-11	0.051	0.044	0.026
mich08-12	0.050	0.025	0.042
mich08-13	0.051	0.025	0.044

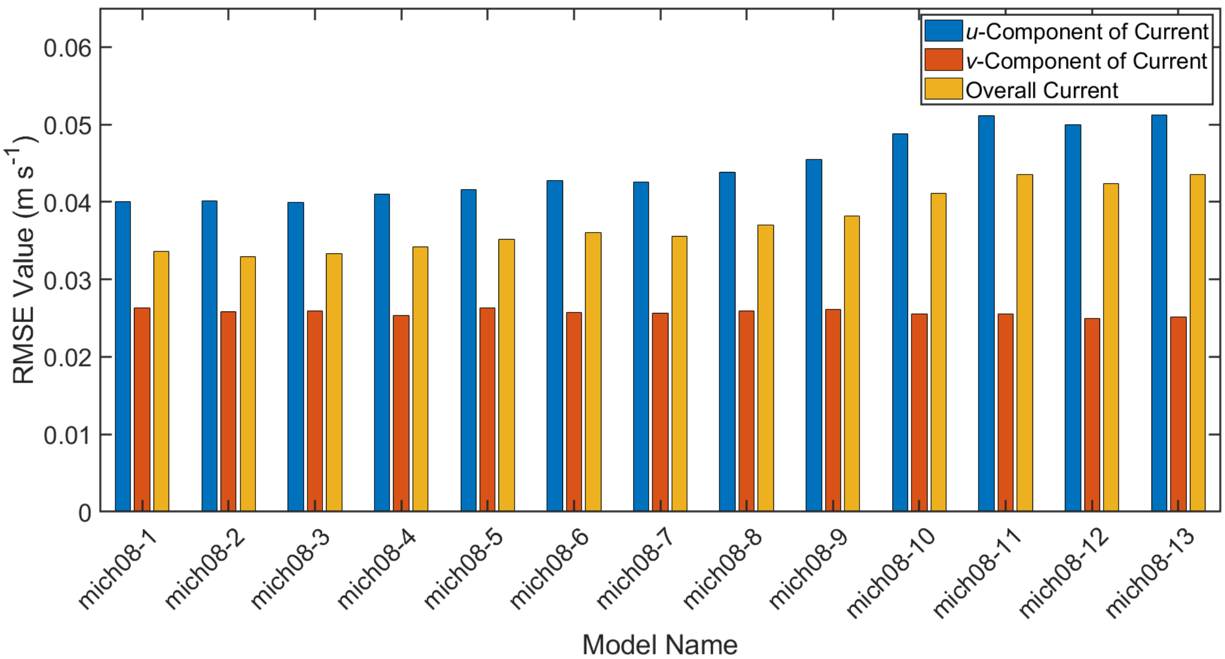

Figure 3-7: Comparison plot of RMSE values for u- and v-components of current (blue and orange bars, respectively) and overall currents (yellow bars) at the MADCP location, between the 13 models

Combining the *u*- and *v*- current components via Eq. 3-26 above, RMSE values for overall currents at MADCP range from 0.026 to 0.044 m s^{-1}. These values are comparable to the ranges of RMSE values for *u*- and *v*- components. RMSE for overall currents was minimized for models mich08-10, mich08-11 and mich08-2 and maximized for models mich08-13, mich08-12 and mich08-9 (Table 3-3, Figure 3-7). These discrepancies between ADCP locations, and current variables highlight the importance of using multiple metrics to evaluate model predictive ability and optimize model approaches.

3.3.3. Model Comparisons with Observed *E. coli* Concentrations at Ogden Dunes Beach

To assess the ability of the 13 models to predict water quality conditions in southwestern Lake Michigan, results of *E. coli* simulation via the WQM were quantitatively compared to observed *E. coli* concentrations at Ogden Dunes beach, Indiana using six validation metrics. While no single evaluation metric can definitively validate a model's full predictive ability, the combination of all six metrics can give researchers a fuller picture of whether models are truly predicting conditions (Legates and McCabe, 1999).

Following the evaluation of model results for temperature and currents, RMSE was calculated for observed and modeled *E. coli* concentrations at Ogden Dunes beach. RMSE for the 13 models varied from 0.39 to 0.42 $\log_{10}$(MPN 100 ml^{-1}) of water (Table 3-4, Figure 3-8). RMSE was minimized for models mich08-3 (RMSE = 0.39 $\log_{10}$(MPN 100 ml^{-1})), mich08-1 (RMSE = 0.39 $\log_{10}$(MPN 100 ml^{-1})) and mich08-2 (RMSE = 0.39 $\log_{10}$(MPN 100 ml^{-1})). The highest RMSE values were calculated for mich08-11 (RMSE = 0.42 $\log_{10}$(MPN 100 ml^{-1})), mich08-13 (RMSE = 0.42 $\log_{10}$(MPN 100 ml^{-1})) and mich08-12 (RMSE = 0.42 $\log_{10}$(MPN 100 ml^{-1})).

Table 3-4: Model evaluation statistics comparing modeled and observed E. coli concentrations at Ogden Dunes beach for 13 models

Model Name	RMSE	R^2	F_n	NSE	PBIAS	RSR
mich08-1	0.39	0.45	0.26	-0.80	16.95	1.43
mich08-2	0.39	0.45	0.26	-0.81	17.10	1.34
mich08-3	0.39	0.45	0.26	-0.77	16.90	1.33
mich08-4	0.40	0.45	0.26	-0.82	16.71	1.35
mich08-5	0.40	0.45	0.26	-0.83	17.46	1.35
mich08-6	0.40	0.46	0.26	-0.82	17.95	1.35
mich08-7	0.40	0.46	0.26	-0.82	18.16	1.35
mich08-8	0.39	0.47	0.26	-0.81	18.19	1.35
mich08-9	0.40	0.47	0.26	-0.86	19.18	1.36
mich08-10	0.41	0.48	0.27	-1.00	20.98	1.41
mich08-11	0.42	0.49	0.28	-1.09	22.04	1.45
mich08-12	0.42	0.49	0.27	-1.02	21.29	1.42
mich08-13	0.42	0.49	0.28	-1.06	21.84	1.44

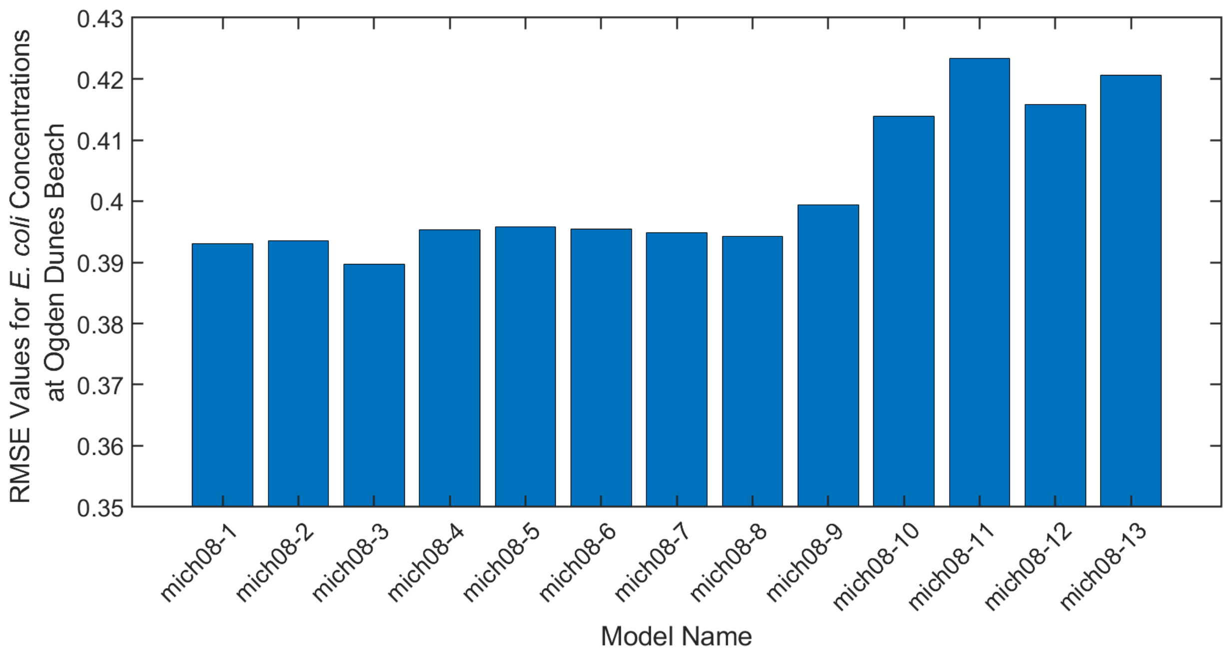

Figure 3-8: Comparison plot of RMSE values for simulated and observed E. coli concentrations at Ogden Dunes Beach, between models mich08-1 to mich08-13

Coefficients of determination for the models indicate that all 13 combinations of Prandtl numbers capture less than 50% of the observed *E. coli* data from the summer of 2008 (Table 3-4, Figure 3-9). However, these R^2 values are comparable to those published for similar models corresponding to the location of interest in southwestern Lake Michigan (Safaie et al., 2016a). The coefficients of determination differ between models by up to 0.04, suggesting that adjustments to Prandtl numbers alone within the FVCOM framework may have a considerable impact on ability to capture observed data. The values of R^2 are maximized for models mich08-13 (R^2 = 0.49), mich08-11 (R^2 = 0.49) and mich08-12 (R^2 = 0.49). Conversely, R^2 values are minimized by models mich08-5 (R^2 = 0.45), mich08-4 (R^2 = 0.45) and mich08-1 (R^2 = 0.49).

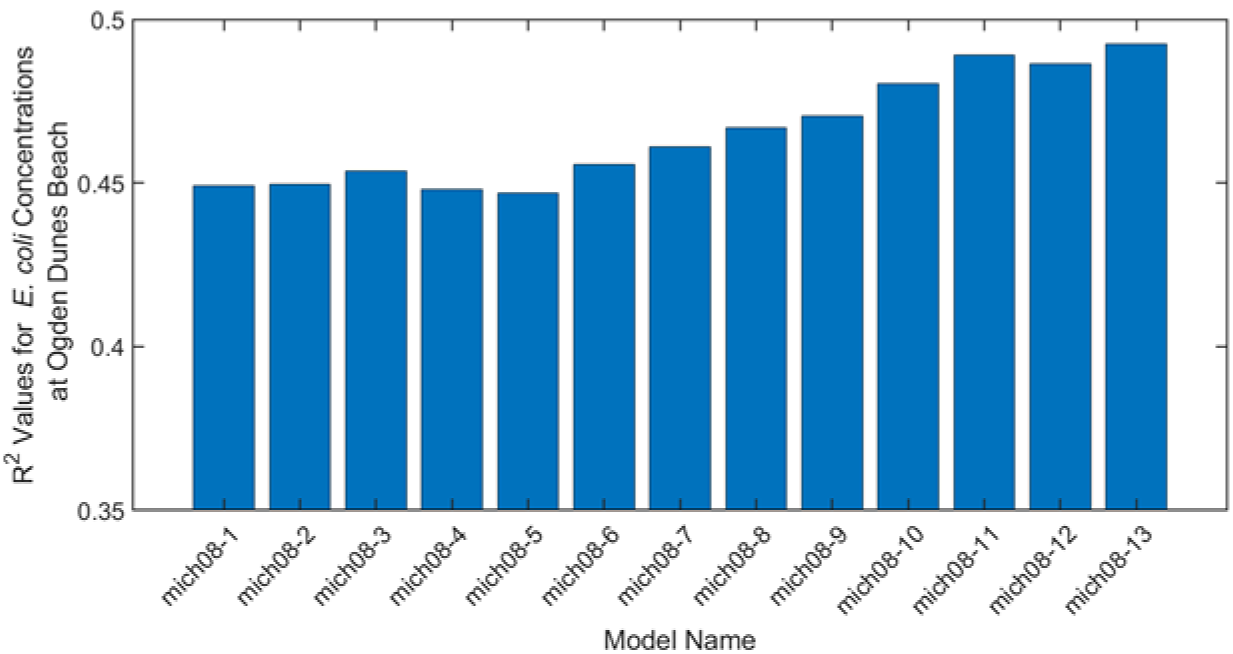

Figure 3-9: Comparison plot of R^2 values for simulated and observed E. coli concentrations at Ogden Dunes beach, between models mich08-1 to mich08-13

Calculated normalized Fourier Norm (F_n) statistics, measuring variance in observed data not captured by the 13 models range from 0.26 to 0.28. Models mich08-3, mich08-1 and mich08-2 minimize F_n, while mich08-11, mich08-13 and mich08-12 yielded the greatest magnitude of F_n. However, the standard deviation of these values is 0.007, indicating that the models are similar in their ability to capture variance in observed data, despite some models showing marginal improvement over others (Table 3-4, Figure 3-10). None of the F_n values are negative, suggesting that the input *E. coli* concentrations and WQM simulations do improve *E. coli* prediction, over a model that would use an input *E. coli* concentration of 0.

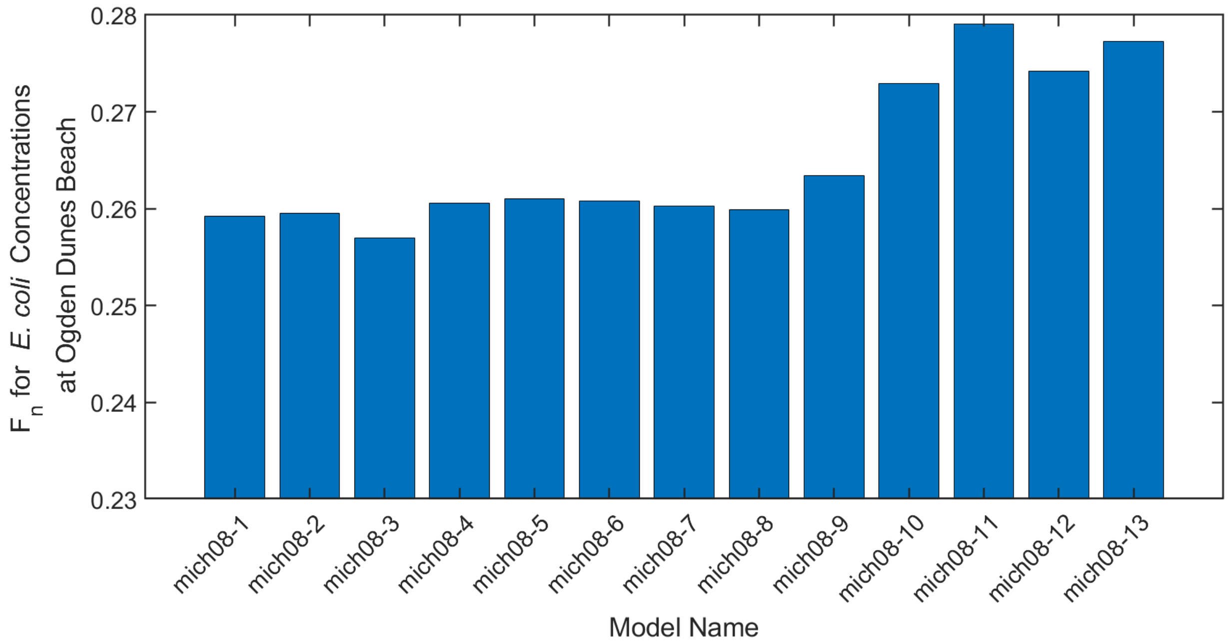

Figure 3-10: Comparison plot of F_n values for simulated and observed E. coli concentrations at Ogden Dunes beach, between models mich08-1 to mich08-13

NSE, or a measure of the ratio of the root mean squared error and the standard deviation of observational data, is useful in hydrological modeling because of its sensitivity to biases in model predictions and its applicability to a wide range of modeling data (Ritter and Munoz-Carpena, 2013). For models mich08-1 through mich08-13, NSE varied from -1.09 to -0.77 (Table 3-4, Figure 3-11). Models mich08-3, mich08-1 and mich08-2 optimized their NSE values (NSE = -0.77, -0.80 and -0.81, respectively), while mich08-11, mich08-13 and mich08-12 yielded NSE values furthest from the optimal value of +1.0 (NSE = -1.09, -1.06 and -1.02, respectively). In spite of these differences in NSE values that suggest that models mich08-1, mich08-2 and mich08-3 have higher predictive ability than models mich08-4 through mich08-13, all NSE values are negative. This may indicate that none of the models are adequately simulating *E. coli* at Ogden Dunes beach, because negative NSE values suggest that the average of observations may be a better predictor than the model results (Ritter and Munoz-Carpena, 2013). However, the NSE values for this location are somewhat comparable to those from previously published models (Safaie et al., 2016).

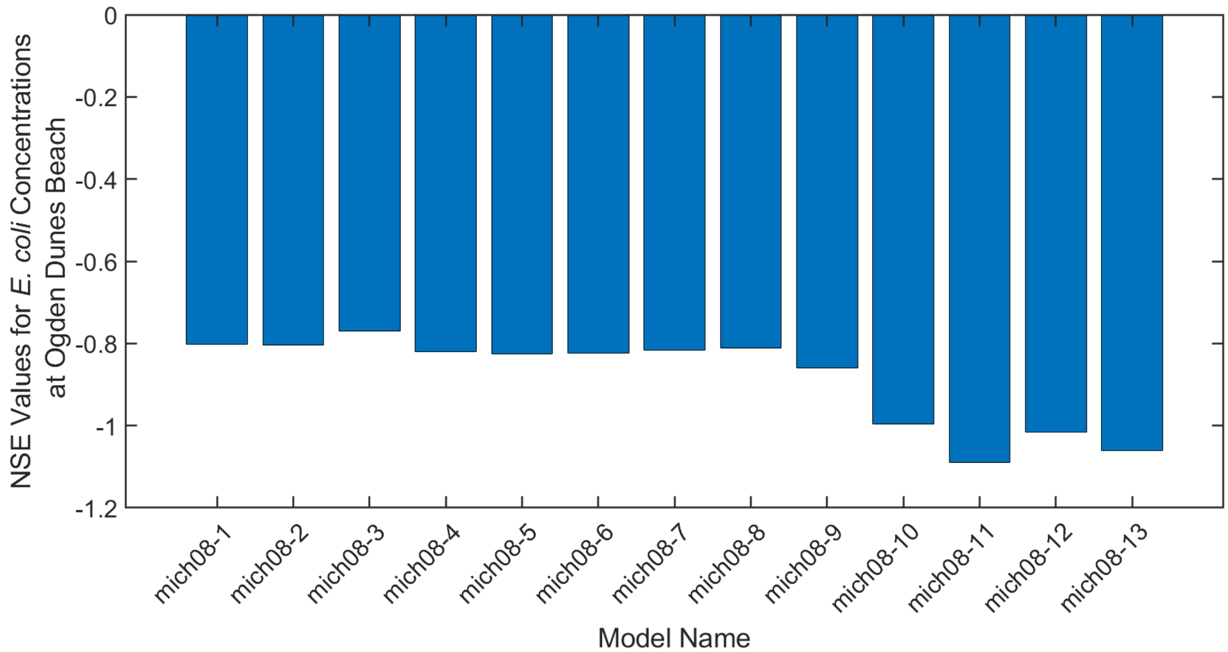

Figure 3-11: Comparison plot of NSE values for simulated and observed E. coli concentrations at Ogden Dunes beach, between models mich08-1 to mich08-13

Percent bias (PBIAS), or the tendency for simulated *E. coli* values to be above or below observed values, varies between 16.71 and 22.04 for the 13 models (Table 3-4, Figure 3-12). Models mich08-4, mich08-3 and mich08-1 minimized the PBIAS of their results (PBIAS = 16.71, 16.90, 16.95, respectively), showing improved predictive ability relative to other models. Conversely, PBIAS was maximized for models mich08-11, mich08-13 and mich08-12 (PBIAS = 22.04, 21.84 and 21.29, respectively), indicating relatively poor predictive capacity of these models. All models yielded positive PBIAS statistics, indicating that all of the models underpredicted observed *E. coli* concentrations at Ogden Dunes beach.

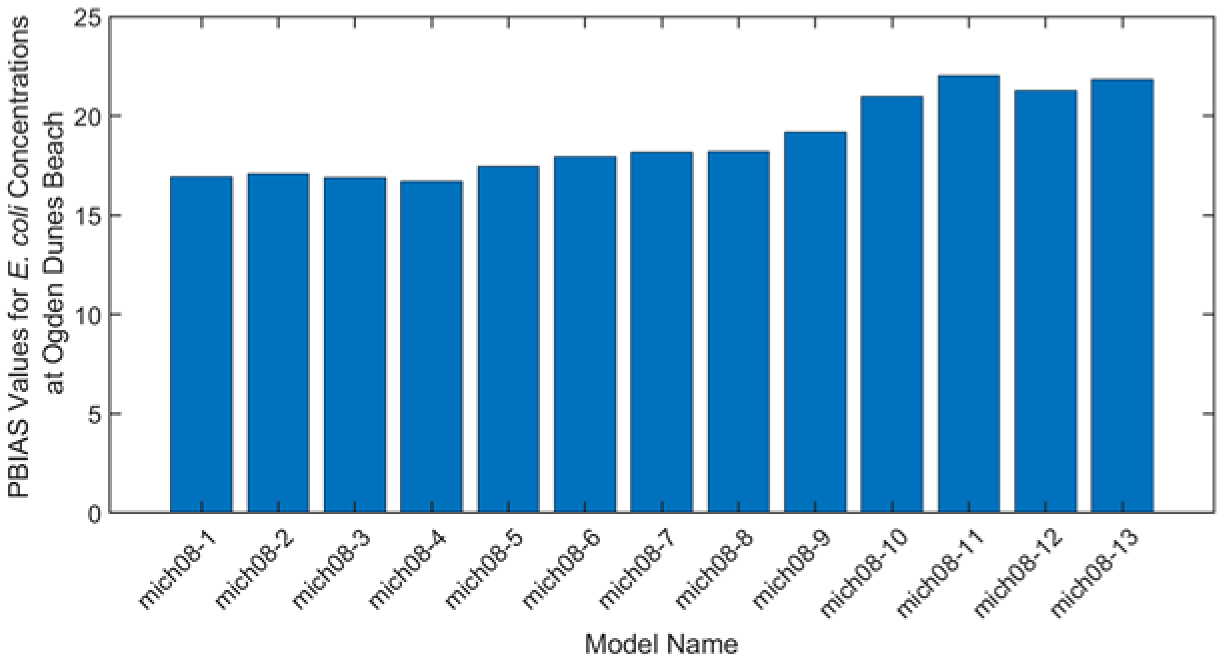

Figure 3-12: Comparison plot of PBIAS values for simulated and observed E. coli oncentrations at Ogden Dunes beach, between models mich08-1 to mich08-13

The final model validation statistic used, RSR, showed a similar pattern amongst the 13 models (Table 3-4, Figure 3-13). Following PBIAS, NSE, F_n and RMSE, RSR was minimized for models mich08-3, mich08-1 and mich08-2 (RSR = 1.33, 1.34 and 1.34 $\log_{10}$(MPN 100 ml^{-1}), respectively). Likewise, RSR was maximized in models mich08-11, mich08-13 and mich08-12 (RSR = 1.45, 1.44 and 1.42 $\log_{10}$(MPN 100 ml^{-1}), respectively). Because RSR is a normalized form of RMSE, the hierarchy of models optimized for RSR reflects the hierarchy of models optimized for RMSE. Similarly, the calculation of RSR and NSE is very similar, as both are a ratio of RMSE to standard deviation of observations (Moriasi et al., 2007; Ritter and Munoz-Carpena, 2013). It would thus be expected that, as seen here, the hierarchies of models in the context of RSR and NSE predictability would match.

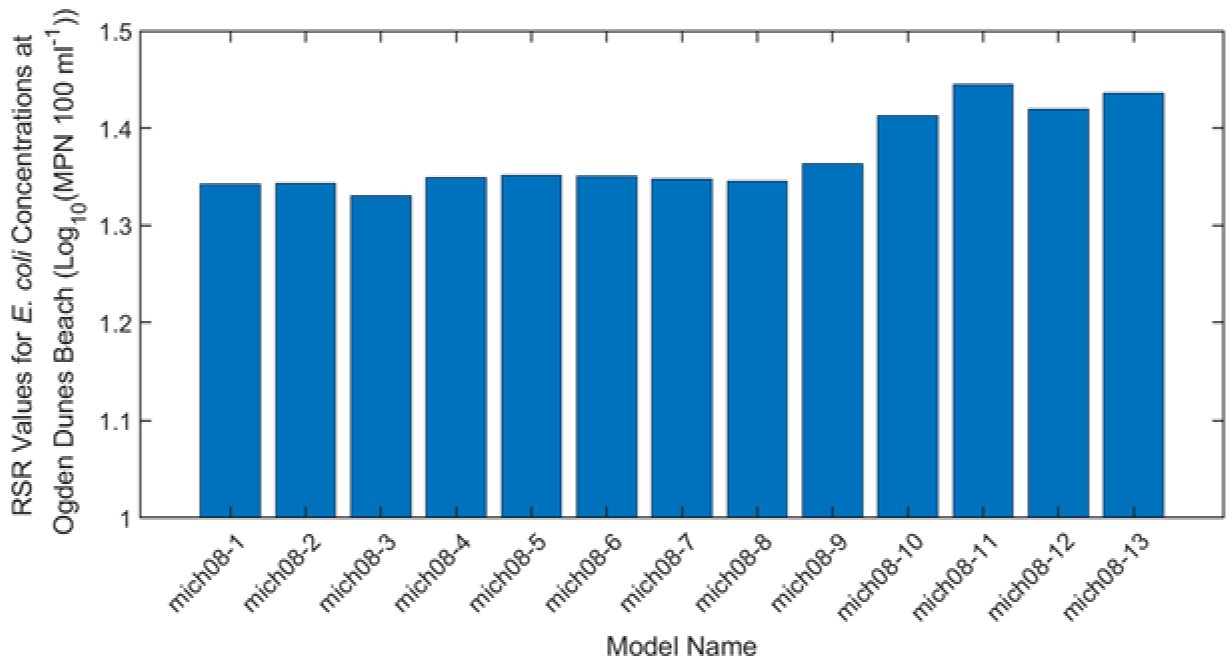

Figure 3-13: Comparison plot of RSR values for simulated and observed E. coli concentrations at Ogden Dunes beach, between models mich08-1 to mich08-13

3.3.4. Model Selection Based on the Combination of Evaluation Statistics

Because no single metric can fully characterize a model's predictive ability, especially for microbial water quality variables such as *E. coli* concentration, evaluation of all presented statistics must be undertaken when selecting an optimal model for simulation of *E. coli* spatiotemporally.

Seven of the models were calculated to be optimized model for at least one of the evaluation statistics (mich08-1, mich08-2, mich08-3, mich08-4, mich08-6, mich08-12 and mich08-13). Due to their lack of optimization for any metric, it can be concluded that models mich08-7 through mich08-11 are not desirable for the simulation of hydrodynamics or *E. coli* concentrations in southwestern Lake Michigan. Since these suboptimal models reflect the usage of horizontal turbulent Prandtl numbers greater than one, it may also be reasonably established that horizontal turbulent Prandtl number inputs to FVCOM that are less than one lead to more reliable simulations of water quality than those greater than one. At the same time, model mich08-7 reflects $Pr_{t,H}$ and $Pr_{t,V}$ values of one and seems to simulate temperature, currents and *E. coli* concentrations at Ogden Dunes beach with reasonable reliability as well. This may suggest that the Reynolds analogy approximation for Pr_t values (Pr_t values = 1) can be appropriate for simulating hydrodynamics and water quality in large lake systems such as southwestern Lake Michigan.

Of the models that optimized at least one evaluation metric, model mich08-3 minimized RMSE values for *u*-component of current at MADCP RMSE (RMSE = 0.04 m s^{-1}), and *E. coli* concentration RMSE (RMSE = 0.39 $\log_{10}$(MPN 100 ml^{-1})). Mich08-3 also minimized F_n and RSR (F_n = 0.26, RSR = 1.33) and maximized NSE (NSE = -0.77) for *E. coli* concentration simulation, among the 13 models tested. Though not the most optimized model, mich08-3 showed the second lowest PBIAS value and fifth-highest *E. coli* R^2 value (PBIAS = 16.90, R^2 = 0.45). These statistics indicate that mich08-3 is the optimal model for simulation of hydrodynamics and *E. coli* concentrations in southwestern Lake Michigan, of those tested herein. This model corresponds to horizontal and vertical turbulent Prandtl numbers equal to 0.14 and 0.1, respectively.

It is important to note that this model, while capturing variability in *u*-components of current and overall currents, is relatively poor at capturing the smaller and more difficult to simulate *v*-components of current, compared to other models in the analysis. Because of the smaller scale and higher difficulty in simulating *v*-components of current, it is possible that results indicating applicability of this model are misleading. For modeling contexts that rely on high degrees of predictive ability in the *v*-component of currents, use of Pr_t values corresponding to those from models mich08-4, mich08-12 or mich08-13, though selection of these models may come with a tradeoff in predictive ability in other contexts.

The optimal model for reliably simulating *E. coli* at Ogden Dunes beach was not necessarily the same as the optimal model for reproducing hydrodynamic conditions like surface water temperature and currents. Model mich08-3 was able to minimize RMSE values for *u*-components of current at the BBADCP and MADCP but did not minimize RMSE values for LST, *v*-components of currents at the ADCP locations or overall currents at the ADCP locations. Instead, RMSE in *v*-components of current at the MADCP were minimized for model mich08-12, with $Pr_{t,H}$ = 10 and $Pr_{t,V}$ = 7. These values are, in fact, the inverse of the values in model mich08-3. RMSE values for overall currents at the ADCP locations were minimized for model mich08-2, with $Pr_{t,H}$ = 0.1 and $Pr_{t,V}$ = 0.14.

The differences in optimal models for simulation of hydrodynamics and *E. coli* concentrations in southwestern Lake Michigan may lend credence to the idea that an additional model parameter signifying the turbulent Schmidt number (Sc_t) would improve water quality models. As previously discussed, Sc_t is a common model parameter in direct numerical simulations (DNS) of any scalar in a computational fluid dynamics context, but it is assumed to be similar to the $Pr_{t,H}$ value within the FVCOM modeling framework. In many cases, this number is used to estimate the relative impacts of momentum diffusivity and mass diffusivity on contaminant concentrations in aquatic or atmospheric settings within the Advection-Diffusion-Reaction equation (ADR, Eq. 3-13) (Donzis et al., 2014; Graf and Cellino, 2002; Gualtieri et al., 2017; Rauen et al., 2012). Research to date has largely determined that models of contaminant fate and transport are optimized for Sc_t values between 0.1 and 2.0, but that optimal Sc_t values can be highly context-dependent (Gualtieri et al., 2017). This context-dependence is similar to that seen with turbulent Prandtl numbers, where the optimal values of Pr_t in models can vary by location, hydrometeorological factors and mixing regime (Ye et al., 2019).

Results presented herein indicate that Sc_t and Pr_t may not be similarly sensitive to location, hydrometeorology and mixing factors. Therefore, it is possible that the incorporation of an additional model parameter denoting Sc_t in FVCOM would further improve water quality and *E. coli* fate and transport simulation. To assess this possibility, an additional sensitivity analysis may be conducted, whereby $Pr_{t,H}$ and $Pr_{t,V}$ values are held constant at optimal values of 0.14 and 10, respectively, and various Sc_t values are introduced to the modeling environment. Developing a hierarchy of optimal Sc_t values for Lake Michigan would not only lend insight into how Sc_t may impact simulation of nearshore water quality but would also show potential differences in the optimization of Pr_t and Sc_t values. This could lead to further support for the addition of an Sc_t model parameter in FVCOM that is separate from the Pr_t parameter.

3.4. Conclusions

Models of hydrodynamics and water quality rely upon effective combinations of input parameters to simulate conditions in natural water bodies. However, it can be difficult to find parameter combinations that lead to optimal predictions. Often-overlooked input parameters to models like FVCOM are horizontal and vertical turbulent Prandtl numbers, which weight the relative contributions of eddy viscosity and thermal diffusivity to hydrodynamics. A sensitivity analysis was conducted to determine an optimal combination of horizontal and vertical turbulent Prandtl number inputs to FVCOM, to maximize predictive ability for water temperature, currents and *E. coli* concentrations at a beach in southwestern Lake Michigan.

While several of the 13 evaluated models optimized various validation metrics such as R^2, RMSE, NSE, F_n, PBIAS and RSR, one model stood out as employing an optimal turbulent Prandtl number combination for the majority of metrics. Model mich08-3 yielded the lowest RMSE, RSR, and F_n values for *E. coli* concentrations of all models, while maximizing NSE for *E. coli* concentrations. This model also minimized RMSE values for some currents in the model, compared to the other 12 models. Given these evaluation metric results, it is recommended that hydrodynamic and water quality modeling for southwestern Lake Michigan include a $Pr_{t,H}$ value of 0.14 and a $Pr_{t,V}$ value of 10 within FVCOM. This is especially true in the context of water quality modeling, as the model with $Pr_{t,H}$ = 0.14 and $Pr_{t,V}$ = 0.1 was the optimal model for 67% of the water quality-associated evaluation metrics and was a top-5 optimal model for all six water quality model validation metrics.

The differences between optimal models for hydrodynamic and water quality evaluation metrics underscore the importance of using multiple metrics for model evaluation. They also highlight the distinction between vertical and horizontal turbulent Prandtl number combinations for effective modeling of hydrodynamics and those for modeling water quality variables like *E. coli* concentration. While the optimal model for simulating surface water temperature uses Prandtl numbers near 1 ($Pr_{t,H}$ = 0.85 and $Pr_{t,V}$ = 0.85), the model that best captured nearshore *E. coli* used a much lower horizontal turbulent Prandtl number ($Pr_{t,H}$ = 0.14) and a much higher vertical turbulent Prandtl number ($Pr_{t,V}$ = 0.1). Because of these differences, it is important to consider the geographic and hydrodynamic context and goals of FVCOM modeling when determining effective combinations of turbulent Prandtl numbers to input to the modeling framework.

Differences between optimal Pr_t values for hydrodynamics and water quality models herein also highlight a potentially important omission within the FVCOM modeling framework. The turbulent Schmidt number (Sc_t) is often used in direct numerical simulations to characterize relative impacts of diffusivity of momentum and diffusivity of mass for contaminants in aquatic systems, in similar fashion to how Pr_t is utilized for hydrodynamics (Gualtieri et al., 2017, Rauen et al., 2012). However, Sc_t is not explicitly defined or used in current FVCOM frameworks, with these models instead relying solely on Pr_t to characterize diffusivity and viscosity impacts (Chen et al., 2006). The difference in optimal $Pr_{t,H}$ and $Pr_{t,V}$ value combinations for simulation of hydrodynamics and water quality in southwestern Lake Michigan may highlight the shortcoming associated with omitting the Sc_t parameter from simulations. The incorporation of an additional, calibrated Sc_t parameter within FVCOM may lead to improvements in water quality modeling for environmental flows and natural waters.

4. Simulating Storm-Associated River Plumes in Southern Lake Michigan: Model Selection Process

4.1. Introduction

Water is an essential part of life; from drinking water to wastewater and recreational water, humans rely on safe and adequate water for survival and comfort. As a result, lakes, oceans and shoreline environments are integral parts of people's lives, especially in the summer and during swimming seasons. This is particularly true in the Laurentian Great Lakes of the United States of America, a basin that houses hundreds of beaches and over 15,000 km of shoreline (Canada, 2011; EGLE, 2016; IDEM, 2016; IDPH, 2018; NOAA, 2020a; ODH, 2020; WDNR, 2000). The beaches and shoreline communities draw millions of visitors annually (Nevers and Whitman, 2011) and contribute substantial tourism revenue to local municipalities (Kinzelman, 2009; Shaikh, 2012). This tourism and revenue is dependent upon the safety and quality of water in the nearshore region of the lakes. Recreational activities at beaches are advised against when public health is threatened by recreational activities in the nearshore region (Canada, 2011; EGLE, 2016; IDEM, 2016; IDPH, 2018; ODH, 2020; WDNR, 2000).

At beaches, public health hazards can come from multiple sources, including rip currents and rip tides, strong waves, debris on the beach, sunburn and other solar impacts, storm effects and degraded water quality, as well as combinations of such sources (NOAA, 2020c). Many of these impacts affecting public health are expected to change in response to climate change. For instance, changes in wind patterns associated with climate change can also influence waves and nearshore water quality (Smith et al., 1999). Similarly, the predicted increase in frequency and intensity of storms in the Great Lakes region (IPCC, 2014) are likely to lead to more frequent and intense water quality degradation and high wave energy conditions at local beaches.

The degradation of water quality associated with runoff from more frequent and intense storm events is a specific public health threat to beaches in the Chicago area of southwestern Lake Michigan due to the local management of stormwater in Chicago (MWRD, 2019). The three main river channels in the Chicago area, the North Shore Channel, the Chicago River and the Calumet River, have all been engineered to flow westward and away from Lake Michigan unless there is substantial threat of flooding within the city (ASCE, 2020; Hansen, 2009). When heavy storms produce enough rain to flood Chicago or areas west of the city, infrastructure at Wilmette Pumping Station, Chicago River Controlling Works (CRCW) and O'Brien Lock and Dam engage and reverse river flows to send water eastward to Lake Michigan (MWRD, 2019; USACE, 2014). These storms can lead to the release of stormwater plumes in the nearshore of Lake Michigan via "backflow" events, and there may be significant urban and agricultural water quality contamination in the resulting stormwater plumes (Masoner et al., 2019; MWRD, 2019; Paule-Mercado et al., 2016; USACE, 2014).

Beach and stormwater managers in Chicago recognize the risk that storm-associated river plumes present to nearshore environments and recreational water. However, there is a noticeable lack of observational data characterizing water quality in response to storm events, largely due to the inherent dangers in sampling for water quality during and immediately after storms. The Chicago Park District (CPD) and Metropolitan Water Reclamation District (MWRD) take a conservative approach to managing recreational water in the face of heavy storms and backflow events. During backflow events at the Wilmette outlet, CPD and MWRD close all beaches between Wilmette, IL to Ohio St. beach in Chicago. Similarly, if either CRCW or O'Brien outlets backflow stormwater into Lake Michigan, all beaches between Ohio St. and Calumet beach are closed to preserve public health and safety (USACE, 1996). During such backflows, these beaches remain closed until after water quality samples at representative beaches (Table 4-1) yield Fecal Indicator Organism (FIO) concentrations below Beach Action Value (BAV) thresholds (MWRD, 2019; USACE, 2014). These BAV thresholds are 2.37 $\log_{10}$(MPN 100 ml^{-1}) for culturable *E. coli* or 1000 CCE 100 ml^{-1} for enterococci via quantitative Polymerase Chain Reaction (qPCR) (USEPA, 2014b).

Table 4-1: Representative beaches sampled for water quality, post-backflow event in Chicago

Representative Beach Name	Nearest River Outlet
Kenilworth	Wilmette
Wilmette	Wilmette
Gillson	Wilmette
Lighthouse	Wilmette
Northwestern (Lincoln St.)	Wilmette
Dempster St.	Wilmette
North Ave.	CRCW
Oak St.	CRCW
12^{th} St.	CRCW
Margaret T. Burroughs	CRCW
Rainbow	O'Brien
Calumet	O'Brien

This conservative approach to beach management during and after backflow events is borne in part from necessity. It can be dangerous to collect water quality monitoring samples during storms, and backflow events are frequently triggered by extreme storms (USACE, 1996), so closing all beaches in response to such events can ensure public health to the extent possible while keeping beach managers and water quality researchers safe. While this approach is beneficial for safety of researchers, beach managers and the public during storms, it also means that some beaches may be closed when they are not experiencing degraded water quality, potentially leading to economic losses. At the same time, automatically closing beaches during backflow events can lead to a paucity of *in situ* water quality data available for storm events. Similarly, satellite imagery collected from sources like Moderate Resolution Imaging Spectroradiometer (MODIS) Terra and

Sentinel satellites can be valuable in assessing conditions during storms (Vermote, 2015), but the imagery is often obstructed by clouds associated with the storms (Figure 4-1). As a result, there are few observational data from which insight can be drawn regarding exactly how these storm-associated river plumes impact the nearshore during and after extreme storm events that lead to backflows.

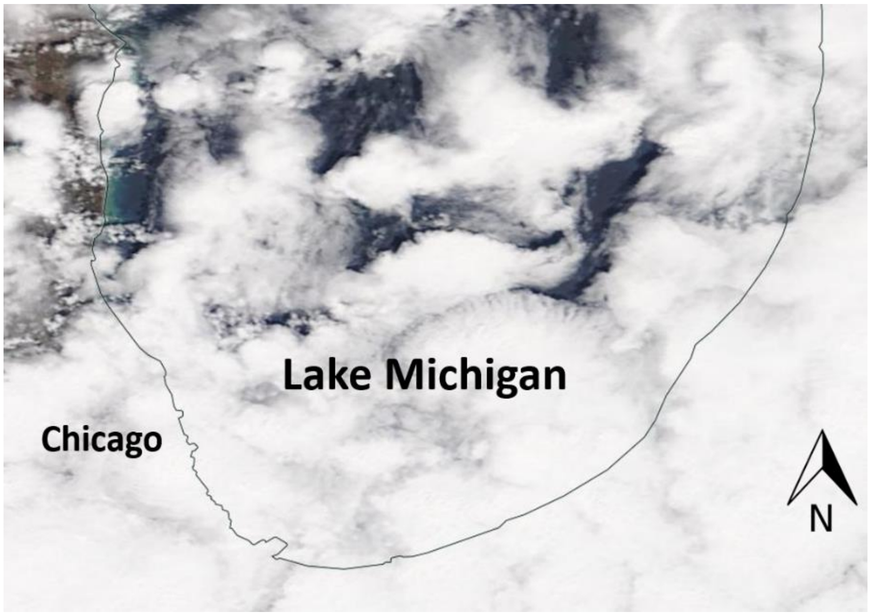

Figure 4-1: MODIS-Terra true color image from September 2013 highlighting obstruction of Lake Michigan and the Chicago shoreline due to storm-associated cloud cover

Despite the lack of observational data associated with conditions during and after storms, understanding how storms and backflow events can affect the nearshore is important for effective beach management, public health, and research (MWRD, 2019; USACE, 2014). Therefore, alternative approaches to collecting *in situ* data must be employed to supplement and increase our understanding of storms and their impacts on nearshore environments.

Statistical and numerical models can be useful in supplementing the scarce observational data for the water quality and plume dynamics resulting from storms. Data-driven statistical and mechanistic models have been used in nowcasting and hindcasting contexts, to predict water quality at Great Lakes beaches (Francy and Darner, 2007; Nevers and Whitman, 2005; Safaie et al., 2016; Thupaki et al., 2010; Zhang et al., 2018). Though still being actively refined (Weiskerger and Phanikumar, 2020), these types of model frameworks can be valuable in characterizing hydrodynamic and water quality conditions in situations with little observational data, such as backflow events. While models can be useful in the absence of observational data, multiple modeling approaches can be applied to answer environmental questions and selecting the most appropriate model for specific hydrodynamic and water quality questions remains a challenge. To determine the modeling approach that is optimized in its applicability for assessment of nearshore conditions during backflow events, we tested two potential transport modeling approaches for the simulation of storm-induced river plumes in southwestern Lake Michigan. These approaches, including one Eulerian method and one Lagrangian method (Chen et al., 2006), were coupled with a mechanistic model of hydrodynamics, applied for backflow events in September 2008 and October 2017. Results of the modeling approaches were visually and quantitatively compared to the spatial extents of the plumes, as captured by MODIS-Terra satellite imagery after the storm (Vermote, 2015). Comparisons were used to determine which approach best approximated the plumes from the satellite imagery. While model testing was limited to comparisons with data obtained after the storm event, these comparisons can lend some confidence to the modeling approaches, in terms of their ability to simulate the storm-associated river plume dynamics. Model results for after the storm depend on those calculated during the storm. Therefore, it may be possible to infer that if the modeled plumes reasonably compare to the MODIS data after the storms, they would also reasonably predict the plume dynamics during the storm and at times for which MODIS data are not available.

It was expected that differences in the way that the two approaches calculate dispersion would lead to an overestimation of plume areas in the Eulerian approach, compared to the Lagrangian framework (Zhang and Chen, 2007). Therefore, it was hypothesized that the Lagrangian approach would simulate the storm-induced plumes with higher confidence than the Eulerian method. Results from this model selection exercise can be used to inform future plume modeling work, which in turn can lead to inferences about the spatiotemporal scales of backflow-induced plumes, dynamics of the tracers in the plumes, and risks to public health as a result of the backflow events. Beach management recommendations regarding when and where to limit recreation in the nearshore in response to backflow events can be made based on simulations, and results can also be used to help prioritize management efforts for areas at highest risk of water quality degradation due to plumes.

4.2. Methods

4.2.1. Study Area and Temporal Context

The city of Chicago sits on the southwestern shore of Lake Michigan (Figure 4-2). Chicago's metropolitan area includes three major rivers: the North Shore Channel, the Chicago River and the Calumet River. While these rivers have been engineered to commonly flow westward, *away* from Lake Michigan, extreme storms can trigger backflow events. During these backflow events, water in the rivers is diverted to flow east into the lake to prevent overland flooding (MWRD, 2019), via infrastructure at Wilmette Pumping Station (referred to hereafter as Wilmette), Chicago River Controlling Works (CRCW) and O'Brien Lock and Dam (referred to hereafter as O'Brien) (Figure 4-2, inset). Models were developed to simulate flows from these three outlets into Lake Michigan during backflow events in 2008 and 2017, and to track the plumes, as they were transported throughout the nearshore environment during and after the backflow events. While the model domain was the whole of Lake Michigan, the focus of the simulations was on the Chicago nearshore area, extending from Wilmette, IL to in the Illinois-Indiana border.

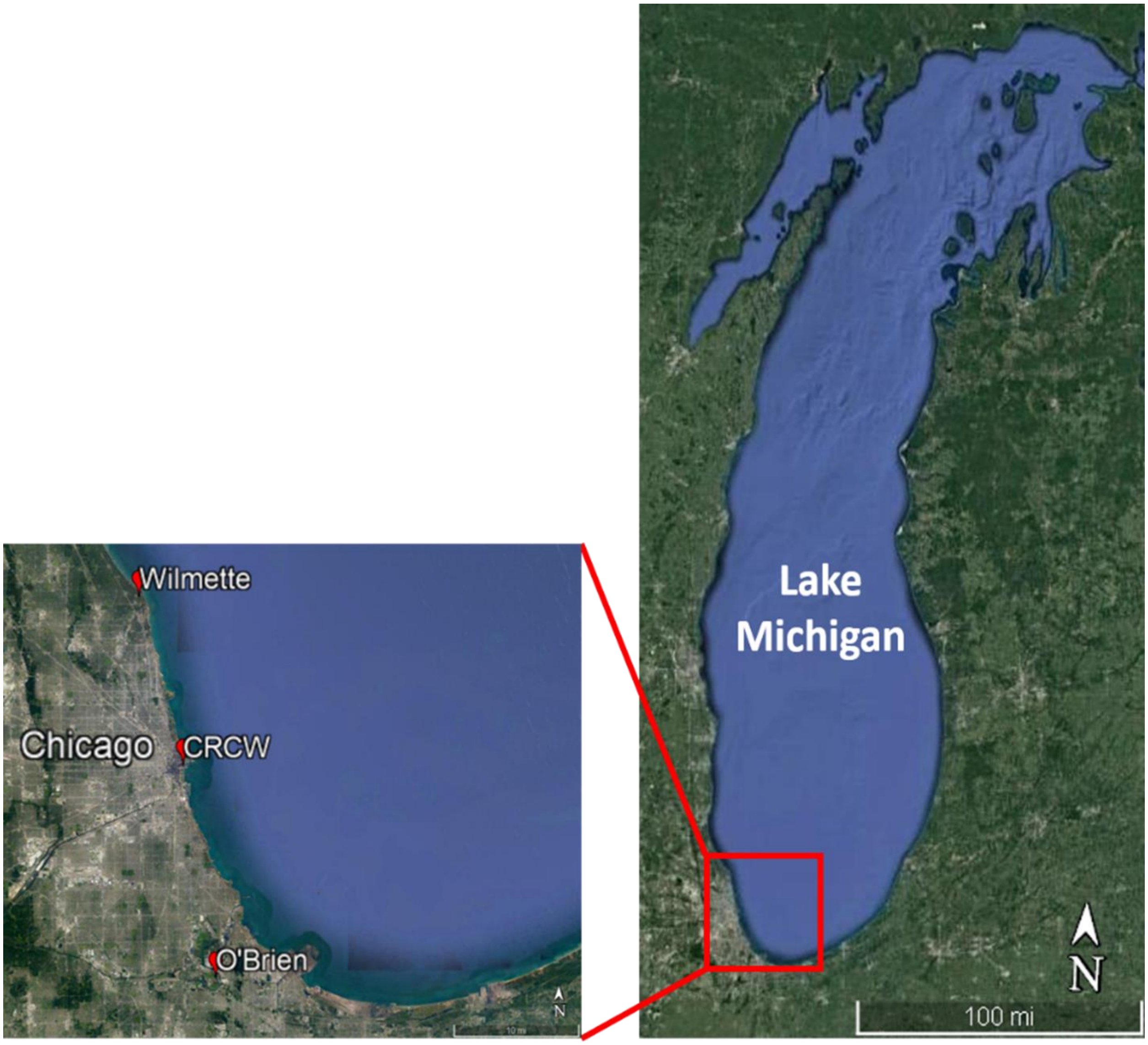

Figure 4-2: Google Earth imagery showing Lake Michigan and the Chicago area (inset), including the three flow control infrastructure locations (Wilmette, CRCW and O'Brien)

Numerical simulations were performed for the backflow events that occurred on September 13th – 16th, 2008 and October 14th – 15th, 2017. These events were chosen due to the availability of satellite imagery against which model results could be evaluated. The 2008 storm event led to the release of 41,825,393.34 m^3 of water into Lake Michigan, via releases from all three outlets, while the 2017 event released 10,395,497.84 m^3 of stormwater to the lake via the Wilmette and CRCW outlets (USACE, 2014). To ensure that all of the dynamics of the 2008 storm plumes were captured in the simulations, models began at 12:00 AM on September 12th, 2008, and continued simulation through 11:00 PM on September 30th, 2008. Likewise, the models for 2017 simulated plumes from October 13th – 31st, 2017. Plume release timing was controlled in the models via input of river flux observations (see Appendices B-1 and B-5 for river flux data input into the model); all three river outlets began and ended the model with flux values of zero, and their flows to the lake were dynamic depending on the timing and volume of the backflows at each outlet. This reflected the true conditions at the outlets; the outlets have infrastructure that prevents flow to Lake Michigan except during backflow events and the infrastructure can control the discharge rates during backflow events. Thus, discharge in each location was zero before and after the backflow event, and that flow was temporally dynamic at the outlets during the backflow in response to MWRD control of the backflow infrastructure.

4.2.2. Overview of FVCOM Hydrodynamics Modeling and Model Setup

Models were developed and run using the Finite Volume Community Ocean Model (FVCOM), an unstructured-grid, finite volume, fully three-dimensional model framework for simulating conditions in coastal communities (Chen et al., 2006, 2003). This framework utilizes the primitive Navier-Stokes equations for momentum, continuity, temperature and salinity, together with the equation of state for density, to characterize hydrodynamics spatiotemporally over a model domain, given hydrometeorological and geophysical inputs. Further details on FVCOM hydrodynamics equations can be found in Chapter 2: Numerical Modeling of Microbial Fate and Transport in Natural Waters: Review and Implications for Normal and Extreme Storm Events

(Eq. 2-1 – 2-4). These equations are solved for nodes and cells within the model domain, to characterize hydrodynamics over time within the focal area of the model.

Inputs to FVCOM include boundary and initial conditions, in terms of hydrometeorological and geophysical data. A model mesh was created to discretize the model domain into a series of non-overlapping unstructured grid cells containing nodes and cell faces. Scalar variables such as water surface elevations, total water depth, salinity, temperature, horizontal and vertical eddy diffusivity and eddy viscosity values are defined at the nodes while currents (e.g., u and v) are placed at the centroids of the grid cells. For the backflow simulations, this mesh encompassed all of Lake Michigan but incorporated a variable mesh resolution. This variable mesh resolution allowed for a balance between focusing detailed modeling computational efforts on the Chicago area and capturing the localized impacts from hydrodynamics throughout the lake. As a result, the mesh resolution varied between ~50 m in the nearshore areas extending from Wilmette, IL to Gary, IN and ~2 km in offshore zones and areas north and east of Chicago (see Figure 1-6).

Lake bathymetry was interpolated to the grid nodes using a natural neighbor interpolation method. The bathymetry data came from the National Oceanic and Atmospheric Administration's (NOAA) National Centers for Environmental Information (NCEI), in the form of 5 m contour data compiled at a spatial resolution of 1/3 to 1 arc-second (10 – 30 m) (National Geophysical Data Center, 1996).

Meteorological inputs to the model framework came from NOAA National Data Buoy Center (NDBC) and NCEI (NOAA, 2018a, 2018b). Temperature, wind and pressure data from a total of 118 NDBC and NCEI stations surrounding Lake Michigan were used as weather forcing data for the 2008 model simulations, frequently at a temporal resolution of 1 hour.

To track the plumes associated with river discharges to Lake Michigan, river flow data were also input to the models. Hourly hydrograph data were obtained from MWRD at Wilmette, CRCW and O'Brien (Appendices B-1 and B-5). Time series data for the flowrates (Figures 4-3 and 4-4) were directly input to the models at the river outlet locations via a river input forcing file for the model.

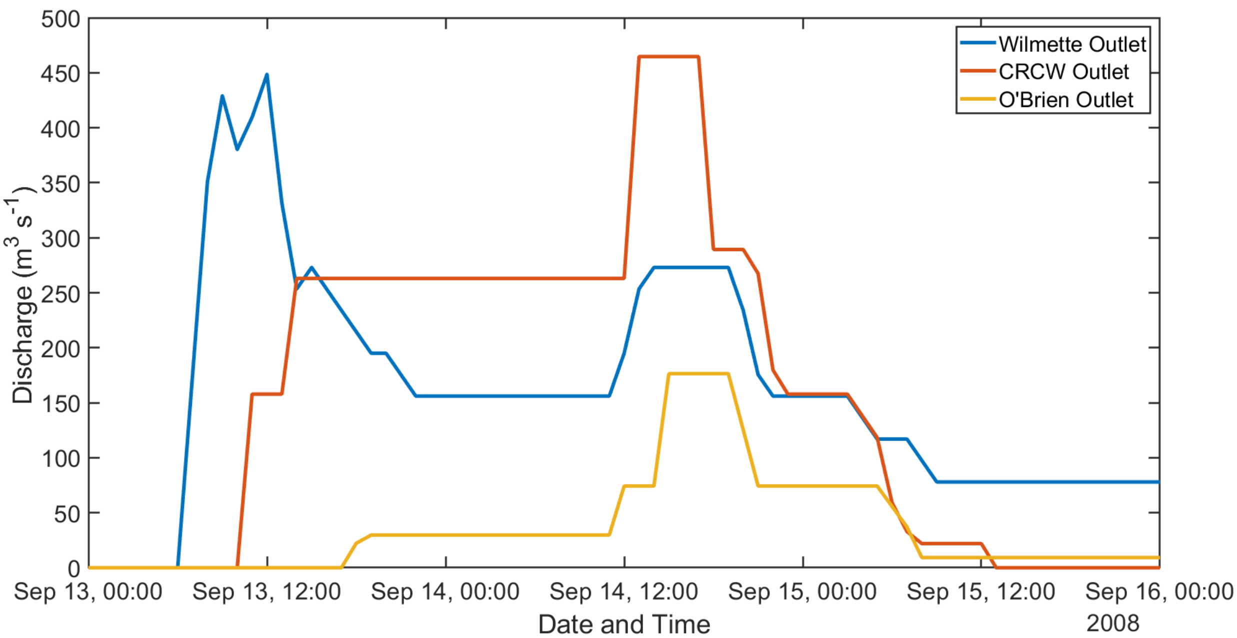

Figure 4-3: Flow hydrograph for Wilmette (blue line), CRCW (orange line) and O'Brien (yellow line) discharges during the September 13-16, 2008 backflow event

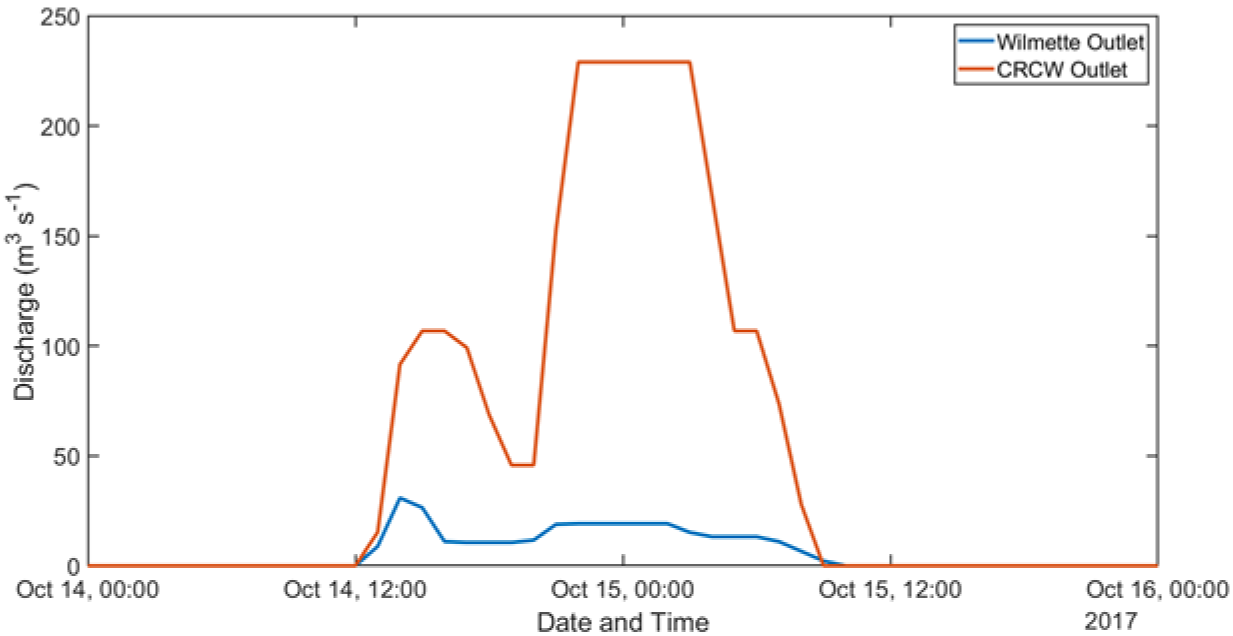

Figure 4-4: Flow hydrograph for Wilmette (blue line) and CRCW (orange line) discharges during the October 14-15, 2017 backflow event

4.2.3. Plume Numerical Simulation Approaches

There are multiple options for modeling river plumes in the lake. Two approaches were tested to determine the option that best simulated observed plumes during and after the backflow events. Both approaches involved tracking plumes via tracer concentrations, but they differ in the way that they calculate tracer concentrations. As a result of the differences between the plume simulation approaches, it can be expected that one would model plumes better than the other.

4.2.3.1. Eulerian Model

One approach to simulating river plumes within FVCOM involves coupling the physical hydrodynamics model with the river inputs using the Eulerian formulation to calculate dispersion. The model takes tracer concentrations across the spatial model domain as initial conditions and incorporates hydrodynamics to track the movement of the tracer over time. Tracer concentrations at the river outlets are specified as elevated above bulk tracer concentrations to simulate plumes.

As a result, the model yields tracer concentrations across time and space. The transport and dispersion of tracers within the model are calculated using the Eulerian formulation and the advection-dispersion equation (Eq. 4-1).

$$\frac{\partial C}{\partial t} + u\frac{\partial C}{\partial x} + v\frac{\partial C}{\partial y} + w\frac{\partial C}{\partial z} = \frac{\partial}{\partial x}\left(K_H\frac{\partial C}{\partial x}\right) + \frac{\partial}{\partial y}\left(K_H\frac{\partial C}{\partial y}\right) + \frac{\partial}{\partial z}\left(K_V\frac{\partial C}{\partial z}\right) \tag{4-1}$$

In these equations, t is time, C is tracer concentration, x, y, and z are the three coordinate directions and u, v and w are velocity components in the x, y, and z directions, respectively (m s^{-1}). K_H and K_V represent the horizontal and vertical mixing coefficients, respectively (m^2 s^{-1}).

To simulate the backflow-associated plumes in September 2008 and October 2017 using the Eulerian method, a tracer with initial concentration of 10000 mg L^{-1} was specified for each of the three river outlets during the backflow event. This high initial tracer concentration ensured that the tracer could be tracked over a longer period of time before dissipating into the lake, while also allowing for straightforward calculation of normalized concentrations from modeled results.

Tracer concentrations were linked to the time series of river flows into Lake Michigan, such that the tracer only contributed to the model domain during the backflow events. After tracer was added to the model domain via the rivers, the hydrodynamics in the lake drove the transport of the plumes over time. As a result, plumes were delineated for evaluation by elevated tracer concentrations in the nearshore area of southern Lake Michigan.

4.2.3.2. Lagrangian Particle Tracking Model

An alternative modeling approach for the simulation of tracer plumes in natural waters involves the tracking of discrete particles through the model domain over time (Huang et al., 2019; Nekouee et al., 2015b). This approach relies on the Lagrangian formulation to calculate dispersion of the particles over time, rather than the Eulerian formulation. As part of FVCOM, a three-dimensional

Lagrangian particle tracking model solves Eq. 4-2 and uses the explicit Runge-Kutta (ERK) method to solve Eq. 4-3 (Chen et al., 2006).

$$\frac{d\vec{x}}{dt} = \vec{v}(\vec{x}(t_n), t_n) \tag{4-2}$$

$$\vec{x}(t_{n+1}) = \vec{x}(t_n) + \int_{t_n}^{t_{n+1}} \vec{v}(\vec{x}(t_n), \boldsymbol{\tau}) d\boldsymbol{\tau} \tag{4-3}$$

In these equations, $\vec{x}$ is the position of a particle at time t_n, $\frac{d\vec{x}}{dt}$ is the rate of particle position change over time, $\vec{v}(\vec{x}, t_n)$ is a three-dimensional velocity field from the hydrodynamics model. t_n represents the current time step in the explicit method, $\vec{x}_n$ is the particle position at time t_n and $\boldsymbol{\tau}$ represents time between t_n and t_{n+1} in the explicit scheme. At the next time step ($t_{n+1} = t_n + d\boldsymbol{\tau}$) the particle position is represented by x_{n+1}. In three-dimensional space, a 4-stage ERK algorithm can be utilized to solve the x, y and σ velocity equations explicitly (Eq. 4-4 – 4-8) and track particles spatiotemporally. In this case, σ replaces z because of the use of terrain-following σ coordinates in the vertical plane of the water column. ϖ replaces w as the vertical velocity component in the context of these σ vertical coordinates, and $\hat{\varpi}$ is related to ϖ by water depth H and free surface elevation ζ, via Eq. 4-9. Additional details regarding the application of a 3-dimensional, 4-stage ERK algorithm to particle tracking in FVCOM can be found in Chen et al. (2006).

$$\xi_n = x_n \tag{4-4a}$$

$$\eta_n = y_n \tag{4-4b}$$

$$\gamma_n = \sigma_n \tag{4-4c}$$

$$\xi_2 = x_n + \frac{1}{2}\Delta t u(\xi_1, \eta_1, \gamma_1) \tag{4-5a}$$

$$\eta_2 = y_n + \frac{1}{2}\Delta t v(\xi_1, \eta_1, \gamma_1) \tag{4-5b}$$

$$\gamma_2 = \sigma_n + \frac{1}{2}\Delta t \hat{\varpi}(\xi_1, \eta_1, \gamma_1) \tag{4-5c}$$

$$\xi_3 = x_n + \frac{1}{2}\Delta t u(\xi_2, \eta_2, \gamma_2) \quad (4\text{-}6a)$$

$$\eta_3 = y_n + \frac{1}{2}\Delta t v(\xi_2, \eta_2, \gamma_2) \quad (4\text{-}6b)$$

$$\gamma_3 = \sigma_n + \frac{1}{2}\Delta t \widehat{\varpi}(\xi_2, \eta_2, \gamma_2) \quad (4\text{-}6c)$$

$$\xi_4 = x_n + \Delta t u(\xi_3, \eta_3, \gamma_3) \quad (4\text{-}7a)$$

$$\eta_4 = y_n + \Delta t v(\xi_3, \eta_3, \gamma_3) \quad (4\text{-}7b)$$

$$\gamma_4 = \sigma_n + \Delta t \widehat{\varpi}(\xi_3, \eta_3, \gamma_3) \quad (4\text{-}7c)$$

$$x_{n+1} = x_n + \Delta t \left[\frac{u(\xi_1,\eta_1,\gamma_1)}{6} + \frac{u(\xi_2,\eta_2,\gamma_2)}{3} + \frac{u(\xi_3,\eta_3,\gamma_3)}{3} + \frac{u(\xi_4,\eta_4,\gamma_4)}{6}\right] \quad (4\text{-}8a)$$

$$y_{n+1} = y_n + \Delta t \left[\frac{v(\xi_1,\eta_1,\gamma_1)}{6} + \frac{v(\xi_2,\eta_2,\gamma_2)}{3} + \frac{v(\xi_3,\eta_3,\gamma_3)}{3} + \frac{v(\xi_4,\eta_4,\gamma_4)}{6}\right] \quad (4\text{-}8b)$$

$$\sigma_{n+1} = \sigma_n + \Delta t \left[\frac{\widehat{\varpi}(\xi_1,\eta_1,\gamma_1)}{6} + \frac{\widehat{\varpi}(\xi_2,\eta_2,\gamma_2)}{3} + \frac{\widehat{\varpi}(\xi_3,\eta_3,\gamma_3)}{3} + \frac{\widehat{\varpi}(\xi_4,\eta_4,\gamma_4)}{6}\right] \quad (4\text{-}8c)$$

$$\widehat{\varpi} = \frac{\varpi}{H+\zeta} \quad (4\text{-}9)$$

Random-walk processes can also be included in the Lagrangian particle tracking model, to help account for particle movement at spatial resolutions lower than the model's mesh size (Gräwe, 2011; Visser, 1997).

For the simulation of storm-associated plumes in southwestern Lake Michigan with the Lagrangian particle tracking model, an offline modeling approach was coupled with the hydrodynamic model results from FVCOM. Hydrodynamics were simulated for the backflow period using FVCOM, and those hydrodynamic results were then used as a velocity field input to the Lagrangian model, to influence particle movement in the model domain.

Previous research has indicated a tradeoff in the use of Eulerian and Lagrangian formulations for modeling fluid dynamics. The Lagrangian formulation often yields lower dispersion than the Eulerian formulation (Zhang and Chen, 2007). The cost of this reduction in dispersion may come in the form of computational demand. The Lagrangian scheme uses a moving coordinate system, calculating locations for each individual particle, calculating a concentration or density of particles at a given location after determining particle locations (Suh, 2006; Van Wageningen-Kessels et al., 2016, Rowe et al., 2016). This can lead to higher computational demand and extensive computational time for Lagrangian-based models, compared to Eulerian-based simulations. As a result, it was necessary to balance the need for a high number of particles simulated (to resolve plume details) with the additional computational demand of increasing the number of particles in the model. Previous research has shown that at least 100000 particles should be released from a source to ensure stable simulation (Zhang and Chen 2007). To optimize both the number of particles simulated and the computational efficiency, 5000 particles were released from each river outlet every hour during the 2008 and 2017 backflow events. This number allowed for more than 100000 particles to be released from each outlet during each backflow event, while also minimizing the computational effort required for the model.

Because the outlets released water to Lake Michigan over varying time periods from during the backflow events, different numbers of particles were released from each outlet (Table 4-2). Over the course of the entire 2008 backflow event, a total of 955000 particles were released to southwestern Lake Michigan while at total of 205000 particles were released during the 2017 event. The transport, dispersion, locations and 3-dimensional concentrations of particles were simulated via the Lagrangian particle tracking model. Plumes resulting from the Lagrangian model were visualized, delineated and evaluated in terms of particle concentration values across the spatial model domain.

Table 4-2: September 2008 and October 2017 backflow event times for the three river outlets in the Chicago area, and corresponding numbers of particles released from each outlet during the backflow event

River Outlet	Year	Backflow Starting Date/Time	Backflow Ending Date/Time	Backflow Period (hours)	Total Number of Particles Released During Backflow
Wilmette	2008	9/13/2008 7:00 AM CDT	9/16/2008 8:00 AM CDT	73	365000
CRCW	2008	9/13/2008 11:00 AM CDT	9/15/2008 1:00 PM CDT	50	250000
O'Brien	2008	9/13/2008 6:00 PM CDT	9/16/2008 2:00 PM CDT	68	340000
Wilmette	2017	10/14/2017 1:00 PM CDT	10/15/2017 10:00 AM CDT	21	105000
CRCW	2017	10/14/2017 1:00 PM CDT	10/15/2017 9:00 AM CDT	20	100000

4.2.4. Evaluation of Model Results

Results from the two model approaches were compared in terms of their ability to simulate the river plumes from Wilmette, CRCW and O'Brien during and after the September 2008 backflow event and plumes from Wilmette and CRCW associated with the October 2017 event. Due to the differences between the models in terms of what they were simulating, concentrations in the lake were normalized to ensure effective comparison of plumes between model results. In the Eulerian model, tracer was released uniformly throughout the width and depth of each of the river channels, prior to moving out to the lake. However, due to differences in the widths and depths of the river channels and the time periods over which the tracers were released during the backflow event, differential tracer concentrations were calculated at the three river outlets. Similarly, the three river channels are of different dimensions, so that the release of discrete numbers of particles in each channel leads to different particle concentrations at the river outlets in the Lagrangian model.

These resulting differences in concentration of particles and tracer at river outlets to the lake can make normalization of concentrations in the plumes challenging. Further complicating the normalization process was the potential coalescence of plumes and their associated tracer/particle concentrations, which prevented normalization of each plume concentration individually. In light of these challenges, maximum plume concentrations were calculated at each river outlet, and all tracer and particle concentrations from the models were normalized to the lowest of the three calculated maximum concentrations. This ensured that high tracer/particle concentrations could be represented while also guaranteeing that results for all three plumes would be visible, even if tracer or particle concentrations were relatively low. Plumes were delineated using a normalized concentration threshold of 0.01, such that any tracer or particle concentration greater than or equal to 1% of the lowest maximum concentration at the river outlets constituted part of a plume, following Huang et al. (2019). Normalized plume concentrations were plotted as contours within Tecplot 360 EX 2018 (Tecplot, Inc., Bellevue, WA) and then overlaid on satellite-derived imagery of the plumes, to visually assess the comparability of the observed and simulated plumes in the nearshore.

Modeled plumes were compared to observational data in the form of satellite-derived ocean color imagery from the MODIS-Terra satellite (NASA Goddard Space Flight Center et al., 2008) and downloaded from the National Aeronautics and Space Administration's (NASA) EarthData Ocean Data repository (https://oceandata.sci.gsfc.nasa.gov/). Plume observational data were scarce due to obstruction of the satellite imagery by clouds during much of the backflow event periods. MODIS images captured on September 16th, 2008 and October 16th, 2017 (captured at 11:40 AM and 11:55 AM CDT, respectively) were not obstructed and most clearly showed plumes in the area of the river outlets, so these images were selected for model validation. Data from these images were downloaded and imported into the NASA SeaDAS data analysis software (NASA, https://seadas.gsfc.nasa.gov/) (Figure 4-5). MODIS level-1A data, composed of scans of raw radiances obtained by the satellite, were directly imported into SeaDAS. Within SeaDAS, the level-1A data were used as input to three processes: modis_GEO to create a geolocation file for the data, modis_L1B to create level-1B data calibrated 1 km resolution radiances, and l2gen to create level-2 data including reflectance spectra and water quality data. The l2gen process in SeaDAS allows for atmospheric correction, to convert atmospheric data to surface reflectance data, and specification of spatial resolution. Following Mendes et al., (2014), the standard SeaDAS atmospheric correction was used, and level-2 data for southwestern Lake Michigan were generated at a spatial resolution of 250 m when possible.

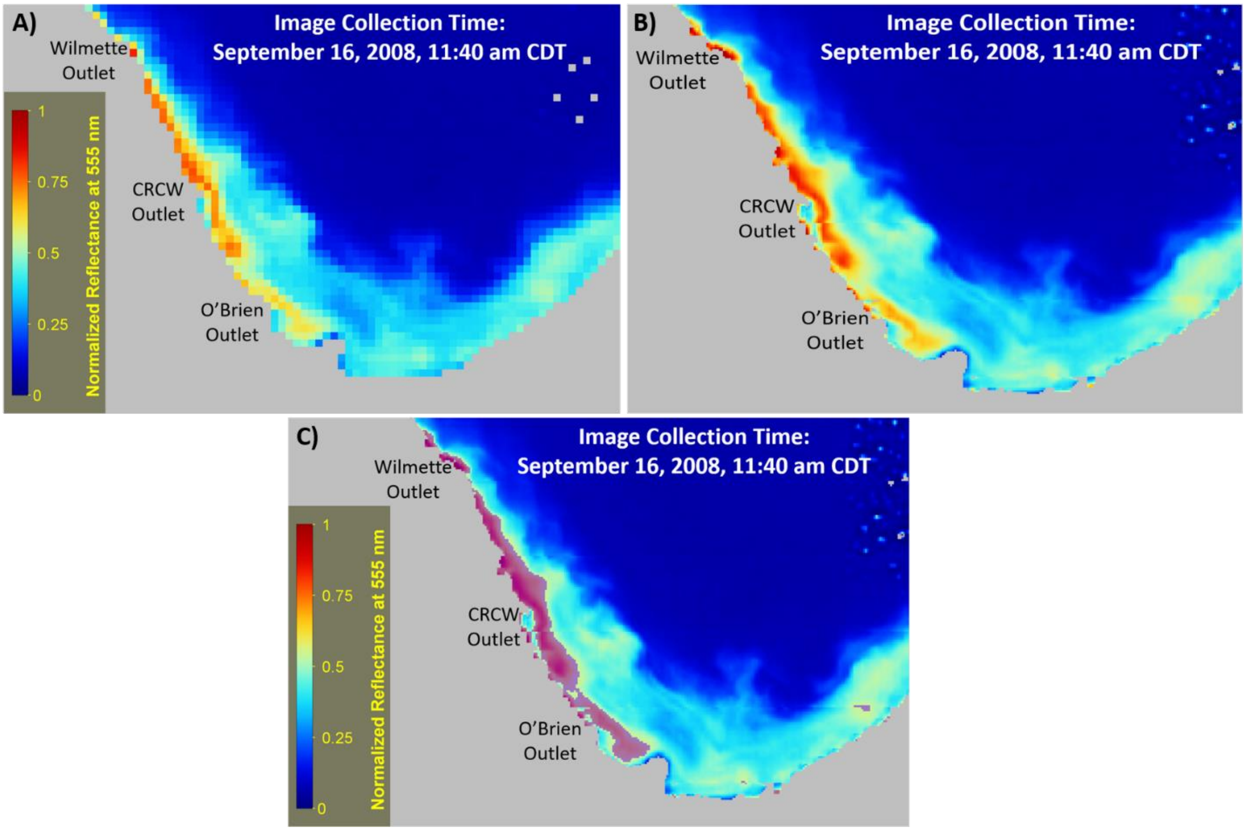

Figure 4-5: Processing of MODIS imagery to delineate storm--induced river plumes in the Chicago area (following Mendes et al, 2014). The original, 1 km spatial resolution normalized reflectance data at the 555 nm band for September 16th (A, top-left) shows the plumes, but the processing tools in SeaDAS allowed for development of data with higher spatial resolution of 250 m (B, top-right). Panel C (bottom) shows the data overlaid with the mask excluding normalized reflectance values < 0.55 (purple color)

Because of its ability to approximate turbidity and suspended solids in the water (Mendes et al., 2014; Nezlin et al., 2005; Nezlin and DiGiacomo, 2005; Thomas and Weatherbee, 2006), the reflectance band at 555 nm (corresponding to green visible light) was used to delineate the plumes from the MODIS level-2 data. Reflectance values in southwestern Lake Michigan were normalized with respect to the maximum reflectance value. River plume zones of influence were denoted by areas in southwestern Lake Michigan showing normalized reflectance values between 0.60 and 1.0. High normalized reflectance values would signify high turbidity levels in relation to those in offshore waters, which could then be interpreted as plumes (Eadie et al., 1996; Vanderploeg et al., 2007). The threshold normalized reflectance value of 0.60 was adapted from previous work from Mendes et al. (2014) and Nezlin et al. (2005), which used normalized reflectance thresholds between 0.325 and 0.8. A data mask was created to focus on these areas of plume influence, and the georeferenced area of the mask was directly calculated in the SeaDAS software program via the Mask Area tool.

Additionally, plume distances from the three outlets were measured directly within the SeaDAS software program, using the Range Finder tool. Distances normal to shore were measured from each river outlet, normal to the shoreline, while distances along the shore were measured from the outlets in a southerly direction and parallel to the shoreline. Measurements were made from the center of each river outlet to the end of the furthest pixel within the mask denoting the plumes (Figure 4-6). It is important to note that, at times, the representation of plumes in SeaDAS indicated that the plumes were not connected to the outlets. Nonetheless, plume distances were measured from the outlets to avoid discrepancies in where the measurements were conducted between backflow events.

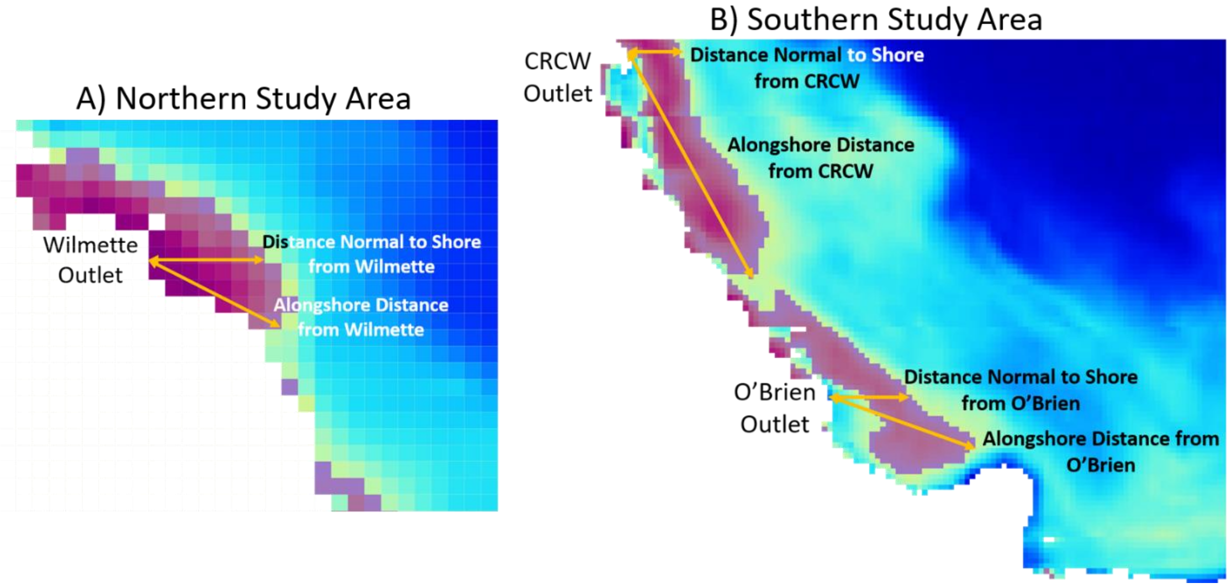

Figure 4-6: MODIS imagery with orange-colored arrows showing how plume alongshore and normal-to-shore distances from Wilmette (A, left) and CRCW and O'Brien (B, right) were measured directly in SeaDAS

Plume data from the FVCOM model results were then exported from Tecplot as image files, imported into ArcMap and georeferenced to overlay MODIS-Terra true color satellite imagery. The newly-georeferenced plume image files were reclassified to delineate pixels representing the plumes (Figure 4-7). The Zonal Geometry tool was then used to automatically calculate the area of the reclassified pixels representing the plumes. Also following the protocols for measuring alongshore and normal-to-shore plume dimensions from MODIS imagery, reclassified plumes from FVCOM results were manually measured in ArcMap to determine alongshore and normal-to-shore dimensions of the simulated plumes (Figure 4-8).

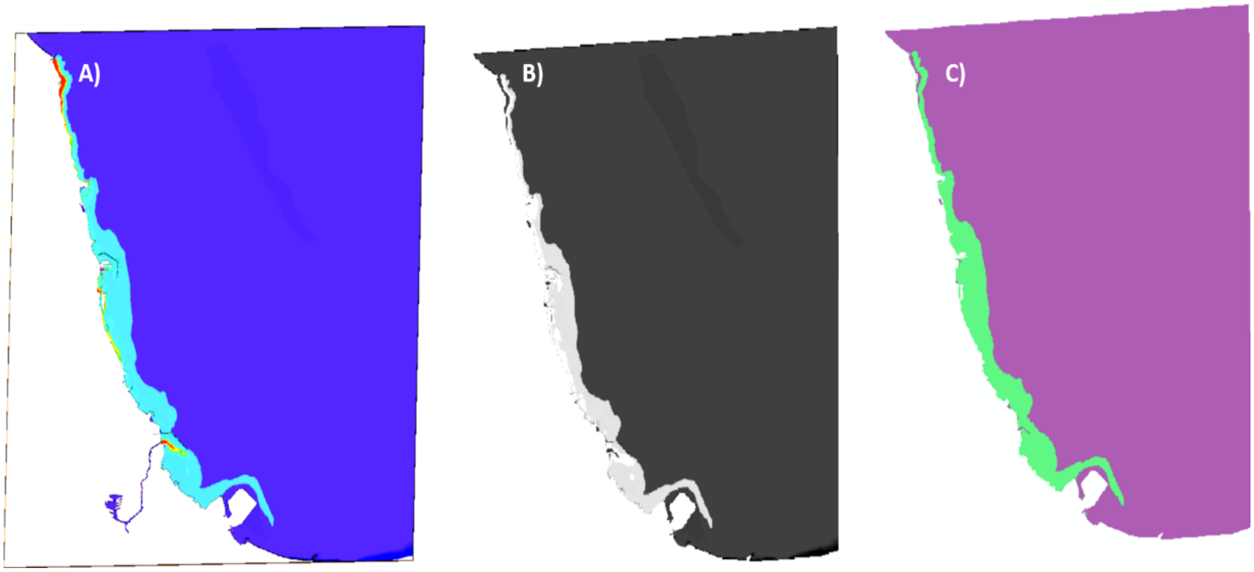

Figure 4-7: Processing of FVCOM Lagrangian particle transport model results to delineate storm-induced river plumes in the Chicago area. The original image from September 16^th^ (A, left) shows the plumes, but reclassification of the pixels is more straightforward when the blue and red bands of the image are removed (B, center). The reclassified image (C, right) clearly shows the extent of the modeled plumes in green

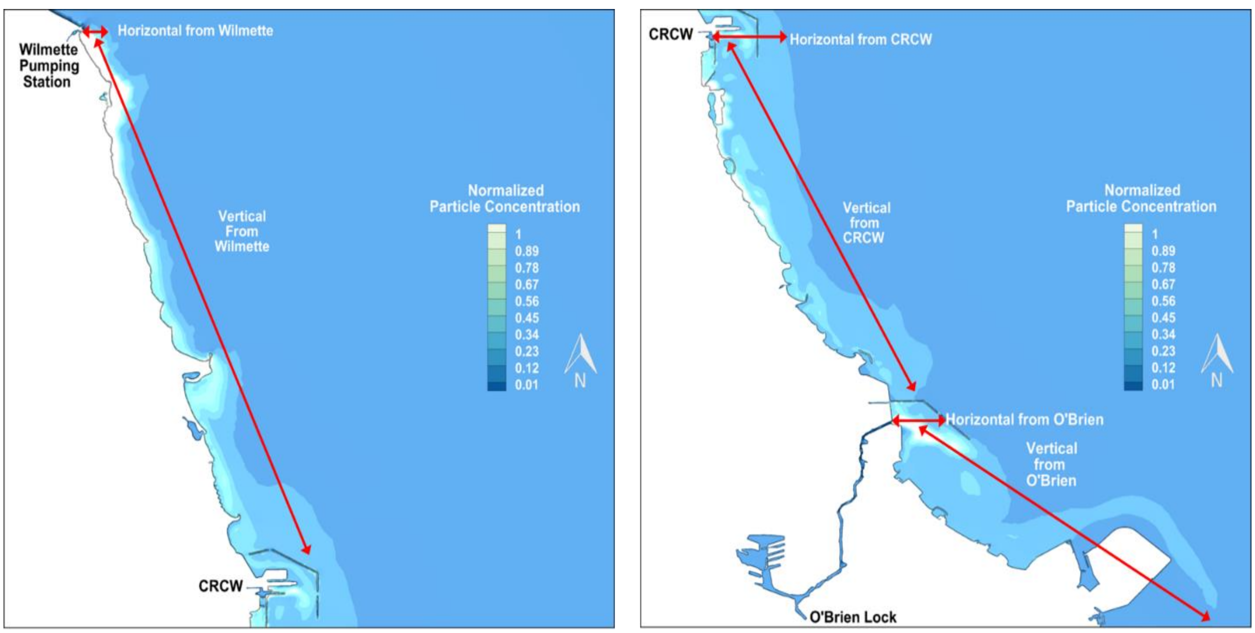

Figure 4-8: MODIS imagery with arrows showing how plume alongshore and normal-to-shore distances from Wilmette (A, left) and CRCW and O'Brien (B, right) were measured directly in ArcMap

Modeled plume surface areas as well as alongshore and normal-to-shore dimensions were then compared to the observed surface areas and dimensions from the MODIS imagery to evaluate the ability of the models to re-create observed plumes. Absolute errors in total plume surface area and dimensions from each river outlet (err_j) were computed by subtracting the MODIS-associated plume distances and areas (O_j) from the modeled plume distances and areas (P_j) (Eq. 4-10). The model approach that minimized the error for a majority of distance/area calculations was selected as the optimal approach for simulating storm-induced river plumes in southern Lake Michigan.

$$err_j = P_j - O_j \tag{4-10}$$

4.3. Results and Discussion

4.3.1. MODIS-Derived Plumes

Satellite data from the MODIS-Terra satellite were obtained for southwestern Lake Michigan on September 16th, 2008 and October 16th, 2017. These data showed minimal cloud-obstruction while also having been obtained less than 24 hours after the cessation of their respective backflow events, so they were deemed to be appropriate for modeled plume evaluation. Reflectance data for the 555 nm band were used to delineate and measure the plumes in the nearshore area for both days, after processing the original 1 km resolution data to 250 m spatial resolution.

Assessment of the plumes captured by MODIS-Terra on September 16th, 2008 indicate that the stormwater affected an area of the nearshore equal to 125.59 km^2 (see Figure 4-5c). Plumes associated with CRCW and O'Brien outlets seem to have combined into a single, large plume extending the length of the shoreline between the two, while there is a separate and smaller plume near the Wilmette outlet. Normal-to-shore distances from the Wilmette, CRCW and O'Brien outlets were measured to be 1.92 ± 0.0065, 2.72 ± 0.0091 and 4.58 ± 0.015 km, respectively, while alongshore distances were measured as 2.80 ± 0.0094, 19.00 ± 0.064 and 8.16 ± 0.027 km, respectively.

Plume data obtained by MODIS-Terra on October 16th, 2017 suggest a plume surface area of 189.43 km^2. Similar to September 16th, 2008 imagery, plumes associated with CRCW and O'Brien outlets covered the length of the shoreline between the two outlets. However, the plume data for the 2017 event also show that the plume area of influence also extended northward to the Wilmette outlet (Figure 4-9). Alongshore distances measured from the MODIS data for October 16th, 2017 were 20.76 ± 0.070 and 24.59 ± 0.082 km from Wilmette and CRCW outlets, respectively. Normal-to-shore distances were measured as 6.69 ± 0.022 and 3.77 ± 0.013 km, respectively.

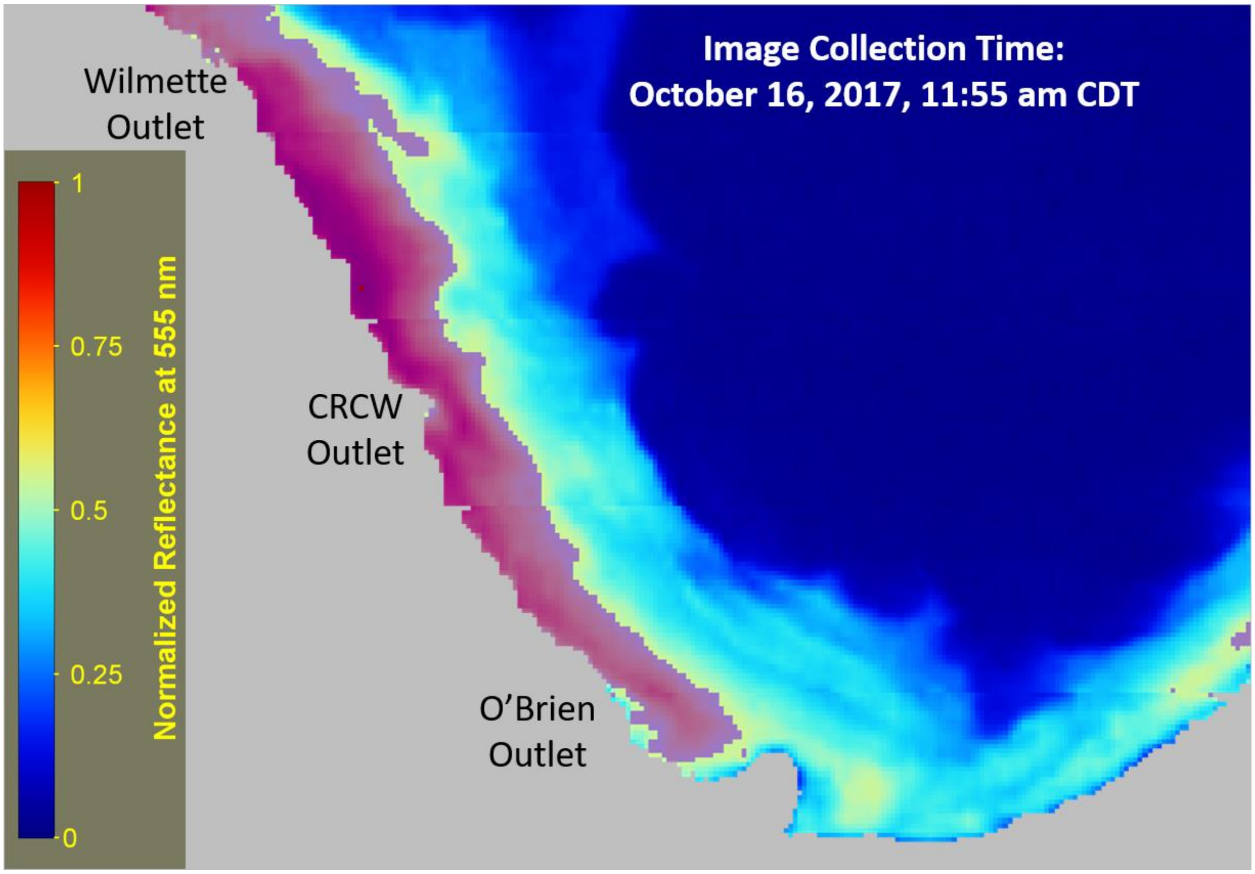

Figure 4-9: Map of southwestern Lake Michigan derived from MODIS-Terra data reflectance data at the 555 nm (green) band. Purple areas overlaying the map indicate areas of normalized reflectance > 0.55, indicative of elevated turbidity and storm-associated river plumes

4.3.2. 2008 Storm Event Plume Simulation

Eulerian simulation of the three storm-associated plumes in 2008 indicate that plumes extended from the Wilmette Pumping station outlet, south through the city of Chicago and beyond the Indiana Harbor peninsula, on September 16th, 2008 (Figure 4-10). This suggests that the hydrodynamics in the nearshore drive the plumes along the shore in the days immediately after a backflow event like that in September 2008, rather than pushing the plumes offshore and to the open water. This also shows that the plumes do not remain distinct over time, at least for large magnitude backflow events. Instead, they seem to coalesce along the shore, potentially leading to the accumulation of tracer from multiple formerly separate plumes and even from multiple additional sources at nearby beaches along the shore.

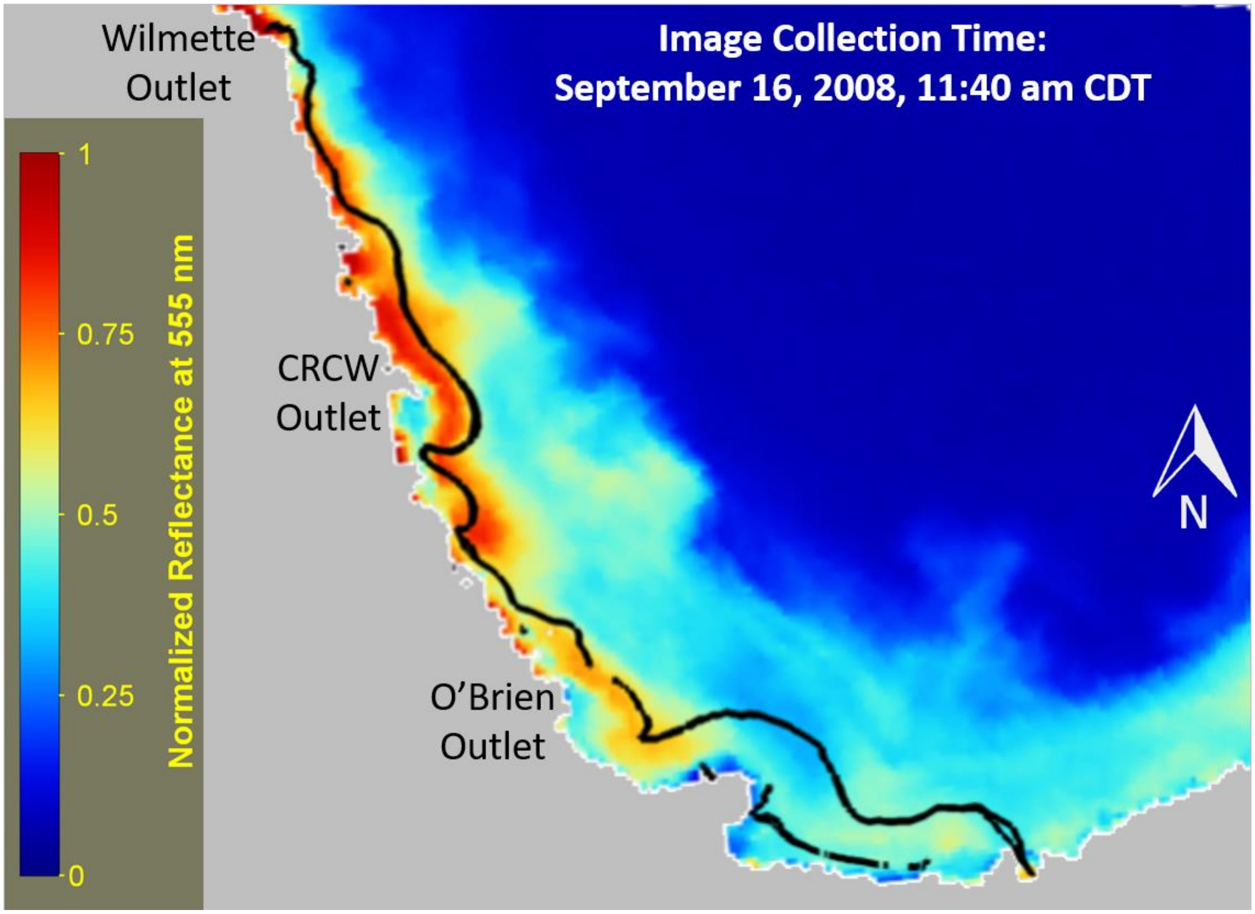

Figure 4-10: MODIS-derived reflectance data and corresponding results from the Eulerian model simulating the plumes associated with the September 2008 backflow event. Black contour lines indicate the extent of the plumes, denoted by normalized tracer concentrations ≥ 0.01, while MODIS-derived plumes are represented by yellow, orange and red areas on the heat map (normalized reflectance at 555 nm ≥ 0.55)

The total surface area of the modeled plumes on September 16th was 201.64 km^2, which is only 0.12 km^2 smaller than the plume derived from MODIS satellite data (Table 4-3). The modeled plume dimensions in the *x*-direction (normal-to-shore) at Wilmette, CRCW and O'Brien outlets were measured as 3.16 km, 6.10 km and 2.40 km, respectively. The modeled normal-to-shore distances from Wilmette and CRCW outlets both overpredicted those obtained from the MODIS data (absolute errors = 0.69 and 2.84 km, respectively). However, the modeled normal-to-shore distance at the O'Brien outlet was 4.87 km smaller than the corresponding MODIS-derived distance (Table 4-3). Modeled distances in the *y*-direction (alongshore) from Wilmette, CRCW and O'Brien outlets were measured as 22.76 km, 17.62 km and 7.30 km, respectively. At Wilmette and O'Brien outlets, these matched the corresponding measured distances from MODIS data. This is due to the Wilmette plume extending from the Wilmette outlet to the CRCW outlet, while the plume dispersion from the O'Brien outlet was limited by the presence of a breakwall. The plume from the CRCW outlet did not extend all the way to the O'Brien outlet, so its alongshore distance was measured to be 1.44 km smaller in magnitude than the corresponding distance measured from the MODIS-derived data (Table 4-3).

Table 4-3: Evaluation results comparing quantitative metrics of predictive ability of the Eulerian model, relative to plumes derived from MODIS reflectance data for the 2008 and 2017 backflow events

Model Year	Dataset	Plume Total Surface Area (km^2)	Along-shore Distance from Wilmette (km)	Along-shore Distance from CRCW (km)	Along-shore Distance from O'Brien (km)	Normal-to-Shore Distance from Wilmette (km)	Normal-to-Shore Distance from CRCW (km)	Normal-to-Shore Distance from O'Brien (km)
2008	MODIS	201.76	22.76 ± 0.076	19.06 ± 0.064	7.30 ± 0.025	2.47 ± 0.0083	3.26 ± 0.011	7.27 ± 0.024
	Eulerian Model	201.64	22.76	17.62	7.3	3.16	6.1	2.4
	Lagrangian Model	94.44	22.76	17.82	7.3	0.43	3.15	2.4
	Eulerian Model – MODIS Absolute Error	-0.12	0	-1.44	0	0.69	2.84	-4.87
	Lagrangian Model – MODIS Absolute Error	-107.32	0	-1.24	0	-2.04	-0.11	-4.87
2017	MODIS	295.94	21.66 ± 0.073	24.59 ± 0.082	N/A	8.02 ± 0.029	5.57 ± 0.019	N/A
	Eulerian Model	53.48	0.31	11.49	N/A	0.32	2.1	N/A
	Lagrangian Model	48.11	20.76	10.16	N/A	0.77	3.39	N/A
	Eulerian Model – MODIS Absolute Error	-242.46	-21.35	-13.1	N/A	-7.7	-3.47	N/A
	Lagrangian Model – MODIS Absolute Error	-247.83	-0.9	-14.43	N/A	-7.25	-2.18	N/A

Lagrangian simulation of the river plumes associated with the September 2008 backflow event, like the Eulerian simulation, suggest that the plumes from all three outlets coalesced by September 16th, 2008. As a result, the modeled plumes were shown to impact the entire Chicago shoreline on September 16th. In contrast to the plumes simulated by the Eulerian model, plumes derived from the Lagrangian model extended partially around the Indiana Harbor peninsula but did not spread beyond the peninsula. The modeled plumes stayed relatively close to shore, potentially indicating that nearshore wind and hydrodynamics were driving plume movement along the shore rather than out to the open water (Figure 4-11).

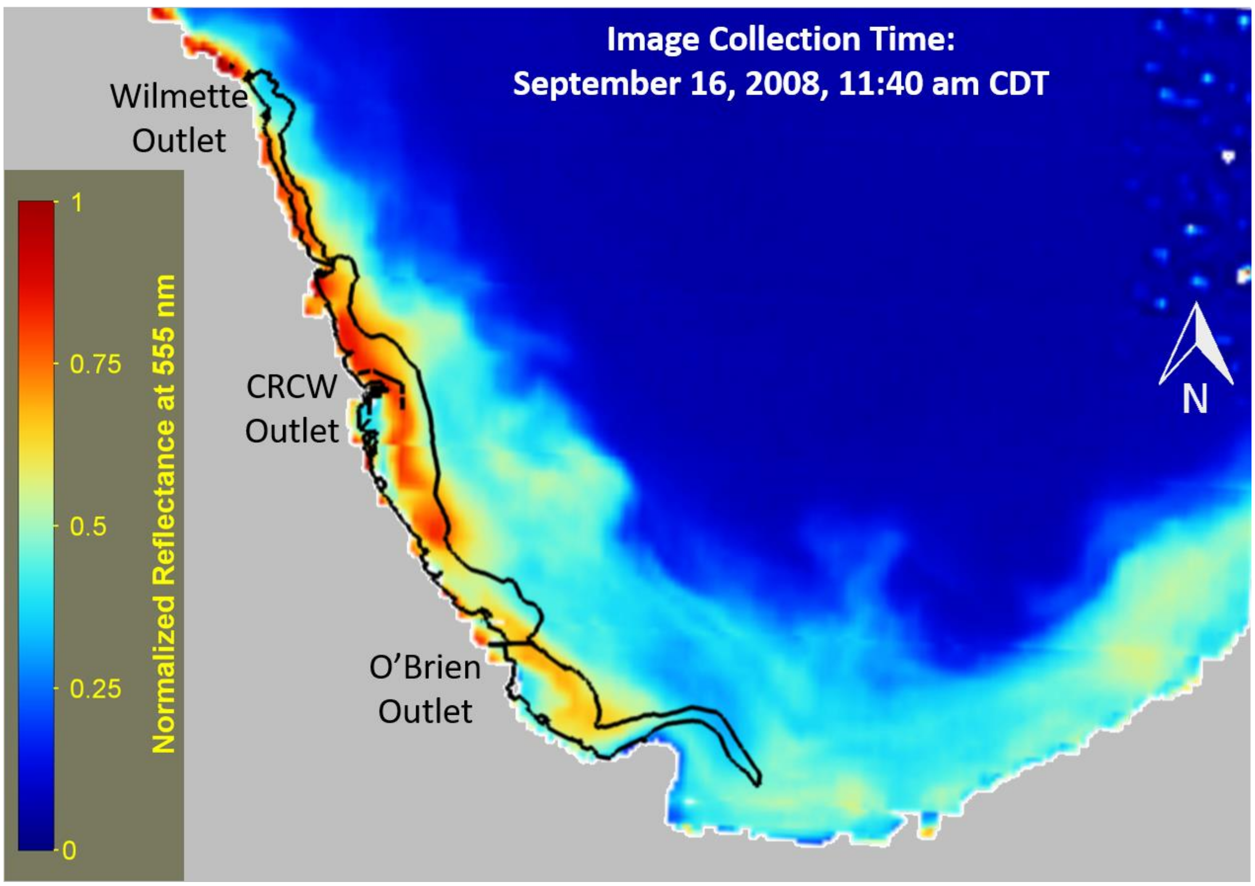

Figure 4-11: Storm-associated river plumes, overlaid on MODIS imagery for September 16, 2008. Modeled plumes are represented by the black contour corresponding to the normalized particle concentration of 0.01. The contours show the modeled plume's zone of influence, compared to the plume from the MODIS imagery, denoted by yellows, oranges and reds in the heat map

On September 16th, 2008, the plume surface area generated by the Lagrangian model was calculated to be 94.44 km^2. This area is 107.32 km^2 smaller than the area calculated from the MODIS-Terra derived reflectance data (Table 4-3). In the *x*-direction (normal-to-shore), modeled plume distances measured from Wilmette, CRCW and O'Brien were 0.43 km, 3.15 km and 2.40 km, respectively. These measurements were all smaller than the distances measured from MODIS-Terra data, with absolute errors between modeled and MODIS distances ranging from 0.11 km at the CRCW outlet to 4.87 km at the O'Brien outlet (Table 4-3). In the *y*-direction (alongshore), modeled distances were measured as 22.76 km from Wilmette, 17.82 km from CRCW and 7.30 km from O'Brien. Because the modeled alongshore plumes from the CRCW outlet did not extend to the O'Brien outlet, it underpredicted the MODIS-derived alongshore distance by 1.24 km. At the Wilmette and O'Brien outlets, though, the Lagrangian model simulated plumes that extended as far as the MODIS-derived plumes did, because the Wilmette plumes extended to CRCW and the O'Brien plumes were limited in extent by the Indiana Harbor peninsula (Table 4-3).

4.3.3. 2017 Storm Event Plume Simulation

Simulated plumes associated with the October 2017 backflow event were smaller in size, compared to those associated with the September 2008 event. This was likely due to the smaller magnitude discharge connected to the 2017 event. Plumes resulting from the Eulerian model were shown to stay close to the shore on October 16th, much like the plumes associated with the 2008 backflow event. However, the modeled plumes do not capture the extent of the MODIS-derived plumes associated with the October 2017 backflow event, especially between the Wilmette and CRCW outlets (Figure 4-12).

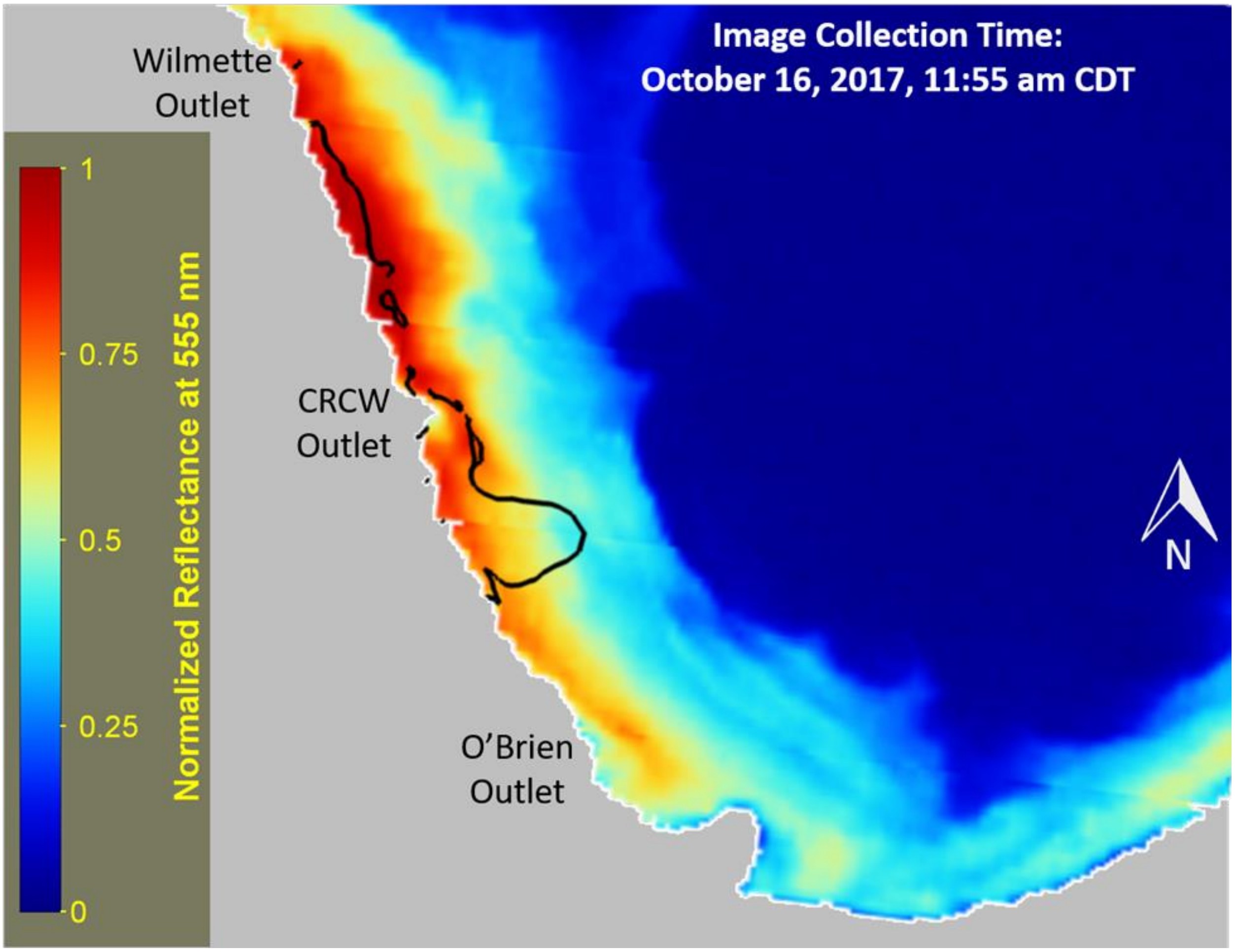

Figure 4-12: MODIS-derived reflectance data and corresponding results from the Eulerian model simulating the plumes associated with the October 2017 backflow event. Black contour lines indicate the extent of the plumes, denoted by normalized tracer concentrations ≥ 0.01, while MODIS-derived plumes are represented by yellow, orange and red areas on the heat map (normalized reflectance at 555 nm ≥ 0.55)

The Eulerian model simulated a total plume surface area of 53.48 km^2 on October 16th, 2017. This area is 242.46 km^2 smaller than the plume surface area derived from the MODIS reflectance data (Table 4-3, above). Distances from the outlets in the *x*-direction (normal-to-shore) at Wilmette and CRCW outlets were measured from the modeled plumes as 0.32 km and 2.10 km, respectively. These distances are 7.70 and 3.47 km smaller, respectively, than those distances measured from MODIS-Terra reflectance data. The O'Brien outlet did not release stormwater as part of the October 2017 backflow event, so normal-to-shore and alongshore distances were not measured.

Along the shore, distances measured corresponding to the Eulerian model-derived plumes were measured as 0.31 km from the Wilmette outlet and 11.49 km from the CRCW outlet. These distances are also substantially smaller in magnitude than the distances measured from the MODIS-derived reflectance data, with measurements differing by 21.35 km at the Wilmette outlet and 13.10 km at the CRCW outlet (Table 4-3).

In similar fashion to the plumes from the September 2008 backflow event, the Lagrangian model-derived plumes associated with Wilmette and CRCW outlets coalesced at 11:00 am on October 16th, 2017. This coalescence occurred at the CRCW outlet, just outside of the breakwater infrastructure at CRCW. As a result, the modeled combined plume extended from the Wilmette outlet south through the CRCW outlet and roughly 7 km south of CRCW (Figure 4-13).

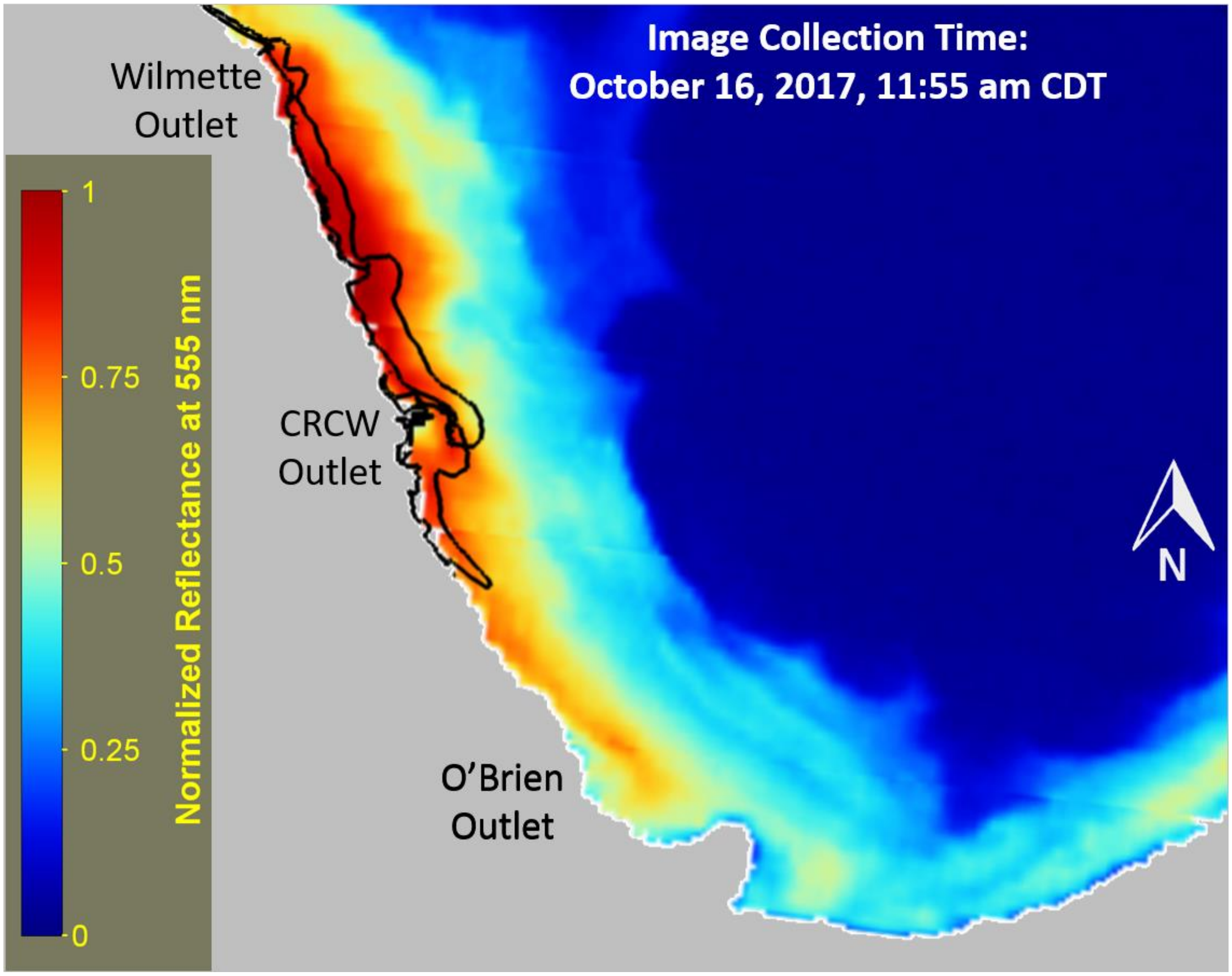

Figure 4-13: Storm-associated river plumes, overlaid on MODIS imagery for October 16, 2017. Modeled plumes are represented by the black contour corresponding to the normalized particle concentration of 0.01. The contours show the modeled plume's zone of influence, compared to the plume from the MODIS imagery, denoted by yellows, oranges and reds in the heat map

The total surface area of the Lagrangian-modeled plumes on October 16th, 2017 was calculated as 48.11 km^2. This area, like that generated by the Eulerian model, is significantly smaller than the MODIS-derived plume surface area (absolute error of 247.83 km^2, Table 4-3). Normal-to-shore distances from the Wilmette and CRCW outlets were measured as 0.77 km and 3.39 km for the Lagrangian modeled plumes, respectively. These distances were smaller than those measured from the MODIS-Terra data. The modeled normal-to-shore distance from the Wilmette outlet is 7.252 km smaller than the corresponding distance from the MODIS-Terra data. Modeled normal-to-shore distance from the CRCW outlet is 2.18 km shorter than that derived from the MODIS data (Table 4-3). Modeled alongshore distance from the Wilmette outlet matched the alongshore distance derived from the MODIS-Terra data (20.76 km) because both the modeled and MODIS-derived plumes extended from the Wilmette outlet to the CRCW outlet along the shore. South of the CRCW outlet along the shore, the modeled plume extended 10.16 km. This modeled distance is 14.43 km shorter than the alongshore distance from CRCW that was derived from the MODIS-Terra data (Table 4-3).

Seasonal turbidity trends and mixing effects may be attributable to the lack of predictive ability for the Eulerian model in the context of the October 2017 backflow event. As a large lake, Lake Michigan is often stably stratified through the summer, but the water column begins to mix vertically in the autumn and often experiences an overturning through the winter and spring (Belestky and Schwab, 2001). The mixing of the water column, supplemented by seasonal changes in primary productivity may lead to an increase in turbidity in the water in the autumn months (Fahnenstiel et al., 2010; Rousar 1973; Son and Weng, 2019). This seasonal turbidity would be in addition to the turbidity generated by the storm-associated river plumes and may lead to an overestimation of plume dimensions in the nearshore region via MODIS-derived data. Nonetheless, the differences between modeled and satellite-derived plume dimensions presented here suggest that the Eulerian model may not be an effective approach to plume simulation, especially as the lake begins to mix.

4.3.4. Model Selection

Plume simulation results from the Eulerian and Lagrangian models for September 16th, 2008 and October 16th, 2017 show comparable simulation of plumes, in a quantitative sense. Visually, though, the comparability between the models is less clear. In both cases in 2008, modeled plumes from the three river outlets quickly coalesce along the shoreline, forming one large plume that extends through the entire study area. In 2017, there is a discrepancy between the Eulerian and Lagrangian models. On October 16th, 2017, the Eulerian model simulated multiple smaller plumes along the shoreline, while the Lagrangian model simulated a single large plume from the coalescence of the Wilmette and CRCW plumes. In all cases, the models also show that the plumes remain close to the shoreline in the days post-backflow event, indicating that the plumes pose a threat to nearshore areas and beaches in Chicago.

Qualitatively, plumes resulting from the Lagrangian model tend to follow the curvature of the observed plumes better than those resulting from the Eulerian model, especially near the CRCW outlet. The plumes resulting from the Eulerian model also extend well beyond the Indiana Harbor peninsula east of the O'Brien Lock on September 16th. This extent of the O'Brien plume is not visible in the MODIS reflectance data. The Lagrangian simulated plume for the O'Brien outlet extent more closely matches what is seen in the MODIS reflectance imagery for September 16th. Likewise, the plumes modeled by the Lagrangian approach extend continuously farther along the shoreline as well as farther toward the open water on October 16th, 2017 than the plumes simulated by the Eulerian model. Against the MODIS-Terra reflectance data shown to represent turbidity and plumes effectively, the plume maps generated from model results indicate that the Lagrangian model may predict the plume dynamics more effectively than the Eulerian model.

Quantitatively, the evaluation metrics used to determine model ability to simulate MODIS-Terra generated plumes suggest that the two modeling approaches are similar. Of the 12 evaluation metrics used to compare the Eulerian and Lagrangian model approaches, the absolute errors between the modeled and MODIS-measured metric were the same between the two approaches for 3 metrics (25%). This happened when plumes were limited in their dispersion by breakwater infrastructure or when the plumes extended from one outlet to another continuously for both model approaches and the MODIS data. The Eulerian model minimized the absolute error between the modeled plume and MODIS plume measurements for the normal-to-shore distances from Wilmette and CRCW in 2008 as well as the plume total surface area and alongshore distance from CRCW in 2017. Differences between modeled and MODIS-Terra derived metrics were minimized by the Lagrangian model for the plume total surface area and alongshore distance from O'Brien in 2008. The Lagrangian model also minimizes absolute errors between the model and MODIS data for alongshore and normal-to-shore distance from Wilmette as well as the normal-to-shore distance from CRCW (Table 4-4). Using these metrics as a guide, the Lagrangian model minimized absolute errors for one more metric (5 out of 12, 41.67%) than the Eulerian model (4 out of 12 (33.33%), indicating that the Lagrangian model may be slightly more effective at simulating storm-associated river plumes.

Table 4-4: Results of model comparison, showing whether the Eulerian or Lagrangian model minimized the difference between modeled and MODIS-Terra derived plume dimensions. "N/A" values in right column denote plume dimension metrics for which absolute errors between both models and the MODIS-Terra derived plumes were equal

Evaluation Metric	**Backflow Year**	**Model with lowest model-MODIS Absolute Difference**
Plume Total Surface Area	2008	Lagrangian
Alongshore Distance from Wilmette	2008	N/A
Alongshore Distance from CRCW	2008	N/A
Alongshore Distance from O'Brien	2008	Lagrangian
Normal-to-Shore Distance from Wilmette	2008	Eulerian
Normal-to-Shore Distance from CRCW	2008	Eulerian
Normal-to-Shore Distance from O'Brien	2008	N/A

Table 4-4 (cont'd)

Plume Total Surface Area	2017	Eulerian
Alongshore Distance from Wilmette	2017	Lagrangian
Alongshore Distance from CRCW	2017	Eulerian
Normal-to-Shore Distance from Wilmette	2017	Lagrangian
Normal-to-Shore Distance from CRCW	2017	Lagrangian

As a result of qualitative and quantitative evaluations of the Eulerian and Lagrangian models for plumes in the Chicago area, the Lagrangian model was selected as the optimal model for plume simulation. Qualitatively, the Langrangian model more closely simulated the plumes visible in the MODIS imagery for both September 16th, 2008 and October 16th, 2017, via visual assessment of the plume contours overlaid on MODIS-Terra derived reflectance data. The Lagranigan model also minimized the magnitude of model-MODIS absolute errors in 5 of 12 (41.67%) plume surface area and dimension metrics for both days, while the Eulerian model minimized such errors for 4 of 12 metrics (33.33%). This selection is supported by previous research into river plume effects on nearshore zones. Nekouee et al. (2015) used Lagrangian particle tracking to simulate a river plume along the eastern shore of Lake Michigan, with similar results and comparisons to remotely-sensed plume imagery. Likewise, Huang et al. (2019) relied on Lagrangian particle tracking to simulate footprints and dimensions of water quality areas of concern resulting from wastewater treatment plant releases in northern Lake Ontario.

4.3.5. Limitations of the Validation and Selection Process

There is a considerable lack of observational data associated with storm events and how they impact nearshore regions. Storm events often lead to dangerous conditions and thus discourage the collection of direct, observational data in favor of ensuring safety of researchers and managers. This is especially true for extreme storm events such as those that lead to backflow events in Chicago. By definition, a backflow event occurs to divert water back to the lake and relieve high water in the rivers during heavy rain (USACE, 1996). These events often coincide with localized flooding, high water levels and wind that can threaten health and well-being of people along the lakeshore. As a result, observational data corresponding to conditions during and immediately after backflow events are frequently limited to remotely-sensed observations. Further, before processing, remotely-sensed data are often of coarse spatial resolution (i.e., 1 km) and thus limited in their usability, particularly in the nearshore zone. In the case of satellite imagery captured during and immediately after backflow-inducing storms, obstruction by clouds can severely constrain the application of the data. When satellite imagery is not obstructed, it can be difficult to delineate river plumes with confidence as well. While parts of the plumes are visible in the imagery (Figure 4-7a), parts of the plumes that have been more diluted in the water column may be less clear from the imagery, though they are still part of the plumes. Isolation of the green band of images can be helpful in delineating plumes (Mendes et al., 2014; Nezlin et al., 2005; Nezlin and DiGiacomo, 2005; Thomas and Weatherbee, 2006) (Figure 4-7b), but still leaves some uncertainty due to a continuous gradient of color or shade in the images and bands.

An additional confounding factor in the collection of *in situ* observational data associated with backflow events is the timing of the events themselves. Of the 19 backflow events that occurred in Chicago since 2000, only 58% occurred during the swimming season (Memorial Day to Labor Day annually) (USACE, 2014). Further, these swimming season backflow events are all relatively small in magnitude, releasing and average of 60% less stormwater to the lake, compared to backflow events occurring outside the swimming season. Since beach water quality sampling associated with backflows only occurs during the swimming season (MWRD, 2019), there is a paucity of water quality data to support model validation, particularly for the large backflow events such as that seen in 2008.

Without collecting *in situ* data during and after backflow events themselves, it is difficult for researchers to fully validate models of storm-induced conditions and resulting river plumes in the nearshore. Satellite imagery and remotely-sensed data can be useful, but future work related to water conditions during storms would benefit from additional observational data for model calibration. This is especially important in the context of predicted increases in both the frequency and intensity of storms as a result of climate change (Pachauri et al., 2014). With the development and application of unmanned aerial vehicles such as drones (Morgan et al., 2020) and complex sensor systems that can autonomously collect *in situ* data (Angelescu et al., 2019; Huynh et al., 2016; Safaie et al., 2016; Schimmelpfennig et al., 2012; Zhang et al., 2012), these types of observations are more feasible than they have been historically.

Quantitatively, the differences in plume surface area and dimension calculations between the FVCOM-simulated plumes and plumes visible in the MODIS imagery were not weighted in any way. That is, the model that minimized the errors was ultimately selected as the most reliable approach for subsequent plume modeling. It is interesting to note that the Lagrangian modeled plume surface areas and dimensions are frequently smaller plumes than those observed via MODIS-Terra reflectance. This could be associated with uncertainty in normalized reflectance threshold selection. The threshold of 0.60 was selected because it fell within the range of thresholds used in previous research (Mendes et al., 2014; Nezlin et al., 2005; Nezlin and DiGiacomo, 2005), but the range of threshold values is relatively large (0.33 – 0.80). There is also substantial spatial variability in terms of normalized reflectance values that adequately delineate plumes (Nezlin et al., 2005), so additional investigation normalized reflectance threshold values for southwestern Lake Michigan may be beneficial.

Despite its limitations, the use of satellite imagery for delineation of plumes and validation of model plume simulations may provide an effective step toward more reliable model validation in the future. The 250 m spatial resolution of the processed MODIS-Terra data used herein seems to be high enough to reasonably show plumes. In the absence of other *in situ* or higher-resolution data, satellite imagery thus seems to be useful to begin validating and refining plume models for southwestern Lake Michigan.

4.4. Conclusions

Storm-associated river plumes have the potential to transport substantial amounts of contamination into open water and nearshore areas in large lake and ocean environments (Nekouee et al., 2015b, 2015a). While storm conditions can make it difficult to directly observe resulting plume dynamics in the nearshore zone, model simulations can aid in the understanding of spatiotemporal dynamics of plumes.

Two modeling approaches were compared in terms of their ability to reproduce plumes captured by MODIS satellite imagery after a heavy storm event that resulted in backflow of stormwater to Lake Michigan in September 2008 and October 2017. Qualitative and quantitative comparison of the plume dimensions on September 16th, 2008 showed that plume surface areas and dimensions both along the shore and normal to the shore for the Eulerian model were larger than those modeled using the Lagrangian approach. Though this is not always the case (particularly for the October 16th, 2017 modeled plumes), it supports the idea that Eulerian models tend to overestimate dispersion in the water, compared to Lagrangian models (Zhang and Chen, 2007). Comparison of the model results to MODIS-Terra reflectance data along the southwestern Lake Michigan shoreline indicate that the additional dispersion calculated via the Eulerian model may have diminished the model's ability to simulate the plumes; the Lagrangian model absolute errors were equal to or less than the errors corresponding to the Eulerian model for 8 out of 12 (66.67%) evaluation metrics across the two dates. As a result, the Lagrangian model has been selected as the more reliable approach to simulation of storm-associated river plumes in southwestern Lake Michigan.

While the differences between the two model approaches allowed for selection of an optimal model with reasonable confidence, assessment and study of river plumes would benefit from additional data collection. Availability of observational data to compare with model results was a considerable limiting factor for the effective selection of an optimal modeling approach. The Lagrangian model was selected based on its ability to reproduce plumes visible from MODIS satellite data, but it is unknown whether the MODIS data effectively captured the plumes and to what degree the MODIS data captured non-plume related turbidity. Therefore, additional observational data, particularly imagery and data from unmanned aerial vehicles or water quality data from high-resolution sensor stations (Morgan et al., 2020; Safaie et al., 2016; Schimmelpfennig et al., 2012; Zhang et al., 2012) would increase the confidence with which modeling and model selection could be completed. Outreach and citizen science approaches may be beneficial for data collection and accumulation of anecdotal evidence regarding plume conditions as well (Jennings et al., 2020), as long as the safety of the public is ensured.

In the absence of such complementary data for plume conditions and dynamics, Lagrangian particle tracking appears to be an effective approach to simulation of storm-induced river plumes in the nearshore zone. Therefore, in future hindcasting assessment of storm-induced plume conditions and effects, it is recommended that Lagrangian models be prioritized over Eulerian approaches.

5. Simulating Storm-Associated River Plumes in Southern Lake Michigan: Characterization of Plume Spatiotemporal Scales

5.1. Introduction

Shoreline systems such as beaches and nearshore areas are dynamic and complex environments and can be impacted by both the aquatic and terrestrial ecosystems nearby (Graham et al., 2018; Jones and Lennon, 2015; Lee et al., 2016; Viau et al., 2011; Whitman et al., 2014). These systems are also important for tourism and local economies (Kinzelman, 2009; Klein et al., 2004; Leggett et al., 2014; Nevers and Whitman, 2011; Shaikh, 2012), so their effective management is imperative for the viability of surrounding communities.

Nearshore water quality can be impacted by a variety of influences, including both point- and non-point sources. Point sources of contamination, distinct sources whose locations can be pinpointed, can include rivers and wastewater or stormwater outlets near the shore (Boehm et al., 2002; Garcia-Armisen and Servais, 2007; Huang et al., 2019; Mika et al., 2009). Diffuse sources that are not easily tracked or can be attributed to large areas rather than single locations are deemed non-point sources. These non-point sources can include animals and humans, beach sand, urban and agricultural runoff and wave-induced contamination along the shore (Bernhard and Field, 2000; Lin et al., 2009; Vogel et al., 2016; Wu et al., 2017; Yamahara et al., 2007). The effects of nonpoint sources on water quality can be much more challenging to predict or model, compared to the impacts of point sources. Nevertheless, beaches and other nearshore areas are susceptible to contamination by pathogens of human health concern from both point- and non-point sources.

While recent research has focused on characterizing non-point sources of pollution at beaches and in nearshore areas, the effects of contamination plumes on water quality remain a substantial knowledge gap. While some plume-related research has begun to characterize the effects of sewage releases and river flows on beaches (Bravo et al., 2017; Connolly et al., 1999; Huang et al., 2019; McLellan et al., 2007; Thupaki et al., 2010; Wong et al., 2013), assessments of impacts from plumes associated with large storm events on the nearshore are limited (Nekouee et al., 2015; Wilkinson et al., 2011). Research into the effects of storm-induced plumes on nearshore environments is key to understanding the overall connections between terrestrial and aquatic systems during and after disruptions to typical flow regimes, such those associated with storms. This is especially true given that storm frequency and intensity are predicted to increase in the coming decades, as a result of climate change (IPCC, 2014).

Nearshore areas in the Chicago region, along the southwestern shore of Lake Michigan, may be increasingly sensitive to the effects of storm-induced river plumes, compared to other regions, due to the nature of the region's flow regime. Where the majority of rivers flow out to lakes or oceans under typical flow patterns, the three major rivers in the Chicago area have been engineered to flow away from Lake Michigan unless there is a threat of river flooding (MWRD, 2019; USACE, 2014). Under these circumstances, known as backflow events, infrastructure at the Wilmette Pumping Station (referred to hereafter as "Wilmette"), Chicago River Controlling Works (CRCW) and O'Brien Lock and Dam (referred to hereafter as "O'Brien") (Figure 4-2) engages to reverse the flows of the North Shore Channel, Chicago River and Calumet River, respectively (MWRD, 2019). As a result, the rivers flow into Lake Michigan only during these backflow events. Therefore, the Chicago shoreline is not only impacted by the stormwater from the city that runs off directly to the lake, but also may be susceptible to additional runoff from west of the shore via these backflows and the plumes that they release to the lake (USACE, 2014). Since the nearshore zone in the Chicago area is not typically vulnerable to the contamination associated with the three rivers, the Chicago Park District automatically closes all 24 Lake Michigan beaches in its jurisdiction during backflow events (MWRD, 2019). These beaches remain closed to recreation until water quality samples at representative locations consistently show water that is safe for recreation (*E. coli* concentrations < 2.37 $\log_{10}$(MPN 100 ml^{-1}) or enterococci concentrations < 1000 CCE 100 ml^{-1}) (MWRD, 2019).

A limiting factor for the effective management of Chicago beaches and nearshore zones may be a lack of water quality monitoring during and immediately after the backflow events. Only select beaches are monitored for water quality associated with the backflow event, and they are monitored only after the backflow has ended (MWRD, 2019). Further, sampling for water quality during storms that can produce high waves and strong winds can be dangerous for beach managers or researchers. Hence, regular water quality monitoring at beaches does not resume until conditions are safe again and the beaches reopen for recreation (IDPH, 2018). This can lead to scarce water quality or observational data at beaches during and immediately after backflow events, despite their potential to impact the nearshore considerably (MWRD, 2019).

In the absence of *in situ* observational data surrounding backflow events and their resulting river plumes in Lake Michigan, remotely-sensed data can be useful, but also have their own drawbacks for research and management (Morgan et al., 2020; NASA Goddard Space Flight Center et al., 2008; Vermote, 2015). The same dangerous conditions that limit sampling at beaches can also negatively impact data collected remotely via sensors, by creating conditions that can damage sensors. Aerial and satellite imagery can also be valuable, but only if the data are of sufficient spatial resolution to draw conclusions and if the shoreline in the images is not obstructed by clouds (Song et al., 2004).

In recent years, numerical modeling has become an intriguing alternative to *in situ* data collection, especially in situations where observational data may be difficult to obtain (Huang et al., 2019;

Nekouee et al., 2015). Well-calibrated models can effectively simulate hydrodynamic and water quality conditions given hydrometeorological inputs (Liu et al., 2006; Safaie et al., 2016; Thupaki et al., 2010). These models may then be able to help researchers and managers characterize water quality and hydrological conditions without the need for additional observational data. Numerical models can be especially valuable for simulation of conditions during and after storm events for which sample collection is particularly dangerous. These models may supplement any available data and allow for inferences to be made regarding plume dynamics and contaminant fate and transport (Bravo et al., 2017; Nekouee et al., 2015).

We aimed to apply a validated numerical model that couples hydrodynamic simulation for Lake Michigan with nearshore Lagrangian particle tracking simulation to model the dynamics of river plumes resulting from five backflow events in the Chicago area. Combining the model validated in Chapter 4 with observed river flow data for the five different backflow events, river plumes from the release of stormwater along Chicago's shoreline were simulated. The coupled particle tracking model followed distinct but inert particles throughout the basin as a proxy for conservative tracers in the plumes. Results from the models allowed inferences to be made regarding the spatiotemporal scales at which these plumes impact the nearshore zone in Chicago, showing plume areas of influence in the basin as well as the timing of plume dispersion, growth and contraction. Plume simulations also allowed for the determination of which beaches were likely impacted by the plumes, and when. By evaluating plume dynamics over time, we aimed to draw conclusions about the relative influences of localized wind patterns and larger-scale lake circulation on plume dynamics during and after large storm events. All of these results can help predict plume dynamics and risks to the nearshore zone that may be connected to future backflow events.

5.2. Methods

5.2.1. Study Area and Temporal Context

Models were developed to focus on the Chicago region of southwestern Lake Michigan. The area between the North Shore Channel in Wilmette, IL (42.077°N, 87.681°W) and the Calumet River at the Illinois/Indiana border (41.733°N, 87.529°W) was the main study area for this analysis (Figure 1-2). However, storm-induced plumes were expected to occasionally extend beyond these limits along the shore.

There have been 32 backflow events in the Chicago area between 1985 and 2017, but this work focused on five major events between 2008 and 2017 (Table 5-1). These events were chosen because they represented the five largest backflow events in the region since 2000, in terms of volume of stormwater released to Lake Michigan. Wilmette and CRCW both released stormwater to the lake on all five occasions, while O'Brien released water to the lake in 2008 and 2013 only.

Table 5-1: Timing and volume of stormwater released during five backflow events selected for simulation

Year	Dates of Backflow Event	Locations Releasing Water to Lake Michigan	Total Volume of Water Released (m^3)
2008	September 13 – 16	Wilmette, CRCW, O'Brien	41,825,393.34
2010	July 24	Wilmette, CRCW	24,737,287.48
2011	July 23	Wilmette, CRCW	8,405,506.87
2013	April 18 – 19	Wilmette, CRCW, O'Brien	40,577,721.62
2017	October 14 – 15	Wilmette, CRCW	10,395,497.84

The timing of releases to Lake Michigan during the backflow events varied between the three river outlet locations (Table 5-2). For instance, in both the 2008 and 2013 events, in which the O'Brien outlet released stormwater to the lake, O'Brien began and ended its backflow release later than Wilmette and CRCW.

Table 5-2: Timing of stormwater release from Wilmette, CRCW and O'Brien outlets during five backflow events

Backflow Event	River Outlet	Date/Time of Backflow Start	Date/Time of Backflow End	Backflow Duration (hr)
2008	Wilmette	September 13, 7:00 am	September 16, 8:00 am	73
	CRCW	September 13, 11:00 am	September 15, 1:00 pm	50
	O'Brien	September 13, 6:00 pm	September 16, 2:00 pm	68
2010	Wilmette	July 24, 2:00 am	July 24, 7:00 pm	17
	CRCW	July 24, 2:00 am	July 24, 7:00 pm	17
	O'Brien	N/A	N/A	N/A
2011	Wilmette	July 23, 2:00 am	July 23, 1:00 pm	11
	CRCW	July 23, 3:00 am	July 23, 1:00 pm	10
	O'Brien	N/A	N/A	N/A
2013	Wilmette	April 18, 1:00 am	April 19, 12:00 am	23
	CRCW	April 18, 12:00 am	April 19, 1:00 am	25
	O'Brien	April 18, 5:00 am	April 19, 4:00 am	23
2017	Wilmette	October 14, 1:00 pm	October 15, 9:00 am	20
	CRCW	October 14, 1:00 pm	October 15, 8:00 am	19
	O'Brien	N/A	N/A	N/A

5.2.2. Modeling of Plumes

The model framework used to simulate backflow plumes for 2008, 2010, 2013 and 2017 was selected via the process detailed in Chapter 4. Briefly, a coupled hydrodynamic and Lagrangian particle tracking model was used to simulate plume dynamics associated with the backflow events. This model approach was deemed optimal compared to an Eulerian simulation approach because it tracked discrete particles rather than concentrations of contaminants over time. It also used a fundamentally different approach to calculate dispersion of the particles over time, compared to the Eulerian method (See Chapter 4.2.3 for details on the two approaches). As a result, the plumes simulated using Lagrangian particle tracking were smaller and matched plume observational dimensions from MODIS satellite imagery better than those simulated using the Eulerian model. To focus solely on the plume dynamics, the model simulated a worst-case scenario in which the particles represented conservative tracers that were not subject to decay factors over time.

Backflow-associated plumes were modeled by incorporating river discharge data into a base hydrodynamic model within the Finite Volume Community Ocean Model (FVCOM), to simulate the additional volume of water released during and after the storms. The Lagrangian particle tracking model was then coupled to this hydrodynamic simulation. Previous research has determined that release of at least 100000 particles from a source is likely to ensure a stable and reliable particle concentration solution of the Lagrangian particle tracking model (Zhang and Chen, 2007). While the number of particles to be released is problem- and context-dependent, this 100000-particle value can provide an initial threshold to help guide particle number determination for models. Therefore, the number of particles released at each river outlet varied between the backflow events, in response to the number of hours over which the backflow event occurred at the outlets. For the 2008, 2013 and 2017 backflow events, 5000 particles were released at each of the river outlets when stormwater began to enter the lake. Since the 2010 and 2011 backflow events were shorter in duration (18 hours and 10 – 11 hours, respectively), they required additional particles to be released at the outlets to fulfill the 100000-particle requirement for model stability. As a result, 6000 particles were released per hour at the Wilmette and CRCW outlets during the 2010 backflow event, while 11000 particles were released per hour at Wilmette and CRCW during the 2011 event.

Particles were randomly distributed throughout the outlets' channel cross-sectional areas. After the initialization of the backflow, 5000 additional particles were released to the lake for every hour that each river was releasing water. The movement and spatially-variable concentrations of these particles was tracked in the model for 14 – 25 days after each backflow event began. Model temporal extent depended upon the magnitude of the stormwater release associated with each backflow event, as well as other environmental factors such as wind speed and direction. To account for the different storm magnitudes, plumes associated with smaller events in 2010, 2011 and 2017 were modeled for 14 days, while those associated with the large events in 2008 and 2013 were simulated for 25 days.

5.2.3. Plume Spatiotemporal Scale Assessment

From the results of each backflow event's Lagrangian particle tracking model, plume scale assessment involved creating animations of the plumes over time, calculating maximum plume areas of influence in the nearshore, and developing breakthrough curves for particle concentrations at select beach locations along the shore.

Animations of the plumes were created using Tecplot 360 EX 2018 (Tecplot, Inc., Bellevue, WA USA) to visualize and track the plumes over time (see supplemental files SF-1 – SF-5 for animations). To delineate the plumes, particle concentrations were normalized with respect to the smallest-magnitude maximum concentration between the three river outlets, such that all plumes could be visualized without losing data due to differences in concentration between the three river outlets. A plume's spatial extent was defined as the area encompassing plume concentration contours corresponding to a normalized concentration of 0.01 or greater (concentration of 1% or more of the smallest maximum concentration at the river outlets). These animations directly showed the spatiotemporal scales of the plumes, indicating areas of influence at any given time step within the model. From the animations, images of the plumes at specific time steps could be extracted for use in subsequent quantitative plume surface area evaluation, and alongshore and normal-to-shore distance calculations.

5.2.3.1. Spatial Scales

To calculate maximum areas of influence for the plumes following each backflow event, images from Tecplot were extracted from timesteps where plumes extents were maximized. These images were imported into ArcMap 10.7.1 (ESRI, Redlands, CA USA) and georeferenced to match processed 250 m spatial resolution MODIS-Terra reflectance data for the 555 nm (green visible light) band. This type of georeferencing to the MODIS data along the Chicago shoreline allowed plume areas to be effectively calculated from pixel areas (Figure 5-1a). The green bands of the images were extracted from these georeferenced Tecplot images, to better show the contrast between the plumes and the bulk water of the lake (Figure 5-1b). Pixels in the georeferenced, green bands of the plume images from Tecplot were then reclassified to delineate the plumes (Figure 5-1c), and the number of pixels representing the plumes were counted using the Zonal Histogram feature in ArcMap. The number of pixels representing the plumes was multiplied by the surface area of a pixel to obtain the total surface area of the plumes when their extent was maximized. Alongshore and normal-to-shore extents of the plumes were also directly measured within ArcMap via the Measure tool.

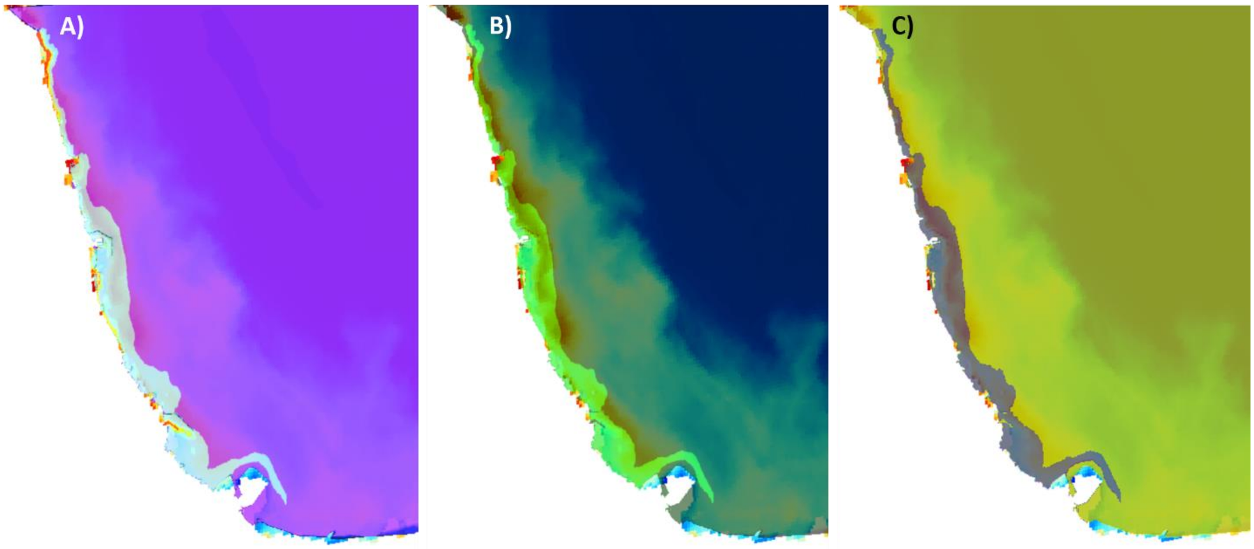

Figure 5-1: Images showing overlays of processed MODIS-Terra data and an original Tecplot plume image (A, left), and extracted green band image of the plume from Tecplot (B, center) and reclassified pixels showing the plume from Tecplot (C, right), showing the process to calculate the plume surface area

5.2.3.2. Temporal Scales

Animations of the backflow-induced river plumes qualitatively showed the spatial and temporal scales of the plumes, but they were supplemented by particle concentration breakthrough curves developed for the water surface at nearby beach locations. Plotting the surface particle concentrations over time at various beaches along the shore was expected to show not only the magnitude of concentrations over time at the beaches, but also the time scales over which each beach was likely impacted by the plumes.

Breakthrough curves were plotted in MATLAB 2019b (MathWorks, Natick, MA USA) for 12 beaches along the Chicago shoreline (See Table 4-1, Figure 5-2). Selected beaches correspond to those locations that are monitored for water quality after backflow events and used to determine when to open all beaches along the shore after storm events. Concentrations for the breakthrough curves were normalized with respect to the lowest magnitude maximum surface concentration at the three river outlets. These curves were generated for each beach during each of the five backflow events. In addition, combined plots showing all breakthrough curves for beaches near a given river outlet were also developed, to lend insight into the direction of travel of the plumes and the order in which different beaches were impacted by the plumes.

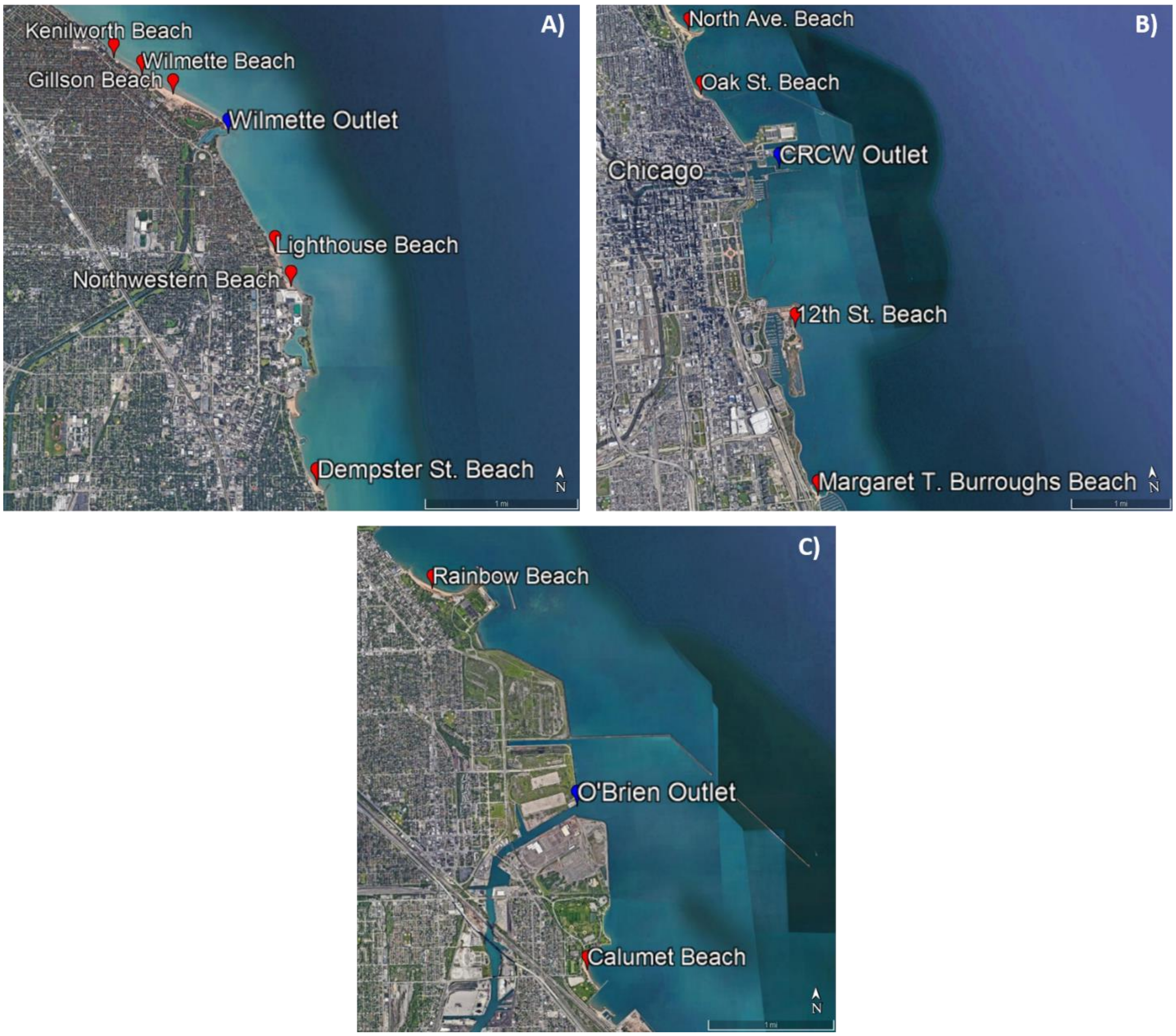

Figure 5-2: Google Earth imagery showing locations of beaches sampled after backflow events from Wilmette (A, top-left), CRCW (B, top-right) and O'Brien (C, bottom) outlets along the Chicago shore of Lake Michigan

5.2.3.3. Relating Stormwater Release Data to Plume Spatiotemporal Scales

Data regarding the time periods and volumes of water released from each of the three outlets were tested to determine their ability to predict the modeled spatiotemporal scales of resulting plumes in southwestern Lake Michigan. RStudio software (RStudio, PBA, Boston, MA) was used to determine Spearman correlations between stormwater release durations and volumes at the Wilmette and CRCW outlets, and plume maximum areas of influence and durations in the nearshore. Additionally, multiple regression analyses and stepwise Akaike Information Criterion (AIC) model selection were used to determine relationships between the release volume and timing data from the outlets and resulting spatiotemporal scales of the storm-induced plumes. In these analyses, statistical significance was determined at the $\alpha = 0.05$ level. Model selection utilized a comparison of AIC, p, and R^2 values between regression models, where the optimal model was signified by a minimized AIC and p-value, and a maximized R^2 value.

5.3. Results and Discussion

5.3.1. 2008 Backflow Event

The largest of the five backflow events simulated occurred in September of 2008. Between September 13th and 16th, 2008, the Wilmette Pumping Station released 11,135,545.84 m^3 of stormwater to Lake Michigan, while CRCW released 20,585,826.36 m^3 and O'Brien Lock and Dam released 10,104,021.13 m^3 (Table 5-3, Figure 5-3). Once released to the lake, plume animations indicate that the plumes initially moved out toward the open water, before moving back toward the shore. Along the shore, the simulated plumes began to move northward late on September 13th, before shifting and moving southward between the afternoon of September 14th and the evening of September 16th (see Supplemental File SF-1 for an animation of the plumes over time). While the plumes were confined to areas relatively close to the shoreline for the first four days of the model simulation, they began to disperse into the basin on September 17th, extending as far as 8.02 km into the nearshore zone at 9:00 am on September 21st. Modeled plumes remained distinct along the shore until 6:00 pm on September 15th, when the plumes from Wilmette and CRCW outlets coalesced near the breakwall north of the CRCW outlet. Two days later, this plume merged with the plume from the O'Brien outlet at 6:00 pm on September 17th, forming a single plume that impacted the entire Chicago shoreline before moving northward again, beginning on September 20th.

Table 5-3: Volume of stormwater released from Wilmette, CRCW and O'Brien outlets during the September 2008 backflow event

Outlet Name	Volume of Water Released in 2008 Backflow Event (m^3)
Wilmette	11,135,545.84
CRCW	20,585,826.36
O'Brien	10,104,021.13
TOTAL:	41,825,393.34

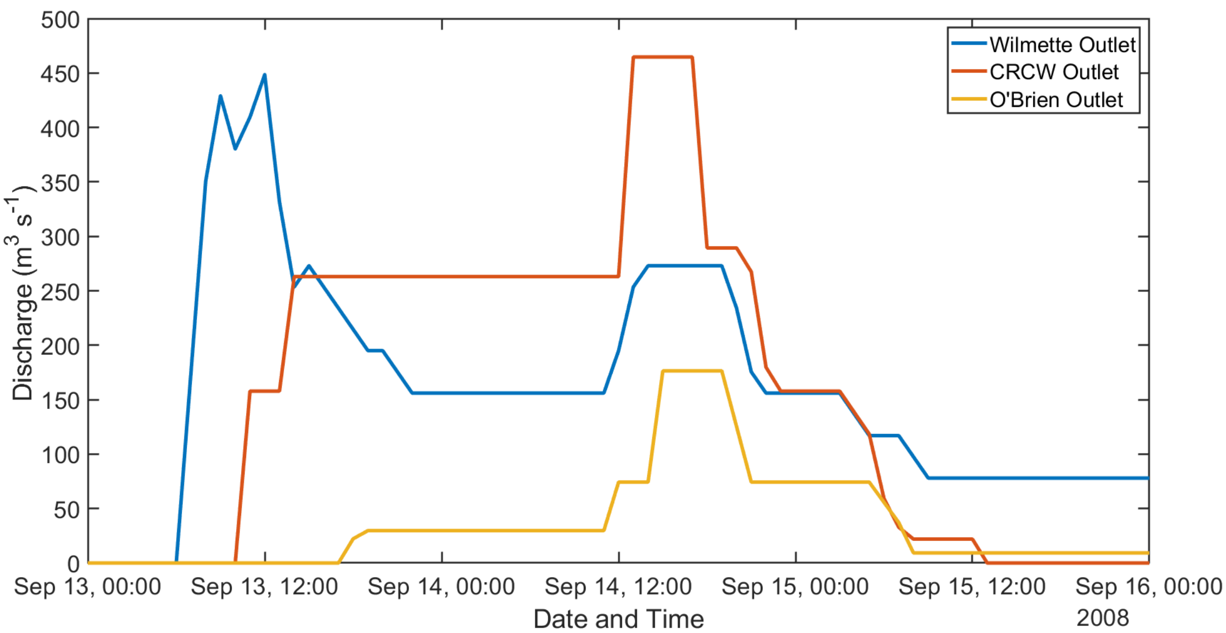

Figure 5-3: Discharge hydrograph showing stormwater releases from Wilmette, CRCW and O'Brien outlets in September 2008

The simulated plume footprint in the nearshore zone was maximized 125, 144 and 119 hours after the cessation of the backflow event at Wilmette, CRCW and O'Brien outlets, respectively, at 9:00 am on September 21st, 2008. This maximized plume footprint was calculated as 291.01 km^2 (Figure 5-4). The simulated plume would be expected to impact 64.06 km of the shoreline, from north of Wilmette to the O'Brien outlet and extending over 8 km offshore in places north of Wilmette.

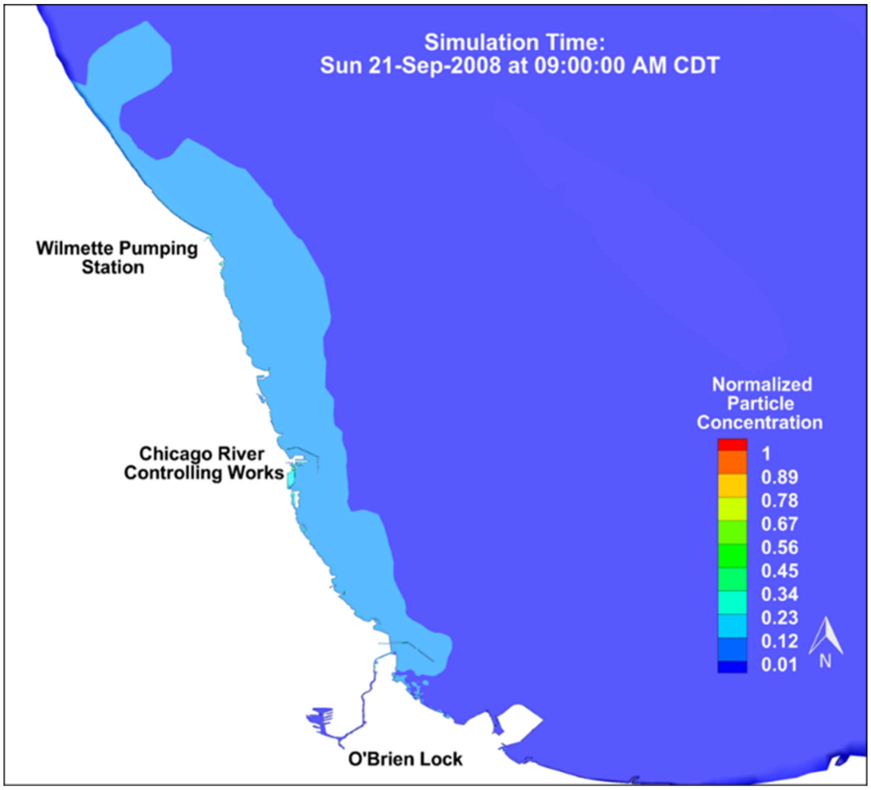

Figure 5-4: Tecplot image of the largest plume resulting from the September 2008 backflow event

Breakthrough curves generated for the 12 beaches that are monitored post-backflow event provide additional insight into plume dynamics and the potential impacts of storm-induced river plumes on beach water quality. Particles from the simulated plume released at the Wilmette outlet reached Gillson, Wilmette and Kenilworth beaches, before being observed at Northwestern, Lighthouse and Dempster St. beaches (Figure 5-5). This supports the inference from plume animations that the plume moved northward shortly after its release, shifting and moving south in subsequent hours. Simulated particles were first observed at Gillson beach at 2:00 pm on September 13th, moving to Wilmette and Kenilworth beaches by 12:00 am on September 14th. To the south of the Wilmette outlet, particles reached Northwestern and Lighthouse beaches at 9:00 am on September 14th and were extended further south to Dempster St. beach three hours later (12:00 pm on September 14th). Higher particle concentrations in the breakthrough curves for Lighthouse, Northwestern and Dempster St. beaches than at Gillson, Wilmette and Kenilworth beaches may be due to the continued release of particles from the Wilmette outlet from September 13 – 16. Additional particles were released at the outlet as the plume moved toward the beaches. It is likely that particles accumulated in the plume between the time that it reached the beaches north of the outlet and when it reached those beaches south of the outlet, leading to higher concentrations at Northwestern, Lighthouse and Dempster St. beaches than at Gillson, Wilmette and Kenilworth beaches.

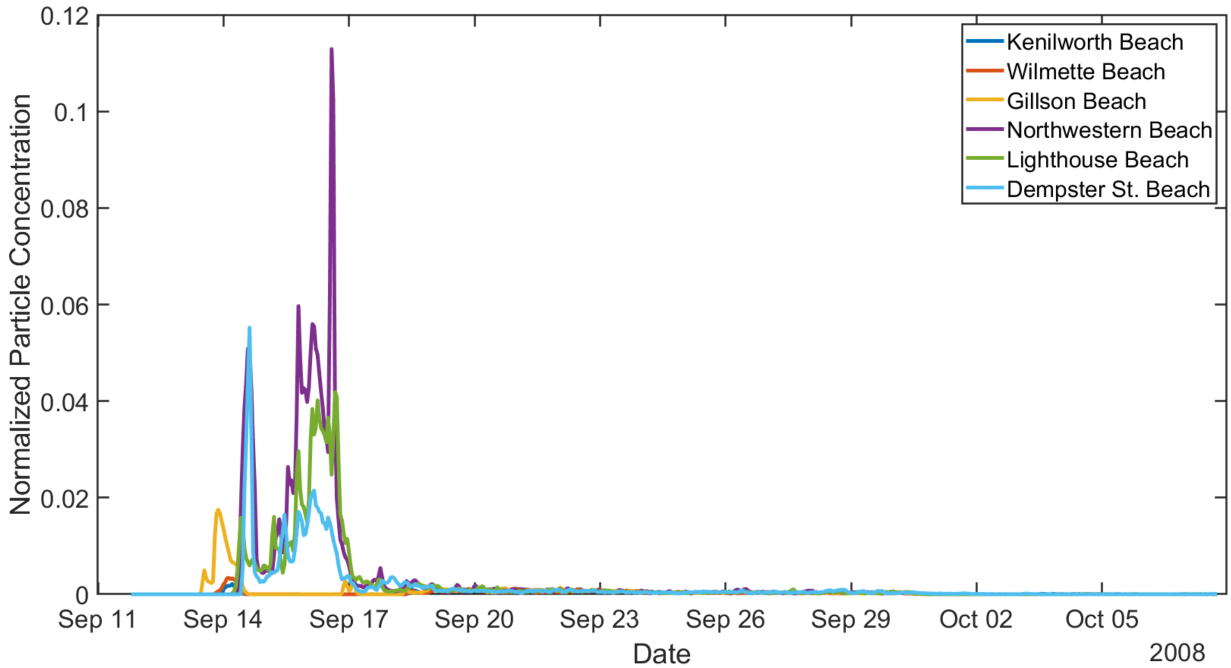

Figure 5-5: Combined breakthrough curves for the 2008 backflow event, showing timing of plume transport from the Wilmette outlet to six nearby beaches

Breakthrough curves developed for North Ave., Oak St., 12th St. and Margaret T. Burroughs beaches near the CRCW outlet indicate a similar trend in plume movement, compared to the breakthrough curves associated with the Wilmette plume. Simulated particles were observed at Oak St. and North Ave. beaches first (on September 13th at 11:00 pm), before the plume shifted its direction of travel and impacted 12th St. and Margaret T. Burroughs beaches south of the CRCW outlet on September 14th at 1:00 pm (Figure 5-6).

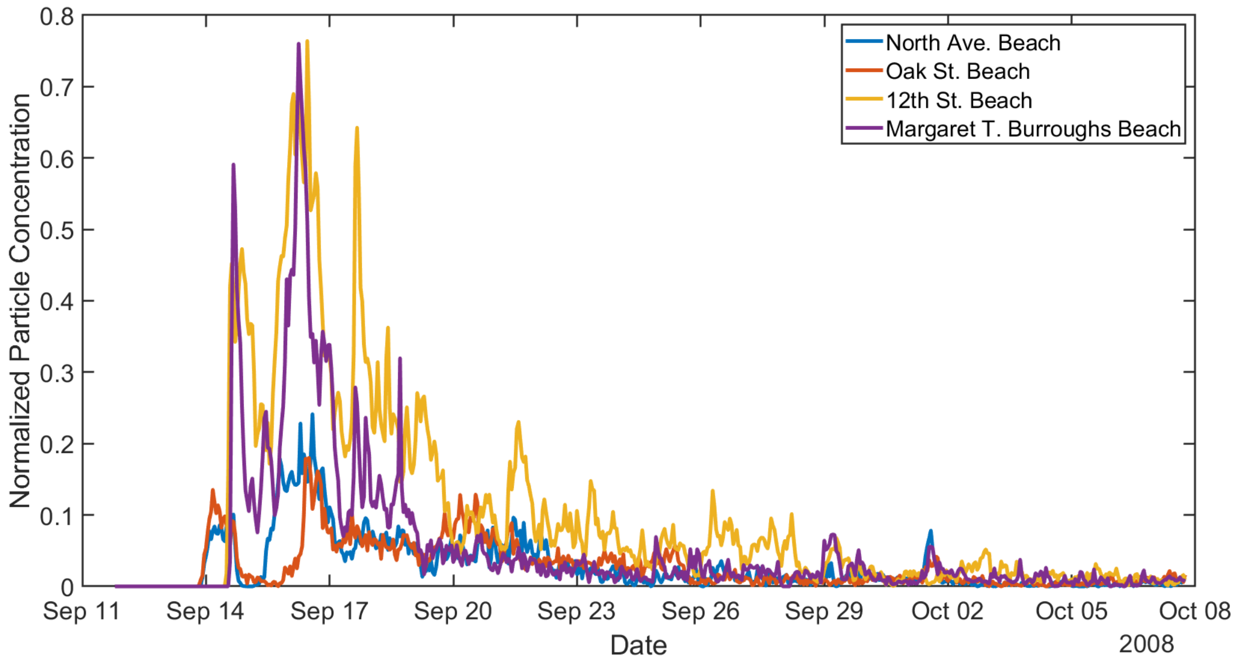

Figure 5-6: Combined breakthrough curves for the 2008 backflow event, showing timing of plume transport from the CRCW outlet to four nearby beaches

In similar fashion to the Wilmette plume breakthrough curves, the curves associated with the CRCW plume suggest that the plume affected most of the nearby beaches as an initial pulse of particles. However, these breakthrough curves show a ~2-day cycle over which particle concentrations peak locally, then decline before increasing to another peak. This pattern is particularly evident for 12th Street beach, the closest beach to the CRCW outlet in the southern direction. The cycle may represent the movement of the plume up and down the shoreline over time in response to lake circulation patterns, as also seen in the plume animations.

Simulation data indicate that the plume associated with the O'Brien outlet was substantially impacted by breakwall infrastructure north and east of the outlet. Particles from the simulated plume were first observed at Calumet beach, south of the outlet, at 1:00 pm on September 14th.

Concentrations of particles reached Rainbow beach 36 hours later (Figure 5-7), after dispersing and moving around the breakwalls north of the outlet. It is interesting to note, also, that the plume animation suggests that the CRCW plume reached Rainbow beach by 11:00 pm on September 15th and that the CRCW and O'Brien plumes had coalesced by the time the particle concentrations increased considerably at Rainbow beach, at 6:00 pm on September 16th. It is difficult to determine whether increased particle concentrations at Rainbow beach at 6:00 pm on September 16th can be attributed to the CRCW or O'Brien plumes.

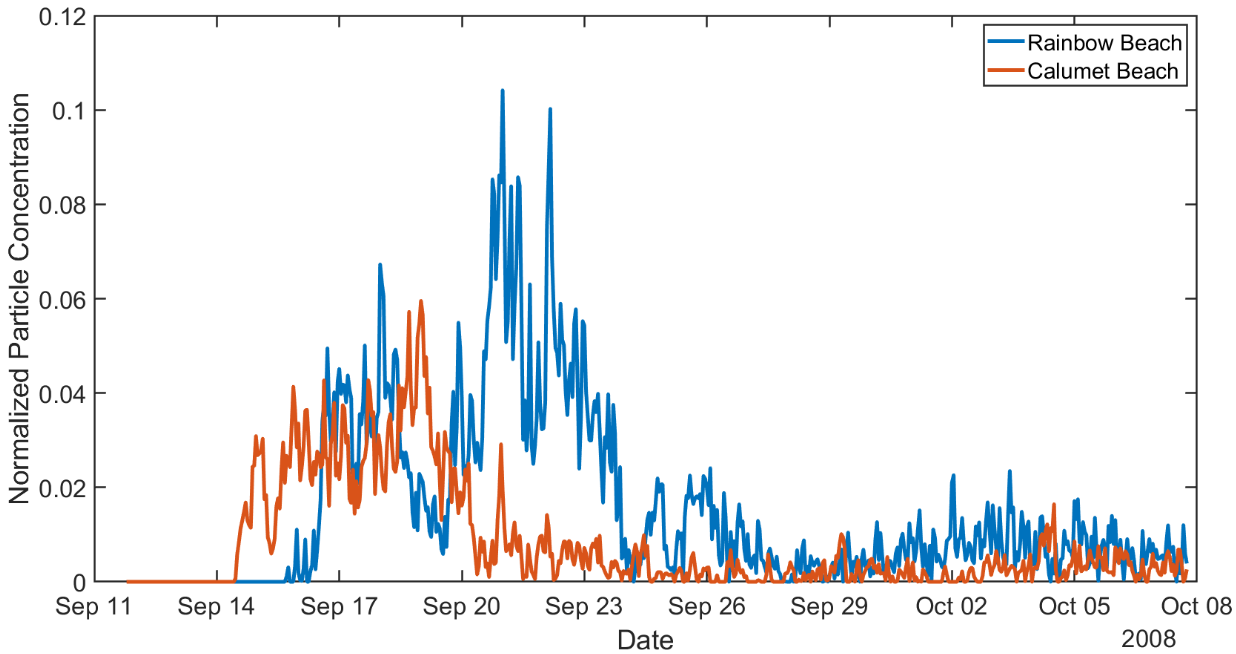

Figure 5-7: Combined breakthrough curves for the 2008 backflow event, showing timing of plume transport from the O'Brien outlet to two nearby beaches

5.3.2. 2010 Backflow Event

The 2010 backflow event released a much smaller volume of water to Lake Michigan, compared to the 2008 event. This event released 24,737,287.48 m^3 of stormwater to the lake from only the Wilmette and CRCW outlets (Table 5-4, Figure 5-8). The CRCW and Wilmette outlets released stormwater on July 24, 2010, from 2:30 am to 7:15 pm. Immediately after release to the lake, simulated plumes flowed away from shore and toward the open water, but over longer time scales, the plumes remained in the nearshore zone and were transported along the shore rather than normal to the shoreline. This follows the pattern seen in the simulation of plumes associated with the 2008 backflow event. After release to the lake, the plumes initially moved northward along the shore on July 24th. Beginning at 7:00 pm on July 24th, the plume dynamics shifted and the plumes began to travel south. This southern plume movement continued until 3:00 pm on July 26th, when the plumes shifted again and began to move north along the shore. Roughly two days later, at 1:00 pm on July 28th, movement of the plumes switched to a southern direction again (see Supplemental File SF-2 for plume animation over time). Because of the smaller volume of water released from both CRCW and Wilmette, the two resulting plumes remained distinct for the entire model simulation period and until they fully dispersed into the lake. The plume released from the CRCW outlet persisted in the nearshore until 8:00 pm on July 26th, while the simulated plume associated with the Wilmette outlet remained visible south of the outlet until 7:00 pm on July 30th.

Table 5-4: Volume of stormwater released from Wilmette and CRCW outlets during the July 2010 backflow event

Outlet Name	Volume of Water Released in 2010 Backflow Event (m^3)
Wilmette	2,840,194.46
CRCW	21,897,093.01
O'Brien	N/A
TOTAL:	24,737,287.48

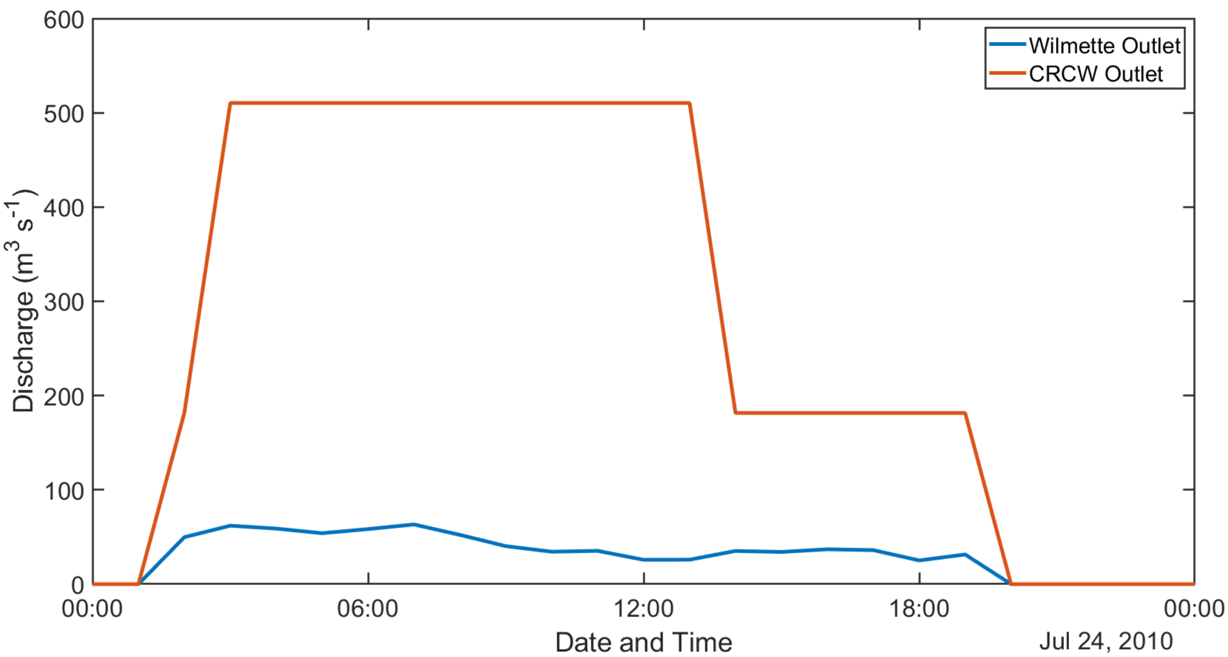

Figure 5-8: Discharge hydrograph showing stormwater releases from Wilmette and CRCW outlets during the July 2010 backflow event

The maximum area of influence of the plumes associated with the 2010 backflow event was considerably smaller than the area of influence connected to the 2008 event, as expected. Plume footprints were maximized after the 2010 backflow event on July 25th at 7:00 am. This was 29 hours after the beginning of the backflow event at both outlets and only 12 hours post-release at both Wilmette and CRCW. Within the nearshore zone, the maximum total surface area of the plumes was calculated as 7.88 km^2 (Figure 5-9).

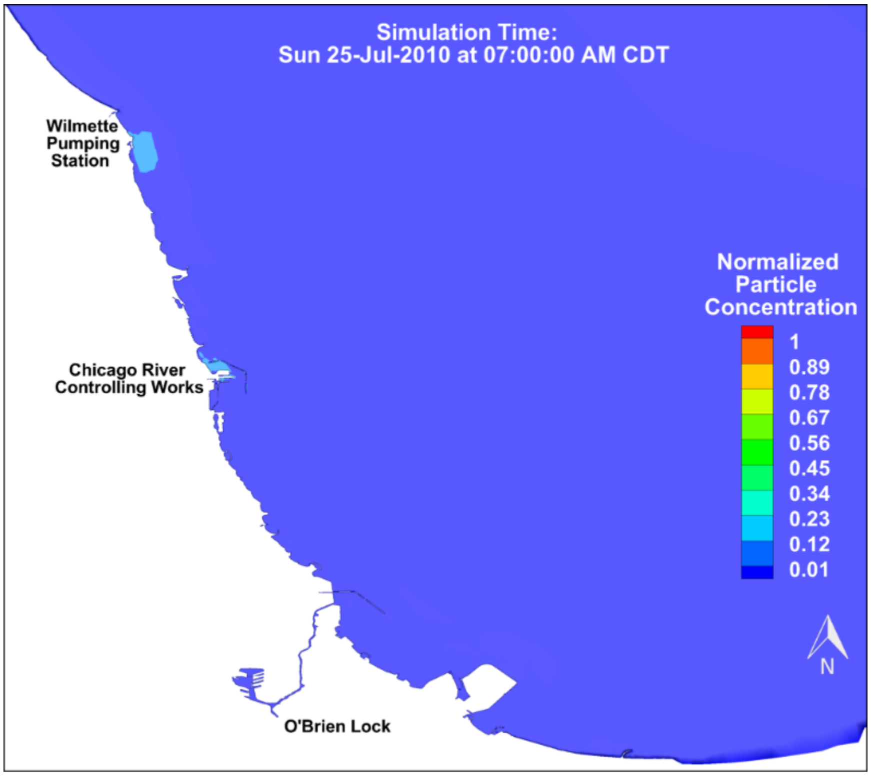

Figure 5-9: Tecplot image of the largest plume resulting from the July 2010 backflow event

Because the O'Brien outlet did not release stormwater during the 2010 backflow event, no particles associated with the plumes reached Rainbow or Calumet beaches. Breakthrough curves generated for the beaches near the Wilmette outlet suggest that particles within the plume were transported to Gillson and Wilmette beaches initially after release to the lake (at 11:00 am and 12:00 pm on July 24th, respectively). However, the plume did not reach Kenilworth beach before shifting direction and moving southward and reaching Lighthouse and Northwestern beaches at 6:00 pm and 8:00 pm on July 24th. Nine hours later, the simulated plume reached Dempster St. beach at 5:00 am on July 25th. After shifting direction again, the plume finally reached Kenilworth beach at 7:00 pm on July 27th (Figure 5-10) (see Supplemental File SF-2 for an animation of the plumes over time). The highest normalized particle concentrations were simulated at Gillson and Lighthouse beaches; the two closest beaches to the Wilmette outlet.

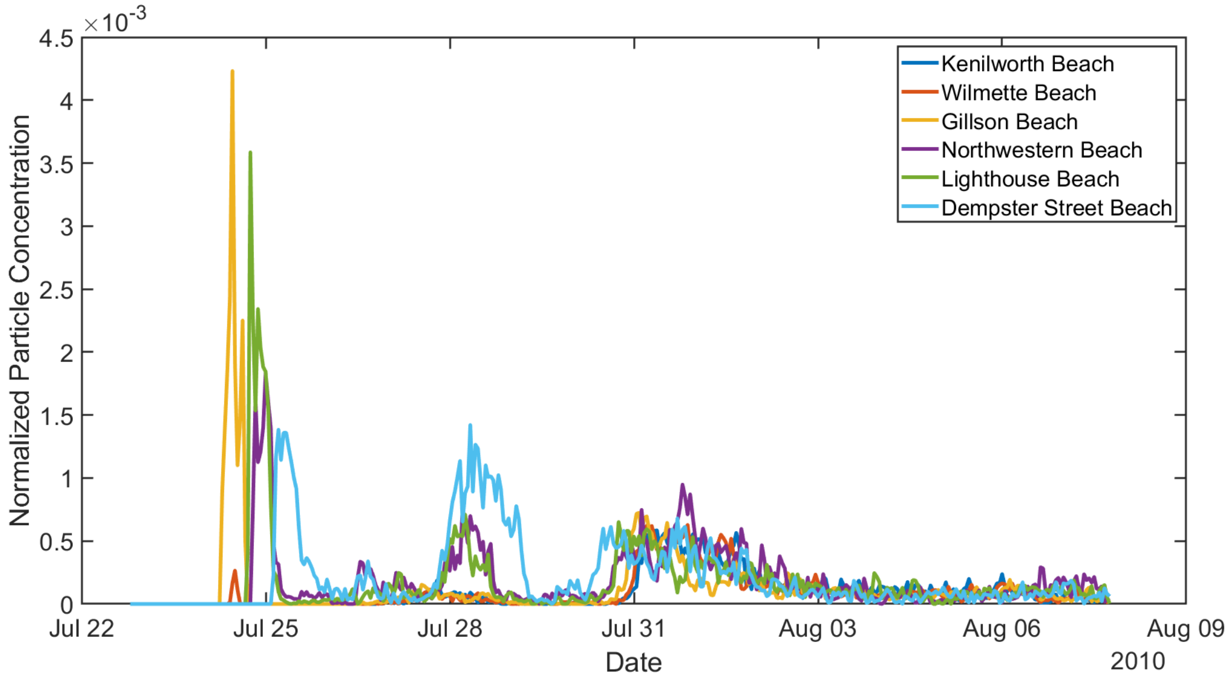

Figure 5-10: Combined breakthrough curves for the 2010 backflow event, showing timing of plume transport from the Wilmette outlet to six nearby beaches

Breakwater infrastructure heavily influenced the spatial and temporal scales of the plume originating from the CRCW outlet in 2010. Breakwaters north and northeast of the outlet inhibited initial flow of the plume toward the north, forcing the plume to disperse near the shore until it could flow around the breakwater. Once it was able to flow around the breakwater infrastructure, the plume moved northward, impacting Oak St. and North Ave. beaches at 11:00 am and 12:00 pm, on July 24th, respectively. After the plume shifted direction and began to move south, it reached 12th St. beach at 9:00 am on July 25th before moving to Margaret T. Burroughs beach at 12:00 pm on July 25th (Figure 5-11).

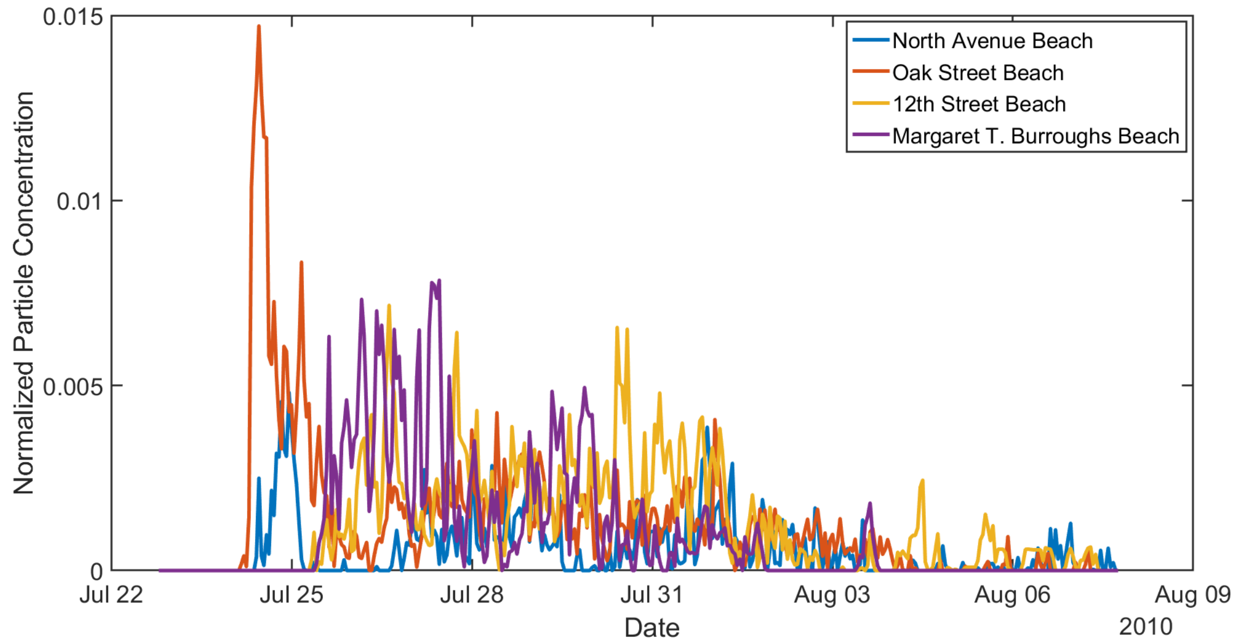

Figure 5-11: Combined breakthrough curves for the 2010 backflow event, showing timing of plume transport from the CRCW outlet to four nearby beaches

Both the CRCW plume and the Wilmette plume were rapidly diluted after their release to Lake Michigan. Normalized particle concentrations at beaches near the CRCW outlet never exceeded 0.015, while normalized concentrations near the Wilmette outlet were on the order of 10^{-3} or less throughout the model simulation period. Therefore, the plumes associated with the 2010 backflow event may not be expected to have impacted beach water quality considerably during this time. However, this would depend on the actual concentration of *E. coli* that the concentrations are normalized with respect to.

5.3.3. 2011 Backflow Event

A relatively small backflow event occurred on July 23rd, 2011. Following the 2010 backflow event, this event led to the release of stormwater to Lake Michigan via the Wilmette and CRCW outlets; there was no need to release stormwater from the O'Brien outlet. The backflow event began at 2:30 am on July 23rd, when the Wilmette Pumping Station began releasing stormwater to the lake.

Stormwater began to flow to the lake from CRCW one hour later. The storm and resulting backflow event were short-lived, with releases to Lake Michigan ending at 1:00 pm on July 23rd (Table 5-5, Figure 5-12). Over the course of the 11-hour backflow event, the two outlets released a total of 8,405,506.87 m^3 of stormwater to the lake.

Table 5-5: Volume of stormwater released from Wilmette and CRCW outlets during the July 2011 backflow event

Outlet Name	Volume of Water Released in 2011 Backflow Event (m^3)
Wilmette	1,908,983.16
CRCW	6,496,523.70
O'Brien	N/A
TOTAL:	8,405,506.87

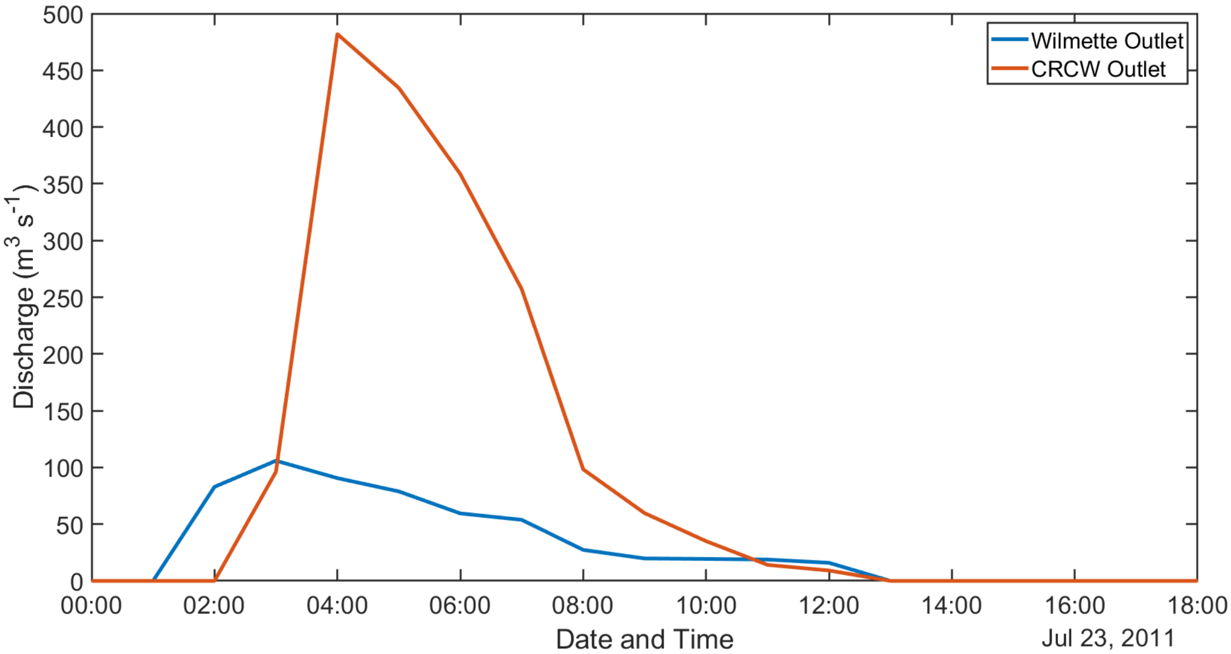

Figure 5-12: Discharge hydrograph showing stormwater releases from Wilmette and CRCW outlets during the July 2011 backflow event

From discharge hydrograph in Figure 5-12, the majority of the water released during the backflow event was released within four hours of the beginning of the backflow. This is supported by data from the National Weather Service, which suggest that the Chicago area received a record 17.42 cm (6.86 inches) of rain between 1:00 and 3:00 am on July 23rd (NOAA National Weather Service, 2011).

After the backflow releases at Wilmette and CRCW ended, the plumes continued to disperse in the basin, growing to a maximum surface area on July 25th at 1:00 pm. This maximum plume surface area occurred 44 hours after the end of the backflow releases from both CRCW and Wilmette outlets, when the plumes were moving northward along the shoreline (Figure 5-13). At this point in time, the footprint of the plumes in the basin was 22.74 km^2, with the largest plume footprint associated with the Wilmette plume and the dispersion of the CRCW plume largely limited by breakwater infrastructure.

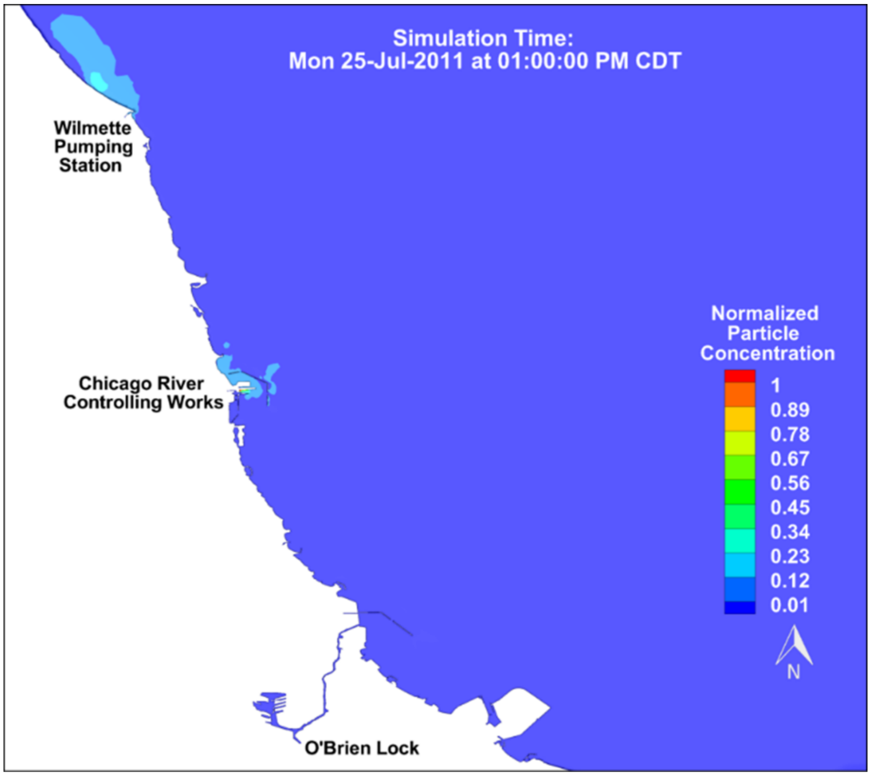

Figure 5-13: Tecplot image of the largest plume resulting from the July 2011 backflow event

Beaches near each river outlet were affected by the 2011 backflow plumes differently. At the Wilmette outlet, Lighthouse and Northwestern beaches were impacted by particles from the plume first, at 4:00 am on July 23rd. Before the plume could reach Dempster St. beach, though, its trajectory switched and it began to move northward. Particles were then modeled at Gillson, Wilmette and Kenilworth beaches at 11:00 pm on July 23rd, 3:00 am on July 24th and 11:00 am on July 24th, respectively. Roughly 12 hours later, the plume began to move southward again, showing elevated particle concentrations at Gillson beach at 1:00 am on July 25th. Increased particle concentrations were then modeled at Lighthouse and Northwestern beaches again at 9:00 am and 10:00 am on July 25th, respectively. The modeled plume then continued to move southward, impacting Dempster St. beach at 3:00 pm on July 25th (Figure 5-14). After roughly July 27th, concentrations at all six beaches declined and stabilized, indicating that the majority of the plume had dispersed into the water column within four days of the backflow event (see Supplemental File SF-3 for an animation of the plumes over time). The maximum normalized particle concentration from the Wilmette plume was modeled at Gillson beach, which stands to reason since Gillson beach is the closest beach to the outlet. However, normalized concentrations across the board are relatively low, suggesting that the beaches may not have been heavily impacted by the plume.

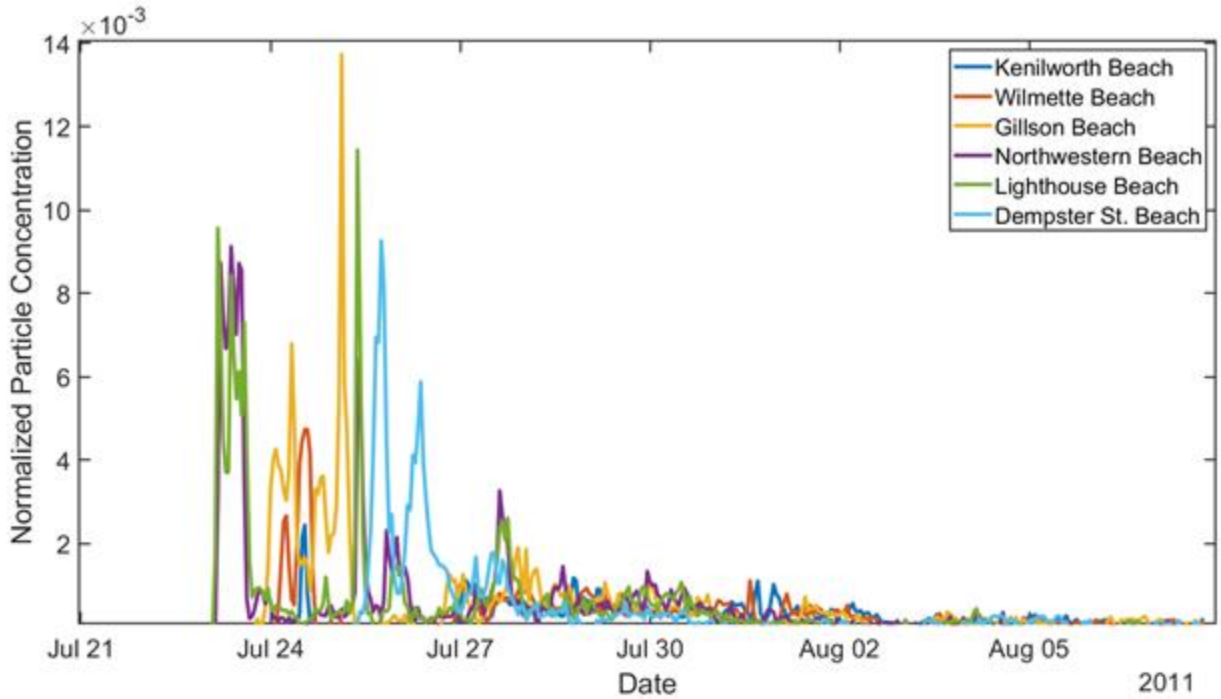

Figure 5-14: Combined breakthrough curves for the 2011 backflow event, showing timing of plume transport from the Wilmette outlet to six nearby beaches

Modeled normalized particle concentrations at beaches near the CRCW outlet were frequently an order of magnitude larger than those normalized concentrations modeled for beaches near the Wilmette outlet. The CRCW-generated plume moved northward initially, with particles reaching Oak St. beach at 6:00 am on July 24th. A very low concentration of particles ($5.20*10^{-4}$) was then modeled at North Ave. beach at 11:00 am on July 24th. 12 hours later, the modeled plume had begun to move southward, with increased normalized particle concentrations modeled at 12th St. beach as early as 11:00 pm on July 24th. Normalized particle concentrations then increased Margaret T. Burroughs beach at 11:00 am on July 25th, before declining. 12th St. beach experienced subsequent increases in modeled particle concentrations at 2:00 am on July 31st and at 12:00 am on August 6th. Margaret T. Burroughs beach saw increased particle concentrations at 11:00 pm on August 5th as well, potentially indicating a 5-day cycle of plume movement along the shore south of the outlet (Figure 5-15). The maximum normalized particle concentration from the CRCW outlet occurred at Oak St. beach, on July 24th at 11:00 pm. Concentrations modeled for Oak St. beach and 12th St. beach are generally higher than those modeled for North Ave. beach and Margaret T. Burroughs beach, likely due to their relative proximity to the outlet.

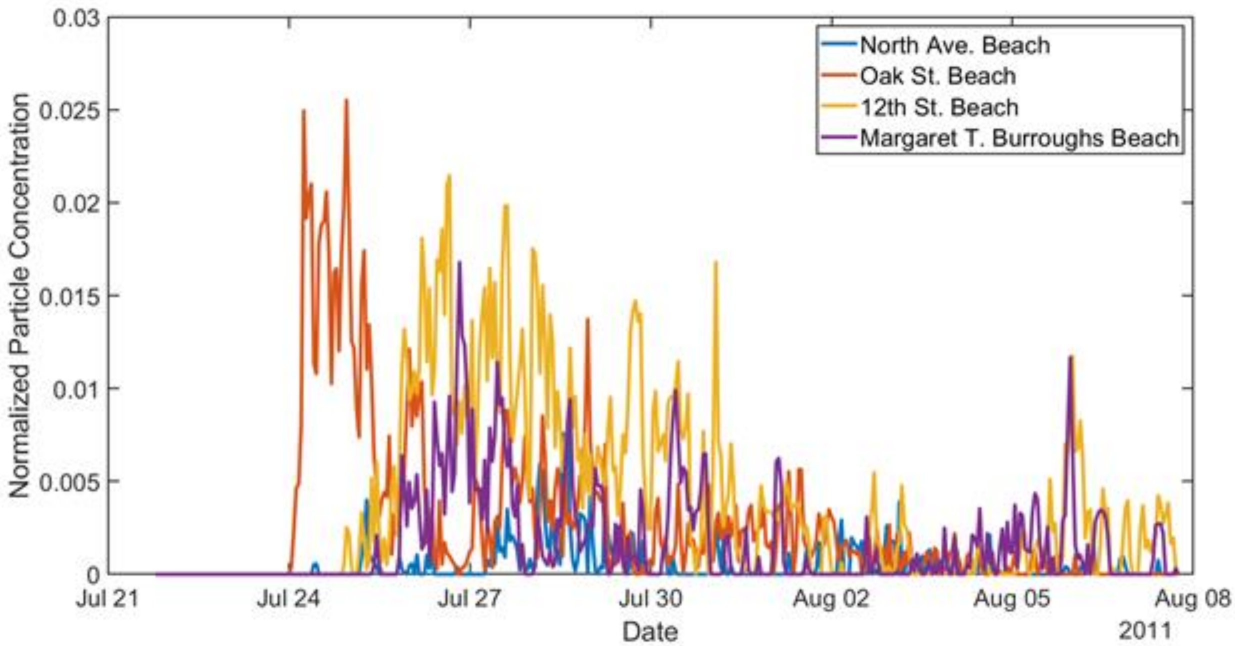

Figure 5-15: Combined breakthrough curves for the 2011 backflow event, showing timing of plume transport from the CRCW outlet to four nearby beaches

5.3.4. 2013 Backflow Event

In April of 2013, a major storm caused a backflow event in Chicago, which led to a backflow release of stormwater from all three river outlets along the shoreline. A total of 40,577,721.62 m^3 of stormwater was discharged to Lake Michigan from Wilmette, CRCW and O'Brien outlets during this event, which began on the morning of April 18th, 2013 and lasted roughly 24 hours (Table 5-6, Figure 5-16). The backflow event began at 12:00 am on April 18th, when CRCW started releasing stormwater. Wilmette began releasing water to the lake at 1:00 am April 18th and O'Brien began backflowing water four hours later, at 5:00 am. The releases at Wilmette and O'Brien each lasted 23 hours, ending at 12:00 am and 4:00 am on April 19th, respectively. At CRCW, the backflow event lasted 25 hours, ending at 1:00 am on April 19th.

Table 5-6: Volume of stormwater released from Wilmette, CRCW and O'Brien outlets during the April 2013 backflow event

Outlet Name	Volume of Water Released in 2013 Backflow Event (m^3)
Wilmette	5,410,110.52
CRCW	23,108,803.32
O'Brien	12,058,807.78
TOTAL:	40,577,721.62

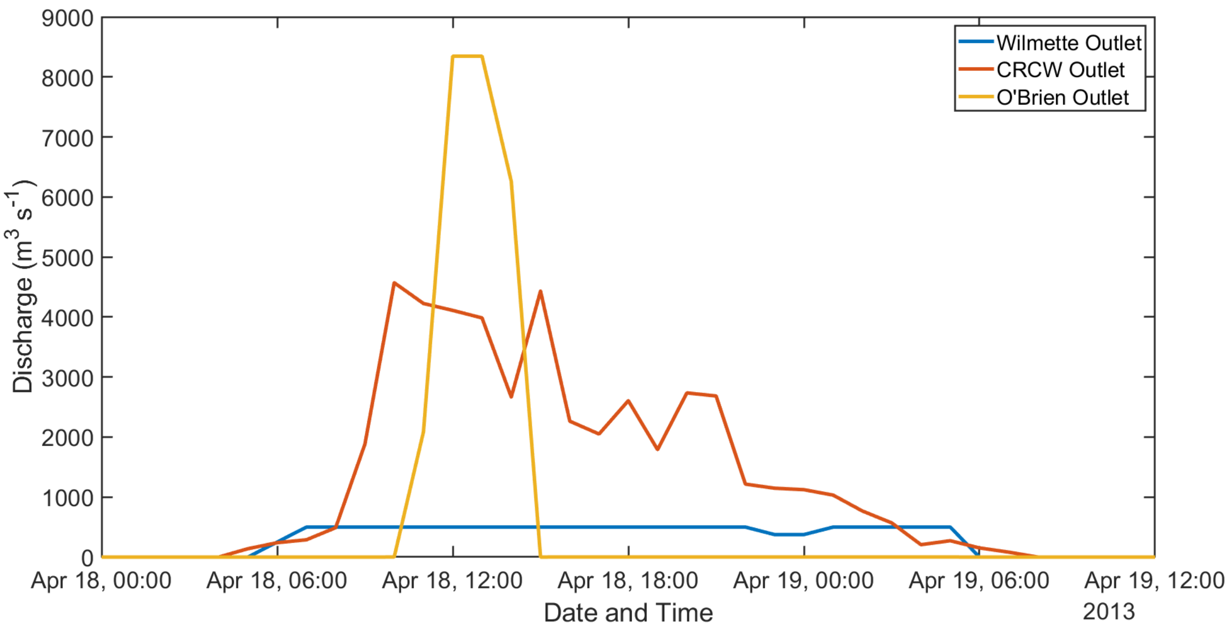

Figure 5-16: Discharge hydrograph showing stormwater releases from Wilmette, CRCW and O'Brien outlets during the April 2013 backflow event

As the plumes from the three outlets dispersed post-backflow, the maximum plume area of influence was simulated at 12:00 am on April 21st. This was 48 hours after the end of the Wilmette release, 47 hours after the end of the CRCW release and 44 hours after the end of the O'Brien release period. The three plumes remained distinct throughout the simulation period, so the resulting area of influence of the three combined plumes at this time measured 96.53 km^2 (Figure 5-17). At this point in time, the largest plume was associated with the CRCW release, as expected due to the volume of water released from CRCW that was at least twice as large in magnitude of those volumes released from Wilmette and O'Brien.

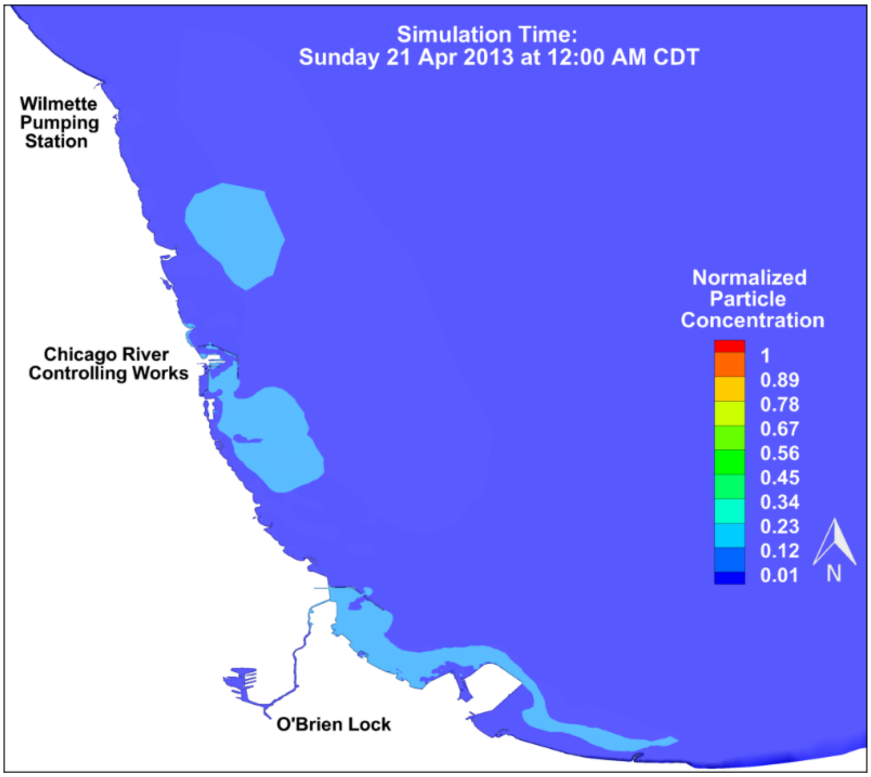

Figure 5-17: Tecplot image of the largest plume resulting from the April 2013 backflow event

Plumes associated with the 2013 backflow event behaved similarly to the plumes associated with the 2008 and 2010 events. Upon release to the lake, all three plumes moved northward initially, before shifting direction and moving southward later (see Supplemental File SF-4 for an animation of the plumes over time). The data from the 2013 backflow event suggest that the plumes changing direction every 1 – 3 days for the first eight days after the backflow event. Starting April 26th, the plumes continuously move northward for five days, changing direction on May 2nd. This shift in direction on May 2nd is the last of the model simulation period, with the plumes continuing to move southward along the shore until they dissipate into the lake. The cycles of plume movement indicate that beaches near the outlets may be impacted by increased particle concentrations every few days within the simulation period. This may be associated with the general circulation pattern within the lake, especially since the plumes seem to move in response to currents in the nearshore zone.

Breakthrough curves corresponding to the plume from the Wilmette outlet show that the plume traveled northward and impacted Wilmette, Gillson and Kenilworth beaches first, after release to Lake Michigan, though it reached all six associated beaches within 11 hours after initially spreading to Wilmette beach at 2:00 am on April 22nd. The plume then began to impact Gillson beach two hours later. By 5:00 am on April 22nd, the plume had traveled further north, to Kenilworth beach before shifting direction and moving southward. At 6:00 am on April 22nd, the plume reached Lighthouse beach, south of the Wilmette outlet and continued moving toward the south, reaching Northwestern and Dempster St. beaches at 7:00 am and 1:00 pm on April 22nd (Figure 5-18). The highest normalized particle concentration (C = 0.085) from the Wilmette plume was simulated at Dempster St. beach at 4:00 am on May 3rd. This and other concentration peaks at Dempster St. beach in the breakthrough curve show an interesting trend, in that they frequently reflect higher normalized concentrations than those simulated at other beaches. Further, these peaks do not always coincide with peaks at nearby Lighthouse or Northwestern beaches. This may indicate that Dempster St. beach was simultaneously impacted by particles from both the Wilmette and CRCW plumes at times in 2013.

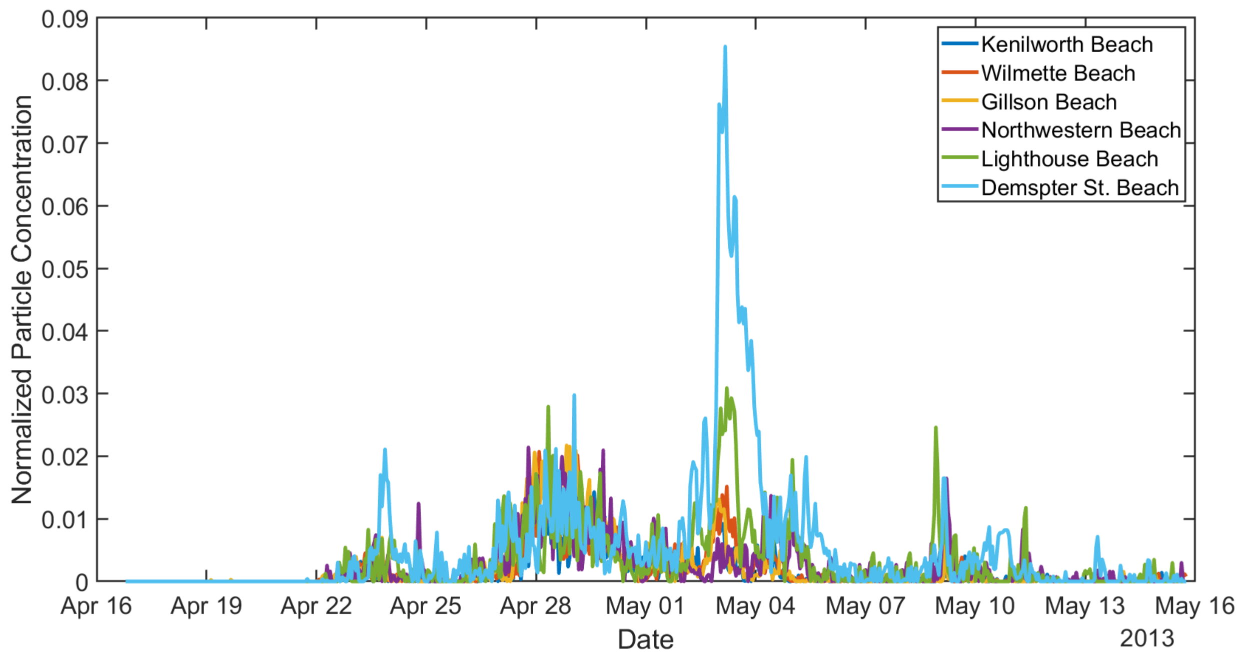

Figure 5-18: Combined breakthrough curves for the 2013 backflow event, showing timing of plume transport from the Wilmette outlet to six nearby beaches

The simulated plume from CRCW also moved northward soon after its release to the lake, following the Wilmette plume's behavior. Upon release, the plume impacted Oak St. beach at 6:00 am on April 18th before moving further north to North Ave. beach at 1:00 am on April 19th. Then, the plume began to change direction, moving southward and impacting 12th St. beach and Margaret T. Burroughs beaches on April 20th at 2:00 pm and April 21st at 2:00 am, respectively (Figure 5-19). Over the following three days, the simulated plume shifted to move northward, extending over much of the shoreline between CRCW and Wilmette outlets by 5:00 am on April 23rd. After moving southward again between April 23rd and 25th, the plume then shifted and move northward once more, extending beyond the Wilmette outlet to the north between April 27th and 29th, when the plume eventually moved north of the study area altogether (see supplemental file SF-4 for animation of the plumes in 2013). Interestingly, the highest magnitude normalized particle concentrations associated with the CRCW plume were simulated at Margaret T. Burroughs and

12^{th} St. beaches (C = 0.074 and 0.073, respectively), which were not the first beaches to be impacted by the plume. However, in similar fashion to Dempster St. beach near the Wilmette outlet, it is possible that the elevated normalized particle concentrations at 12^{th} St. and Margaret T. Burroughs beaches are associated with particle from both the CRCW and O'Brien outlet plumes. The plume animation in SF-4 indicates that both plumes from CRCW and O'Brien extend to both 12^{th} St. and Margaret T. Burroughs beaches during the course of the simulation period, so it is possible that the plumes have a compounding effect on normalized particle concentrations at these beaches.

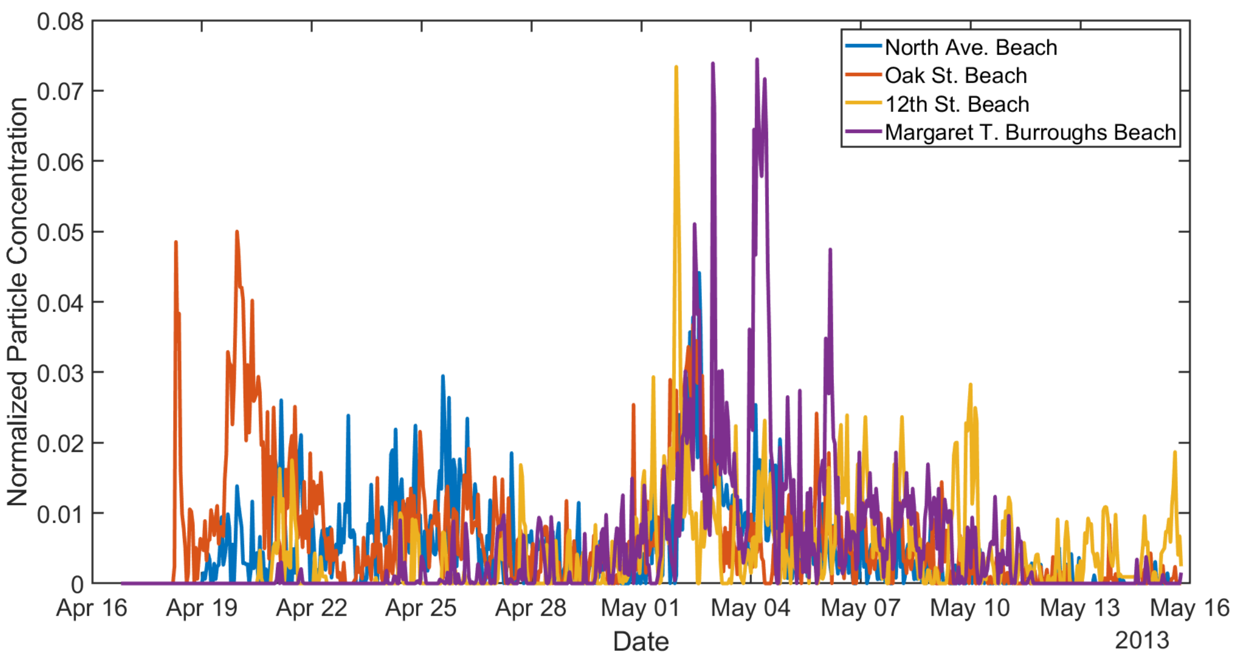

Figure 5-19: Combined breakthrough curves for the 2013 backflow event, showing timing of plume transport from the CRCW outlet to four nearby beaches

Breakwater infrastructure, again, limited much of the movement of the plume associated with the O'Brien outlet, particularly in shorter time periods after the release. These anthropogenic limits to northerly flow led to plume dispersal within the embayment between the Indiana Harbor peninsula and the breakwater infrastructure north of the O'Brien outlet for the first 28 hours after the backflow discharge began at the outlet. As a result, Calumet beach was the first beach near the outlet to see increases in normalized simulated particle concentrations from the plume. Particles from the simulated plume reached Calumet beach at 7:00 pm on April 19th. After these initial impacts on Calumet beach, the plume did not travel northward to Rainbow beach until 11:00 am on April 21st (Figure 5-20). The highest magnitude normalized particle concentration (C = 0.060) was simulated at Calumet beach, the first beach affected by the plume after release. However, the peak normalized particle concentration at Rainbow beach is similar to the normalized concentration at Calumet beach, at C = 0.059. This peak normalized particle concentration at Rainbow beach occurred 14 days after the peak normalized particle concentration at Calumet beach.

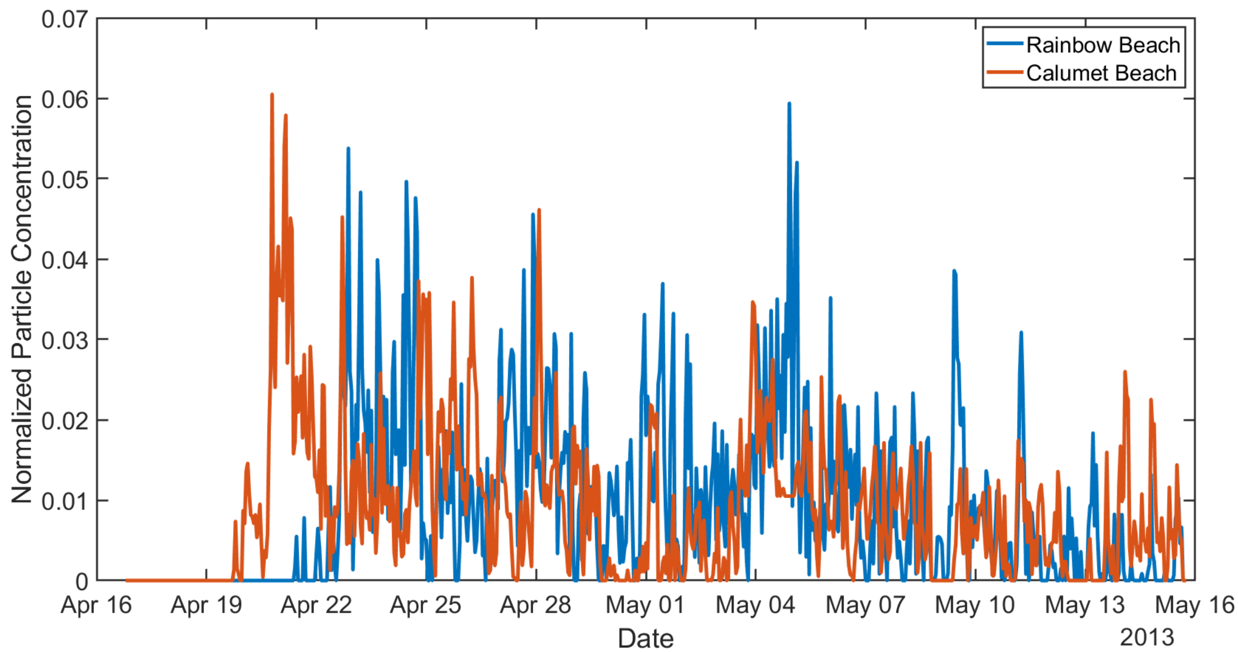

Figure 5-20: Combined breakthrough curves for the 2013 backflow event, showing timing of plume transport from the O'Brien outlet to two nearby beaches

5.3.5. 2017 Backflow Event

The October 2017 backflow event was a smaller storm event in the Chicago area, compared to the 2008, 2010 and 2013 events. Like the 2010 and 2011 backflow events, the 2017 event led to releases from only the Wilmette and CRCW outlets. Both outlets began releasing stormwater to Lake Michigan at 1:00 pm on October 14th. Wilmette's release lasted 20 hours, ending at 9:00 am on October 15th. At CRCW, the release ended one hour earlier, at 8:00 am on October 15th (Figure 5-21). Between the two outlets, 10,395,497.84 m^3 of stormwater to the nearshore of Lake Michigan (Table 5-7).

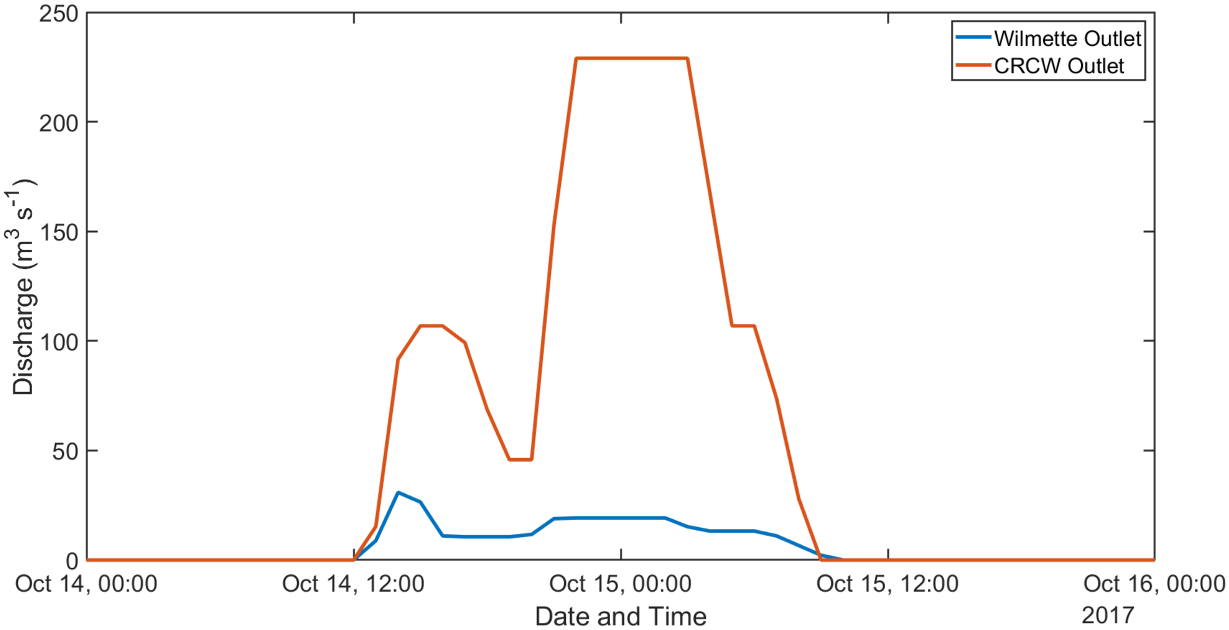

Figure 5-21: Discharge hydrograph showing stormwater releases from Wilmette and CRCW outlets during the October 2017 backflow event

Table 5-7: Volume of stormwater released from Wilmette and CRCW outlets during the October 2017 backflow event

Outlet Name	Volume of Water Released in 2017 Backflow Event (m^3)
Wilmette	1,097,012.34

Table 5-7 (cont'd)

CRCW	9,298,485.51
O'Brien	N/A
TOTAL:	10,395,497.84

Plumes resulting from the releases at Wilmette and CRCW outlets in 2017 coalesced at 11:00 am on October 16th and the single, large plume moved north along the shoreline in the following days, before dispersing into the lake. The maximum combined area of influence of the plumes in the nearshore zone was simulated at 6:00 pm on October 17th, 77 hours after the commencement of the backflow event, 58 hours after CRCW stopped releasing stormwater and 59 hours after Wilmette ended its release. At this point in time, the total surface area of the plumes was 69.76 km^2, with the combined Wilmette and CRCW plume extending 28.86 km from near the Wilmette outlet, though the CRCW outlet to 8.10 km south of the CRCW outlet (Figure 5-22).

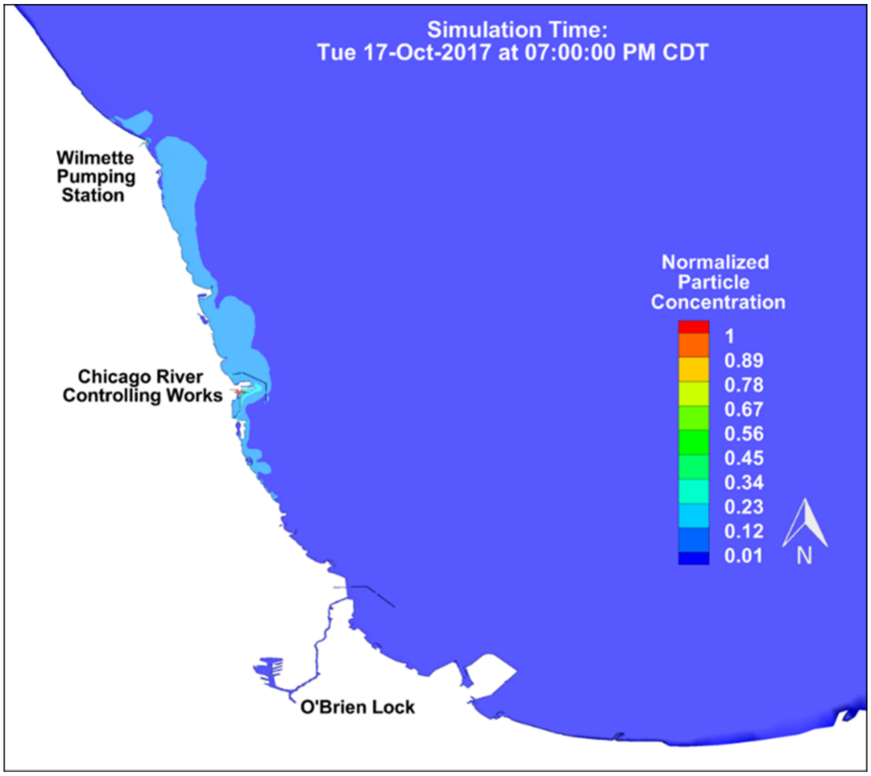

Figure 5-22: Tecplot image of the largest plume resulting from the October 2017 backflow event

Plumes from both Wilmette and CRCW traveled northward upon their release to Lake Michigan, before shifting direction and moving southward 17 hours later on October 15th. This southward movement lasted for 34 hours before the plumes shifted direction again. The plumes moved northward again until October 19th. For a brief period (six hours), the plumes began to move southward, but ultimately shifted once again and moved northward and away from the Chicago shoreline. The plumes moved southward and into the Chicago shoreline area again on October 23rd – 25th and October 27th – 31st before dissipating into the lake late on October 31st (see Supplemental File SF-5 for an animation of the plumes over time). The initial northward movement of the CRCW plume was limited by the breakwater infrastructure north of the outlet in 2017, in similar fashion to the CRCW plumes in 2008, 2010, 2011 and 2013.

Breakthrough curves developed for beaches near the Wilmette outlet indicate that Gillson beach was the first location impacted by the plume, at 4:00 pm on October 14th. Two hours later, the plume reached both Wilmette and Kenilworth beaches. The plume then continued to move northward until 6:00 am on October 15th, when it changed direction and began to move alongshore in a southerly direction. Beaches located south of the Wilmette outlet were impacted by the plume beginning at 8:00 am on October 15th, when the plume reached Lighthouse and Northwestern beaches. Dempster St. beach began to see elevated normalized particle concentrations at 11:00 am 1:00 pm on October 15th (Figure 5-23). Following other plumes, the highest magnitude normalized particle concentration was simulated at Gillson beach, the closest beach to the Wilmette outlet. Interestingly, normalized particle concentrations declined rapidly in this plume; simulated concentrations at Lighthouse, Northwestern and Dempster St. beaches were nearly one order of magnitude lower than those at Gillson, Wilmette and Kenilworth beaches. The shoreline experienced strong currents between October 14th and 16th, so it is possible that those currents fostered substantial dispersion of particles in the lake while also driving the plume toward the beaches south of the outlet. This is also supported by the beach breakthrough curves, which suggest that the beaches were only impacted by particles in the plume once, rather than showing a three-day cycle like those seen in 2013. The curves, compared with the normalized particle concentration threshold of 0.01 to denote a plume suggest that the simulated plume originating from Wilmette was no longer impacting beaches near the Wilmette outlet by October 16th, only two days post-backflow event.

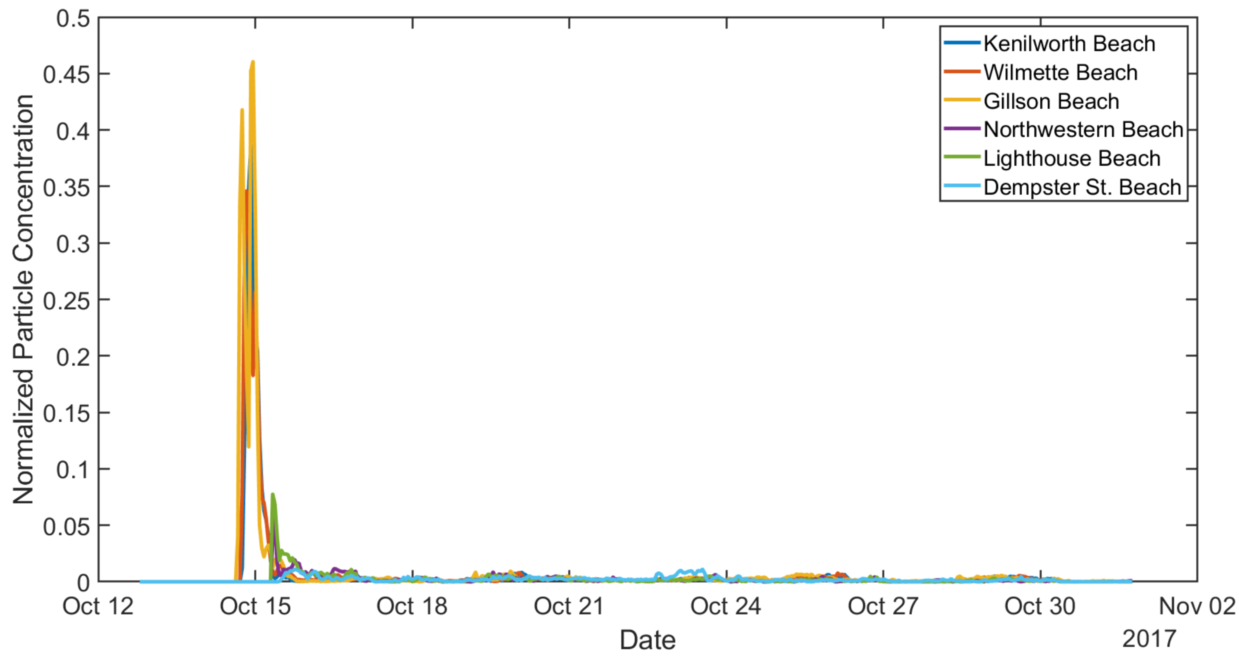

Figure 5-23: Combined breakthrough curves for the 2017 backflow event, showing timing of plume transport from the Wilmette outlet to six nearby beaches

The plume associated with the CRCW outlet follows a similar pattern to the Wilmette plume, initially moving northward before changing direction after its release. The first beach to be impacted by particles from the plume was Oak St. beach, at which increased particle concentrations were initially simulated at 10:00 pm on October 15th. It took the plume 33 hours from its initial release for the plume to move to the shore at Oak St. beach, likely due to the limited ability of the plume to flow around breakwater infrastructure north of the CRCW outlet. This idea is supported by the plume animation (Supplemental File SF-5), which shows that the CRCW-associated plume remains between the shore and the breakwater infrastructure for 14 hours after initial release. The lag in northward movement may have then forced the plume to disperse and begin moving southward before it could reach North Ave. beach, as seen in the breakthrough curve where North Ave. beach was not impacted until after Oak St., 12th St. and Margaret T. Burroughs beaches were affected (Figure 5-24). Particles from the plume reached 12th St. beach at 11:00 pm on October

15th and traveled to Margaret T. Burroughs beach at 4:00 am on October 16th. Later, the plume traveled northward again, reaching North Ave. beach at 5:00 am on October 17th.

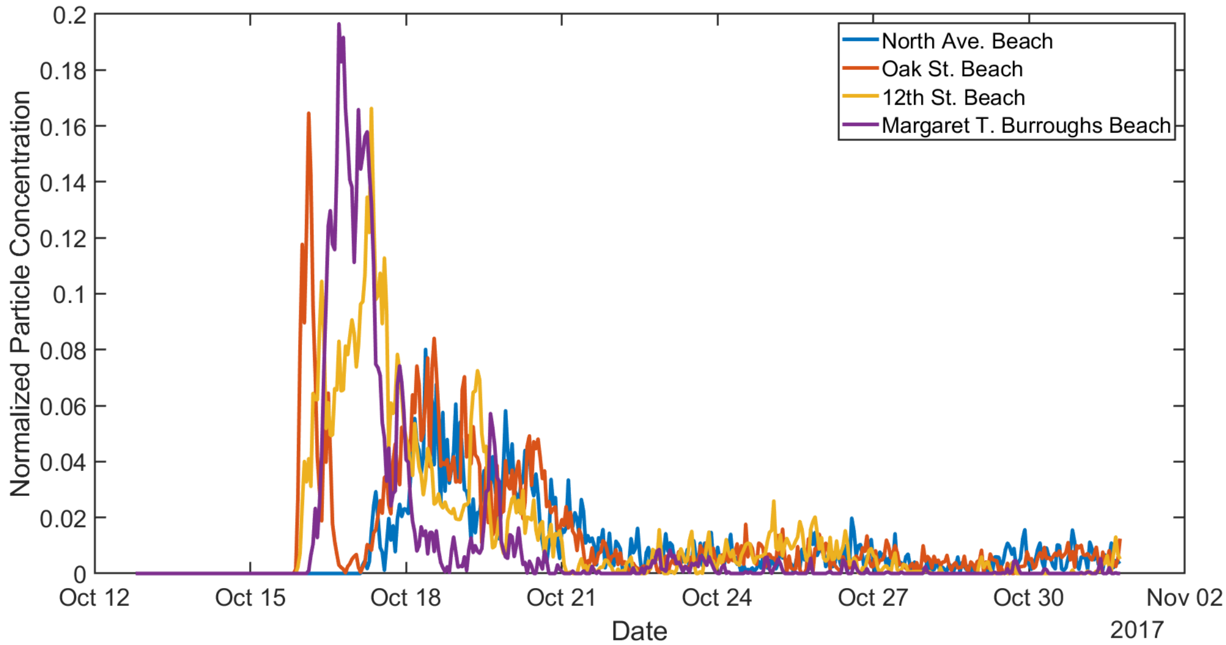

Figure 5-24: Combined breakthrough curves for the 2017 backflow event, showing timing of plume transport from the CRCW outlet to four nearby beaches

Interestingly, the highest normalized particle concentration from the CRCW plume in 2017 was simulated at Margaret T. Burroughs beach on October 16th at 5:00 pm. Margaret T. Burroughs beach is the farthest of the four focal beaches from the CRCW outlet (~6 km distance as the crow flies), so it would not be expected that it would experience the highest normalized particle concentrations. However, Margaret T. Burroughs beach is the only beach facing the direction of the CRCW outlet. It is also the least sheltered of the four beaches as well, with just a small breakwater on its northern edge. Since Oak St. and North Ave. beaches both face away from the CRCW outlet and 12th St beach is embayed and facing the open water of the lake, it is possible that the plume from the CRCW outlet was inhibited in its ability to impact these three beaches. On the other hand, Margaret T. Burroughs beach may be easily affected by the plume because of its orientation and relative lack of embayment, potentially leading to normalized particle concentrations that were higher than at the other three beaches. Wind and currents may also play a role in these types of impacts; higher winds and/or stronger currents may drive plumes to beaches in certain locations relative to the outlets, like Margaret T. Burroughs beach.

5.3.6. Overall Trends in Scale of Backflow Events

The five backflow events simulated are very different, in terms of the volumes of stormwater released, which outlets released stormwater, duration of backflow events and currents driving plumes in the nearshore region, largely due to the action of wind. However, some trends may emerge from assessment of all five events together.

Volume of water released during a backflow event can considerably impact the spatiotemporal scales of resulting plumes (Table 5-8). The 2008 backflow event was the largest of the five events, by both volume and backflow event duration. This event released over 1 million more cubic meters of stormwater than the second-largest event in 2013 and the release lasted roughly twice as long as the 2013 backflow event. Simulated plumes resulting from the events in 2008 and 2013 persisted longer in the nearshore region than those from the smaller events, moving along the shore for up to 24 days post-backflow event commencement. Spatially, the 2008 backflow event was the only event that produced large enough water volumes to make the resulting plumes to coalesce in the nearshore, combining to create a single, large plume impacting the entire Chicago shoreline. This single, combined plume yielded the largest plume area of influence simulated for all five events, at 291.10 km^2. This footprint is nearly three times as large as the 2013 maximum plume footprint. Conversely, the 2010, 2011 and 2017 backflow events released the smallest volumes of water, and simulated plume spatiotemporal scales were the smallest in magnitude. As a result of these events, plumes persisted in the nearshore zone for only days after the events, with 2010, 2011 and 2017 plumes persisting for 5 – 408 hours (0.21 – 17.21 days), post-backflow event. Similarly, the maximum simulated plume areas of influence corresponding to these smaller backflow events are 2.71 – 49.51% of those resulting from the larger events.

Table 5-8: Comparison of backflow magnitude details for five modeled backflow events

Backflow Event	**Duration of Backflow Event (hr)**	**Volume of Water Released (m^3)**	**Maximum Simulated Plume Surface Area/Footprint (km^2)**	**Time Until All Plumes Disperse (hr)**
2008	Wilmette: 73 CRCW: 50 O'Brien: 68	41,825,393.34	291.10	575
2010	Wilmette: 18 CRCW: 17	24,737,287.47	7.88	5
2011	Wilmette: 11 CRCW: 10	8,405,506.87	22.74	192
2013	Wilmette: 23 CRCW: 25 O'Brien: 23	40,577,721.62	96.53	586
2017	Wilmette: 20 CRCW: 19	10,395,497.84	69.76	393

Spatial and temporal scales of plume impacts are largely proportional to the volumes of water released during backflow events. The 2010 backflow event provided an interesting deviation from this trend. Despite releasing a larger volume of stormwater to Lake Michigan than the events in 2011 and 2017, the plumes associated with this event were short-lived in the nearshore zone and the maximum plume footprint was much smaller than those footprints calculated for the other four backflow events. In both 2011 and 2017, plumes' particle concentrations remained ≥ 1% of the maximum concentrations at the river outlets for multiple days. The particle concentrations resulting from the 2011 event were diluted to below the 1% threshold in a matter of hours after the backflow event ended. Similarly, the 2010 backflow event yielded the smallest maximum plume footprint of the three smaller-volume backflow events. The maximum plume surface area of 7.88

km^2 in 2010 was 8.85 times smaller than the maximum plume footprint from the 2017 backflow event and 2.89 times smaller than the maximum plume footprint from the 2011 event. These inter-event patterns may be due to differing wind and current conditions in the nearshore zone between the events.

During the 2010 storm, winds over Lake Michigan (at offshore buoy 45007) did not exceed 10 m s^{-1}, while winds reached 11.7 m s^{-1} in 2011 and 13.3 m s^{-1} in 2017. Larger magnitude winds likely play a role in driving plume movement and may inhibit plume dispersion or settling of particles within the plumes. As a result, it is possible that the plumes associated with the 2010 event were not subject to the wind velocities that would keep the plumes in suspension, leading to relatively fast dispersion and small plume footprints (Kastner et al., 2018). Wind direction may also play a role in the differences in modeled plumes between 2010, 2011 and 2017, as has been previously documented in other water bodies (Choi and Wilkin, 2007; Kastner et al., 2018; Otero et al., 2008). During the 2010 storm event, wind direction at the lake ranged from southerly to west-northwesterly. In 2011, wind directions during the backflow event were largely easterly to southeasterly turning westerly at the end of the backflow release period. Similarly, winds during the 2017 backflow release were easterly to southerly until the final three hours of the backflow, during which winds turned southwesterly. Winds during the 2010 backflow event may have the plumes out to open water rapidly upon release at the outlets. This would lead to smaller maximum plume footprint and a shorter temporal scale of nearshore effects in 2010, compared to 2011 and 2017. Additional research to further solidify a connection between wind speed and direction and plume persistence in the nearshore zone may be beneficial.

Due to inherent connections to wind, plume dynamics are also likely driven by currents in the nearshore zone. Immediately upon release to the lake, many plumes expanded outward, toward the open water of the basin. However, over the scale of hours after their release, the plumes quickly became influenced by currents and circulation patterns near the shore (Beletsky and Schwab, 2001; Beletsky et al, 2006), driving their movement along the shore rather than normal to shore. Similarly, the cycles of plume movement direction seen in simulations of plumes for 2008, 2013 and (to a lesser degree) 2017 backflow events correspond closely with cycles of current movement direction in the nearshore zone (see Supplemental Files SF-6 – SF-10 for animation of the plumes and currents over time). Nearshore currents tend to shift direction on a two- to three-day cycle, potentially driving the cycles of modeled plume movement after backflow events.

Beaches near the river outlets in the Chicago area can be heavily impacted by backflow-induced plumes. Simulated particles reached all 12 beaches that are routinely sampled post-backflow to guide beach reopening after the 2008 and 2013 backflow events, while particles were transported to 10 out of the 12 beaches after the 2010, 2011 and 2017 events. Rainbow and Calumet beaches were not impacted by simulated particles after the 2010, 2011 and 2017 events because of the lack of stormwater release from the O'Brien outlet during these events.

In many cases, the highest magnitude of normalized particle concentrations among beaches near outlets was simulated at the first beaches to be impacted by the plumes. This is reasonable considering that the particles within the plumes were subject to constant dispersion. Over time, more particles could be expected to disperse, leading to smaller concentration magnitudes as the plumes moved from beach to beach along the shore. Similarly, the first beaches to be impacted by the plumes were frequently the closest to the river outlets. Dispersion was further limited by the small relative distances that the plumes traveled to reach those initial beaches, leading to higher normalized particle concentrations than those seen at beaches farther from the outlets.

Overall, beaches nearer to the river outlets were more likely to be impacted by plumes than those beaches farther away from the outlets. In some cases, beaches between river outlets were impacted by two different plumes at different times. For example, beaches between Wilmette and CRCW outlets such as Dempster St., Leone/Loyola (42.010°N, 87.659°W) and Montrose (41.967°N, 87.638°W) beaches were likely impacted by both the Wilmette and CRCW plumes after the 2008 and 2013 backflow events. Similarly, beaches between CRCW and O'Brien outlets such as 12th St., Margaret T. Burroughs, 57th St. or 63rd St. beach (41.783°N, 87.573°W) were likely impacted by particles from both the CRCW and O'Brien plumes in 2008 and 2013, especially after the plumes coalesced.

5.3.7. Implications for Beach Management

Without *in situ* monitoring data at beaches, tracking plume effects in real-time can be challenging for stormwater and beach managers in areas like Chicago. However, the results of these models indicate that there may be correlations between the duration of backflow events, the volume of water released at Wilmette and CRCW outlets, and the maximum footprints and time scales of the plumes in the nearshore. These correlations may be valuable in empowering stormwater and beach managers to predict the extent of plume effects along the shore. With knowledge of the total volume of water released from the outlets as well as the duration of the backflow events, managers may be able to calculate an expected plume footprint and duration of plume effects in the nearshore. Multiple regression analyses were conducted using the data in Table 5-8, to determine empirical relationships that could predict the spatiotemporal scales of the plumes during and immediately after backflow events.

Multiple regression analysis for the prediction of the maximum plume area of influence associated with backflow events indicates that the duration of stormwater release at the Wilmette outlet (hr) (rho = 0.98, p = 0.0036) and CRCW outlet (hr) (rho = 0.98, p = 0.0042) are highly correlated with the resulting maximum plume footprint. Volume of water released from the Wilmette outlet (m^3) was also significantly correlated with maximum plume footprint (rho = 0.93, p = 0.022). Despite these significant correlations, AIC analysis determined that only one of the above factors is needed to maximize the prediction of maximum plume footprint (*footprint*, km^2): duration of stormwater release at the Wilmette outlet (*DurationW*) (Eq. 5-1, AIC = 34.33). This regression equation captures 94.46% of the variability within the plume footprint data and is statistically significant (p = 0.0036) and the addition of other factors decreased the coefficient of determination value and increased the AIC value of the equation by 0.32 – 1.91.

$$footprint = 4.44(DurationW) - 30.30 \tag{5-1}$$

While Eq. 5-1 can be useful for predicting plume footprints for the 2008, 2010, 2011, 2013 and 2017 storm events in Chicago, it is notable that the equation does not include a predictor variable for volume of water discharged, either combined or from individual outlets. Plume footprints are, inherently, related to the volume of stormwater entering the nearshore zone. Therefore, it can be informative to develop a predictive model for plume footprints associated with the recent storm events that includes a measure of the volume of water released during the storm. A regression model that predicts maximum plume footprint and includes a measure of stormwater volume was developed using the same input data as those used to develop Eq. 5-1. The resulting regression equation (Eq. 5-2) incorporates terms corresponding to the duration of the backflow event at the CRCW outlet (*DurationC*) as well as the total volume of stormwater released from CRCW and Wilmette outlets (*VolumeT*). This equation is able to capture 94.06% of the variability in plume footprint data between the storm events (p = 0.03) and yields a similar AIC score to Eq. 5-1, with AIC = 34.65.

$$footprint = 8.39(DurationC) - 1.44 * 10^{-6}(VolumeT) - 69.04 \qquad (5\text{-}2)$$

24-hour antecedent rainfall may be a useful predictor for plume footprints as well, especially in the absence of other backflow volume data. Antecedent rainfall amounts have been established as potential predictors of beach water quality (e.g., Ackerman and Weisberg, 2003; Francy et al., 2013; Ramirez and Gelsey, 2021) due to the impacts of rainfall runoff on plumes and contamination in the nearshore zone. Therefore, it stands to reason that antecedent rainfall may be a predictor of plume footprint in response to backflow events. Incorporating 24-hour antecedent rainfall recorded at Chicago O'Hare International Airport into a predictive multiple linear regression model for backflow plume footprints led to a marginal increase in predictive ability. Eq. 5-3 incorporates duration of the backflow event at CRCW (*DurationC)* and antecedent rainfall (*AntePrec)* and captures 95.6% of the variability in the plume footprint data ($p = 0.02$). The resulting AIC of 33.15 is similar, albeit marginally lower, than the AIC values corresponding to Eq. 5-1 and Eq. 5-2, indicating slightly higher predictive ability, compared to the other multiple linear regression models for predicting plume footprint.

$$footprint = 6.67(DurationC) - 16.94(AntePrec) - 41.15 \qquad (5\text{-}3)$$

Maximum plume footprints predicted from Eq. 5-1 were larger than those simulated via the Lagrangian particle tracking model for storm events in 2011, 2013 and 2017, while they were smaller than the particle tracking model plumes in 2008 and 2010. Equations 5-2 and 5-3 both overpredicted maximum plume footprints for backflow events in 2010 and 2017, while underpredicting footprints for events in 2008, 2011 and 2013. Errors between the regression equation-derived plume footprints and the particle tracking model plume footprints ranged from 2.81 km^2 in 2008 to 37.3 km^2 in 2010. The largest errors between the particle tracking model-derived maximum footprints and those calculated from multiple regression equations correspond to the 2010 backflow event and could be associated with the same relatively unique wind conditions in 2010 that contributed to the small overall footprint. It is possible that the wind conditions that may have driven the plumes out to the open water rapidly were truly unique to the 2010 event, in comparison to the other 4 storm events, which would lead to the lower predictive capacity of the equations for the 2010 backflow event.

Using the same backflow duration and volume data, multiple regression analysis suggests that the backflow duration at the Wilmette outlet can be combined with the backflow duration and volume at the CRCW outlet (*DurationC*, hr and *VolumeC*, m^3, respectively) to predict the temporal scale of plume effects along the Chicago shoreline after heavy storm events (*TimeScale*, hr) (AIC = 49.57, Eq. 5-4). Resulting curve-fitting from the analysis shows that the prediction of the duration of plume effects in the nearshore is less reliable than prediction of plume areas of influence in response to backflow events (Eq. 5-1, 5-2, 5-3). The optimal multiple regression relationship (Eq. 5-4) is not statistically significant at the 0.05 level ($p = 0.36$). Nonetheless, the relationship between maximum plume footprint and duration of plume effects captures 67.64% of the variability in the data.

$$TimeScale = -50.52(DurationW) + 99.91(DurationC) - 2.93 * 10^{-5}(VolumeC) - 136.50 \tag{5-4}$$

In the case of the backflow plume duration data, adding antecedent rainfall data as a predictor did not increase predictive ability of the multiple linear regression model. In fact, the addition of 24-hour antecedent rainfall as a predictor led to an R^2 value of 0.23, indicating that the regression model including antecedent rainfall captures less than half of the variability in the data that Eq. 5-4 captures. Further, the regression model that includes antecedent rainfall is less statistically significant than Eq. 5-4 ($p = 0.54$) and the corresponding AIC value is 53.90, higher than that corresponding to Eq. 5-4. Therefore, inclusion of antecedent rainfall in a multiple regression model for predicting plume duration in the nearshore is not advisable.

The relatively large magnitude of the intercept terms in these relationships, along with the associated AIC, R^2 and p values indicate that the strength of the correlations between variables could be stronger. This may be due to low degrees of freedom in the analyses since the relationships are based on only 5 data points. In spite of the low degrees of freedom used, these equations can still capture a substantial amount of variability in the data across the very different backflow conditions. Thus, the empirical relationships based on mechanistic model results hold promise for prediction of storm-induced river plume effects in the nearshore zone of Chicago. Beach and stormwater managers in the Chicago area can use these relationships, along with stormwater release volume and duration data collected during backflow events, to gain insight into the spatiotemporal scales of the plumes. This knowledge may allow for improved prediction of plume impacts on beach water quality, leading to more targeted beach management in the face of the heavy storm events that are predicted to become more intense and frequent with climate change (IPCC, 2014).

5.4. Conclusions

Heavy storm-induced river plumes released to Lake Michigan were simulated for five backflow events between 2008 and 2017, to characterize the spatiotemporal scales of such plumes and lend insight into how the plumes impact beaches and the nearshore environment. Resulting simulations indicated that the storm-induced river plumes can affect the nearshore region for days to weeks, post-backflow event. Likewise, plumes can move along the nearshore at large scales, with plume maximum areas of influence in the lake between 7.88 km^2 and 291.10 km^2.

Results support the idea that plume spatiotemporal scales are generally proportional to the magnitude of the backflow events themselves, though other environmental factors such as wind direction, speed and fetch have been shown to play a role in plume dynamics (Bravo et al, 2017; Choi and Wilkin, 2007; Kastner et al., 2018; Otero et al., 2008). Events in 2010, 2011 and 2017 were all significantly smaller than events in 2008 and 2013, in terms of volume of water released (USACE, 2014). As a result, their simulated spatial and temporal scales were smaller in magnitude than those from 2008 and 2013.

Beaches along the shore are frequently at risk from contamination in water in the nearshore zone. This is especially concerning in backflow situations, where plumes can transport a variety of contaminants to coastal areas from urban, industrial and agricultural environments in the watershed (Dwight et al., 2002; McCarthy et al., 2012; Packett et al., 2009; Paule-Mercado et al., 2016; Topalcengiz et al., 2017; Walters et al., 2011). However, the impacts of such backflow events on nearshore environments remains poorly understood due to a lack of observational data associated with the often physically-dangerous events. In the absence of observational data for these backflow events, model simulations can provide some initial insight into the spatiotemporal scales and dynamics of storm-associated plumes (Nekouee et al., 2015, Wilkinson et al., 2011). Well-calibrated models of plume dynamics in the nearshore may be a useful alternative to *in situ* data collection in the context of understanding the effects of backflow-associated river plumes and predicting the impacts of future backflow events. Results may also be valuable for effective beach management in the context of increased frequency and intensity of storm events, as predicted under climate change scenarios (IPCC, 2014). Empirical relationships using backflow volume and duration at Wilmette and CRCW outlets as predictors of maximum plume area of influence and temporal scale of influence can help beach managers target monitoring and management efforts along the shore.

The collection of additional *in situ* or remotely-sensed observational data will be beneficial for increasing our understanding of plume dynamics in the nearshore as well as refining models. However, the models presented herein are effective starting points in characterizing the plume dynamics and resulting impacts on the nearshore region of southern Lake Michigan. Results of our model simulations largely support the current management approach of the Chicago Park District and Metropolitan Water Reclamation District, which involves closing all beaches along the shore until the 12 representative beaches indicate acceptable water quality for recreation (MWRD, 2019; USACE, 2014). During and after backflow events, plumes can extend for kilometers along the shore, impacting numerous beaches simultaneously and potentially warranting beach closures or swimming advisories. While smaller events like those in 2010, 2011 and 2017 yield plumes that often do not impact all beaches along the shore at once, resulting plumes do frequently move along the shore, potentially transporting contaminants to beaches over time as they disperse into the water. Therefore, maintaining the current, conservative approach to beach closure during and after backflow events is recommended for effective beach management for public health. As is the case with many other spatiotemporally-variable influences on the nearshore, a single beach management approach for all backflow events may be ineffective. Adaptive management of beaches during and after heavy storms and backflow events may be more useful; using data-driven statistical and numerical models to nowcast the impacts of plumes at beaches can help to determine when and where beaches along the shore should be closed. This can help to balance preserving the safety of beaches for visitors via advisories or closures with maintaining the economic value of opening beaches when they are presumed safe, even if other nearby beaches are not.

6. Simulating Storm-Associated River Plumes in Southern Lake Michigan: Modeling Fate and Transport of Fecal Indicator Organisms in Plumes

6.1. Introduction

Extreme storm events can have substantial impacts on both the natural and built environments. Hurricanes and cyclones can devastate cities, thunderstorms can cut power to homes and tornadoes can destroy infrastructure on large scales (Bouwer, 2019; Marshall, 2002; Padgett et al., 2008; Pistrika and Jonkman, 2010). The effects of these storms can already be overwhelmingly damaging, as seen in the destruction of much of New Orleans, Louisiana as a result of 2005's Hurricane Katrina (Pistrika and Jonkman, 2010). However, both the frequency and intensity of these types of extreme storms are predicted to further increase in response to climate change (IPCC, 2014). As a result, even more damage to both the built and natural environments can be expected due to extreme storm events in the future, potentially posing social and economic threats as well (Gasper et al., 2011). It is imperative that planning for and management of such environments account for these predicted effects, so that infrastructural and natural systems can be resilient to the predicted extreme storm events (Childers et al., 2015; Jabareen, 2013).

Coastal areas are of particular interest in the context of extreme storm effects, due to their susceptibility to both terrestrial and aquatic storm impacts. In coastal areas, storm-related risks can involve physical risks from high waves, rip tides/currents or public health risks associated with water quality degradation (NOAA, 2020c). During and after storm events, water quality degradation in the coastal zone can be associated with combined sewer overflows (CSOs), resuspension of contaminants from sand or sediments and river inputs, including runoff from upstream in the watershed (Eregno et al., 2018; Federigi et al., 2019; USEPA, 2014b). It is assumed that river inputs to coastal zones significantly degrade recreational water quality during and after heavy storm events; this assumption has guided coastal and beach management in areas like southern Lake Michigan. Along the southwestern shore of Lake Michigan, the Chicago Park District (CPD) closes all 24 of the beaches in its jurisdiction in conjunction with extreme storms, assuming that the water quality and physical risks at the beaches exceed thresholds for safe recreation (MWRD, 2019). While this cautious approach to coastal management may be preferable to a less conservative approach for recreation in the face of extreme storms, it is based on a lack of understanding of the dynamics of storm-induced sources of contamination.

There is relatively little knowledge of the dynamics of storm-associated river plumes in the nearshore zone of lakes and oceans, and in turn, their impacts on public health at recreational beaches. Observational data regarding plume footprints/areas of influence and dynamics in the nearshore are scarce, due to concerns about safety of data collection during and after storm events (MWRD, 2019). While researchers have found that agricultural, industrial and urban contaminants can be released to the nearshore via storm-associated river plumes (Dwight et al., 2002; Masoner et al., 2019; Walters et al., 2011), knowledge of what happens to those contaminants upon release remains elusive. Water quality sampling is largely impossible during and immediately after heavy storm events, due to the need for sampling to be conducted in the water during dangerous wind and wave conditions (MWRD, 2019; USEPA, 2010). Remotely-sensed data for storm-induced plume dynamics can also be limited, though. Satellite imagery, for example, is often obstructed by cloud cover during storm events (Song et al., 2004). Some unobstructed satellite imagery can be useful for characterizing plumes generally, but this imagery does not indicate specific contaminants within the plumes without additional post-processing of the data. Other remotely-sensed data such as suspended minerals or dissolved organic carbon content (GLOS et al., 2020;

NOAA, 2020b) are valuable for offshore analysis of water quality contamination, but frequently lack the spatial resolution required for use in the nearshore context.

Potential public health concerns at beaches warrant an expansion of knowledge of storm-induced river plume dynamics and impacts in the nearshore coastal zone. Additional insights into how plumes transport contaminants such as fecal indicator organisms like *E. coli* will be integral to the refinement of effective beach management practices in the face of increasingly frequent and intense storms. This is especially true in a region like southwestern Lake Michigan, where extreme storms create very different conditions for the nearshore zone, compared to non-storm conditions. Along the shoreline of Chicago, the North Shore Channel, Chicago River and Calumet River only release water to Lake Michigan during extreme storm events, in phenomena known as backflow events (MWRD, 2019; USACE, 2014). Under typical flow conditions, the three rivers flow away from Lake Michigan and toward the Mississippi River, so they have minimal impacts on nearshore areas in the lake (ASCE, 2020; Hansen, 2009). However, during extreme storm events that threaten flooding in the city, Chicago's Metropolitan Water Reclamation District (MWRD) can release stormwater back to Lake Michigan via the Wilmette Pumping Station, Chicago River Controlling Works (CRCW) and/or O'Brien Lock and Dam (City of Chicago, 2014; MWRD, 2019). During these events, stormwater plumes and their inherent contaminants are released to a nearshore zone that is typically not impacted by river releases in any form, so backflow events may be expected to create highly degraded water quality at recreational beaches.

Since *in situ* data collection during and immediately after extreme storms is inadvisable, numerical modeling of storm-induced river plumes and their impacts on recreational water quality may be useful to fill the existing knowledge gap. There has been some study of plume modeling in nearshore environments (Huang et al., 2019; Jameel et al., 2018; McCorquodale et al., 2004;

Nekouee et al., 2015a), but much of this work has been limited to characterizing general plume dynamics. Existing models have been shown to effectively track plumes in the water column, but often lack a connection back to public health and recreational water quality. A single model that did track fecal indicator organisms (FIO) in plumes (McCorquodale et al., 2004) utilized an Eulerian water quality model, which has been determined to inadequately simulate plumes in the nearshore in comparison to a Lagrangian model (see Chapter 4 and Nekouee et al., 2015). Additionally, this model tracked coliforms in stormwater plumes; coliforms represent a broad category of FIO that is now rarely used for recreational water quality monitoring (McCorquodale et al., 2004). The development and refinement of a coupled numerical hydrodynamic and Lagrangian particle tracking model to simulate storm-induced river plumes and their impacts on recreational beaches can aid in the understanding of how and when extreme storms impact beaches and public health.

In this work, a coupled hydrodynamic and Lagrangian particle tracking model (see Chapter 5) was expanded to simulate microbial fate and transport in storm-induced river plumes released to southwestern Lake Michigan during extreme storm events. *E. coli* concentrations at three river outlets near Chicago were estimated using a discharge-concentration relationship previously developed for southern Lake Michigan (Safaie et al., 2016b). These concentrations were used to initialize particles released from each river outlet during the backflow periods, yielding proxy values for *E. coli* concentrations which served as the boundary conditions for the Lagrangian *E. coli* fate and transport model. Estimated river mouth *E. coli* concentrations used as boundary conditions to the nearshore transport model were then subjected to components of a typical microbial decay function (see Chapter 2) to simulate decay and compute estimated *E. coli* concentrations in the plumes over time. Model results will not only indicate plume dynamics in the nearshore environment of southwestern Lake Michigan but will also draw connections between plume dynamics and the fate and transport of contaminants within the plumes. Estimated *E. coli* concentrations at nearby beaches over time will lend insight into the spatiotemporal dynamics of microbial contamination in storm-induced river plumes. This would be valuable to beach managers in terms of allowing for more targeted management of beaches that can protect public health while permitting recreation when and where water is expected to be reasonably safe.

6.2. Methods

6.2.1. Study Area and Temporal Context

Storm-induced river plumes were simulated and tracked within the southwestern basin of Lake Michigan. Along the southwestern shore of the lake, the Chicago Park District (CPD) manages 24 recreational beaches, along 41.84 km of lakefront (Figure 6-1). All 24 of these beaches are situated between the Wilmette Pumping Station to the north and the O'Brien Lock and Dam to the south. The Chicago River outlet at the Chicago River Controlling Works (CRCW) is located in the city center, roughly halfway between the Wilmette and O'Brien outlets. Because of their relative proximities to multiple river outlets, all 24 of these beaches may be susceptible to contamination from stormwater releases during and after extreme storm events. *E. coli* concentrations were modeled for all 24 CPD recreational beaches.

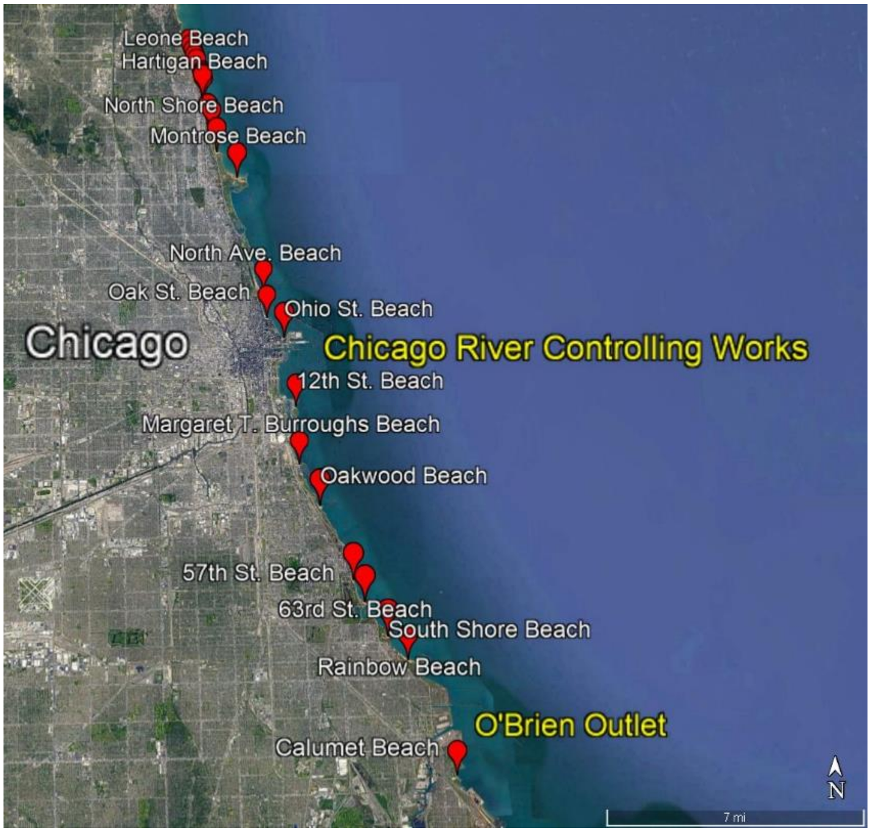

Figure 6-1: Locations of the 24 beaches managed by the Chicago Park District and two of the three river outlets, along the southwestern shore of Lake Michigan. Imagery source: Google Earth

Extreme storm events that result in backflows are relatively rare in Chicago, occurring an average of once per year between 1985 and 2017. Conditions within the city, downstream flood conditions, storm duration, magnitude of rainfall and capacity of stormwater distribution system infrastructure all determine whether a given storm will demand a backflow event (Duncker and Johnson, 2016). Therefore, there is no specific return period or rainfall volume threshold for necessitating release of stormwater to Lake Michigan. Since 1985, storms with return periods of two months to 100 years and durations of 24 to 74 hours have caused backflow events in Chicago (NOAA and NWS 2020).

The two largest backflow events that occurred during the swimming season since 2000 were chosen for modeling of plumes and effects on recreational water quality at CPD beaches. These events are associated with storms in July of 2010 and July of 2011. The storm in 2010 constituted a 25-year, 72-hour storm event, while the 2011 storm was a 100-year, 24-hour event (NOAA and NWS, 2020). Volumes of stormwater released during these events ranged from 8,405,506.87 m^3 in 2011 to 24,737,287.48 m^3 in 2010 (Table 5-1) and the duration of stormwater release ranged from 10 hours at CRCW in 2011 to 17 hours at both CRCW and Wilmette Pumping Station in 2010 (Table 5-2). Neither of these backflow events involved stormwater release from the O'Brien Lock and Dam outlet. However, the events that did involve releases from all three outlets did not take place during the recreational swimming season and thus it is impossible to validate model results against *in situ E. coli* monitoring data for them. As a result, other backflow events that incorporated stormwater release from all three outlets are beyond the scope of this work.

Base hydrodynamic models for Lake Michigan were developed for the years of each backflow event, beginning on January 1st of 2010 and 2011. These models allowed for adequate model calibration and spin-up time, leading to maximally reliable simulations of hydrodynamics in the lake during the backflow events. To model the plumes themselves, hydrodynamic and Lagrangian particle tracking models were coupled and run beginning at 12:00 am on the days that the backflow events began at the river outlets. Models associated with the 2010 and 2011 backflow events simulated for 15 and 16 days, respectively, assuming that the plumes would dissipate into the lake after roughly two weeks (Table 6-1).

Table 6-1: Timing of model simulation periods associated with each of five backflow events, 2000 - 2017

Backflow Year	Start of Hydrodynamic Model	Start of Particle Tracking Model	End of hydrodynamic and Particle Tracking Models
2010	January 1, 2010	July 24, 2010	August 8, 2008
2011	January 1, 2011	July 23, 2011	August 8, 2011

6.2.2. Coupled Hydrodynamic and Lagrangian Particle Tracking Model

A modeling framework that couples a whole-lake hydrodynamic model for Lake Michigan with a near-field Lagrangian particle tracking model for the Chicago shoreline was used to track river plumes and *E. coli* in response to backflows from extreme storm events. These models were developed and run within the larger Finite Volume Community Ocean Model (FVCOM). This unstructured-grid, finite-volume, fully-three-dimensional model takes hydrometeorological and bathymetric data as input. The model then uses primitive equations for calculation of momentum, continuity, temperature, salinity and density across mesh elements and nodes within the model spatiotemporal domain. Additional details regarding the modeling framework and primitive equations can be found in Chapter 2.

Hydrodynamics within the lake were modeled using the optimal turbulent Prandtl number (Pr_t) combination determined from Chapter 3, with a horizontal turbulent Prandtl number ($Pr_{t,H}$) of 0.14 and a vertical turbulent Prandtl number ($Pr_{t,V}$) of 0.1. As discussed in Chapter 3, for modeling frameworks that focus on fate and transport of a contaminant such as *E. coli,* the turbulent Schmidt number Sc_t replaces the turbulent Prandtl number. The turbulent Schmidt number and turbulent Prandtl number are defined similarly as the ratio of eddy viscosity to eddy diffusivity in the context of heat (turbulent Prandtl number) and solute transport (turbulent Schmidt number) (Donzis et al., 2014; Graf and Cellino, 2002; Gualtieri et al., 2017; Rauen et al., 2012). Thus, within the FVCOM framework the turbulent Schmidt number is assumed to be equal to the turbulent Prandtl number, with diffusion coefficient of solute transport equal to that of thermal diffusion (Chen et al., 2006).

Simulation of the storm-associated river plumes was conducted via a Lagrangian particle tracking model developed for FVCOM. Following the recommendations from Chapter 4, the Lagrangian particle tracking model was determined to be the optimal approach for re-creating plumes within the nearshore, compared to Eulerian modeling frameworks. This approach took the results of the hydrodynamic model and combined them with initial positions of discrete particles at the river outlets to track the particles' positions over time, given contemporaneous hydrodynamics. It also uses the Lagrangian formulation to calculate particle dispersion in the water column, as opposed to using the Eulerian formulation to calculate tracer concentration dispersion (see Chapter 4 for additional details). This leads to simulation of tighter plumes than the Eulerian formulation, and these condensed plumes have been shown to better represent available plume observations than those generated by the Eulerian formulation that tend to exhibit numerical dispersion artifacts. The results of this coupled hydrodynamic and Lagrangrian particle tracking model are temporally-variable individual particle locations as well as particle concentrations calculated for each node in the model domain. Particle concentrations can then be related to *E. coli* concentrations at any location within the model, allowing for evaluation of water quality at all of the beaches over time.

6.2.3. Boundary Conditions and FIO Estimation at River Outlets

Simulation of plumes in the models relied upon the use of river discharge (Q) at the river outlets. These discharge boundary conditions were incorporated into the hydrodynamics model, via the use of the rivers module within FVCOM. Hourly averaged discharge data from Chicago's Metropolitan Water Reclamation District (MWRD) were input as part of river initialization files for the models (see Appendices B-2 and B-3 for data). The discharge was assumed to be uniform over the depth of the water at the locations of the Wilmette Pumping Station, CRCW and O'Brien Lock and Dam infrastructure and was only variable over time and between outlets. When the river outlets were not actively releasing stormwater during a backflow event, Q at the outlets was assumed to be zero.

Setting up the model to simulate *E. coli* in storm-induced river plumes involved releasing particles at each of the river outlets for the duration of each backflow event. The number of particles released at each outlet and at any timestep was estimated from the discharge (Q) at the outlet, because contaminant concentrations have been shown to be related to discharge in southern Lake Michigan (Safaie et al., 2016b). This procedure was necessary because the model used small time steps but high-resolution *E. coli* observations at the river outlets matching the model's temporal resolution were not available. Following Safaie et al. (2016), cumulative distribution functions (CDFs) were fitted for logistic distributions of Q data at the river outlets. Fitted distributions yielded parameters μ and s to denote the mean and a scale factor for the data, respectively. A similar cumulative log-logistic distribution function was created for *E. coli* data collected at Burns Ditch river outlet in southern Lake Michigan. New CDFs were developed for discharge at each outlet and during each backflow event, resulting in eight different CDFs for Q. Comparison of the CDFs for the Q and *E. coli* concentration data formed the basis for the assumption that *E. coli* concentrations at the river outlets could be estimated from the Q data (Figure 6-2). CDFs for the z-scores of both Q and *E. coli* concentration match well, indicating that they are related and that the estimation of *E. coli* concentrations at the three Chicago River outlets is likely valid. Similar relations between discharge and *E. coli* concentrations at river outlets were used to drive numerical models in previous work (Bravo et al., 2017)

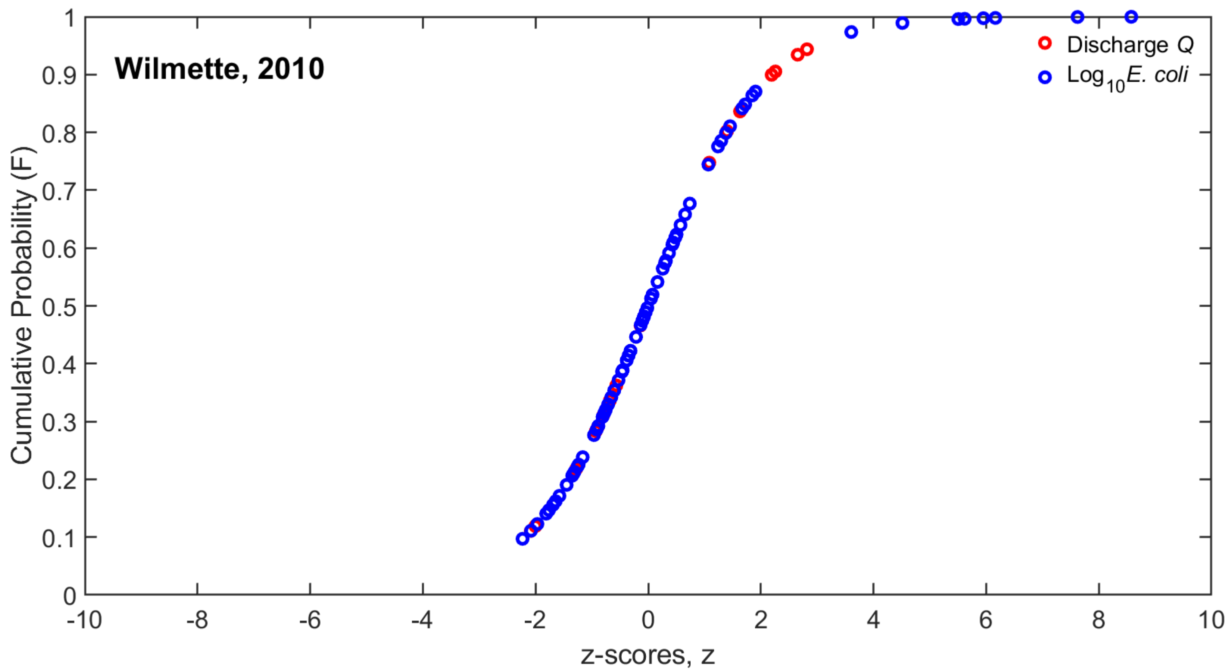

Figure 6-2: Comparison of CDF results for discharge Q *and* $\log_{10}$*(E. coli* concentration*) at the Wilmette outlet in 2010*

Using the established relationship between discharge *Q* and *E. coli* concentration, hourly input concentration values to the backflow models ranged from 1.79 to 3.00 $\log_{10}$(MPN 100 ml^{-1}). However, there is a difference between the number of particles released at a river outlet during a Lagrangian particle tracking model and the concentration of *E. coli* at the outlets. In many cases, assuming that one particle is equal to one MPN 100 ml^{-1} leads to underprediction of observed concentrations as a sufficient number of particles are needed to adequately resolve the *E. coli* dynamics. While multiplying input hourly *E. coli* concentrations by large numbers was not feasible due to limitations on computing power, based on the results of a sensitivity analysis concentrations multiplied by 10^2 were used as the numbers of particles released each hour at the outlets.

Due to the differences between particle concentrations and estimated *E. coli* concentrations in the water, estimated *E. coli* concentrations at the outlets ranged from 1.79 to 3.00 $\log_{10}$(MPN 100 ml^{-}

^{1}), but the number of particles released at the outlets ranged from 6100 to 99700 per hour (Table 6-2). This allowed for a balance between characterizing the spatiotemporal differences in concentration at the outlets during and after the backflow events and minimizing the computational demand for the models.

Table 6-2: Range of estimated E. coli concentrations from Q – concentration relationships and resulting ranges of particle numbers released per hour during backflow events

Backflow Event	**Minimum Estimated *E. coli* Concentration ($\log_{10}$(MPN 100 ml^{-1}))**	**Maximum Estimated *E. coli* Concentration ($\log_{10}$(MPN 100 ml^{-1}))**	**Minimum Number of Particles Released**	**Maximum Number of Particles Released**
2010	1.79	2.95	6100	90000
2011	1.88	3.00	7600	99700

6.2.4. Modeling FIO Fate and Transport

Within a typical Lagrangian particle tracking model, particles are simulated within the water column as conservative tracers. The model uses hydrodynamics to simulate how and where each discrete particle moves over time, resulting in new particle positions at every hourly timestep. After determining new particle positions for every timestep, the model is then able to use an inverse distance weighting scheme, along with the particle positions and node positions from the model mesh, to calculate particle concentrations corresponding to each node in the model domain (Rowe et al. 2016). These calculations of the particle concentration over the model domain only account for advection and dispersion, though. Adjustments to the particle tracking model code are required to incorporate reactions and decay, thus fully characterizing microbial fate and transport.

A microbial decay function modeled after that from Safaie et al. (2016) was incorporated into the concentration calculation within the Lagrangian particle tracking model code. This decay function (S) included terms for dark mortality (k_d), solar inactivation and settling (Eq. 6-1).

$$S = -\left[\frac{f_p v_s C}{z} + k_I I_t e^{-k_e z} C + k_d C\right] \theta^{T-20} \tag{6-1}$$

In this function, f_p is the fraction of microbes attached to solids that may settle out of the water column (unitless), v_s is the settling velocity of the solids settling out the water column (m d^{-1}), and $\boldsymbol{z}$ is the depth coordinate of the solids settling out of the water column (m). These parameters characterize the effects of settling on the microbial concentration in the water. In the second term, k_I denotes the microbial solar inactivation rate (m^2 W^{-1} d^{-1}), I_t is solar irradiance at the water surface at time t (W m^{-2}) and k_e is the solar radiation extinction rate with depth in the water column (m^{-1}). Together, these parameters signify the effects of solar inactivation on aquatic microbes. The final term signifies base mortality in the water, with k_d representing the dark decay rate of a microbial contaminant (d^{-1}). θ is a temperature correction factor (unitless), dependent on water temperature T (°C) and C is the microbial concentration (MPN 100 ml^{-1}).

The parameters in these terms can be locally specific and can vary between microbial taxa. For *E. coli* in southern Lake Michigan, parameter values used in the microbial decay function are represented by Eq. 6-2 – 6-7 (Safaie et al., 2016b).

$$f_p = 0.05 \tag{6-2}$$

$$v_s = 1 \tag{6-3}$$

$$k_I = 0.003 \tag{6-4}$$

$$k_e = 0.55 \tag{6-5}$$

$$k_d = 0.777 \tag{6-6}$$

$$\theta = 1.07 \tag{6-7}$$

These values were directly input into the microbial decay function and incorporated into the particle concentration calculation within the Lagrangian particle tracking model (Eq. 6-8). In this way, the model could simulate the fate and transport of *E. coli* in southern Lake Michigan during and after the backflow events, using fate and transport of non-conservative particles as proxies. For each time step Δt (hr) the following equation was used to update concentration values:

$$C = C_{ad} - \Delta t\left[\frac{0.05*1*C_{ad}}{z} + 0.003*I_t*e^{-0.55*z}*C_{ad} + 0.777*C_{ad}\right]1.07^{T-20} \tag{6-8}$$

where the concentration C_{ad} on the right-hand side of Eq. 6-8 includes the effects of horizontal and vertical mixing processes (advection and dispersion) and C includes the effects of advection, dispersion and decay.

6.2.5. Characterizing FIO at Beaches

Calculated particle concentrations from the output of the Lagrangian particle tracking models were post-processed to obtain estimates of *E. coli* concentrations in plumes in the nearshore during and after backflow events. Spatiotemporally-variable particle concentrations at each beach were multiplied by 10^6. This accounts for a unit conversion between the MPN 100 ml^{-1} units in final *E. coli* concentrations at the beaches and the particles m^{-3} units from the particle tracking model results. It also accounts for the multiplication of the estimated *E. coli* concentrations by 10^2 to ensure adequate particle numbers for the model simulation process.

These calculated concentrations corresponded to the simulated concentrations from the model, given the discharge to concentration relationship, microbial decay function and particle tracking model approach. Isolating the concentrations at locations specific to the 24 Chicago beaches allowed for analysis of the spatiotemporal scales of contaminants in the storm-induced plumes.

Breakthrough curves showed not only maximum expected concentrations of *E. coli* at the beaches, but also how long the elevated concentrations may be expected to persist along the shore.

6.2.6. Validation of Modeled *E. coli* Concentrations for 2010 and 2011 Backflow Events

Backflow events in 2010 and 2011 occurred in July of their respective years, so beach water quality monitoring data were available from the Illinois BeachGuard website (IDPH, 2018). These data were extracted for available beaches (Table 6-3) and used to validate the modeled *E. coli* concentrations at the beaches. In both 2010 and 2011, the O'Brien outlet did not release stormwater, so modeled *E. coli* concentrations at Calumet beach were zero through the entire modeling period. Therefore, observations at Calumet beach were not used for validation. Similarly, in 2010, Rainbow and South Shore beaches were also not impacted by modeled *E. coli* from river plumes, so they were not included in the validation process for that year's model.

Table 6-3: CPD Beaches analyzed for validation of E. coli particle tracking models corresponding to 2010 and 2011 backflow events

Beach Name	Monitoring Data Used for 2010?	Monitoring Data Used for 2011 Validation?
Rogers Park	Yes	Yes
Howard	Yes	Yes
Marion Mahony Griffin	Yes	Yes
Leone	Yes	Yes
Loyola	No	No
Tobey Prinz	No	No
Helen Doria	No	No
North Shore	No	No
Hartigan	Yes	Yes
Lane	No	No
Osterman	Yes	Yes
Foster	Yes	Yes
Montrose	Yes	Yes
North Ave.	Yes	Yes
Oak St.	Yes	Yes
Ohio St.	Yes	Yes

Table 6-3 (cont'd)

12^{th} St.	Yes	Yes
Margaret T. Burroughs	Yes	Yes
Oakwood	Yes	Yes
57^{th} St.	Yes	Yes
63^{rd} St.	Yes	Yes
South Shore	No	Yes
Rainbow	No	Yes
Calumet	No	No

Monitoring data from the beaches were of daily temporal resolution and were collected between sunrise and 8:30 am. Due to the temporal range in possible sampling times, model results were compared to observations three times, once each assuming that sampling occurred at 6:00 am, 7:00 am and 8:00 am. Because the samples could have been taken at any of these three times, the comparisons presented herein represent modeled data from the single timestep (6:00 am, 7:00 am or 8:00 am) that best match with the observational data. Similarly, in the absence of exact GPS coordinates of sampling locations along the beach faces, model results for all nodes along each beach face were compared to observational data and results from the single node at each beach that best represented observational data are presented herein.

Log-transformed results from monitoring at the beaches were temporally aligned with log-transformed simulated *E. coli* concentrations at model nodes corresponding to the beaches. Plots comparing the observed and modeled *E. coli* concentrations allowed for visual comparison of the data and qualitative analysis of whether the models captured the observed data. Quantitatively, the predictive ability of the models was assessed using R^2 coefficient of determination, Root Mean Squared Error (RMSE), normalized Fourier Norm (F_n), Nash-Sutcliffe Efficiency (NSE), Percent Bias (PBIAS) and the RMSE-observations standard deviation ratio (RSR) (Eq. 3-21, 3-23 – 3-26).

Additional details regarding how these statistics are calculated and interpreted can be found in Chapter 3.2.4. Results of these analyses indicated the applicability of the particle tracking model and discharge Q – concentration relationship for simulating the effects of contaminants in storm-induced river plumes in the southwestern Lake Michigan nearshore zone.

6.2.7. Assessing *E. coli* Patterns at 24 Chicago Beaches

Calculated *E. coli* concentrations from the validated coupled hydrodynamic and Lagrangian particle tracking model in the context of the two backflow events in 2010 and 2011 were used to develop time series *E. coli* concentration data and plots for analysis of spatiotemporal patterns. Resulting *E. coli* concentrations were compared to the 2.37 $\log_{10}$(MPN 100 ml^{-1}) threshold for imposing a swimming advisory (USEPA, 2012), to determine when and at which beaches *E. coli* concentrations exceeded safe recreation levels. Spatiotemporal variability in the *E. coli* results were assessed to determine any temporal cycles or spatial trends in the *E. coli* at the beaches.

To aid beach management organizations, statistical relationships between beach proximities to the river outlets, *E. coli* time of final exceedance during the model simulation period after the backflow event and average *E. coli* concentration at the beaches were developed. Beach proximity to the outlets was also statistically compared to the time that it took the *E. coli* particles to initially reach the corresponding beach. In this case, the timing of the initial elevation of modeled *E. coli* concentration above 0 MPN 100 ml^{-1} was noted as the variable *time of initial E. coli increase* for statistical analysis. Spearman correlations between these variables were evaluated, to determine which variables may be used to predict others. Multiple regression analysis was then performed to generate equations that can be used to estimate average *E. coli* concentration and time before *E. coli* levels begin to rise at beaches from beach proximity to outlets. All statistical models were developed in RStudio (RStudio, Boston, MA USA) with a significance threshold of $\alpha = 0.05$.

6.3. Results and Discussion

E. coli concentrations in storm-induced river plumes were simulated using a coupled FVCOM hydrodynamic and Lagrangian particle tracking model, equipped with a microbial decay function specific to *E. coli* in southern Lake Michigan, to track microbial contamination in the plumes. Model results were compared with observational *E. coli* enumeration data at Chicago beaches after the backflow events that produced the plumes in 2010 and 2011. Comparisons were used to assess the model's predictive capacity and provide insight into recreational water quality in response to heavy storms.

6.3.1. Validation Results for 2010 Backflow Model

Modeled *E. coli* concentrations were truncated such that they ranged from one to 2420, following the range of concentrations detectable by the Colilert-QuantiTray method of enumeration of *E. coli* in samples (IDEXX Laboratories, Westbrook, ME). Plots comparing log-transformed concentrations observed at the beaches to the modeled concentrations in 2010 visually indicate that the model captures the observational data reasonably well, but the model's predictive ability varies between the beaches. For example, the model seemed to simulate *E. coli* concentrations at North Ave., Oakwood and 57th St. beaches (Figure 6-3) more effectively than it did at Leone, Hartigan and Foster beaches (Figure 6-4). As seen in Figure 6-4, the model frequently overpredicts observed *E. coli* concentrations at beaches between the Wilmette and CRCW outlet, at times by orders of magnitude. This may be due, in part, to the model simulating the effects of two plumes on these beaches. The three beaches represented in Figure 6-4 are all between the CRCW and Wilmette outlets but are closer to the Wilmette outlet than CRCW. These beaches may be substantially impacted by both plumes, leading to higher modeled *E. coli* concentrations that encompass *E. coli* from both CRCW and Wilmette outlets. In contrast, North Avenue beach in

Figure 6-3 is just north of the CRCW outlet and Oakwood and 57th Street beaches are south of the CRCW outlet. These three beaches are not as likely to be impacted by plumes from both CRCW and Wilmette, so it is possible that the model better predicted *E. coli* at these locations because it was only predicting effects from one plume instead of the synergistic effects from both outlets.

Other potential factors influencing the model predictive ability at specific beaches may include differences in beach morphology and resulting dynamics. Additional comparison plots for the remaining 10 beaches in July 2010 can be found in Appendices C-1 – C-10.

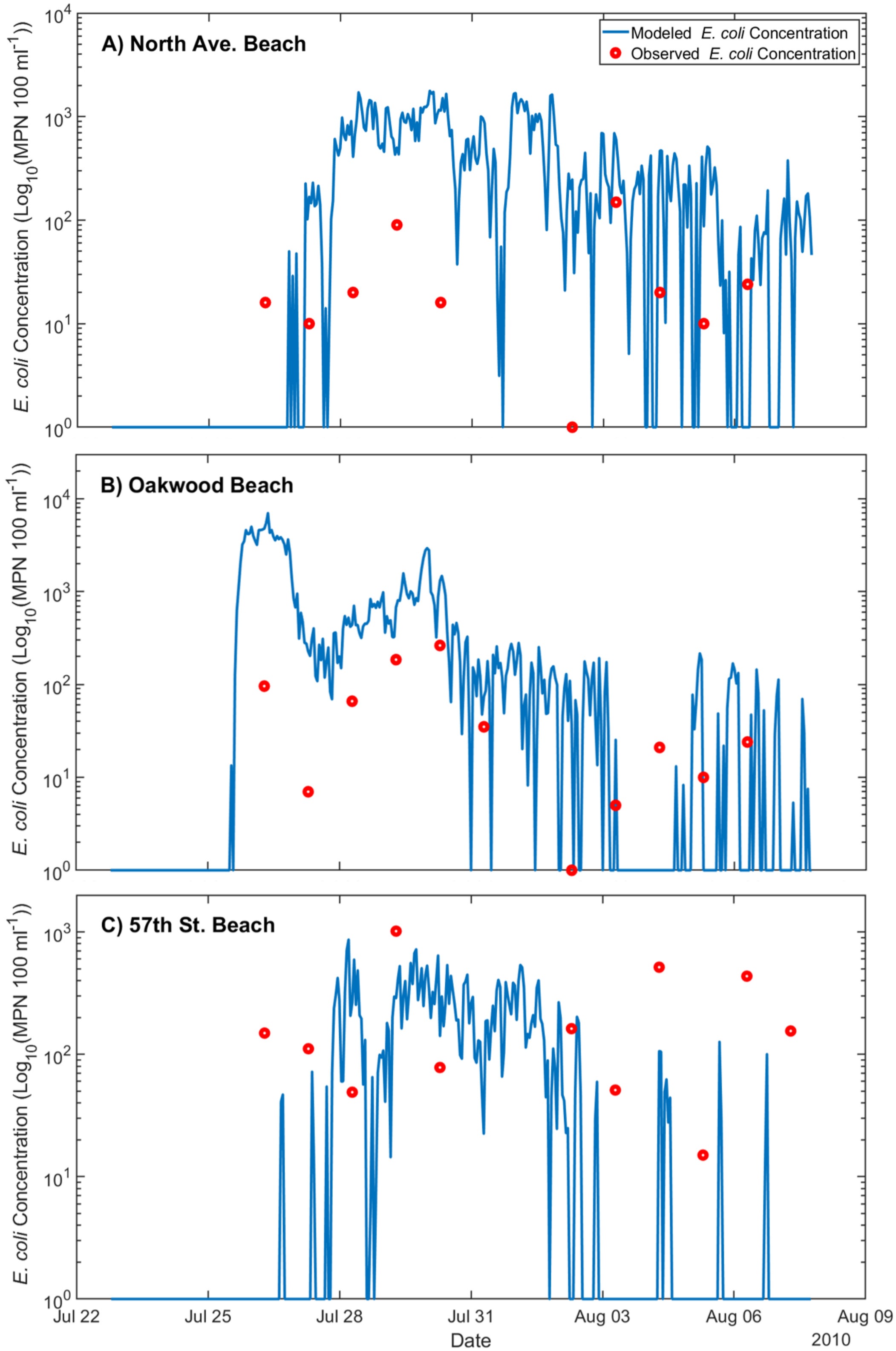

Figure 6-3: Plots comparing observed (red circles) and modeled (blue lines) log-transformed E. coli concentrations at North Ave. (A, top), Oakwood (B, center) and 57th St. (C, bottom) beaches in July 2010

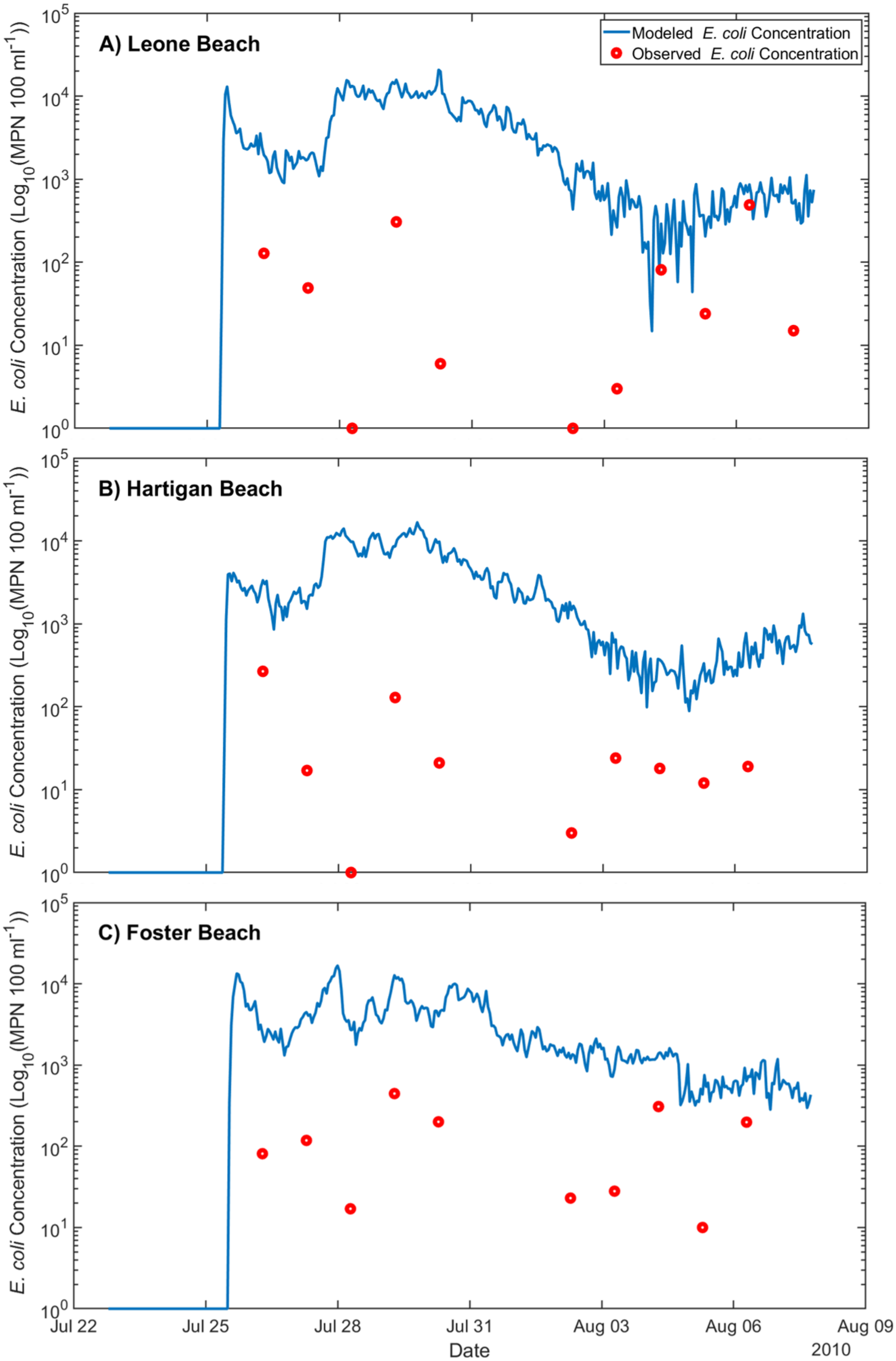

Figure 6-4: Plots comparing observed (red circles) and modeled (blue lines) log-transformed E. coli concentrations at Leone (A, top), Hartigan (B, center) and Foster (C, bottom) beaches in July 2010

Quantitative analysis of comparisons between modeled and observed *E. coli* concentrations during and after the 2010 backflow event suggest that the model may be capturing the observations at some beaches more reliably than the plots would suggest. At the same time, quantitative analysis also indicates that model predictive ability is highly variable between beaches. Across all 16 beaches analyzed for the 2010 backflow event, R^2 values for the model ranged from -0.33 at Marion Mahony Griffin beach to 0.75 at Oakwood beach (Table 6-4). The model yielded positive R^2 values at 13 of 16 beaches (81.25%) but at Marion Mahony Griffin, Montrose and 63rd St. beaches, the model simulated *E. coli* concentration at a lower capacity than a constant *E. coli* concentration value over time would be expected to predict.

Table 6-4: Summary of validation statistics for the July 2010 backflow E. coli concentration model, at individual beaches along the Chicago shoreline

Beach	F_n	NSE	PBIAS	R^2	RMSE	RSR
Marion Mahoney Griffin	1.08	-4.53	-98.68	-0.33	1.99	2.35
Montrose	0.87	-4.15	-61.23	-0.27	1.71	2.27
63rd St.	0.88	-3.78	49.34	-0.13	1.58	2.19
Leone	1.33	-4.70	-135.63	0.01	2.14	2.39
Margaret T. Burroughs	0.81	-9.57	34.59	0.03	1.86	3.25
Hartigan	1.52	-9.68	-157.41	0.04	2.15	3.27
Oak St.	0.61	-2.41	-31.41	0.05	1.15	1.85
Rogers Park	1.38	-8.59	-141.31	0.15	2.08	3.10
Howard	1.28	-8.55	-127.98	0.17	2.02	3.09
12th St.	0.48	-2.87	-7.87	0.19	1.08	1.97
Ohio St.	0.84	-15.94	-60.26	0.22	1.37	4.11
57th St.	0.77	-10.47	61.36	0.29	1.68	3.39
North Ave.	0.55	-0.86	3.69	0.34	0.76	1.36
Kathy Osterman	0.74	-4.31	-70.65	0.46	1.46	2.30
Foster	0.76	-6.30	-74.81	0.55	1.48	2.70
Oakwood	0.69	-1.39	-10.61	0.75	1.07	1.55

The poor predictive ability of the model at Montrose and 63rd St. beaches may be related to the different beach morphology and dynamics that these beaches are subject to. Both beaches are embayed and sheltered (Grant and Sanders, 2010) by manmade breakwaters. These unique embayment conditions create interesting dynamics for solute transport at the beaches by sheltering the nearshore zones from the offshore currents. As a result, gyres have a tendency to form inside embayments like Montrose and 63rd St. beaches and force *E. coli* that are inside the embayments to stay inside there, often settling out of the water column and becoming available for future resuspension from sand and sediments (Ge et al., 2010; Ge et al. 2012b). In contrast, beaches such as Oakwood, Foster and Kathy Osterman are relatively un-embayed and do not have major breakwater infrastructure to artificially impact hydrodynamics along the shore. These un-embayed beaches also yielded the highest R^2 values for the model. Resuspension dynamics like those often seen at embayed beaches (Ge et al., 2012a) were not incorporated in the model herein and thus provide an interesting opportunity for additional assessment of dynamics affecting plume-associated *E. coli* in the nearshore zone. Beach morphology and embayment may play a role beyond just the poor predictive ability of the model at Montrose and 63rd St. beaches. The four beach locations for which the 2010 backflow model underpredicted *E. coli* concentrations (North Ave., Margaret T. Burroughs, 57th St. and 63rd St.) are all embayed or sheltered by breakwater infrastructure. As a result, it is possible that *E. coli* accumulate at these locations, leading to higher concentrations than those observed at less embayed or sheltered beaches and underprediction of *E. coli* by the model.

In addition to beach morphology, an important factor to consider when evaluating differences in model predictive ability between beaches is native *E. coli* from local sources that are not related to the plumes. Beaches are subject to a number of sources of microbial contamination, and those sources can vary greatly between them. Sources such as humans, wildlife, runoff and stormwater/wastewater discharges can impact beaches differently, based on proximity, beach usage and backshore land use, leading to differential local microbial populations. These populations were not accounted for in the model, since the model was solely looking at plume-associated *E. coli*, so the effects of those local populations may be a substantial factor in the differences in model predictive ability between beach locations in 2010 and 2011.

RMSE values across all beaches range from 0.76 to 2.15 $\log_{10}$(MPN 100 ml^{-1}), with lower RMSE values largely seen at beaches with higher R^2 values, as can be expected. One notable exception is Foster beach, for which the model produced the second-highest R^2 value (R^2 = 0.55), but also yielded a relatively high RMSE value (RMSE = 1.48 $\log_{10}$(MPN 100 ml^{-1}). PBIAS generally follows the same pattern, with PBIAS values closer to zero frequently corresponding to models for beaches with higher R^2 and lower RMSE values (Figure 6-5).

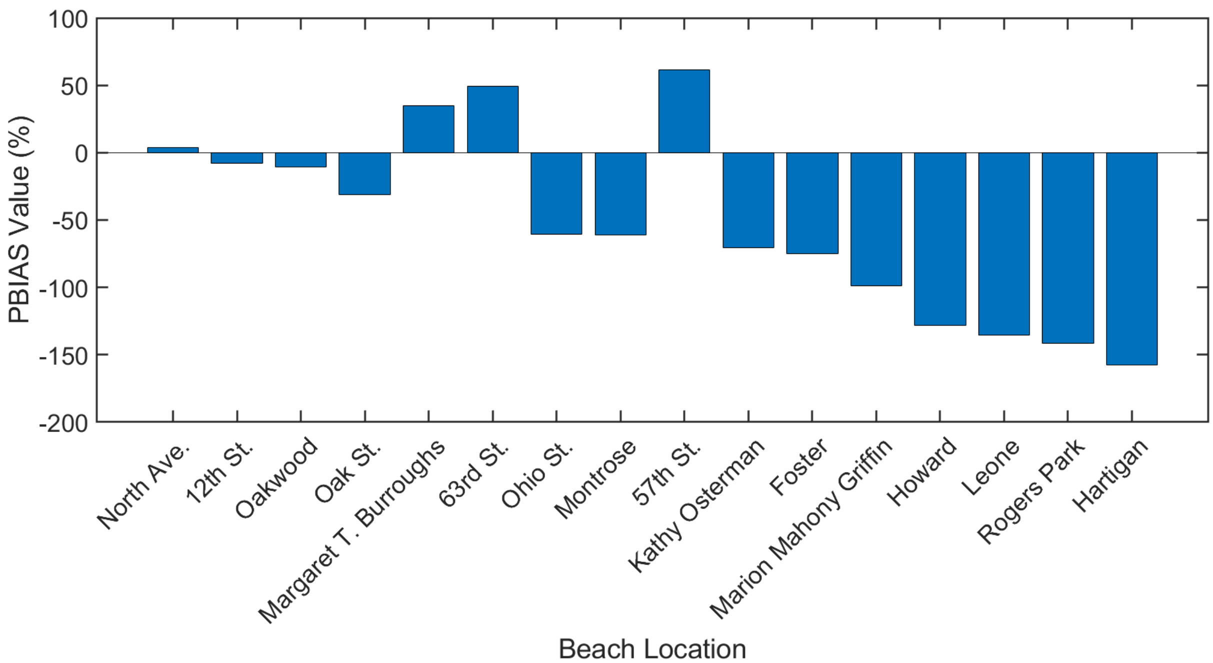

Figure 6-5: Bar chart comparing PBIAS values for the 2010 model of E. coli in backflow plumes at 16 beach locations. The model best simulated observed E. coli concentrations at North Ave. beach, where the PBIAS value is closest to 0.0

PBIAS values in 2010 indicate a systematic overprediction of *E. coli* concentrations at the beaches. The model yielded a positive PBIAS value (suggesting underprediction of *E. coli* concentration) only at North Ave., Margaret T. Burroughs, 57th St. and 63rd St. beaches. This systematic overprediction of *E. coli* concentrations at Chicago beaches may indicate that the simulation of decay processes would benefit from additional model refinement. It is also possible that the model *E. coli* input was unreasonably high, leading to overprediction of *E. coli,* not only at Leone, Hartigan and Foster beaches, but at 14 of the 18 locations modeled (77.78%). The initial *E. coli* concentrations in the model, represented by particle numbers, were determined from statistical relations developed for southern Lake Michigan. However, those statistical relations were generated for non-storm conditions, so it is possible that input concentrations during heavy rain events are different from those input to the models here. Because the model simulated *E. coli* concentrations at some beaches well, though, it can be difficult to pinpoint a specific source of error at other beaches without additional observational data. Overprediction of *E. coli* was maximized at Hartigan, Rogers Park, Leone and Howard beaches, between the Wilmette and CRCW outlets (PBIAS = -157.42, -141.31, -135.63 and -127.98, respectively, Table 6-4). This relatively large magnitude of overprediction at beaches between the outlets, compared to those beaches south of the CRCW outlet, may stand to reason, given that the modeled *E. coli* was associated with storm-induced river plumes at both outlets. Nonetheless, the PBIAS values indicate that the model predicted *E. coli* values with magnitudes twice those of observational data, further supporting the idea that the model framework would benefit from additional testing and refinement.

The other validation statistics applied to the 2010 model show similar trends to the coefficient of determination, RMSE and PBIAS between beaches. At beaches with lower RMSE values and higher R^2 values, NSE values tend to be closest to the optimal value of +1.0, F_n values are closest to 0.0 and RSR values are minimized, though there are some differences between statistics, in terms of which beaches optimize the respective validation statistic (Figures 6-6 – 6-8). Generally, the statistics indicate that the model predicts *E. coli* concentration most reliably at North Ave. and 12th St. beaches, while its simulation is least reliable at Hartigan and Ohio St. beaches.

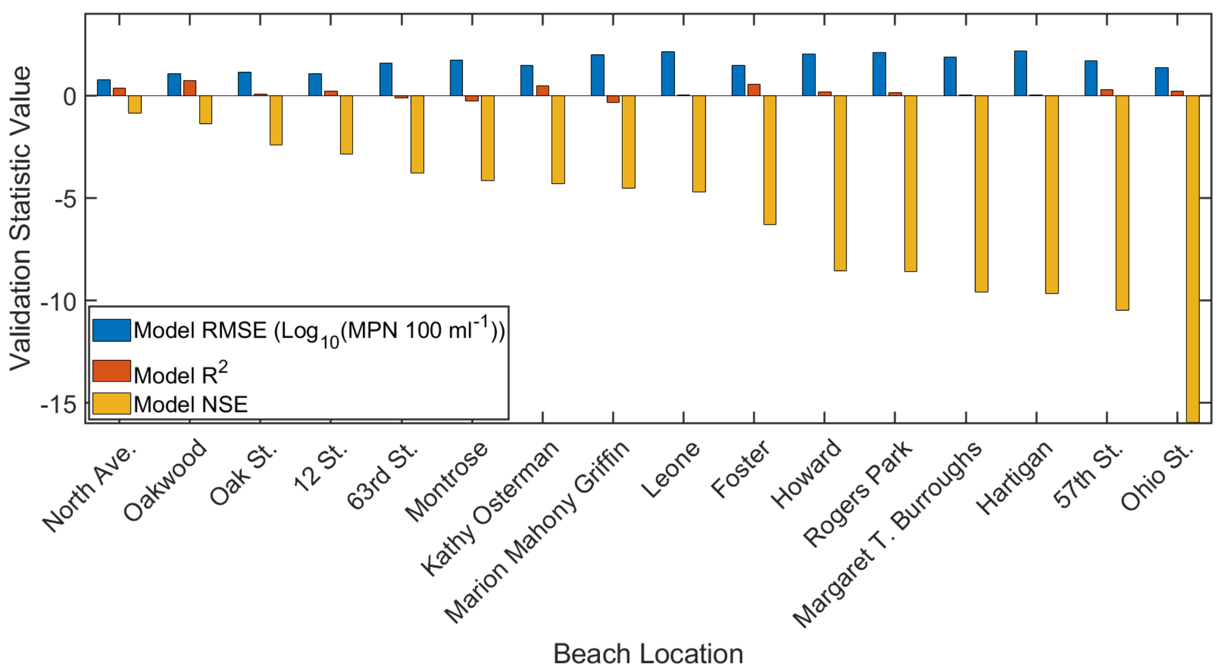

Figure 6-6: Bar chart comparing RMSE, R^2 and NSE values for the 2010 model of E. coli in backflow plumes at 16 beach locations. The model best simulated observed E. coli concentrations at North Ave. beach, where the NSE value is closest to 1.0. The model at North Ave. beach also yielded the lowest RMSE value and fourth-highest R^2 value, compared to other beaches

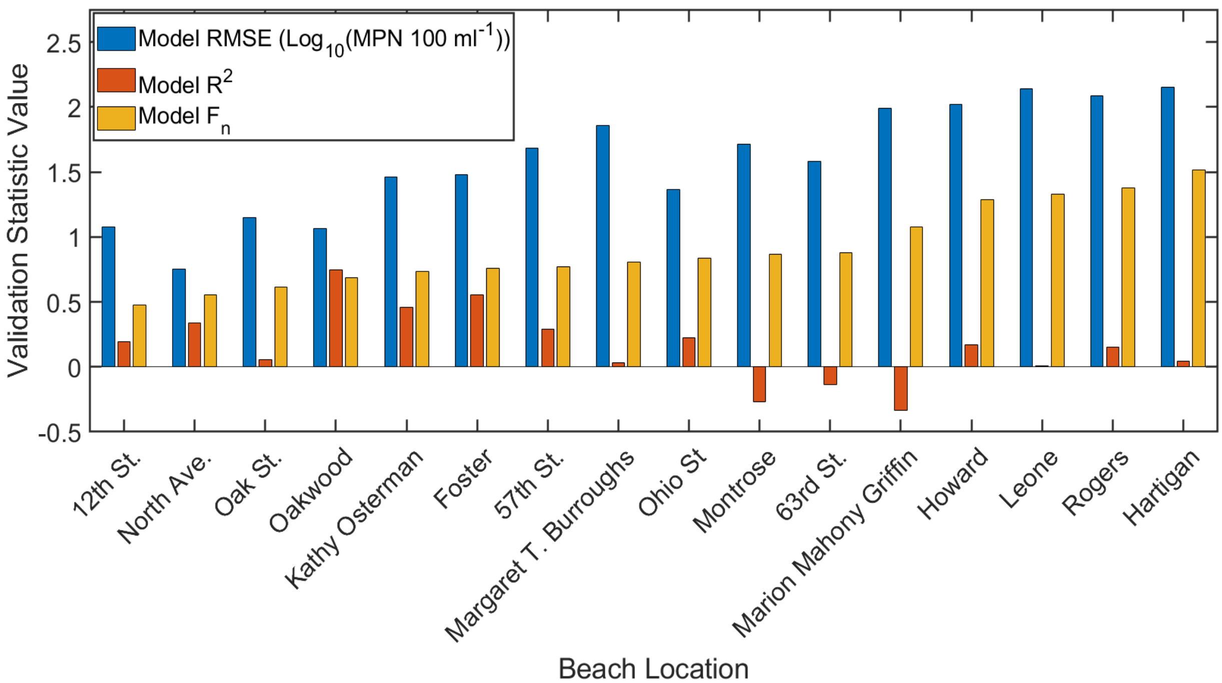

Figure 6-7: Bar chart comparing RMSE, R^2 and F_n values for the 2010 model of E. coli in backflow plumes at 16 beach locations. The F_n value is closest to 0.0 for 12th St. beach. The model at 12 St. beach also yields the third-lowest RMSE value and yields a relatively high R^2 value, compared to the other 15 beaches

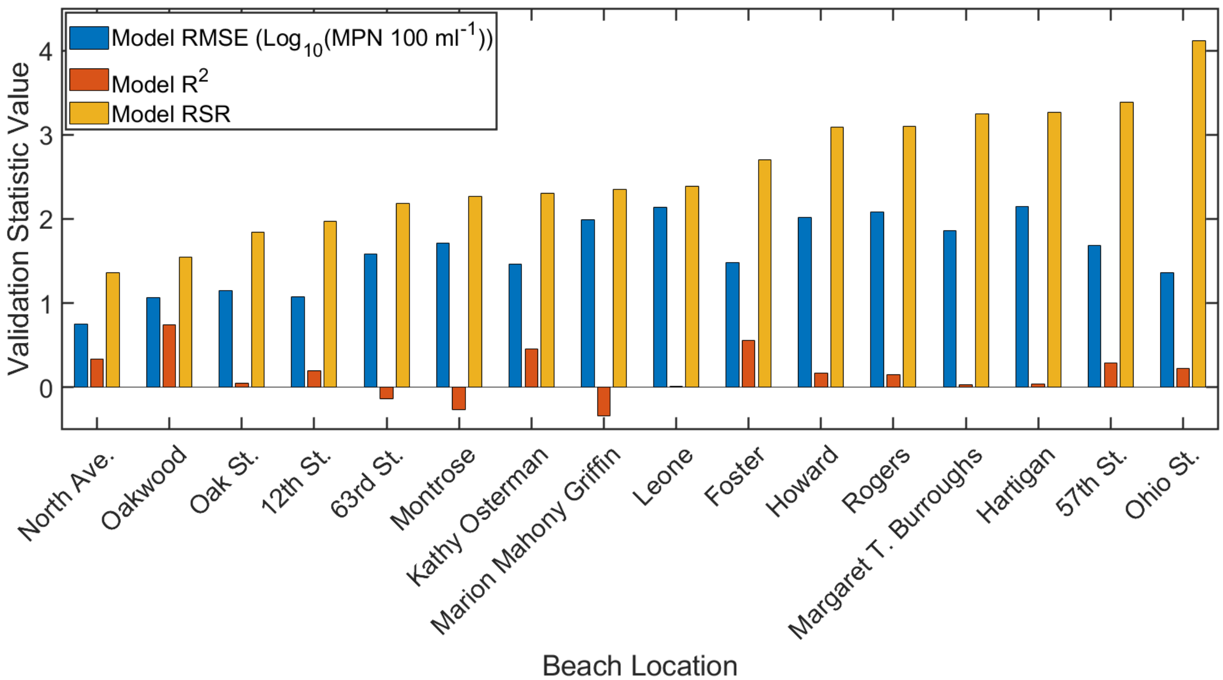

Figure 6-8: Bar chart comparing RMSE, R^2 and RSR values for the 2010 model of E. coli in backflow plumes at 16 beach locations. The model best simulated observed E. coli concentrations at North Ave. beach, where the RSR value is minimized. The model at North Ave. beach also yields the fourth-lowest RMSE value and third-highest R^2 value, compared to other beaches

6.3.2. Validation Results for 2011 Backflow Model

Validation of the model results in the context of the July 2011 backflow event showed that the model predictive capacity was comparable, and in many cases, improved, compared to its predictive capacity in the context of the 2010 backflow event. Similar to the 2010 event, predictive ability of the model for the 2011 backflow event varied considerably between the 18 beaches for which it was validated. Plots comparing the observed and simulated *E. coli* concentrations over time show that the model simulated *E. coli* relatively well at Montrose, North Ave. and Rainbow beaches (Figure 6-9), while it performed relatively poorly for Rogers Park, Howard and Oakwood beaches (Figure 6-10). Figures 6-9 and 6-10 show that the *E. coli* model for the 2011 backflow event often failed to capture relatively low magnitude *E. coli* concentrations at locations like

Rogers Park, Howard and Oakwood beaches (Figure 6-10), but also could underpredict very high concentrations, as seen at Montrose and Rainbow beaches (Figures 6-9a and 6-9c). Plots also suggest that the model did not capture *E. coli* concentrations at the beaches at the beginning of the backflow event. This may lend insight into the temporal scale of the plume effects at the beaches, though. The non-zero observational *E. coli* concentrations at the beaches early in the backflow event may be background concentrations or *E. coli* from sources other than the plumes, and it is possible that the model did not calculate those concentrations because the plumes had not yet reached those beaches. Additional comparison plots can be found in Appendices D-1 – D-12.

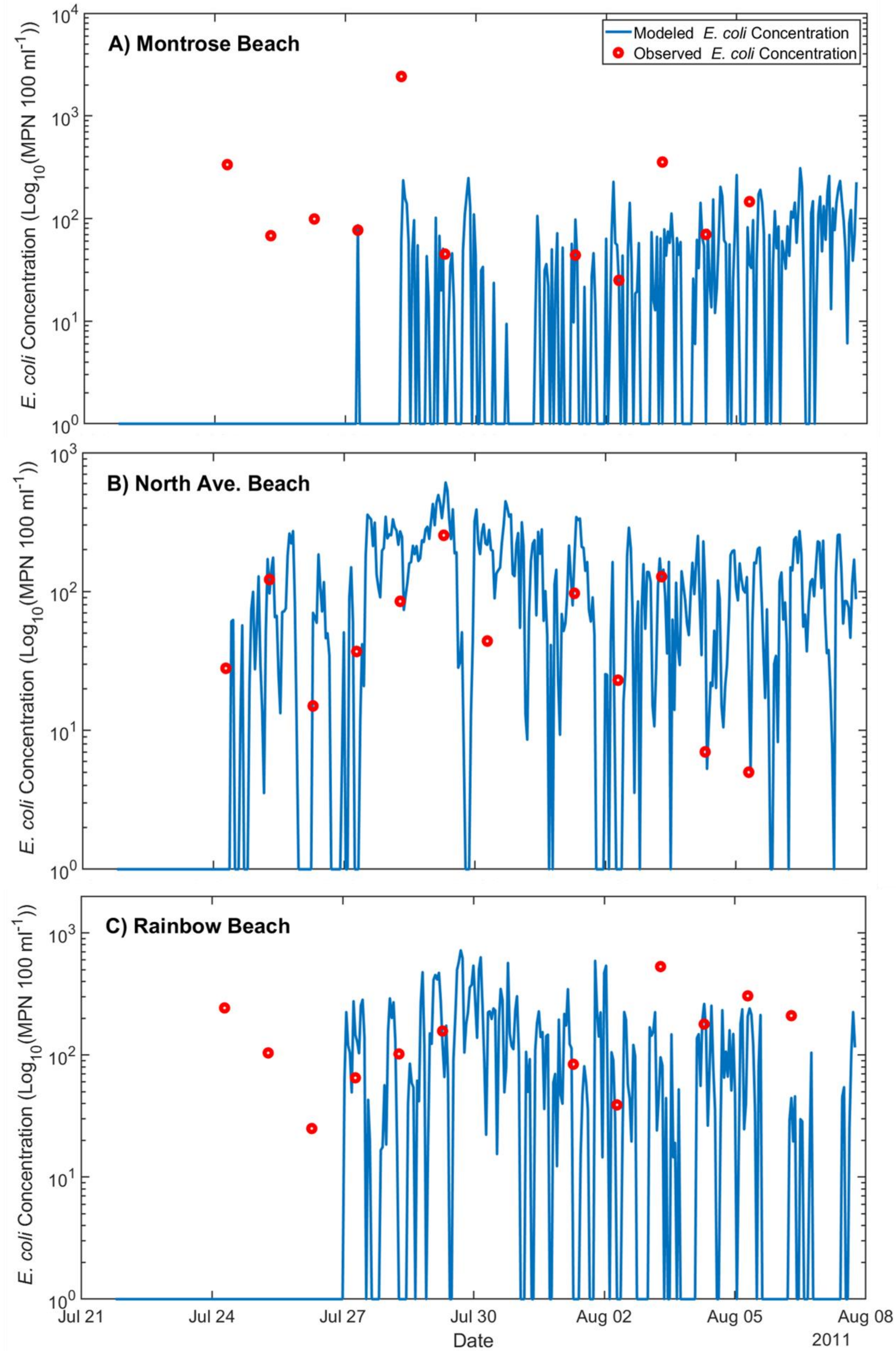

Figure 6-9: Plots comparing observed (red circles) and modeled (blue lines) log-transformed E. coli concentrations at Montrose, (A, top), North Ave. (B, center) and Rainbow (C, bottom) Beaches in July 2011

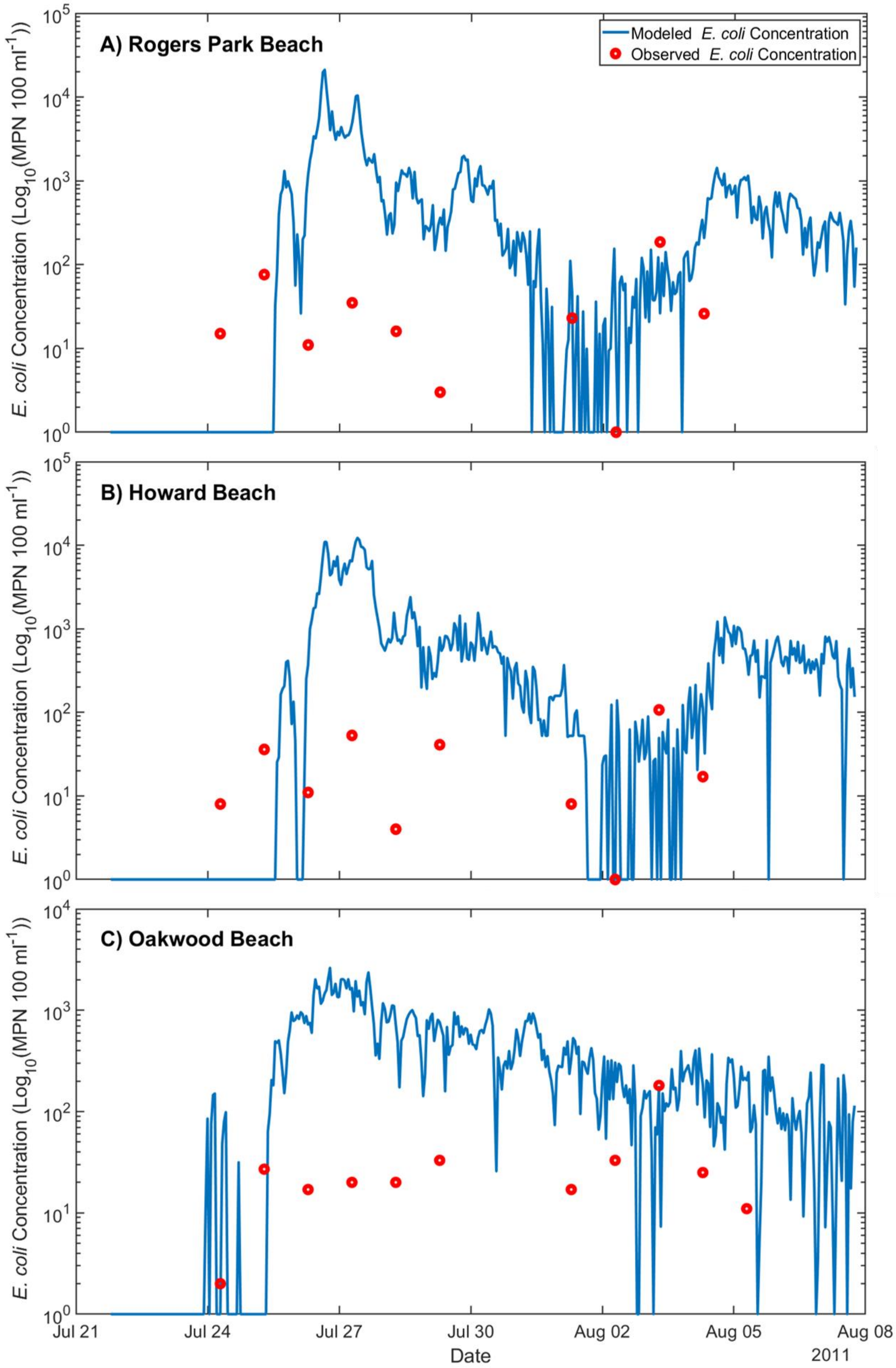

Figure 6-10: Plots comparing observed (red circles) and modeled (blue lines) log-transformed E. coli concentrations at Rogers Park (A, top), Howard (B, center) and Oakwood (C, bottom) beaches in July 2011

Model validation statistics computed for the 2011 backflow model indicate that the model frequently simulated *E. coli* concentrations as well as or better than the 2010 backflow model at specific beach locations. However, the two models' predictive abilities are similar in that their ability to simulate water quality varies by beach location. Validation statistics were calculated for the 2011 backflow model at 18 beaches, including the Rainbow and South Shore locations that were not included in validation of the 2010 model. Across the beaches, R^2 values for the model ranged from -0.44 at 57th St. beach to 0.78 at Oak St. beach (Table 6-5). High R^2 values at beaches such as Oak St., North Ave., Rainbow, Montrose, and Hartigan are comparable to some of the highest R^2 values for other water quality models in Lake Michigan (Liu et al., 2006; Safaie et al., 2016b; Thupaki et al., 2010). This lends some confidence to the ability of the model to predict water quality after backflow events. However, the promise that this shows may be tempered by the 13 out of 18 (72.22%) beach locations for which the R^2 value is less than 0.50, indicating that the model captures less than 50% of the variability in the observed data at nearly ¾ of the beaches in the Chicago area. This high degree of variation in R^2 values amongst the beaches underscores the idea that each beach is unique, with its own set of microbial sources and dynamics. However, lack of understanding of the full picture of microbial dynamics and sources at these beaches often requires the application of "one-size-fits-all" approaches and models, which may not be appropriate at all locations.

Table 6-5: Summary of validation statistics for the July 2011 backflow E. coli concentration model, at individual beaches along the Chicago shoreline

Beach Location	F_n	NSE	PBIAS	R^2	RMSE	RSR
57th St.	0.91	-7.48	20.14	-0.44	1.51	2.91
Kathy Osterman	0.70	-2.73	30.02	0.02	1.36	1.93
Ohio St.	0.73	-2.20	-47.54	0.11	1.32	1.79
Rogers Park	1.15	-5.63	-37.30	0.12	1.58	2.57
Marion Mahoney Griffin	0.99	-7.03	-37.63	0.16	1.37	2.83

Table 6-5 (cont'd)

63rd St.	0.68	-2.92	16.39	0.17	1.18	1.98
12th St.	0.46	-2.69	-15.49	0.28	0.97	1.92
Howard	1.06	-4.75	-52.70	0.36	1.37	2.40
Leone	1.47	-24.35	33.65	0.36	2.24	5.03
South Shore	0.61	-11.39	36.61	0.37	1.12	3.52
Margaret T. Burroughs	0.53	-6.72	-31.59	0.38	0.99	2.78
Foster	0.64	-3.12	43.89	0.39	0.99	2.03
Oakwood	0.91	-7.39	-62.68	0.41	1.27	2.90
Hartigan	0.69	-1.32	16.74	0.52	1.09	1.52
Montrose	0.69	-6.63	59.42	0.54	1.47	2.76
Rainbow	0.65	-13.66	49.80	0.55	1.39	3.83
North Ave.	0.49	-1.68	8.00	0.66	0.82	1.64
Oak St.	0.76	-1.96	-78.92	0.78	1.31	1.72

RMSE values for the 2011 backflow event model are also highly variable, ranging from 0.82 log_{10}(MPN 100 ml^{-1}) at North Ave. beach to 2.24 log_{10}(MPN 100 ml^{-1}) at Leone beach. Generally, beach locations for which the 2011 backflow model exhibits relatively high R^2 values also yield relatively low RMSE values. Oak St. beach, though, provides a notable exception. At Oak St. beach, the R^2 value for the model is 0.78, the highest R^2 value of all of the beaches, indicating high local predictive ability for the model. At the same time, the RMSE value for Oak St. beach was only the ninth-lowest of all 18 beaches, a signal of relatively low predictive ability for the model there, compared to other locations. This discrepancy between validation metrics underscores the necessity for using multiple validation metrics to fully understand a model's predictive ability. Similarly, Montrose beach simultaneously exhibits the fourth-highest R^2 value and the fourth-highest RMSE value, amongst the beach locations. For cases like Oak St. and Montrose beaches, with R^2 and RMSE metrics that contradict one another, a metric like RSR can be used to determine the effect of standard deviation in the observational values on model performance. This standardizes the error values from the model, allowing for more reliable comparison of model predictive ability between beaches with different observational datasets (Moriasi et al., 2007). The RSR for Oak St. beach (1.72 $\log_{10}$(MPN 100 ml^{-1})) is the third-lowest of the RSR values at the 18 beaches, indicating that the model may indeed be predicting observed *E. coli* relatively well at the beach. In contrast, the RSR value corresponding to the model at Montrose beach (2.76 $\log_{10}$(MPN 100 ml^{-1})) is the eighth-highest of the 18 beach locations, suggesting that the high RMSE value may better indicate model performance than the high R^2 value there.

Model RMSE values for 2011 exceeded 1.00 $\log_{10}$(MPN 100 ml^{-1}) at 14 out of the 18 beaches (77.78%), but remained at least one order of magnitude lower than average modeled concentration calculations at 10 out of 18 (55.56%) of the respective beach locations. This indicates that the model errors are small compared to the calculated *E. coli* concentrations at many of the beach locations, another sign of promise for the use of the model.

PBIAS calculations show that the model underpredicted *E. coli* concentrations at 10 of the 18 beaches (55.56%) (Figure 6-11). The beaches for which the model overpredicted *E. coli* concentrations are geographically closest to either the Wilmette or the CRCW outlet. It is therefore possible that beach proximity to the outlets has played an outsized role in the prediction of *E. coli* at nearby beaches. There is the potential that modeled *E. coli* is transported to these relatively close beaches before the microbial decay function can considerably influence the *E. coli* concentrations within the model. This may also highlight a shortcoming of the model. At beaches very close to the outlets, nearfield processes such as buoyant spreading of the *E. coli* plume(s) may become important (Nekouee et al., 2015) and the decay function may be different from that used herein.

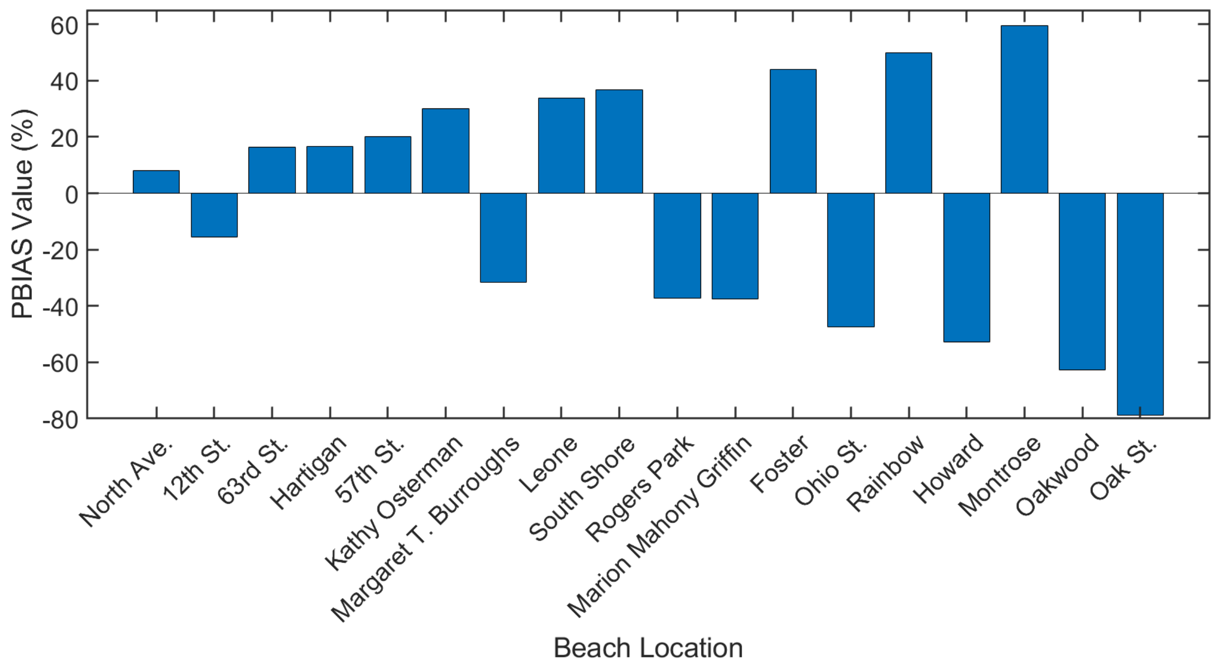

Figure 6-11: Bar chart comparing PBIAS values for the 2011 model of E. coli in backflow plumes at 18 beach locations. The model best simulated observed E. coli concentrations at North Ave. beach, where the PBIAS value is closest to 0.0

Additional validation statistics suggest that the model's predictive ability was maximized at 12th St. and Hartigan beaches. F_n was minimized for the model at 12th St. beach (F_n = 0.46, Figure 6-12), indicating optimal predictive ability in the context of the F_n statistic. Hartigan beach optimized both RSR and NSE (RSR = 1.52 and NSE = -1.32, Figures 6-13 and 6-14). Interestingly, the model at 12th St. and Hartigan beaches yielded RMSE values that were not the two best for the model, instead yielding the second- and fifth-best RMSE values, respectively. Following the discrepancies seen at Montrose beach, this further highlights the importance of using multiple validation metrics for model assessment. A model that indicates high predictive ability via high R^2 value or low RMSE can suggest low predictive ability via the NSE, RSR or F_n metrics, due to biases inherent in the calculation of each metric. For instance, the R^2 metric is inherently biased toward high *E.*

coli values, potentially undervaluing low background levels at the beaches in its estimation of model fit.

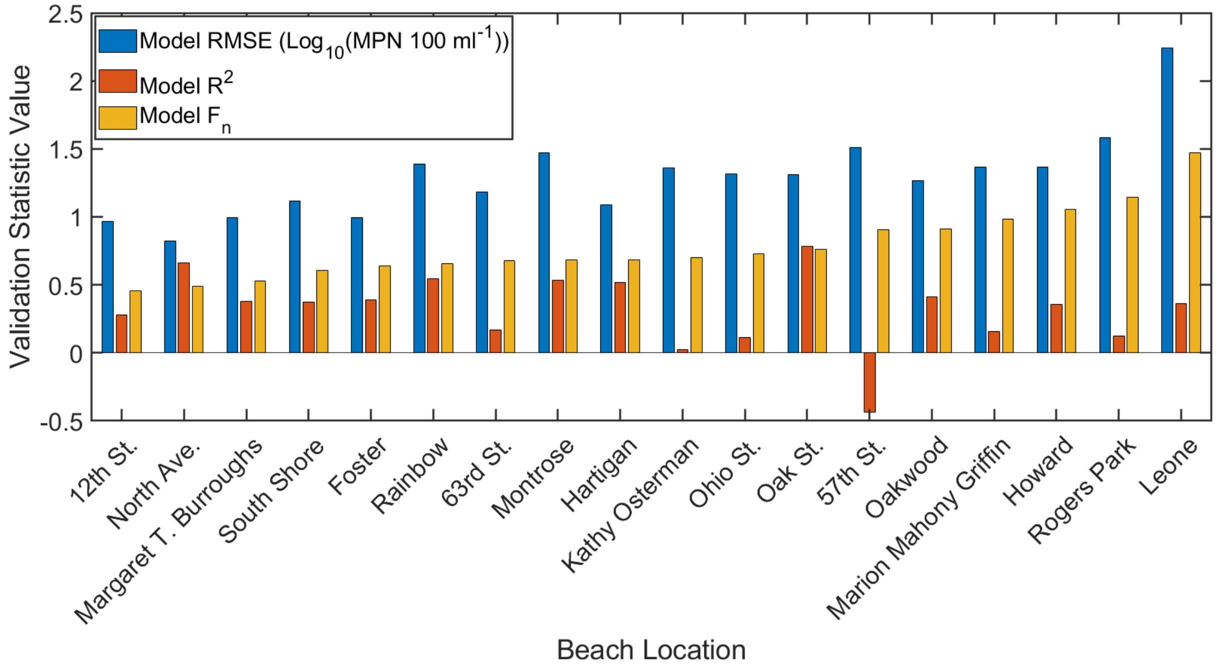

Figure 6-12: Bar chart comparing RMSE, R^2 and F_n values for the 2011 model of E. coli in backflow plumes at 18 beach locations. The model best simulated observed E. coli concentrations at 12th St. beach, where the F_n value is closest to 0.0. The model at 12th St. beach also yielded the second-lowest RMSE value and an R^2 value of 0.28

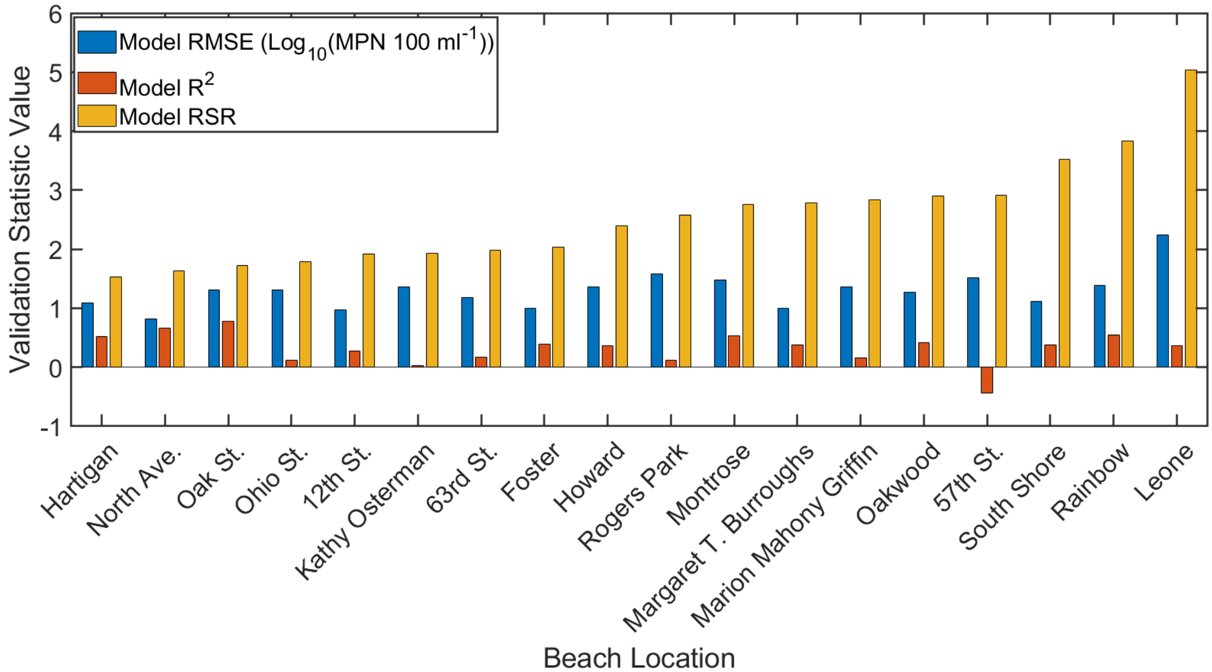

Figure 6-13: Bar chart comparing RMSE, R^2 and RSR values for the 2011 model of E. coli in backflow plumes at 18 beach locations. The model best simulated observed E. coli concentrations at Hartigan beach, where the RSR value is closest to 0.0. Hartigan beach also exhibited the fifth-lowest RMSE and R^2 values

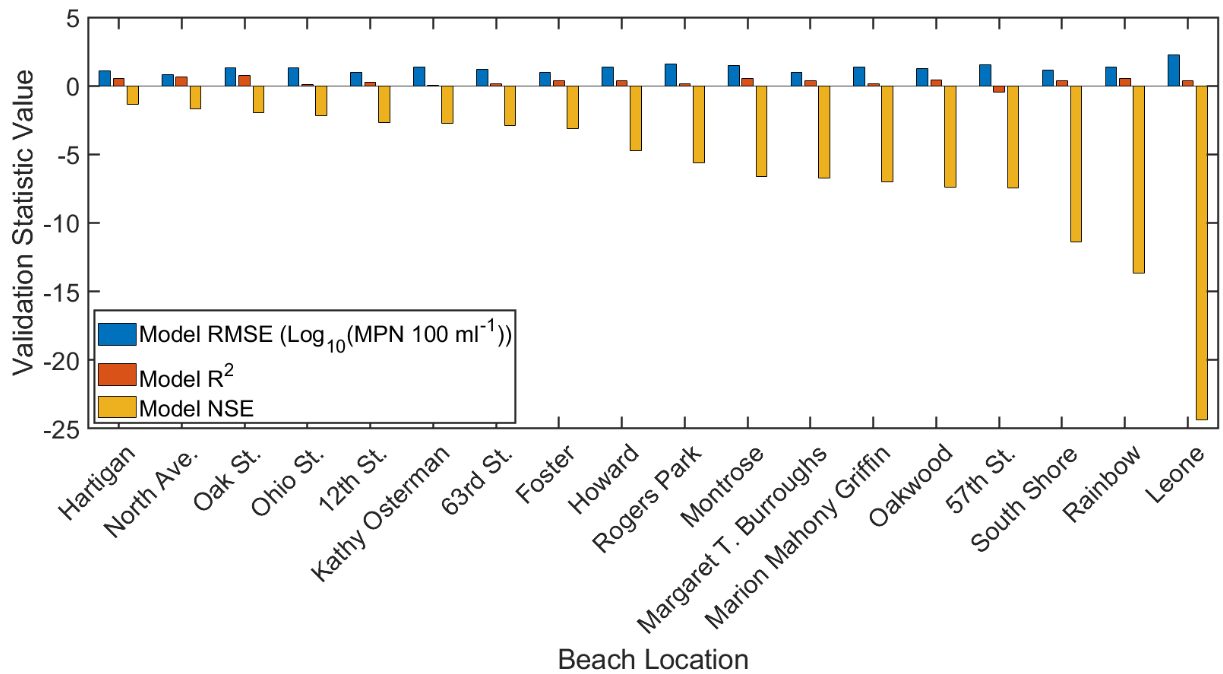

Figure 6-14: Bar chart comparing RMSE, R^2 and NSE values for the 2011 model of E. coli in backflow plumes at 18 beach locations. The model best simulated observed E. coli concentrations at Hartigan beach, where the NSE value is closest to 1.0. Hartigan beach also exhibited the fifth-lowest RMSE and R^2 values

As discussed previously, RSR may be a useful metric to consult in cases like Montrose beach in 2011. There can be conflicting evaluation metric results between R^2, RMSE, PBIAS, RSR and NSE, leading to confusion about whether a model performed well for a specific case. At Montrose beach, the model yielded high R^2 values, but also showed a high RMSE value, so an assessment of RSR could more definitively characterize the model's performance for that particular beach. The corresponding RSR value for Montrose beach was shown to be 2.76 $\log_{10}$(MPN 100 ml^{-1}), the eighth-highest RSR value of all 18 beaches in 2011. Further review of other evaluation metrics, such as PBIAS, NSE and F_n at Montrose beach also indicate relatively mediocre predictive ability of the model at the beach. F_n at Montrose beach was only the eighth-highest of all beaches, at 0.69. Likewise, NSE for Montrose beach was -6.63, the eleventh-best value between the 18 beaches. PBIAS at Montrose beach was also the third-highest in magnitude of the 18 beaches, at 59.42%. These additional metrics suggest that though the R^2 value from Montrose beach is relatively high (R^2 = 0.54), the model did not predict *E. coli* at Montrose beach as well as it did at some of the other locations.

Montrose beach has a unique morphology (Figure 6-15); it is bordered to the south by a marina, from which it is separated by a breakwall. Due to the presence of the marina, the beach is located farther into the lake than other nearby beaches. As a result, it could be subject to higher current velocities that drive plumes, compared to other beaches. The beach is also highly curved on its southern side and has a breakwater on its eastern edge, creating an embayment. This morphology leads to some potential sheltering of the beach from plumes originating to its south or east as well as direct interception of plumes traveling north to south. It is possible that the model overestimated the impacts of sheltering on the southern and eastern sides of the beach on *E. coli* transport to the beach, simulating that the *E. coli* in the plume would move northward along the shore and pass over the Montrose beach area in the process. As a result, the model would simulate that the plume would largely not affect Montrose beach, possibly leading to underprediction of local *E. coli*.

Figure 6-15: Google Earth Image showing the unique morphology and embayment of Montrose beach

NSE values for the 2011 model are negative at all locations, but the negative magnitude of the NSE values for the 2011 model are smaller than those associated with the 2010 model for 11 of the 16 beaches that were assessed for both years (68.75%). This suggests that the model predicts *E. coli* concentrations at beaches better for the 2011 backflow event than for the 2010 backflow event. This is true for F_n values between the backflow model years as well. F_n values corresponding to the 2011 backflow model are closer to the optimal value of 0.00 than those values corresponding to the 2010 backflow model for 75% of beaches, respectively (Table 6-4, Table 6-5). A somewhat different trend is seen upon comparison of RSR values at the beaches; the magnitude of RSR values at 10 of the 16 beach locations (62.50%) are larger for the 2011 model than for the 2010 model.

The difference in predictive ability between 2010 and 2011 backflow events may be due in part to the unique conditions created by the 2011 storm. During the 2011 backflow event, the storm moved over Chicago quickly, and while the CRCW and Wilmette outlets released stormwater for nine and 10 hours, respectively, 83.66% of the precipitation associated with the storm fell within roughly three hours, at the beginning of the storm (NOAA National Weather Service, 2011). Therefore, an excessive amount of water was released to Lake Michigan over a very short period of time, potentially leading to a bias toward the over-estimation of *E. coli* at and near the outlets during the beginning of the backflow event. The over-prediction may then be moderated by the smaller flowrates after the initial stormwater pulse, which could lead to more reliable *E. coli* concentration predictions over time. In contrast, the 2010 backflow event lasted 17 hours, and the outlets released a relatively steady flow of water over the majority of the backflow period. This lack of a strong pulse of stormwater and *E. coli* to the lake may lead to an overprediction of *E. coli* concentrations at beaches for a longer period, post-backflow event. The results presented herein suggest that the current model may be more applicable to backflow releases associated with short, strong storms rather than longer or more steady releases of water to the lake. Coupling of this model and a calibrated watershed model tracking stormwater from upstream of Chicago or additional observational data at the river outlets may improve upon the simulation of nearshore *E. coli* in response to storm events.

6.3.3. Insights From 2010 and 2011 Backflow Plume Model Validation

The negative NSE values, RSR values that exceeded 1.0 and F_n values that approached or exceeded 1.0 at times suggest that there may be substantial room for improvement in the model's predictive ability upon addition of other *E. coli* sources in the nearshore zone. Water quality models in other areas of southern Lake Michigan have been shown to more effectively simulate beach water quality near a river outlet, via higher R^2 values, lower RMSE values, and more optimized values of NSE, PBIAS, RSR and F_n (Safaie et al., 2016b). However, the models that produced those results were developed in the context of a river outlet that consistently releases water to the lake, rather than an outlet that intermittently contributes stormwater to the nearshore zone. For the models presented here, the river outlets do not release water to Lake Michigan until there is an extreme storm and backflow event. These extreme storms may create conditions that impact hydrodynamics and water quality differently than smaller storms or calm conditions, leading to potentially unexpected trends in beach *E. coli* concentrations (Weiskerger et al., 2019). As a result, it is possible that decay parameters and *E. coli* concentration estimates that are reasonable for river outlets that consistently release small volumes of water to the lake may not be applicable to river outlets that intermittently release large volumes of stormwater.

An additional confounding factor associated with these model validations is the lack of observational data corresponding to *E. coli* concentrations at beaches during and immediately after backflow events. The plots comparing observed and simulated *E. coli* concentrations at beaches show that the models seem to capture many of the water quality patterns at the beaches, but the statistics indicate that the simulated values often do not correspond to specific observations at specific times. This may be due to uncertainty in sampling times or a lack of high-resolution observational data. CPD monitors the beaches along the shore daily during the swimming season, but samples can be obtained at any time between sunrise and 8:30 am. The roughly three hours between the typical sunrise time in July of ~5:40 am and 8:30 am (ESRL, 2020), combined with variability in sampling time between beaches likely leads to considerable uncertainty in the resulting *E. coli* concentration data. The monitoring results are accessible only as daily data from Illinois BeachGuard (IDPH, 2018) and do not include an exact sampling time, so the uncertainty in sampling time extends to any analyses performed on the data. This can potentially lead to apparent errors in analyses and low validation statistics. In this analysis, model statistics were presented for model time steps that produced the best match to the observed *E. coli* concentrations at each beach.

Since storm events can cause rapidly changing wind, wave and current conditions at beaches (NOAA, 2018a, 2018b) (Figure 6-16), daily monitoring data may not provide adequate temporal resolution for model validation more broadly. Therefore, effective evaluation of modeled *E. coli* in the context of extreme storms would benefit greatly from observational water quality data at higher temporal resolution. Notation of specific sampling times accompanying monitoring data would also aid in more effective model validation for assessment of water quality conditions at beaches during and after extreme storm events that causes backflows in southern Lake Michigan.

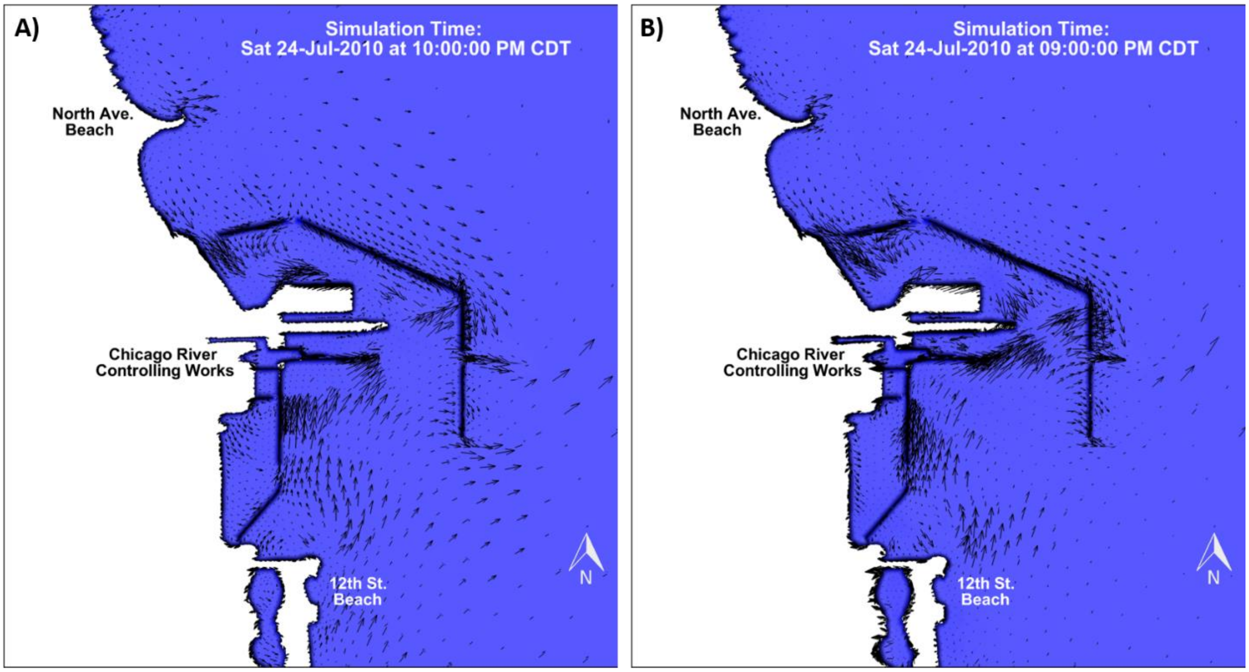

Figure 6-16: Maps of current vectors along part of the Chicago shoreline during two successive hours at the end of the July 2010 backflow event, showing the differences in the current field that can occur within an hour during a storm event. Maps correspond to conditions at 9:00 pm (A, left) and 10:00 pm (B, right) on July 24, 2010

Further uncertainty may come from a lack of specific knowledge of sampling locations at the beaches and depth in the water column that samples were taken from. It is generally accepted that water quality monitoring samples should be obtained from locations at the center of the beach along the shore, rather than on one side or the other (CPD, 2020; USEPA, 2010), but the exact locations of samples at each beach are not tracked within the Illinois BeachGuard repository (IDPH, 2018). With a lack of specific GPS location data for each sample, validation comparisons may be impacted by spatial uncertainty along the beaches. As a result, model output corresponding to each node along beach faces were compared to observational data and the results from the node that indicated the best match between observed and modeled *E. coli* concentrations at respective beaches were used for the validation.

A final source of uncertainty in the model of *E. coli* in storm-induced river plumes presented herein may be the discharge *Q* – concentration relationship used to estimate *E. coli* concentrations at the river outlets. While this relationship seems to have adequately estimated *E. coli* from river discharges, it was originally developed in the context of a river flowing into Lake Michigan at all times (Safaie et al., 2016b). The changes in conditions between a river constantly flowing into the lake and the three rivers in Chicago, which only flow into Lake Michigan during heavy storms, may lead to inability to accurately estimate *E. coli* concentrations from the associated large *Q* values. As a result, it is possible that the initial *E. coli* concentrations at the river outlets are incorrectly estimated. Without observational *E. coli* data at the outlets, though, it is impossible to assess the accuracy of the estimates derived from the *Q* – concentration relationship. Therefore, the reliability of the *E. coli* concentration estimates at the river outlets remains a possible source of uncertainty in the model.

Given the considerable sources of uncertainty that could contribute to low predictive ability in the coupled hydrodynamic and Lagrangian particle tracking model for *E. coli* in storm-induced river plumes, the model simulated *E. coli* concentrations at beaches reasonably well. Validation indicates that the model would benefit from additional refinement and higher resolution input and observational data. However, high R^2 values at several beaches along the Chicago shore suggest that the model can simulate *E. coli* nearly as well as other water quality models in southern Lake Michigan (Liu et al., 2006; Safaie et al., 2016b; Thupaki et al., 2010). While current simulation results may not be reliable for all beach locations, the model results can still provide some insight into water quality at beaches in response to heavy storm events that foster backflows to the Lake Michigan nearshore zone. Likewise, results may be useful in future planning and policy-development for effective beach management that can balance public health with the economic benefits of opening beaches to recreation.

6.3.4. *E. coli* Concentration Patterns in Response to Backflow Events and Implications for Beach Management

In spite of some uncertainty surrounding the reliability of modeled *E. coli* concentrations at beaches, results of models tracking storm-induced river plumes may provide some insight into *E. coli* spatiotemporal patterns at Chicago beaches in response to heavy storm events.

Time series plots of *E. coli* concentration at Chicago beaches from the 2010 and 2011 backflow events suggest that elevated *E. coli* may be detected at the beaches for days to weeks post-backflow event, but that concentrations can be highly variable hour-to-hour. For example, at Oakwood beach, the model simulated *E. coli* concentrations at 10:00 pm and 12:00 am on July 30–31, 2010 as 2.51 $\log_{10}$(MPN 100 ml^{-1}) and 0.00 $\log_{10}$(MPN 100 ml^{-1}), respectively (Figure 6-17a). The 2011 model showed similar results, particularly at locations such as Margaret T. Burroughs beach (Figure 6-17b). This variability was also seen in results for multiple other beaches in 2010 and 2011 and may be associated with changes to currents and wind patterns at small time scales, that can move *E. coli* in the plumes toward and away from shore. Nonetheless, modeled *E. coli* concentrations show that beaches may be contaminated by the storm-induced plumes to a degree that they require a swimming advisory multiple times and up to 14 days after the beginning of the backflow release (Figure 6-18). Simulated *E. coli* concentrations reached the maximum detection value of 2.37 $\log_{10}$(MPN 100 ml^{-1}) at some point in both 2010 and 2011 at all beaches for which validation was completed. This indicates that *E. coli* in storm-induced river plumes has the potential to substantially degrade recreational water quality after backflow events in Chicago. While results seem to support the current CPD practice of closing all beaches during and immediately after backflow events, it is possible that this practice does not go far enough. Elevated *E. coli* levels were simulated for up to 14 days, post-backflow event, so it is possible that storm-induced river plumes may present human health risks at beaches for longer than previously thought.

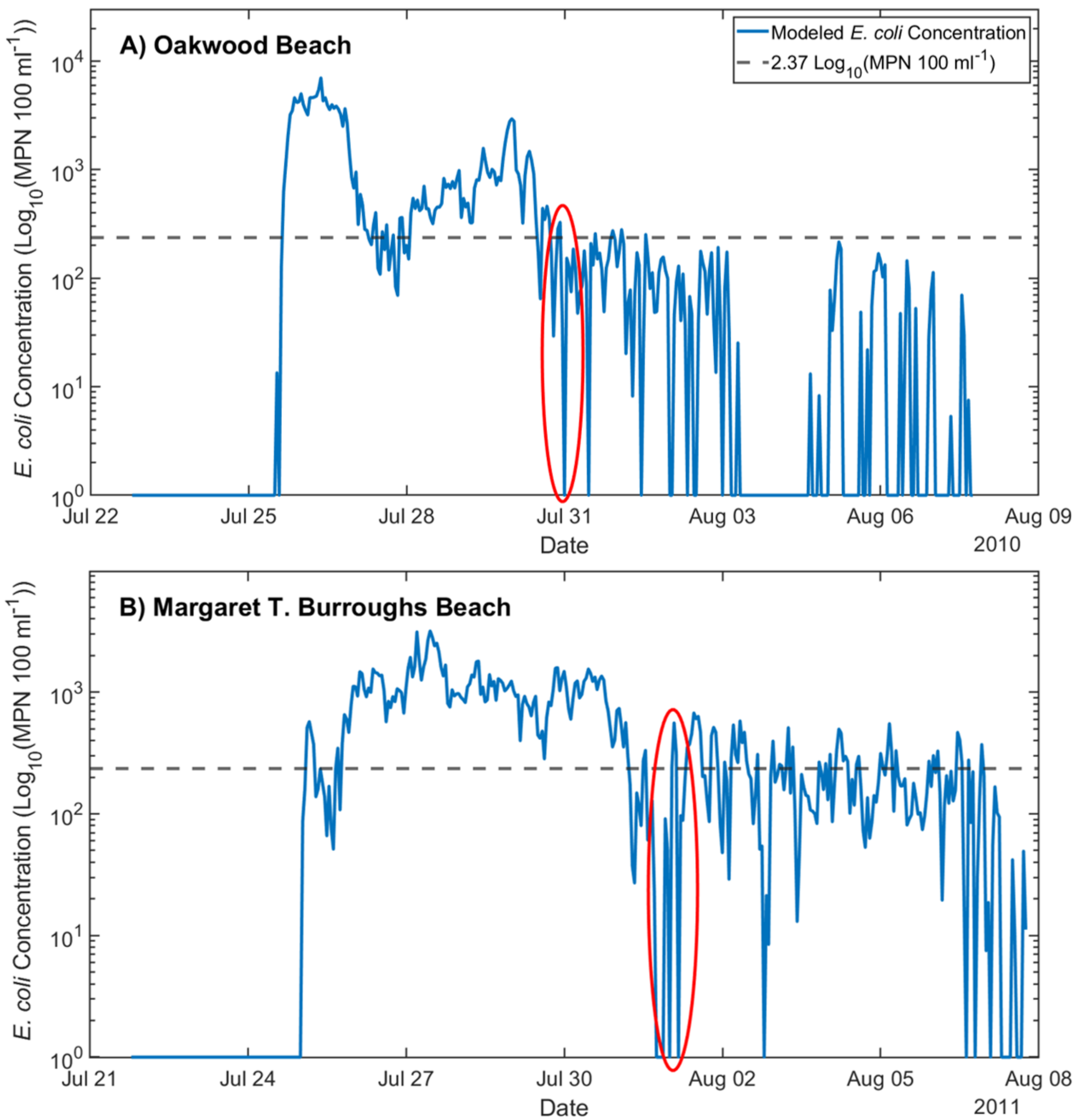

Figure 6-17: Time series plot for E. coli at Oakwood Beach following the July 2010 backflow event (A, top) and Margaret T. Burroughs beach following the July 2011 backflow event (B, bottom), showing large variability in E. coli over hourly time scales (highlighted by the red circle)

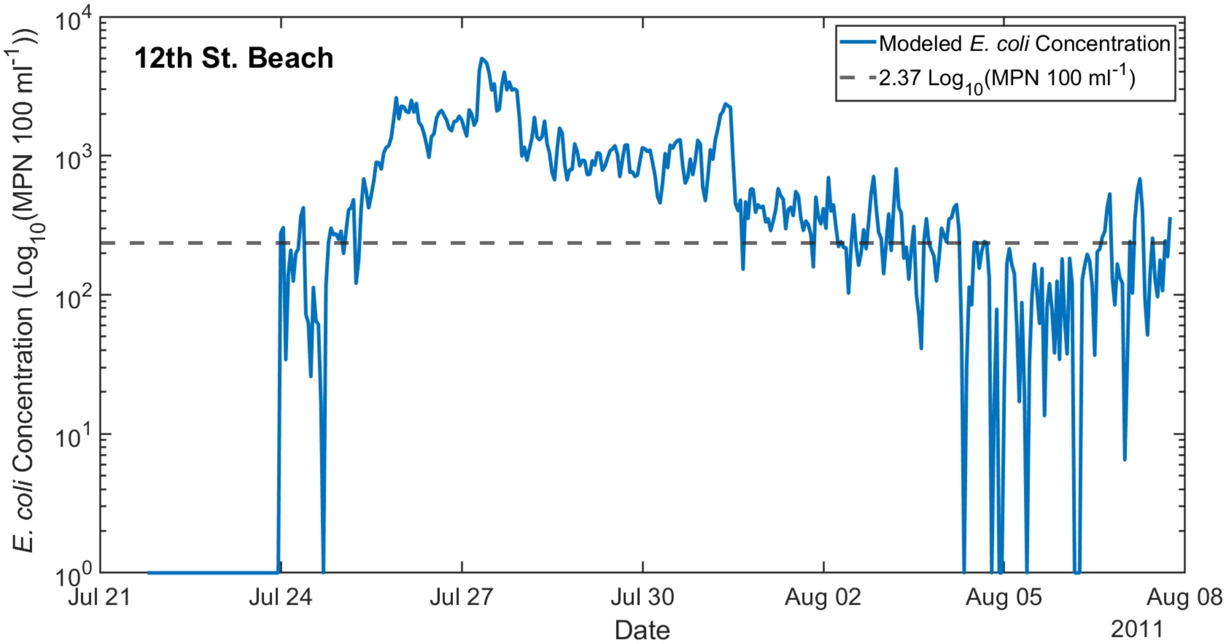

Figure 6-18: Time series plot of E. coli at 12th St. beach following the July 2010 backflow event, indicating that the beach is susceptible to contamination leading to swimming advisories for up to 14 days, post-backflow event

Results also indicate that there may be a diurnal pattern of *E. coli* concentrations at beaches, suggesting that contamination frequently peaks between 12:00 am and 4:00 am daily and is minimized between 12:00 pm and 4:00 pm (Figure 6-19). This pattern follows the diurnal cycle of contamination at previously observed at beaches (Boehm et al., 2002; Ho et al., 2011; Whitman and Nevers, 2004) and is likely a response to the effect that solar inactivation has on microbial contaminants such as *E. coli*.

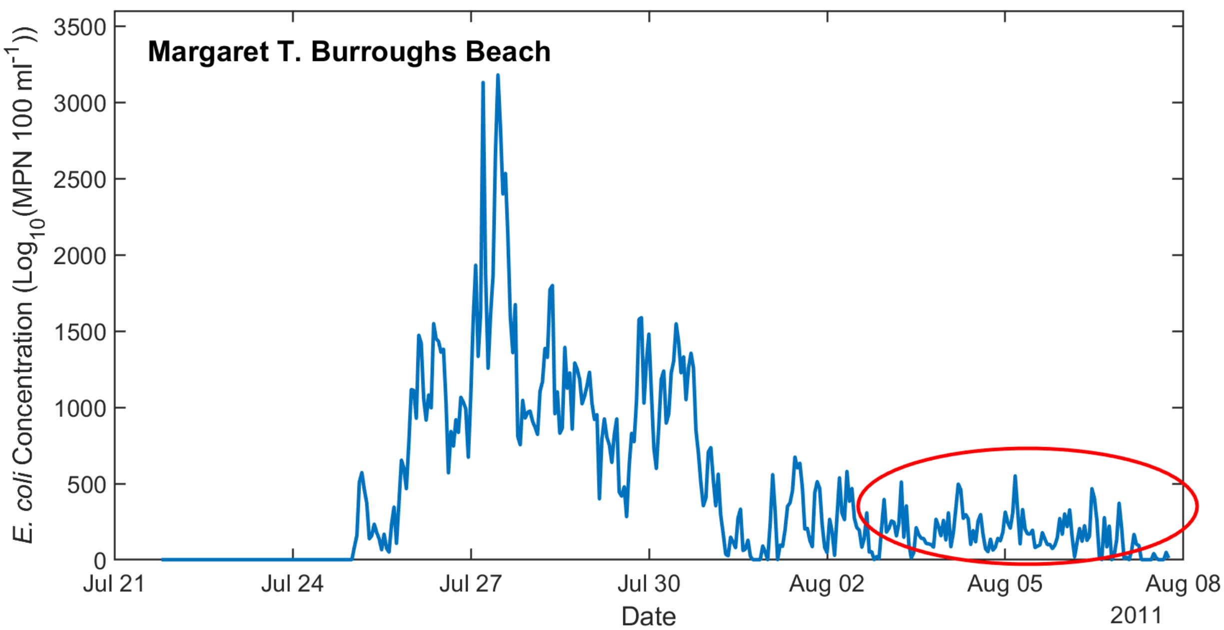

Figure 6-19: Time series plot of E. coli concentration at Margaret T. Burroughs beach, following the July 2011 backflow event. Diurnal patterns in E. coli are highlighted by the red circle

The high degree of spatiotemporal variability in *E. coli* concentrations at beaches following storm and backflow events underscores the importance of vigilance in beach management and monitoring. Model results indicate that *E. coli* concentrations at beaches can change drastically over the course of hours, and that the concentrations obtained from monitoring data collected in the morning may be significantly different from expected concentrations in the afternoon. As a result, daily monitoring occurring in the morning may not lead to reliable indication of beach safety, especially if beachgoers visit the shoreline in the afternoon. Thus, it may be beneficial for beach management agencies to implement more frequent sampling and microbial enumeration at beaches, to better protect public health throughout the day. Similarly, these results show the importance of monitoring at each individual beach because *E. coli* concentration trends at the 24 Chicago beaches have all shown differential responses to the backflow events and their associated river plumes.

Models such as the coupled hydrodynamic and Lagrangian particle tracking model presented herein may not be readily accessible to beach managers, due to the computational and technical resources that they require. However, the results from the model may yield useful statistical relationships that can allow for empirical prediction of some of the impacts of storm-induced plumes on *E. coli* concentrations at Chicago beaches. Spearman correlation and multiple linear regression analyses were performed to determine relationships between beach proximity to the CRCW and Wilmette outlets, time to elevated *E. coli* concentrations (initial increase of modeled *E. coli* concentration to above 0 MPN 100 ml^{-1}), average *E. coli* concentration and timing of the last exceedance of the 2.37 $\log_{10}$(MPN 100 ml^{-1}) concentration threshold for safe recreation over the model time periods.

Spearman correlation analyses suggested that beach proximity to the Wilmette outlet is significantly correlated with average *E. coli* concentration at the beach ($p = 5.62*10^{-6}$) and timing of final exceedance in the model ($p = 2.08*10^{-4}$), but not with time to elevated *E. coli* after backflow release ($p = 0.14$). Beach proximity to the CRCW outlet was not significantly correlated with time to elevated *E. coli* ($p = 0.20$) but was significantly correlated with both average *E. coli* concentration ($p = 0.023$) and timing of final exceedance ($p = 0.01$). Multiple linear regression analysis stemming from these correlations provided predictive equations that could be useful for beach managers in Chicago looking to predict timing and magnitude of plume effects at beaches. These equations may estimate the times of initial *E. coli* increase and final exceedance of 2.37 $\log_{10}$(MPN 100 ml^{-1})) at a beach (*TimeEC* and *TimeExceed*, respectively, hr after backflow event start) and average *E. coli* concentration at a beach, calculated from both 2010 and 2011 model results (*AvgEC*, $\log_{10}$(MPN 100 ml^{-1})) (Eq. 6-9, 6-10 and 6-11, respectively). The equations rely on beach proximity to the Wilmette and CRCW outlets (*ProxW* and *ProxC*, respectively) (km) and backflow duration (*Duration*, hr) as predictors. These predictors are all either known (*ProxW* and *ProxC)* or can be forecast given weather predictions and resulting plans for backflow periods (*Duration)*. The resulting multiple linear regression equations capture 54.25%, 54.93% and 64.43% of the variability in the *TimeEC*, *AvgEC* and *TimeExceed* data from the beaches (p = $1.03*10^{-7}$, p = $7.62*10^{-8}$ and p = $1.40*10^{-10}$, respectively).

$$TimeEC = 1.15(ProxW) + 2.98(ProxC) - 3.71(Duration) - 74.96 \tag{6-9}$$

$$AvgEC = -0.03(ProxW) - 0.02(ProxC) + 0.08(Duration) + 2.44 \tag{6-10}$$

$$TimeExceed = -2.38(ProxW) - 7.21(Duration) + 523.01 \tag{6-11}$$

In the absence of *in situ* monitoring data that may be dangerous to obtain during and after heavy storm events (MWRD, 2019; USEPA, 2010), these equations may be beneficial for beach managers. Estimates can lend insight into when beaches may be impacted by elevated *E. coli* concentrations. They can, in turn, allow for prediction of when to begin issuing swimming advisories and when to potentially remove the swimming advisories at each beach. Similarly, the equations can reasonably estimate average *E. coli* concentrations during and after the storms, allowing for some understanding of the magnitude by which plumes can elevate *E. coli* concentrations during and immediately after heavy storms.

6.4. Conclusions

The impacts of heavy storms and their subsequent river plumes on the nearshore zone in southwestern Lake Michigan were simulated using a coupled numerical hydrodynamic and Lagrangian particle tracking model. Storm-induced river plumes were modeled for storm events that produced backflow of water from the North Shore Channel and Chicago River to Lake

Michigan in 2010 and 2011, to assess the trends in resulting *E. coli* concentrations at 16 – 18 beaches along the shore.

The model developed was able to simulate up to 78.47% of the variability in *E. coli* concentrations at beaches in Chicago. Validation showed substantial variability in the model's predictive ability between individual beaches. At some locations, the model was unable to predict any of the variability in the observed data from Illinois BeachGuard (IDPH, 2018). At other locations, the model predicted observed data at levels comparable to previously published models of ambient *E. coli* levels at the beaches. Generally, *E. coli* concentration observations were better reproduced for beaches south of the CRCW outlet, while observations were relatively poorly simulated at beaches between the Wilmette and CRCW outlets, potentially owing to the simultaneous simulation of two storm-induced river plumes as *E. coli* sources modeled for beaches north of CRCW. The model simulated *E. coli* concentrations corresponding to the 2011 backflow event marginally better than it did for the 2010 backflow event. This may be due to the variation in durations and flowrates of stormwater releases to the lake during the storm events (NOAA National Weather Service, 2011) and underscores the need for additional observational data for both providing initial and boundary conditions as well as for adequate model validation and refinement.

Model results presented herein apply to relatively small backflow events in Chicago, which involve stormwater release from the Wilmette and CRCW outlets but not the O'Brien outlet located south of downtown Chicago (MWRD, 2019; USACE, 2014). Additional model development and validation would be needed for adequate prediction of water quality during and after larger-scale backflow events leading to discharge from all three outlets. Nonetheless, there have only been two backflow events that yielded stormwater releases from the O'Brien outlet between 2000 and 2017, occurring in 2008 and 2013. Currently, there is a notable lack of *in situ* microbial water quality monitoring data associated with the 2008 and 2013 backflow events, due to their timing outside of the swimming season (USACE, 2014). This lack of monitoring data would further challenge the validation process for any model of these larger backflow events. However, the majority of backflow events in recent years (17 of 19, 89.47%) have involved stormwater releases from Wilmette and/or CRCW outlets only (USACE, 2014). As a result, the numerical and statistical models presented herein are expected to reasonably simulate and predict water quality patterns at Chicago beaches in response to the majority of backflow events in southwestern Lake Michigan. Future backflow events may be expected to follow this pattern, whereby most events will likely involve releases from Wilmette and/or CRCW only. This is due to the recent and ongoing implementation of the Tunnel and Reservoir Plan (TARP) (MWRD, 2020), a large-scale infrastructure project designed to prevent flooding and stormwater release via backflow in Chicago.

Storm events and their impacts on the nearshore zone are notoriously understudied because of the physical risk involved in data collection during and after heavy storms (MWRD, 2019; USEPA, 2010). This lack of study, combined with the potential for significant impacts of storms on safety and public health at beaches (IDPH, 2018) warrants additional research and characterization of storm-induced river plume effects in the nearshore zone. Numerical simulation of conditions can provide some of that characterization, via the use of calibrated models (Bravo et al., 2017; Nekouee et al., 2015a), but existing models often do not account for microbial water quality effects of the plumes. The results presented herein not only provide an initial example of how to model the impacts of heavy storms on recreational water quality but highlight considerable gaps in knowledge that can hinder the subsequent assessment of water quality impacts from storms. Model validation results suggest that the coupled hydrodynamic and Lagrangian particle tracking model developed can reproduce observed *E. coli* concentrations at Chicago beaches reasonably well, given a relative lack of *in situ* observational data. While statistics presented here indicate a comparable but somewhat lower predictive ability for this model compared to other water quality models developed for southern Lake Michigan (Liu et al., 2006; Safaie et al., 2016b; Thupaki et al., 2010), they also show that the model holds promise, especially if additional observational data are available for future storm events.

7. Conclusions

Nearshore environments such as beaches are frequently popular destinations for tourism, which can in turn bring revenue to local municipalities. This is the case for areas along the shores of the Laurentian Great Lakes such as Chicago. The 24 beaches along Chicago's shoreline draw 14 – 31 million visitors annually (Nevers and Whitman, 2011), which can lead to millions of dollars of tourism revenue for the area (Shaikh, 2012). However, beach tourism relies upon the safety of recreation at beaches and that safety can be challenged by microbiological contamination in water (DeFlorio-Barker et al., 2016; Dorevitch et al., 2012; Fleisher et al., 2010; Wade et al., 2008).

An association between precipitation events and recreational water quality degradation has been established (Coffey et al., 2018; Curriero et al., 2001). With a projected increase in both frequency and intensity of storm events in response to climate change (IPCC, 2014) it can be expected that water quality degradation will become more common in the coming years. Therefore, it is crucial that research focus on the effects of extreme storm events on nearshore water quality, to ensure the health of beachgoers. This is especially true for the Chicago area, because its flow regime involves stormwater release from the Wilmette, Chicago River Controlling Works (CRCW) and O'Brien outlets only during extreme storms that can cause extreme water quality degradation (City of Chicago, 2014; MWRD, 2019). Despite this need for additional research regarding beach responses to extreme storm events, collection of *in situ* beach monitoring data can be dangerous during and immediately after storms. Therefore, numerical and statistical models can be valuable sources of information and predictions of future conditions and their effects on public health.

Coupled hydrodynamic and Lagrangian particle tracking models (Huang et al., 2019; Nekouee et al., 2015b) were developed and validated to assess the spatiotemporal scales of storm-induced river plumes in southwestern Lake Michigan and along the Chicago shoreline. These models were also expanded to include the fate and transport of *E. coli* within the plumes, to form an initial approach for evaluating the impacts of storm-induced river plumes on beach water quality in Chicago.

Before developing the coupled hydrodynamic and Lagrangian particle tracking model, optimization of the hydrodynamic model for southern Lake Michigan was completed in the context of the turbulent Prandtl number. This number, a ratio of the influence of momentum (eddy viscosity) and temperature (thermal eddy diffusivity) effects on hydrodynamics (Chen et al., 2006; Ye et al., 2019), can impact model predictive ability but is frequently overlooked in modeling research. 13 models were set up and run as a sensitivity analysis to assess the impacts of turbulent Prandtl number on both hydrodynamics and water quality model results. These models suggested that different turbulent Prandtl numbers could optimize model predictions for water temperature, currents and water quality. Overall, it was determined that effective coupled hydrodynamics and water quality models in southern Lake Michigan should use a turbulent Prandtl number derived from a horizontal Prandtl number of 0.14 and a vertical Prandtl number of 0.1, validating its use in some previous southern Lake Michigan models (Safaie et al., 2016b).

Using the optimal turbulent Prandtl number derived from the sensitivity analysis, two approaches to storm-induced river plume modeling were undertaken, an Eulerian approach and a Lagrangian approach. These two methods differ predominantly in the way that they calculate dispersion of tracers or contaminants within plumes and in the way that they characterize tracers or contaminants in plumes. Results of the two approaches were compared via validation against MODIS satellite imagery for southern Lake Michigan in September of 2008 and October of 2017 (Vermote, 2015). As a result of the differences in their calculation of plume dispersion, the Lagrangian method simulated plumes with smaller surface areas than the Eulerian method. At two validation time periods after the 2008 backflow event, September 16, 2008 at 12:00 pm and October 16, 2017 at

12:00 pm, the Lagrangian method produced plume surface areas that were 22.50% and 0.66% smaller than those produced via the Eulerian method.

Via comparison with MODIS satellite imagery of the plumes, it was determined that the Lagrangian method-produced plumes better captured the available observations of the plumes than the Eulerian method-produced plume simulations. The smaller plumes from the Lagrangian approach yielded smaller errors in more of the plume surface area, alongshore and normal-to-shore extent values of the plumes from 2008 and 2017, compared to those plumes produced by the Eulerian method. It was therefore concluded that future storm-induced river plume modeling in southwestern Lake Michigan should involve the use of a Lagrangian plume simulation through a coupled hydrodynamic and particle tracking model.

Following selection of a coupled hydrodynamic and Lagrangian particle tracking model as the most effective approach to simulation of storm-induced river plumes in the Chicago area, this approach was utilized to simulate the storm-induced river plumes for five major storm events in Chicago. These events, occurring in 2008, 2010, 2011, 2013 and 2017 represented a variety of temporal and seasonal contexts, volumes of stormwater released to the lake and durations of stormwater release. The models for each of these events simulated the fate and transport of the overall plumes released from the Wilmette, Chicago River Controlling Works (CRCW) and O'Brien outlets to Lake Michigan. Plumes were characterized by particle concentrations over time, normalized to the smallest maximum particle concentrations at the river outlets releasing stormwater for each backflow event. Results of the models indicated that plumes in the nearshore region of Chicago persist for hours to weeks after the release of stormwater ceases at the outlets, with a range of five hours to 24 days, post-backflow event. The models also suggested that plume footprints in the nearshore ranged from 7.88 to 291.10 km^2. These modeled plume spatial and temporal scales were correlated with both the volume of water released at the river outlets as well as the duration of stormwater release at the outlets. Higher stormwater release volumes and longer duration releases frequently leading to larger plume footprints and plumes that persist for longer time periods in the nearshore zone, as expected.

To connect the simulation of storm-induced river plumes back to recreational water quality at beaches, the coupled hydrodynamic and Lagrangian particle tracking models were expanded to include *E. coli* fate and transport in the plumes. Previously developed statistical relationships between river discharge *Q* and *E. coli* concentration *C* (Safaie et al., 2016b) were used to estimate *E. coli* concentrations at the river outlets during backflow events as initial conditions for the model. In addition, a previously-calibrated microbial decay function determined via literature review was incorporated into the particle concentration calculation in the Lagrangian particle tracking model to account for base mortality, solar inactivation and sedimentation of *E. coli* in the plumes over time (Liu et al., 2006).

Results of this model were validated against beach monitoring data obtained after backflow events in 2010 and 2011 and showed that the model reasonably captures variability in the monitoring data for both backflow events. Across all beaches and both backflow events, the model was able to capture up to 78.47% of the variability in the available monitoring data. In response to these two backflow events, simulated *E. coli* concentrations at the all of the 16 – 18 Chicago Park District-managed beaches exceeded the 2.37 $\log_{10}$(MPN 100 ml^{-1}) threshold for safe recreation at beaches (USEPA, 2012) for at least one hour of simulation time.

Results of this model for 2010 and 2011 suggest that there is considerable variability in model predictive ability between beaches, with model R^2 values ranging from -0.44 to 0.78 and RMSE values ranging from 0.76 to 2.24 $\log_{10}$(MPN 100 ml^{-1}). The presence of high R^2 values and low

RMSE values for some beaches indicates that the coupled hydrodynamic and Lagrangian particle tracking model for *E. coli* fate and transport holds promise for prediction of water quality impacts from storm-induced river plumes. At the same time, the presence of low R^2 and high RMSE values at other locations suggests that the model leaves substantial room for improvement and additional refinement.

In addition to the conclusions and inferences made in response to numerical model results for storm-induced river plume simulation, statistical methods were used to analyze the numerical model results. These analyses allowed for determination of empirical predictions of plume dynamics and recreational water quality from backflow and beach location information. Backflow duration and either 24-hour antecedent rainfall or volume of stormwater released at the Wilmette and CRCW outlets can be used to estimate the maximum plume footprint in the nearshore (R^2 = 0.95 and 0.94, respectively). Volume of stormwater released from the CRCW outlet and backflow duration at the outlets can also predict time over which plumes persist in the nearshore (R^2 = 0.68). Expanding this framework to include *E. coli* fate and transport, beach proximity to river outlets was found to have some ability to predict the time after the backflow event at which *E. coli* concentration at a beach could be expected to increase (R^2 = 0.54). Further, beach proximity to river outlets could predict average log-transformed *E. coli* concentration at the beach over 2 weeks, post-backflow event (R^2 = 0.55) and time of the latest exceedance of the 2.37 $\log_{10}$(MPN 100 ml^{-1}) threshold for safe recreation (R^2 = 0.64). These empirical equations may be useful to beach managers for estimating the spatiotemporal dynamics and recreational water quality effects of storm-induced river plumes in southwestern Lake Michigan. They may be important for understanding the dynamics of these plumes and how they affect beaches, but also may be useful in determining when and where to advise against swimming at beaches along the Chicago shoreline, given information about the beach location and backflow conditions. The use of the numerical models presented herein may be challenging for beach managers, due to the inherent computational and technical requirements of the models, but these empirical equations are more accessible and useful to managers looking to protect public health in real-time.

Heavy storm events are predicted to become more intense and frequent in the coming decades, in response to climate change (IPCC, 2014). However, due to dangers associated with *in situ* data collection during extreme and after storms, the effects of such storms on nearshore environments and recreational water quality are notoriously understudied (Bravo et al., 2017; McLellan et al., 2007; Nekouee et al., 2015b). In the absence of *in situ* data, numerical modeling can be a powerful tool to enhance understanding of dynamics associated with extreme storms. The development and validation of a coupled hydrodynamic and Lagrangian particle tracking model for characterizing storm-induced river plumes and the fate and transport of *E. coli* therein provided a first step toward increasing that understanding. At the same time, the model also underscored the substantial gaps in knowledge. A model can only be as effective as the data used to initiate it, and since there is a notable lack of observational data regarding storm-induced river plumes and storm-associated recreational water quality, the predictive ability of numerical models remains limited.

Future research in this area should focus on supplementing observational water quality data for southern Lake Michigan during and after heavy storms like those in 2008, 2010, 2011, 2013 and 2017. The dangers associated with collecting field data during storms will remain, so it may be beneficial to collect additional water quality data during storms via autonomous means, such as lab-in-vial systems (Angelescu et al., 2019; Huynh et al., 2016). Further, *in situ* water quality data should be supplemented with quality spatiotemporal metadata, allowing for a reduction in uncertainty associated with where and when samples are obtained. Characterization of plume spatial extents via aerial imagery captured with drones or other unmanned aerial vehicles (UAVs) (Morgan et al., 2020) would help with validation of plume models by providing high resolution imagery of plumes when imagery from satellites like MODIS is obstructed by clouds (Song et al., 2004). These additional data will be crucial to model refinement by minimizing variability and uncertainty associated with observational data used in model development and validation. The models presented herein show reasonable predictive ability for simulation of plume spatiotemporal dynamics and subsequent *E. coli* fate and transport in southwestern Lake Michigan. The frameworks can be used for estimation of plumes and recreational water quality in response to heavy storm events, with some confidence. However, these types of models will rely on additional *in situ* data for further calibration and application to additional locations and storm events, to increase confidence in results.

APPENDICES

APPENDIX A:

Current Comparisons for Models Mich08-2 – Mich08-13

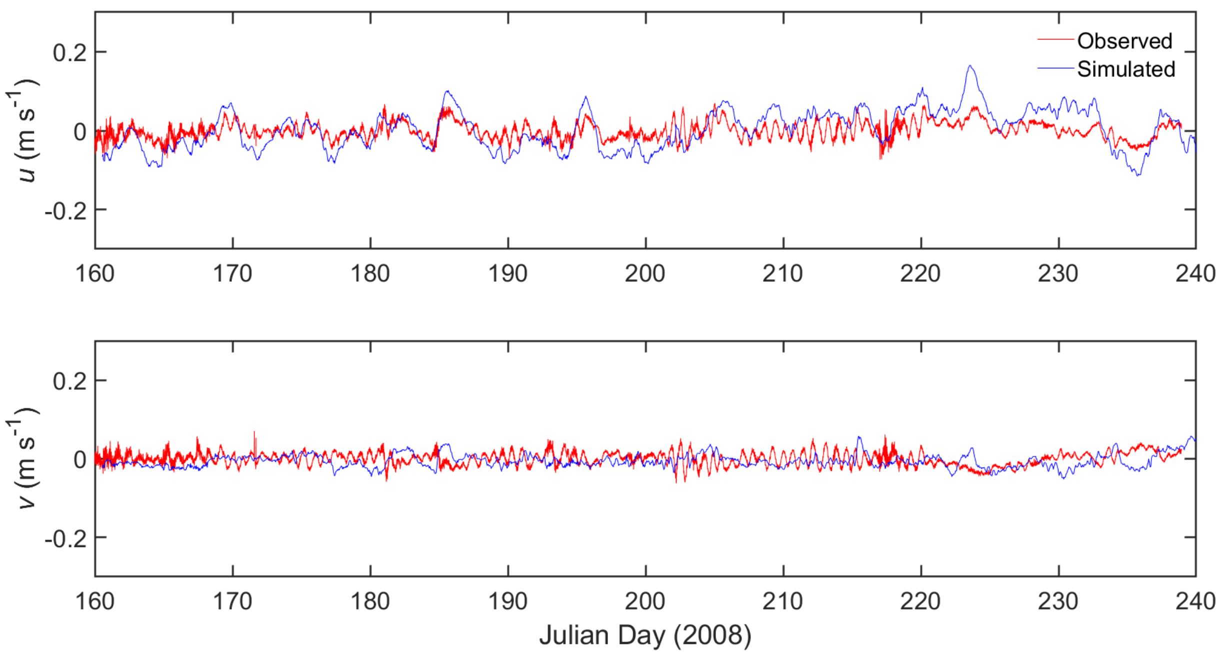

Figure A-1: Plot comparing simulated and observed u- and v-components of current at the MADCP location in Lake Michigan for model mich08-2

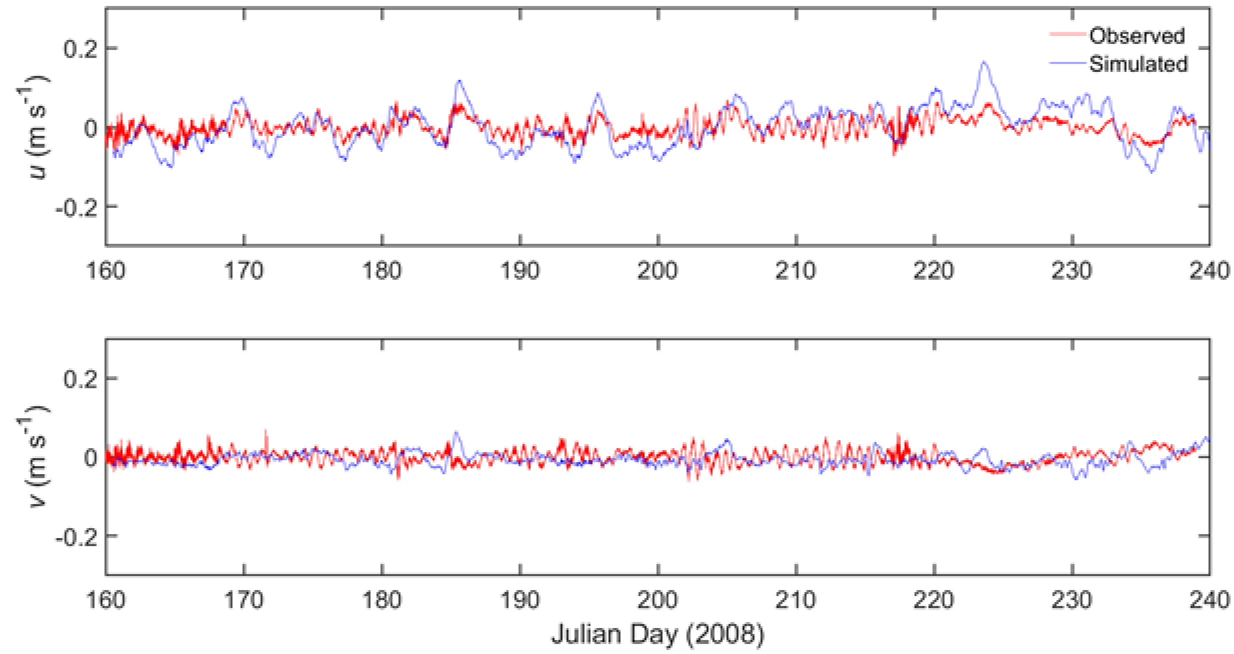

Figure A-2: Plot comparing simulated and observed u- and v-components of current at the MADCP location in Lake Michigan for model mich08-3

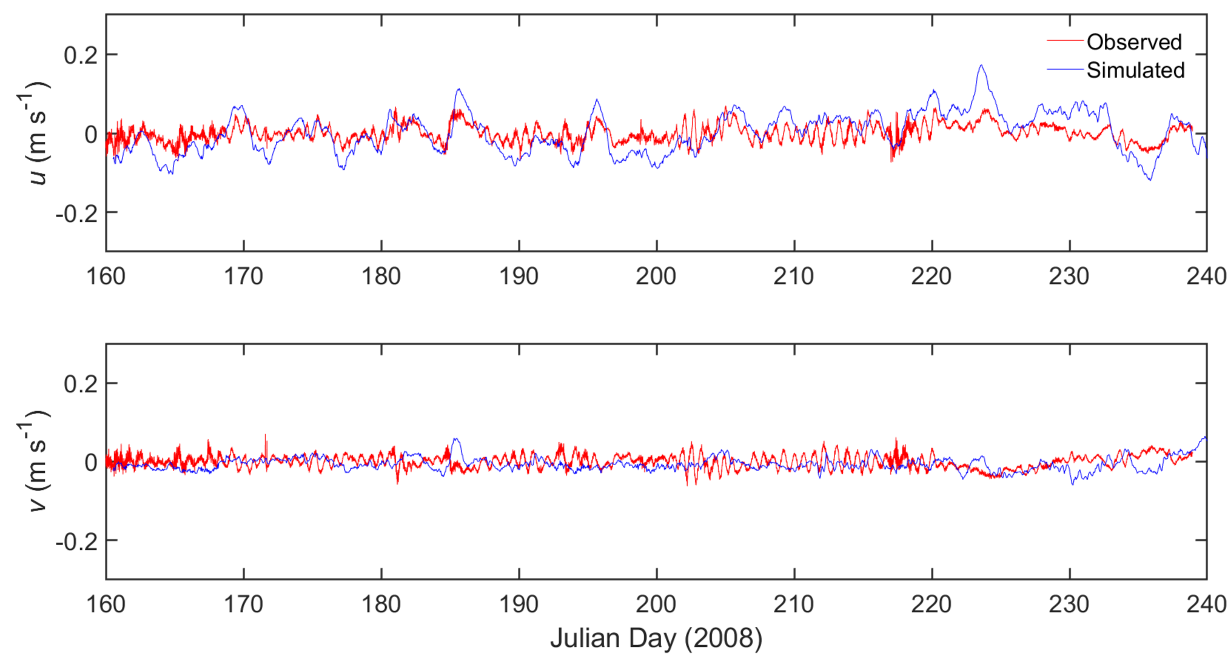

Figure A-3: Plot comparing simulated and observed u- and v-components of current at the MADCP location in Lake Michigan for model mich08-4

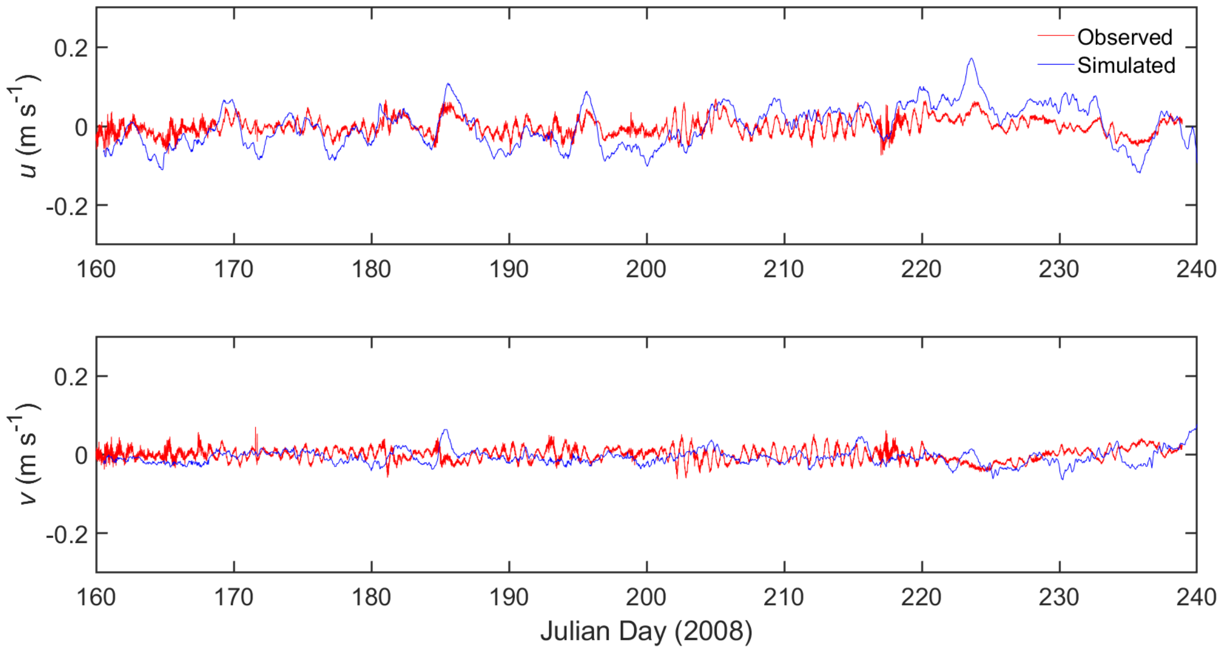

Figure A-4: Plot comparing simulated and observed u- and v-components of current at the MADCP location in Lake Michigan for model mich08-5

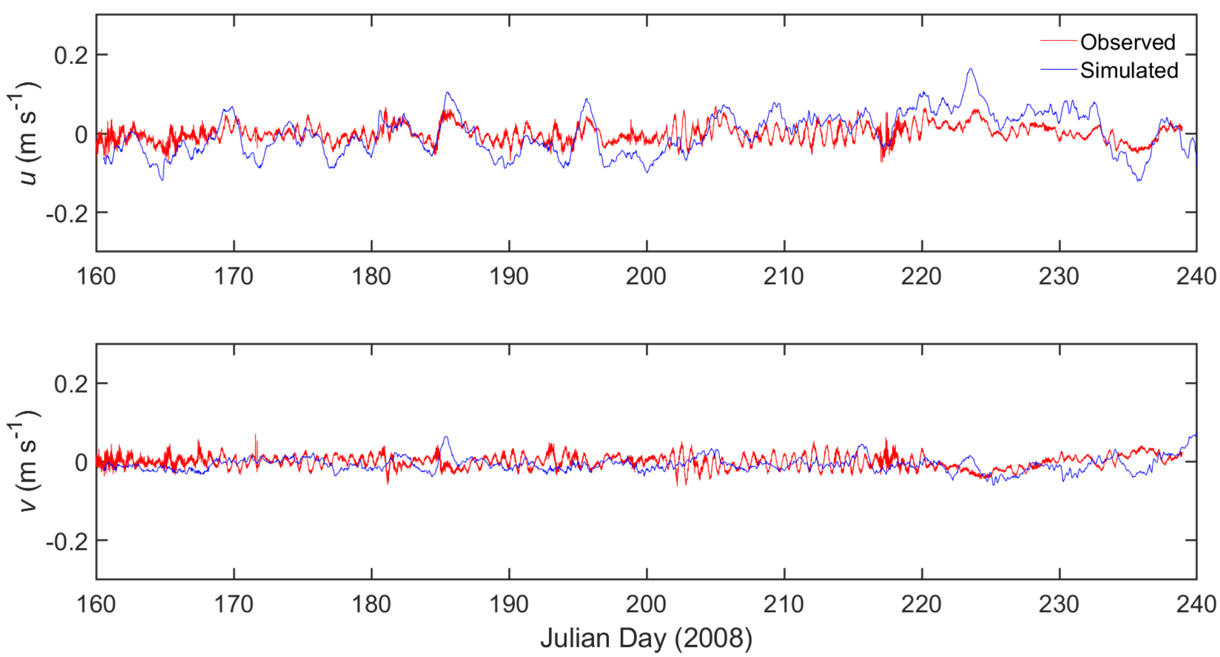

Figure A-5: Plot comparing simulated and observed u- and v-components of current at the MADCP location in Lake Michigan for model mich08-6

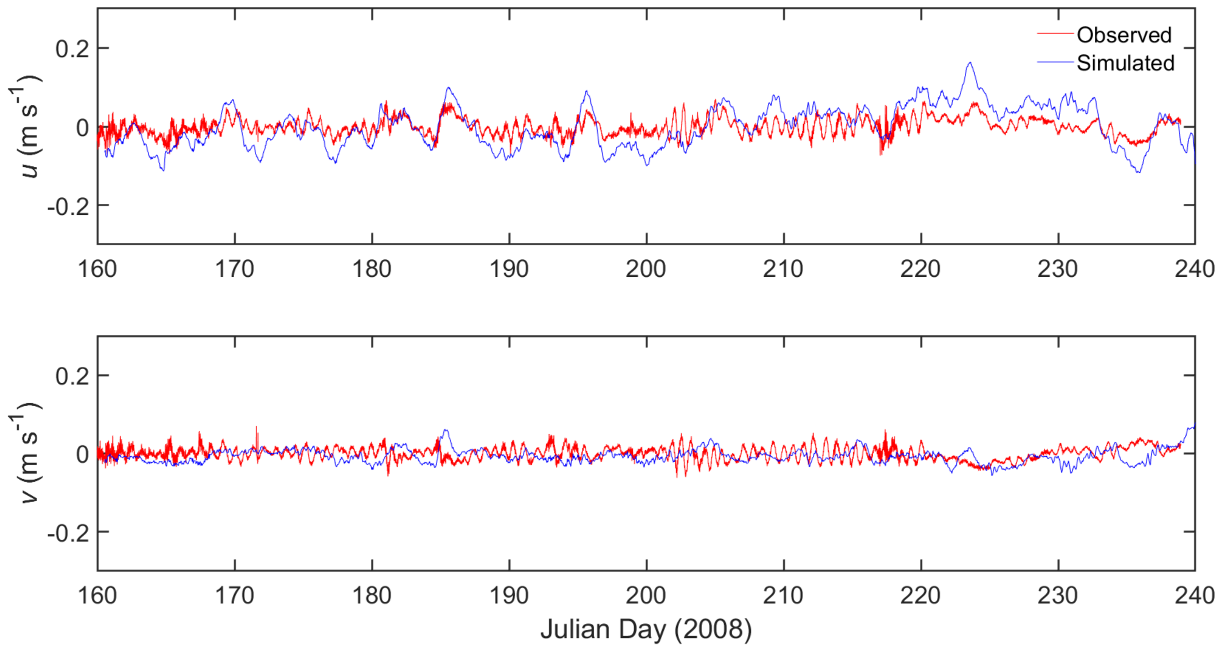

Figure A-6: Plot comparing simulated and observed u- and v-components of current at the MADCP location in Lake Michigan for model mich08-7

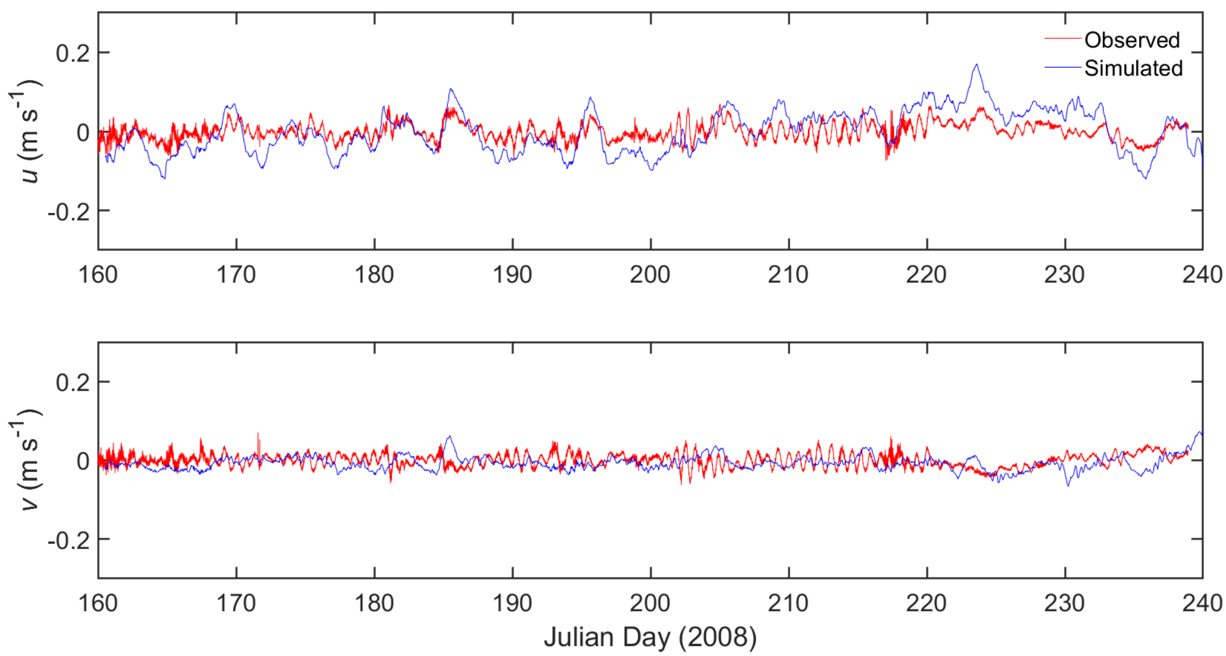

Figure A-7: Plot comparing simulated and observed u- and v-components of current at the MADCP location in Lake Michigan for model mich08-8

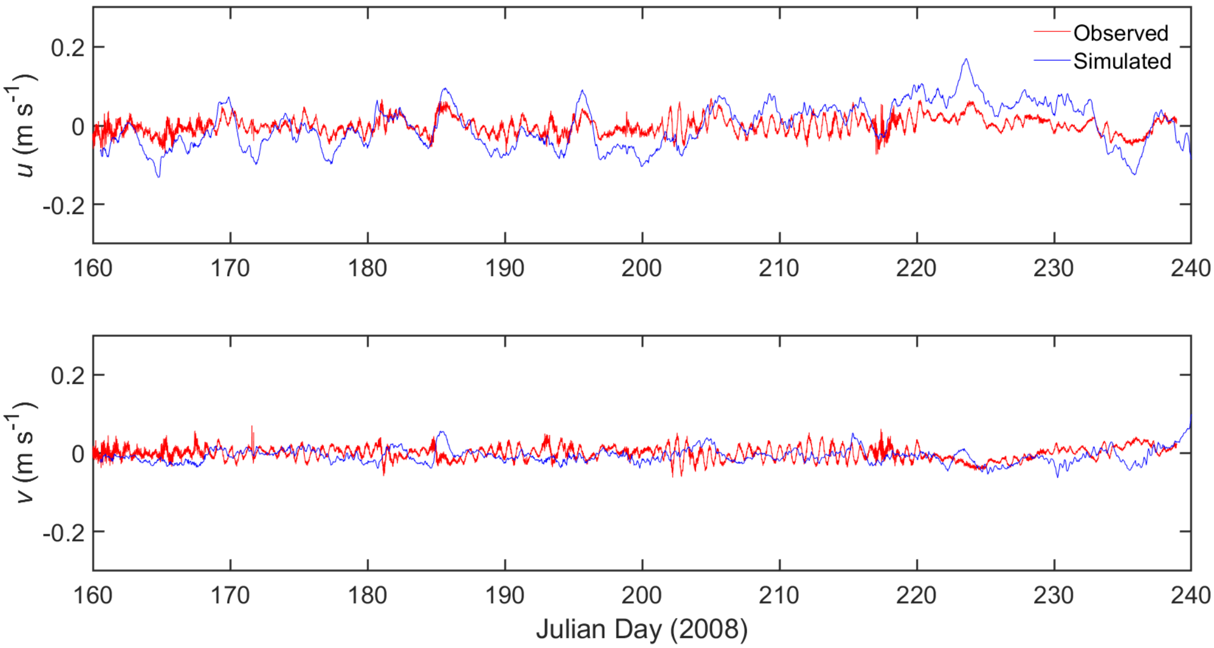

Figure A-8: Plot comparing simulated and observed u- and v-components of current at the MADCP location in Lake Michigan for model mich08-9

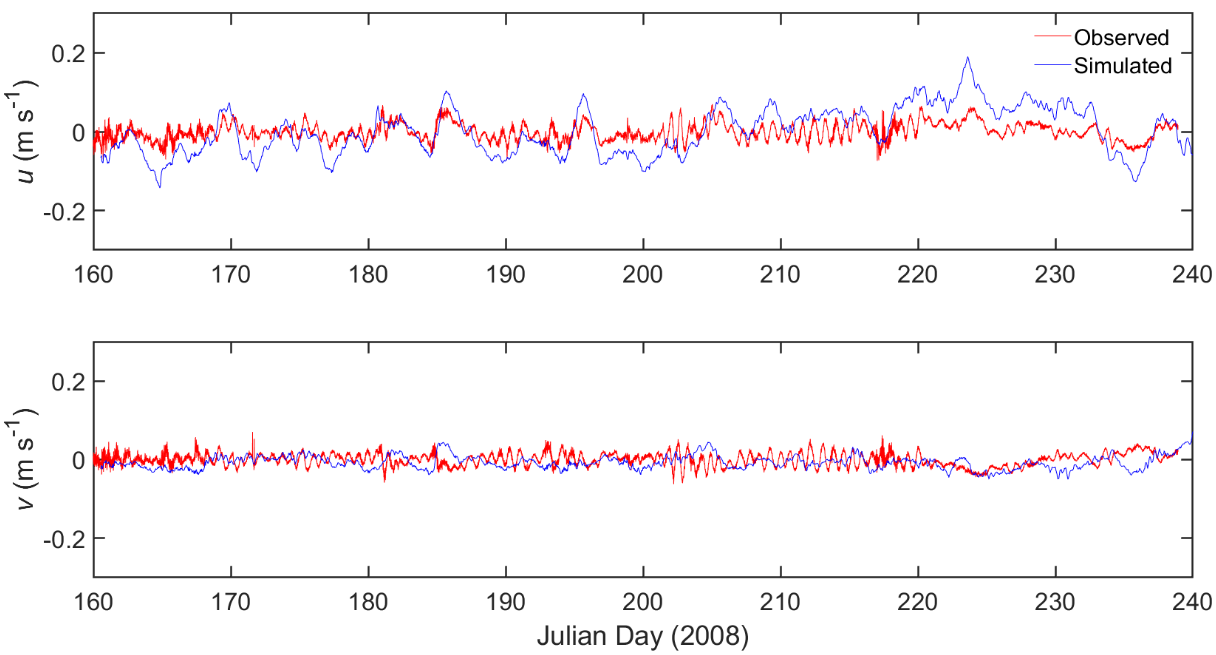

Figure A-9: Plot comparing simulated and observed u- and v-components of current at the MADCP location in Lake Michigan for model mich08-10

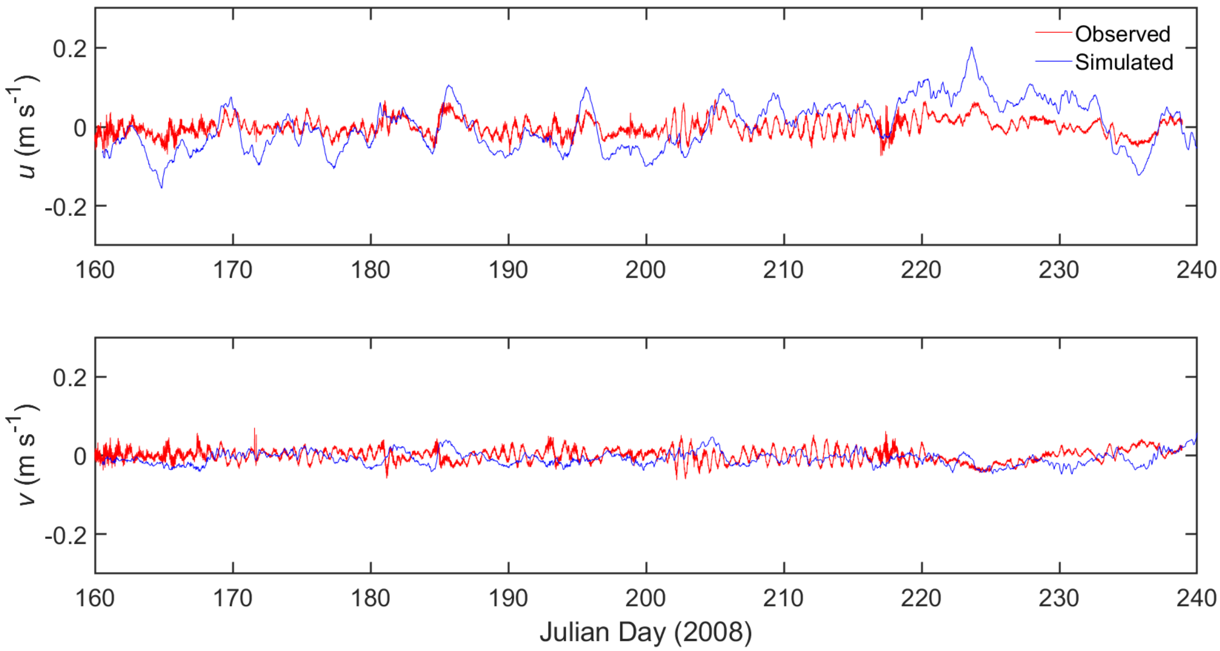

Figure A-10: Plot comparing simulated and observed u- and v-components of current at the MADCP location in Lake Michigan for model mich08-11

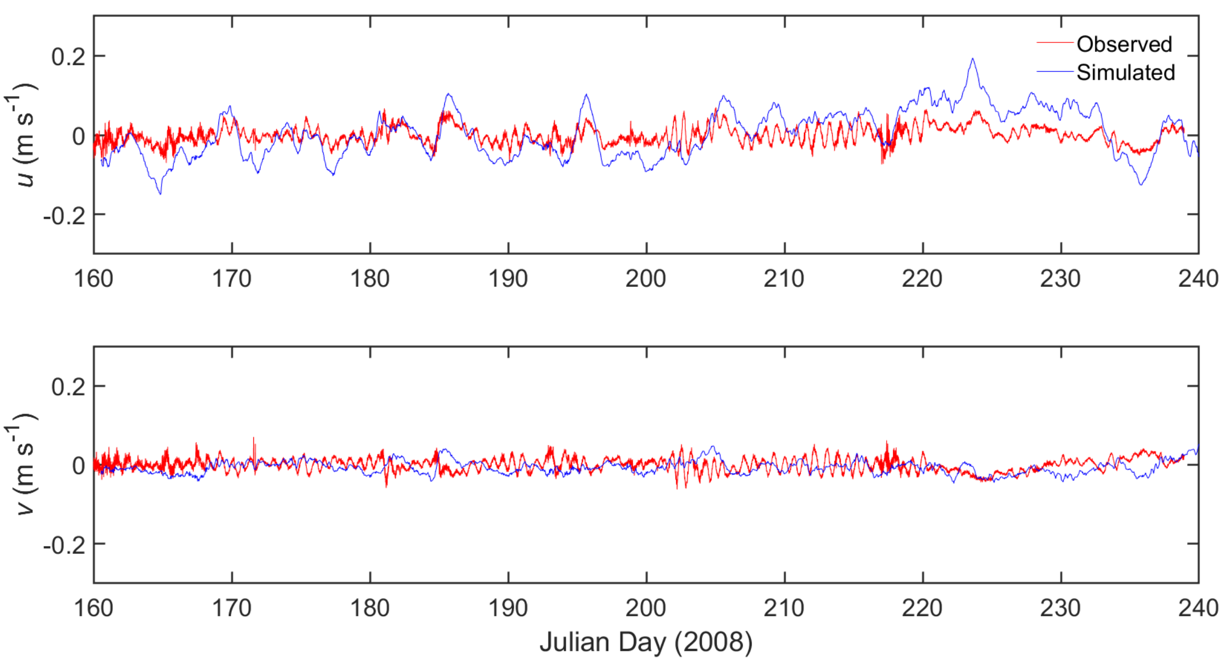

Figure A-11: Plot comparing simulated and observed u- and v-components of current at the MADCP location in Lake Michigan for model mich08-12

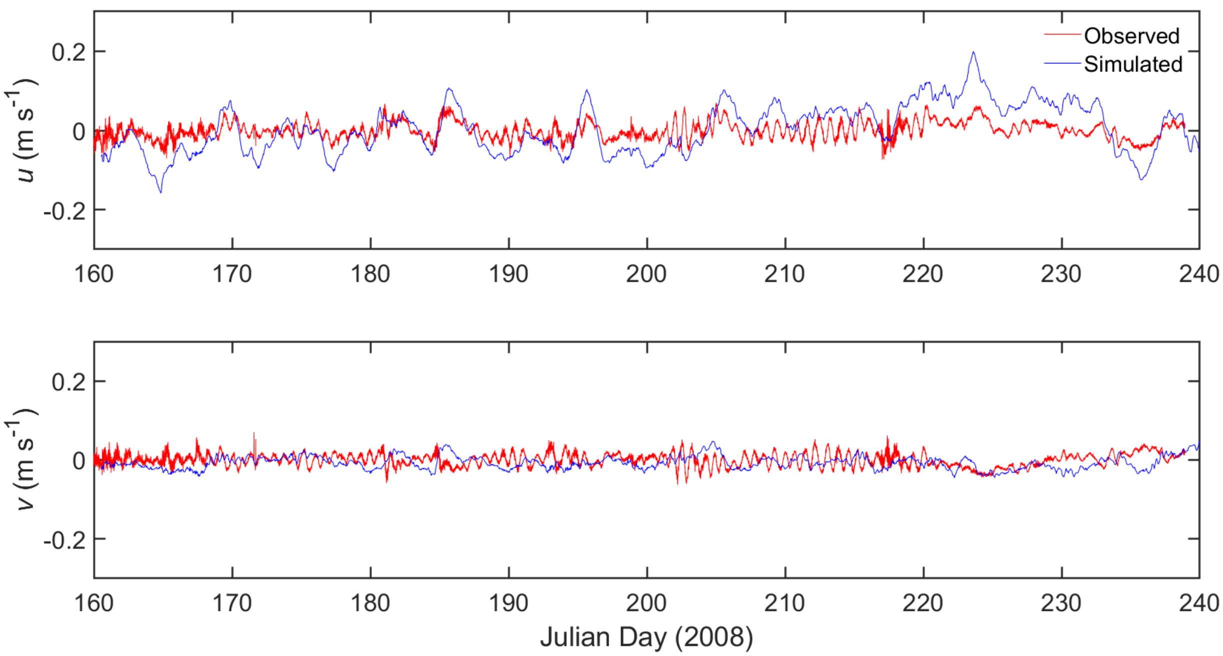

Figure A-12: Plot comparing simulated and observed u- and v-components of current at the MADCP location in Lake Michigan for model mich08-13

APPENDIX B:

Hourly Backflow Data for 2008, 2010, 2011, 2013 and 2017

Table B-1: Discharge time series data showing backflow releases from Wilmette, CRCW and O'Brien outlets in September 2008

Date/Time	Wilmette Discharge ($m^3 s^{-1}$)	CRCW Discharge ($m^3 s^{-1}$)	O'Brien Discharge ($m^3 s^{-1}$)
9/13/2008 0:00	0.00	0.00	0.00
9/13/2008 1:00	0.00	0.00	0.00
9/13/2008 2:00	0.00	0.00	0.00
9/13/2008 3:00	0.00	0.00	0.00
9/13/2008 4:00	0.00	0.00	0.00
9/13/2008 5:00	0.00	0.00	0.00
9/13/2008 6:00	0.00	0.00	0.00
9/13/2008 7:00	175.51	0.00	0.00
9/13/2008 8:00	351.02	0.00	0.00
9/13/2008 9:00	429.03	0.00	0.00
9/13/2008 10:00	380.27	0.00	0.00
9/13/2008 11:00	409.53	157.82	0.00
9/13/2008 12:00	448.53	157.82	0.00
9/13/2008 13:00	331.52	157.82	0.00
9/13/2008 14:00	253.52	263.04	0.00
9/13/2008 15:00	273.02	263.04	0.00
9/13/2008 16:00	253.52	263.04	0.00
9/13/2008 17:00	234.02	263.04	0.00
9/13/2008 18:00	214.51	263.04	22.29
9/13/2008 19:00	195.01	263.04	29.71
9/13/2008 20:00	195.01	263.04	29.71
9/13/2008 21:00	175.51	263.04	29.71
9/13/2008 22:00	156.01	263.04	29.71
9/13/2008 23:00	156.01	263.04	29.71
9/14/2008 0:00	156.01	263.04	29.71
9/14/2008 1:00	156.01	263.04	29.71
9/14/2008 2:00	156.01	263.04	29.71
9/14/2008 3:00	156.01	263.04	29.71
9/14/2008 4:00	156.01	263.04	29.71
9/14/2008 5:00	156.01	263.04	29.71
9/14/2008 6:00	156.01	263.04	29.71

Table B-1 (cont'd)

9/14/2008 7:00	156.01	263.04	29.71
9/14/2008 8:00	156.01	263.04	29.71
9/14/2008 9:00	156.01	263.04	29.71
9/14/2008 10:00	156.01	263.04	29.71
9/14/2008 11:00	156.01	263.04	29.71
9/14/2008 12:00	195.01	263.04	74.28
9/14/2008 13:00	253.52	464.70	74.28
9/14/2008 14:00	273.02	464.70	74.28
9/14/2008 15:00	273.02	464.70	176.42
9/14/2008 16:00	273.02	464.70	176.42
9/14/2008 17:00	273.02	464.70	176.42
9/14/2008 18:00	273.02	289.34	176.42
9/14/2008 19:00	273.02	289.34	176.42
9/14/2008 20:00	234.02	289.34	125.35
9/14/2008 21:00	175.51	267.42	74.28
9/14/2008 22:00	156.01	179.74	74.28
9/14/2008 23:00	156.01	157.82	74.28
9/15/2008 0:00	156.01	157.82	74.28
9/15/2008 1:00	156.01	157.82	74.28
9/15/2008 2:00	156.01	157.82	74.28
9/15/2008 3:00	156.01	157.82	74.28
9/15/2008 4:00	136.51	138.10	74.28
9/15/2008 5:00	117.01	118.37	74.28
9/15/2008 6:00	117.01	59.18	55.71
9/15/2008 7:00	117.01	32.88	37.14
9/15/2008 8:00	97.51	21.92	9.29
9/15/2008 9:00	78.01	21.92	9.29
9/15/2008 10:00	78.01	21.92	9.29
9/15/2008 11:00	78.01	21.92	9.29
9/15/2008 12:00	78.01	21.92	9.29
9/15/2008 13:00	78.01	0.00	9.29
9/15/2008 14:00	78.01	0.00	9.29
9/15/2008 15:00	78.01	0.00	9.29
9/15/2008 16:00	78.01	0.00	9.29
9/15/2008 17:00	78.01	0.00	9.29
9/15/2008 18:00	78.01	0.00	9.29
9/15/2008 19:00	78.01	0.00	9.29
9/15/2008 20:00	78.01	0.00	9.29
9/15/2008 21:00	78.01	0.00	9.29
9/15/2008 22:00	78.01	0.00	9.29
9/15/2008 23:00	78.01	0.00	9.29

Table B-1 (cont'd)

9/16/2008 0:00	78.01	0.00	9.29
9/16/2008 1:00	78.01	0.00	9.29
9/16/2008 2:00	78.01	0.00	9.29
9/16/2008 3:00	78.01	0.00	9.29
9/16/2008 4:00	78.01	0.00	9.29
9/16/2008 5:00	78.01	0.00	9.29
9/16/2008 6:00	78.01	0.00	9.29
9/16/2008 7:00	78.01	0.00	9.29
9/16/2008 8:00	39.00	0.00	9.29
9/16/2008 9:00	0.00	0.00	9.29
9/16/2008 10:00	0.00	0.00	9.29
9/16/2008 11:00	0.00	0.00	9.29
9/16/2008 12:00	0.00	0.00	9.29
9/16/2008 13:00	0.00	0.00	9.29
9/16/2008 14:00	0.00	0.00	9.29
9/16/2008 15:00	0.00	0.00	0.00
9/16/2008 16:00	0.00	0.00	0.00
9/16/2008 17:00	0.00	0.00	0.00
9/16/2008 18:00	0.00	0.00	0.00
9/16/2008 19:00	0.00	0.00	0.00
9/16/2008 20:00	0.00	0.00	0.00
9/16/2008 21:00	0.00	0.00	0.00
9/16/2008 22:00	0.00	0.00	0.00
9/16/2008 23:00	0.00	0.00	0.00

Table B-2: Discharge time series data showing backflow releases from Wilmette and CRCW outlets in July 2010

Date/Time	Wilmette Discharge ($m^3 s^{-1}$)	CRCW Discharge ($m^3 s^{-1}$)
07/24/2010 0:00	0.00	0.00
07/24/2010 1:00	0.00	0.00
07/24/2010 2:00	49.81	181.57
07/24/2010 3:00	62.00	510.35
07/24/2010 4:00	58.92	510.35
07/24/2010 5:00	54.04	510.35
07/24/2010 6:00	58.41	510.35
07/24/2010 7:00	63.28	510.35
07/24/2010 8:00	52.25	510.35
07/24/2010 9:00	40.31	510.35
07/24/2010 10:00	34.40	510.35
07/24/2010 11:00	35.30	510.35
07/24/2010 12:00	25.80	510.35
07/24/2010 13:00	25.93	510.35
07/24/2010 14:00	35.17	181.57
07/24/2010 15:00	34.15	181.57
07/24/2010 16:00	36.97	181.57
07/24/2010 17:00	36.07	181.57
07/24/2010 18:00	25.16	181.57
07/24/2010 19:00	31.45	181.57
07/24/2010 20:00	0.00	0.00
07/24/2010 21:00	0.00	0.00
07/24/2010 22:00	0.00	0.00
07/24/2010 23:00	0.00	0.00

Table B-3: Discharge time series data showing backflow releases from Wilmette and CRCW outlets in July 2011

Date/Time	Wilmette Discharge ($m^3\ s^{-1}$)	CRCW Discharge ($m^3\ s^{-1}$)
07/23/2011 0:00	0.00	0.00
07/23/2011 1:00	0.00	0.00
07/23/2011 2:00	82.87	0.00
07/23/2011 3:00	105.91	96.14
07/23/2011 4:00	90.58	481.93
07/23/2011 5:00	78.87	434.44
07/23/2011 6:00	59.48	358.58
07/23/2011 7:00	53.84	257.19
07/23/2011 8:00	27.34	98.37
07/23/2011 9:00	19.79	59.70
07/23/2011 10:00	19.36	35.04
07/23/2011 11:00	18.81	14.13
07/23/2011 12:00	15.95	9.15
07/23/2011 13:00	0.00	0.00
07/23/2011 14:00	0.00	0.00
07/23/2011 15:00	0.00	0.00
07/23/2011 16:00	0.00	0.00
07/23/2011 17:00	0.00	0.00
07/23/2011 18:00	0.00	0.00
07/23/2011 19:00	0.00	0.00
07/23/2011 20:00	0.00	0.00
07/23/2011 21:00	0.00	0.00
07/23/2011 22:00	0.00	0.00
07/23/2011 23:00	0.00	0.00

Table B-4: Discharge time series data showing backflow releases from Wilmette, CRCW and O'Brien outlets in April 2013

Date/Time	Wilmette Discharge ($m^3 s^{-1}$)	CRCW Discharge ($m^3 s^{-1}$)	O'Brien Discharge ($m^3 s^{-1}$)
4/18/2013 0:00	0	139.13	0
4/18/2013 1:00	249.81	239.47	0
4/18/2013 2:00	499.62	288.08	0
4/18/2013 3:00	499.62	490.01	0
4/18/2013 4:00	499.62	1883.39	0
4/18/2013 5:00	499.62	4571.19	1.05
4/18/2013 6:00	499.62	4225.17	2087.50
4/18/2013 7:00	499.62	4109.96	8345.96
4/18/2013 8:00	499.62	3984.86	8345.63
4/18/2013 9:00	499.62	2666.69	6259.19
4/18/2013 10:00	499.62	4431.84	0.67
4/18/2013 11:00	499.62	2264.02	1.08
4/18/2013 12:00	499.62	2050.30	1.25
4/18/2013 13:00	499.62	2605.82	1.21
4/18/2013 14:00	499.62	1789.88	1.33
4/18/2013 15:00	499.62	2735.33	1.36
4/18/2013 16:00	499.62	2684.26	1.32
4/18/2013 17:00	499.62	1215.65	1.33
4/18/2013 18:00	374.72	1147.42	1.26
4/18/2013 19:00	374.72	1122.88	1.20
4/18/2013 20:00	499.62	1032.29	1.03
4/18/2013 21:00	499.62	767.32	0.91
4/18/2013 22:00	499.62	569.40	0.97
4/18/2013 23:00	499.62	206.68	0.94
4/19/2013 0:00	499.62	272.25	0.84
4/19/2013 1:00	0	152.35	0.50
4/19/2013 2:00	0	82.18	0.34
4/19/2013 3:00	0	0	0.34
4/19/2013 4:00	0	0	0.17
4/19/2013 5:00	0	0	0
4/19/2013 6:00	0	0	0
4/19/2013 7:00	0	0	0
4/19/2013 8:00	0	0	0

Table B-4 (cont'd)

4/19/2013 9:00	0	0	0
4/19/2013 10:00	0	0	0
4/19/2013 11:00	0	0	0
4/19/2013 12:00	0	0	0

Table B-5: Discharge time series data showing backflow releases from Wilmette and CRCW outlets in October 2017

Date/Time	Wilmette Discharge ($m^3 s^{-1}$)	CRCW Discharge ($m^3 s^{-1}$)
10/14/2017 12:00	0.00	0.00
10/14/2017 13:00	8.83	15.26
10/14/2017 14:00	30.88	91.60
10/14/2017 15:00	26.48	106.87
10/14/2017 16:00	11.03	106.87
10/14/2017 17:00	10.59	99.24
10/14/2017 18:00	10.59	68.71
10/14/2017 19:00	10.59	45.79
10/14/2017 20:00	11.69	45.79
10/14/2017 21:00	18.87	152.67
10/14/2017 22:00	19.20	229.00
10/14/2017 23:00	19.20	229.00
10/15/2017 0:00	19.20	229.00
10/15/2017 1:00	19.20	229.00
10/15/2017 2:00	19.20	229.00
10/15/2017 3:00	15.22	229.00
10/15/2017 4:00	13.22	167.93
10/15/2017 5:00	13.22	106.87
10/15/2017 6:00	13.22	106.87
10/15/2017 7:00	11.02	73.80
10/15/2017 8:00	6.63	27.98
10/15/2017 9:00	2.21	0.00
10/15/2017 10:00	0.00	0.00
10/15/2017 11:00	0.00	0.00
10/15/2017 12:00	0.00	0.00

APPENDIX C:

Plots Comparing Modeled and Observed *E. coli* at Chicago beaches in 2010

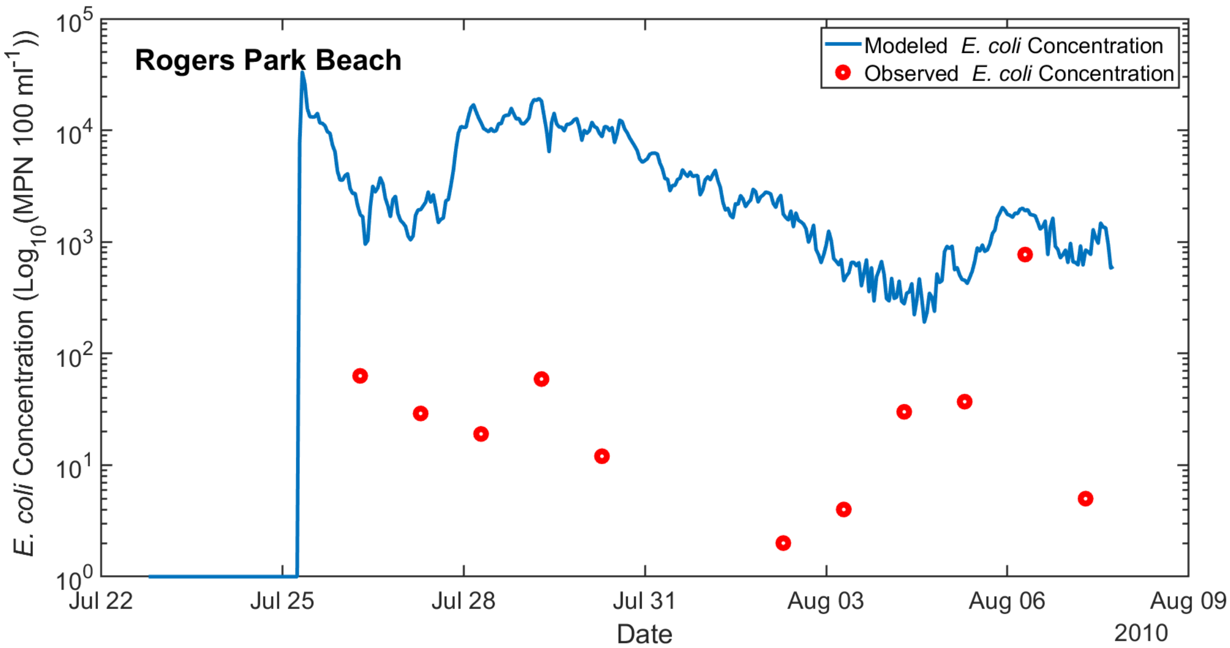

Figure C-1: Validation plot comparing modeled (blue line) and observed (red circles) E. coli concentrations during and after the July 2010 backflow event at Rogers Park beach

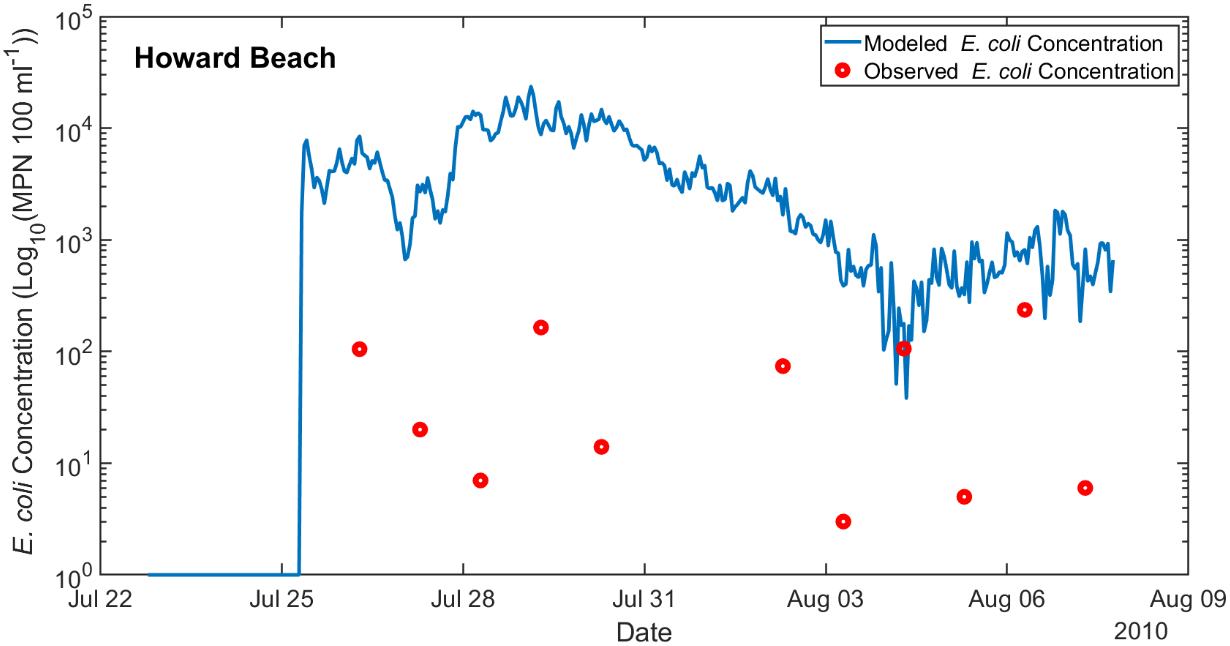

Figure C-2: Validation plot comparing modeled (blue line) and observed (red circles) E. coli concentrations during and after the July 2010 backflow event at Howard beach

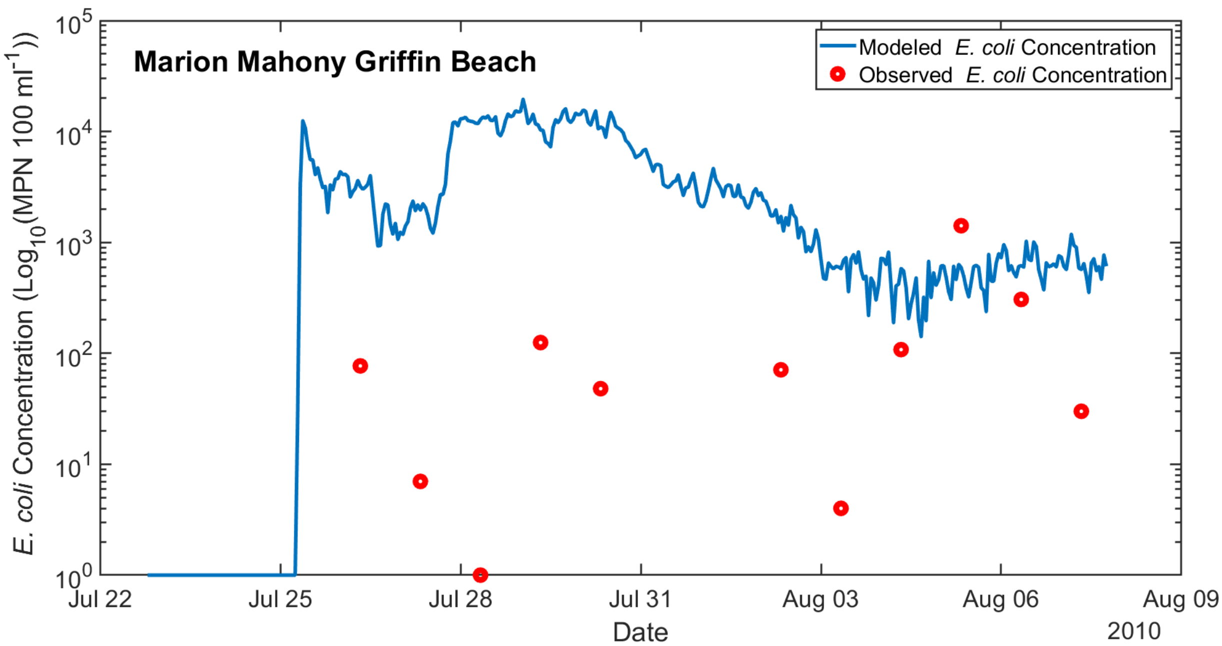

Figure C-3: Validation plot comparing modeled (blue line) and observed (red circles) E. coli concentrations during and after the July 2010 backflow event at Marion Mahony Griffin beach

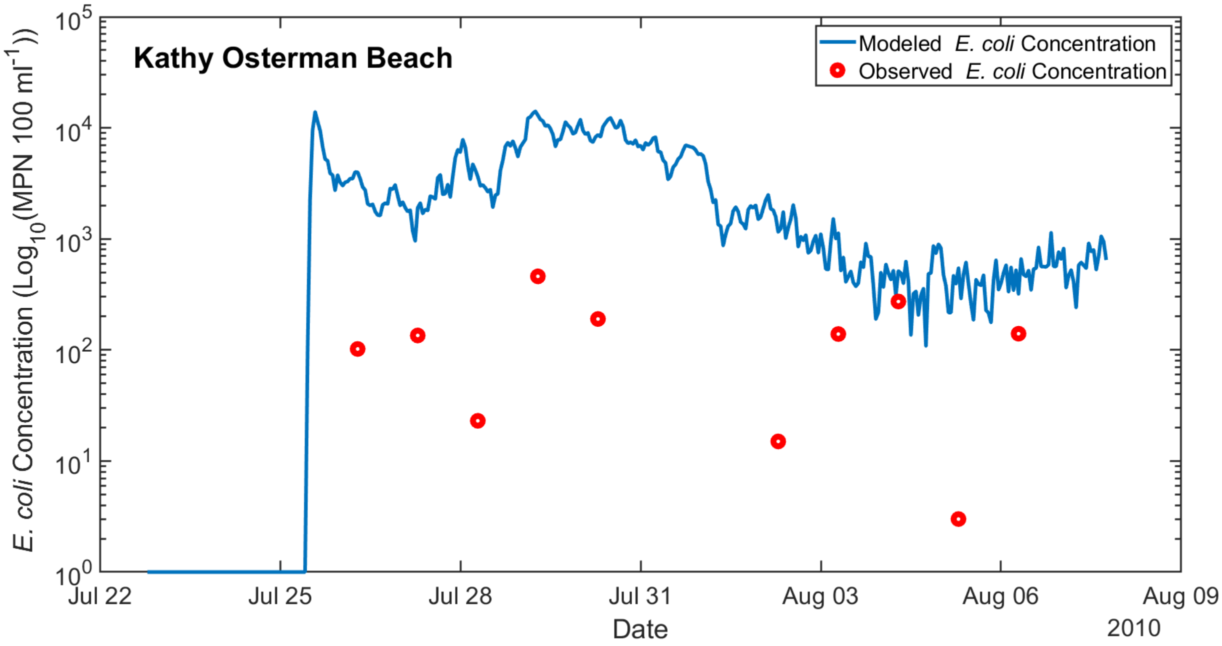

Figure C-4: Validation plot comparing modeled (blue line) and observed (red circles) E. coli concentrations during and after the July 2010 backflow event at Kathy Osterman beach

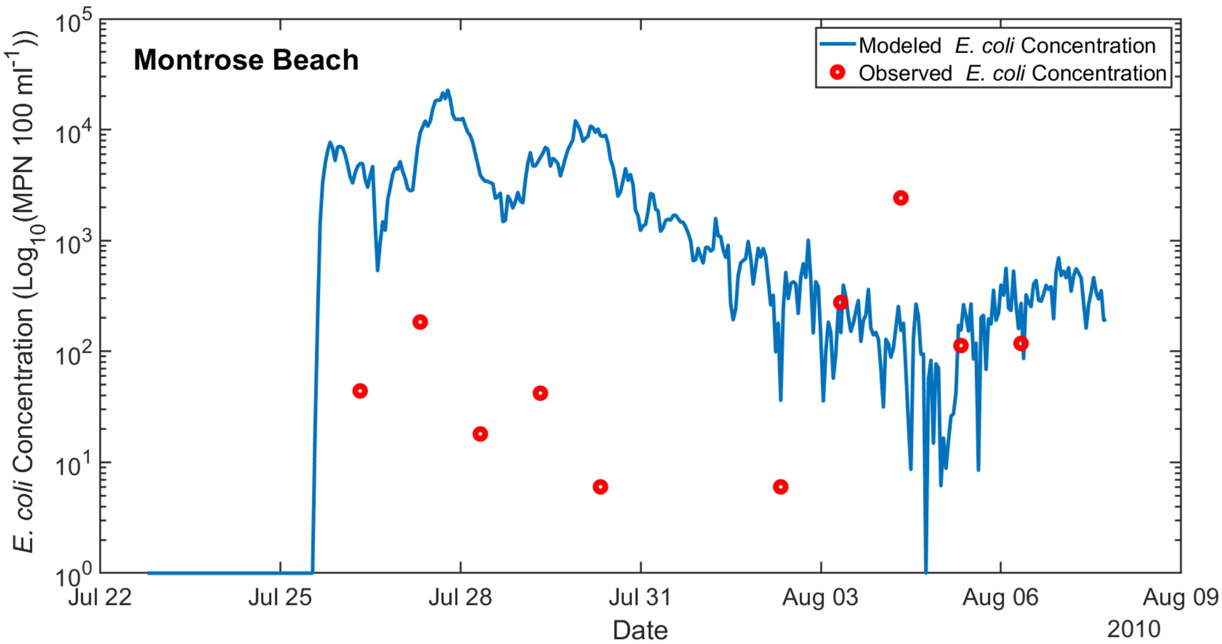

Figure C-5: Validation plot comparing modeled (blue line) and observed (red circles) E. coli concentrations during and after the July 2010 backflow event at Montrose beach

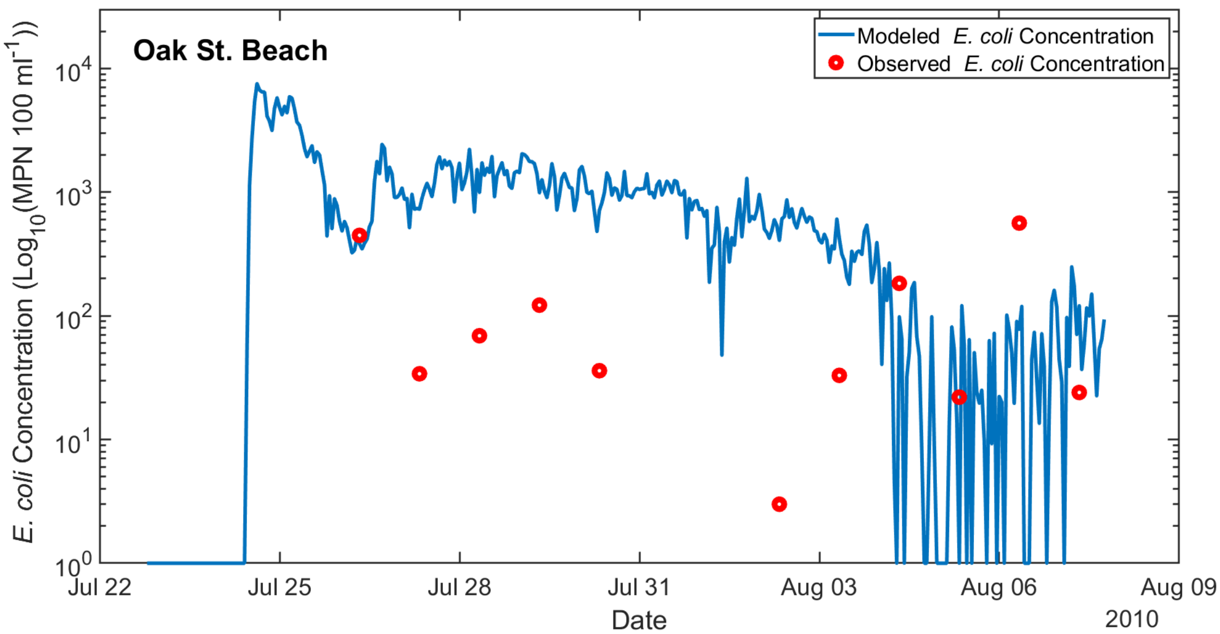

Figure C-6: Validation plot comparing modeled (blue line) and observed (red circles) E. coli concentrations during and after the July 2010 backflow event at Oak St. beach

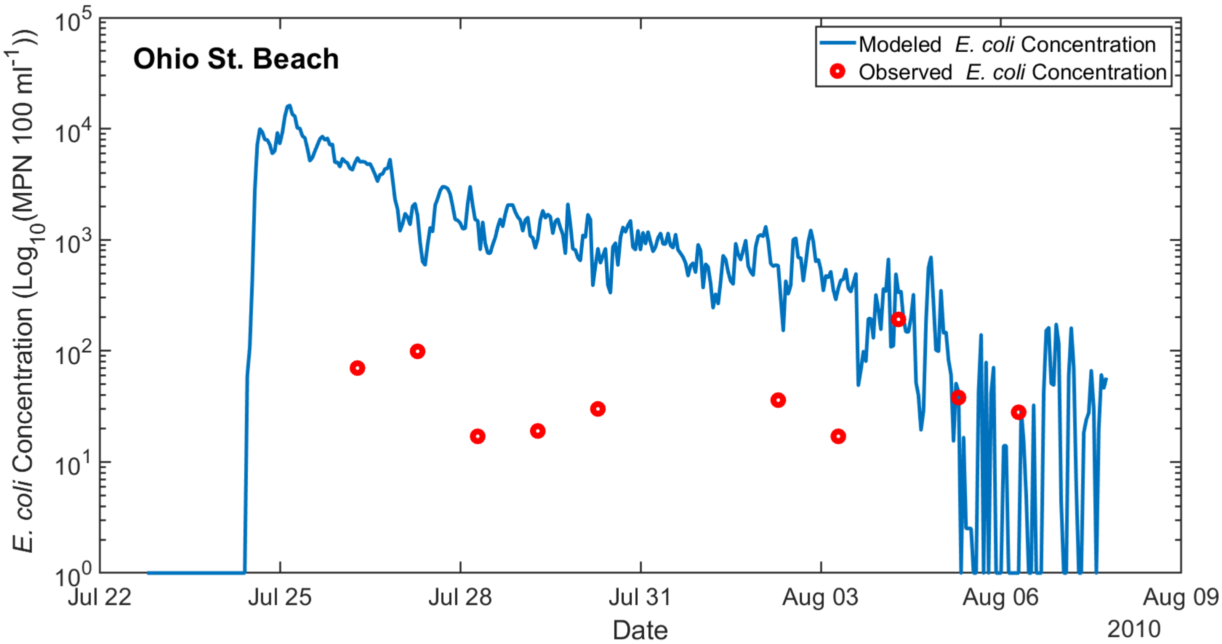

Figure C-7: Validation plot comparing modeled (blue line) and observed (red circles) E. coli concentrations during and after the July 2010 backflow event at Ohio St. beach

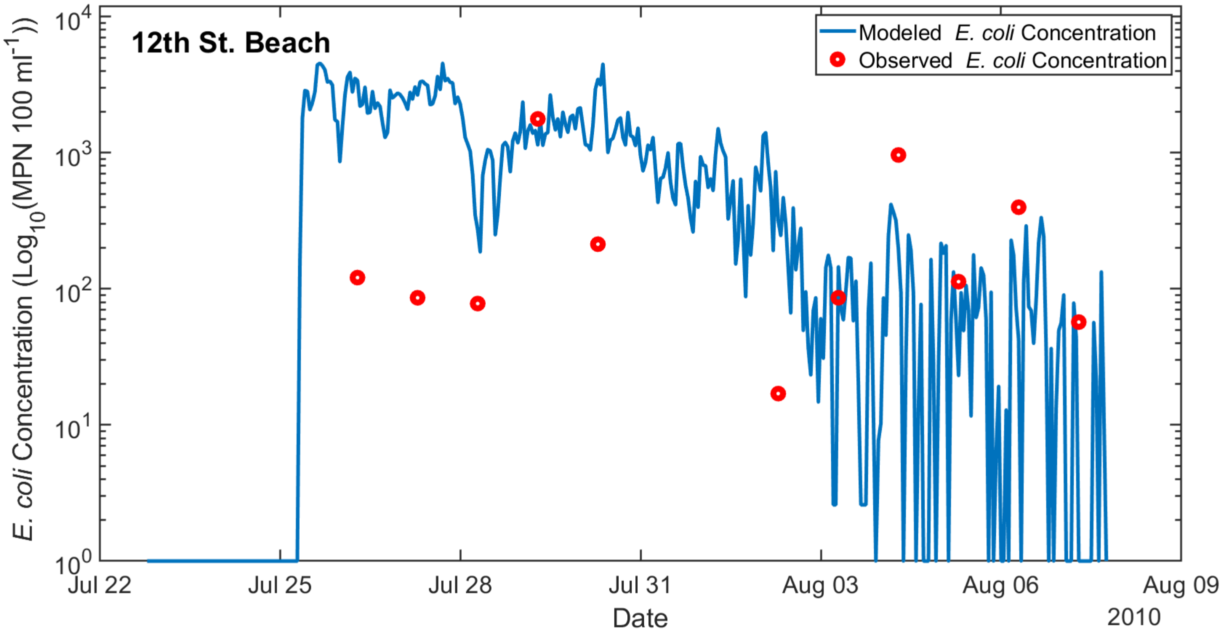

Figure C-8: Validation plot comparing modeled (blue line) and observed (red circles) E. coli concentrations during and after the July 2010 backflow event at 12th St. beach

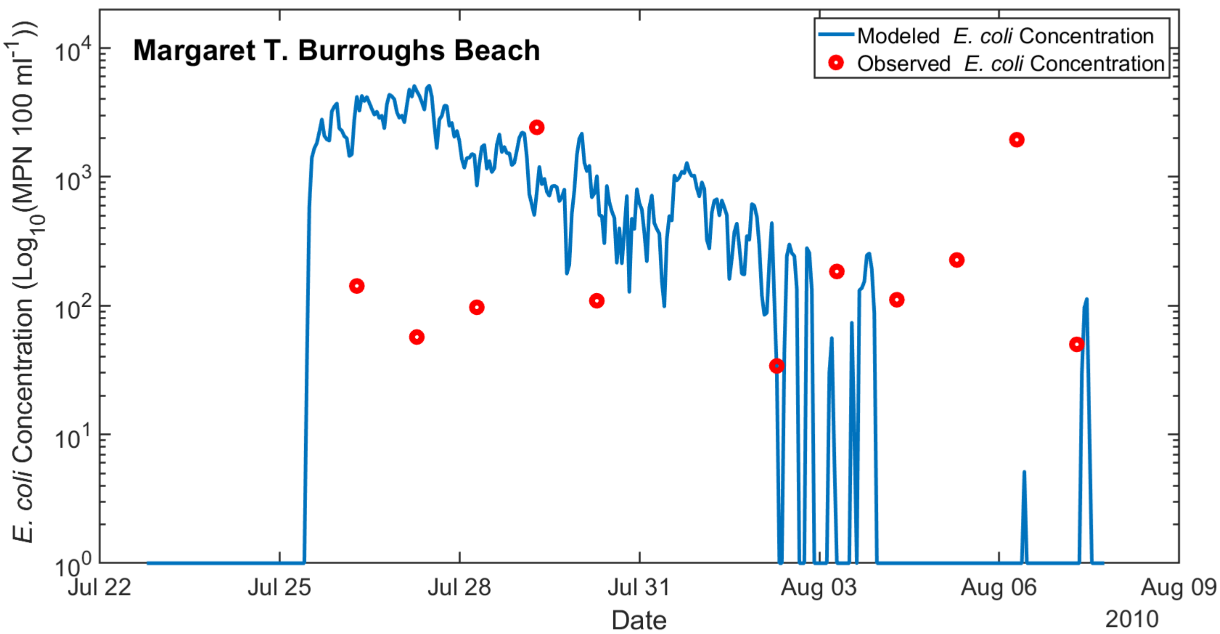

Figure C-9: Validation plot comparing modeled (blue line) and observed (red circles) E. coli concentrations during and after the July 2010 backflow event at Margaret T. Burroughs beach

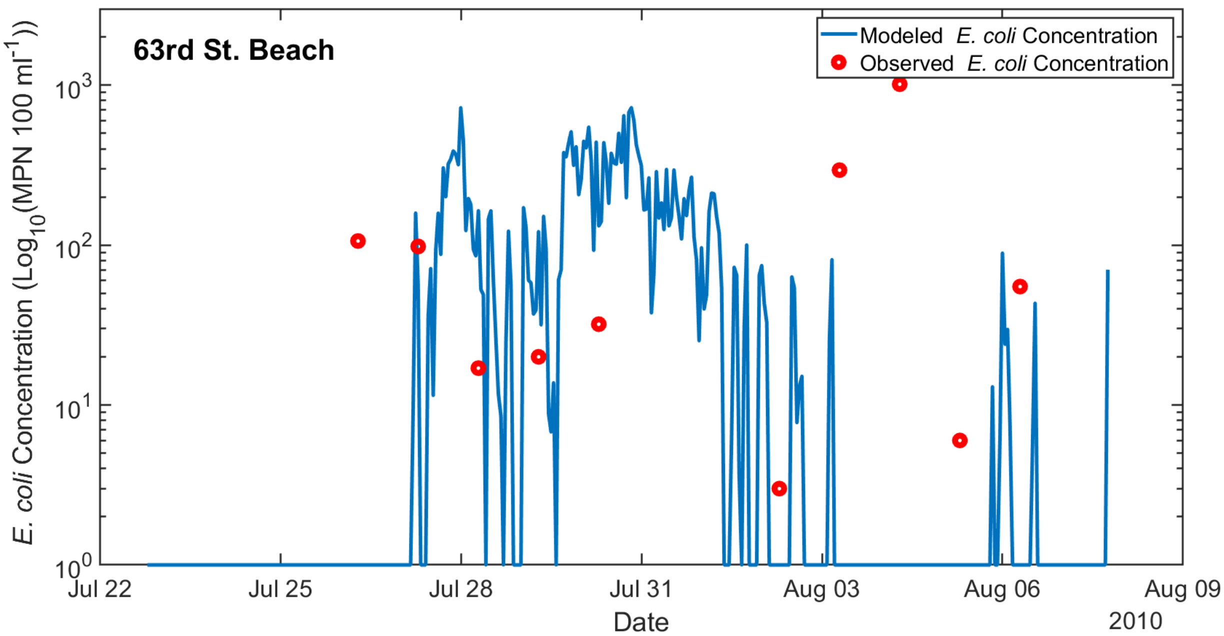

Figure C-10: Validation plot comparing modeled (blue line) and observed (red circles) E. coli concentrations during and after the July 2010 backflow event at 63rd St. beach

APPENDIX D:

Plots Comparing Modeled and Observed *E. coli* at Chicago beaches in 2011

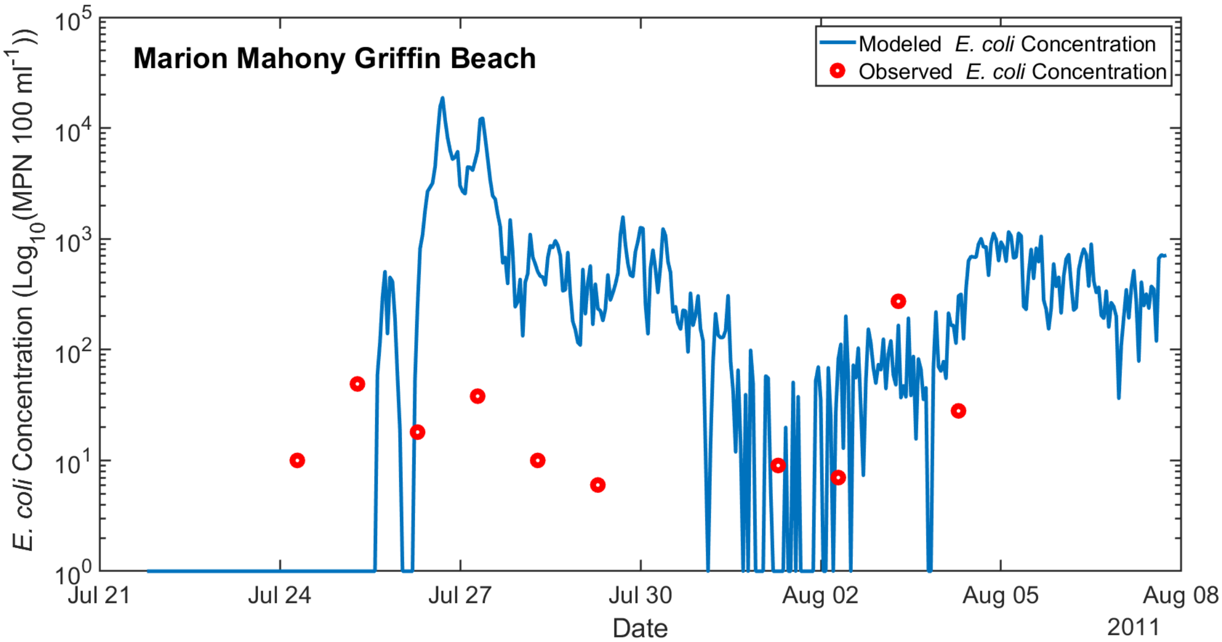

Figure D-1: Validation plot comparing modeled (blue line) and observed (red circles) E. coli concentrations during and after the July 2011 backflow event at Marion Mahony Griffin beach

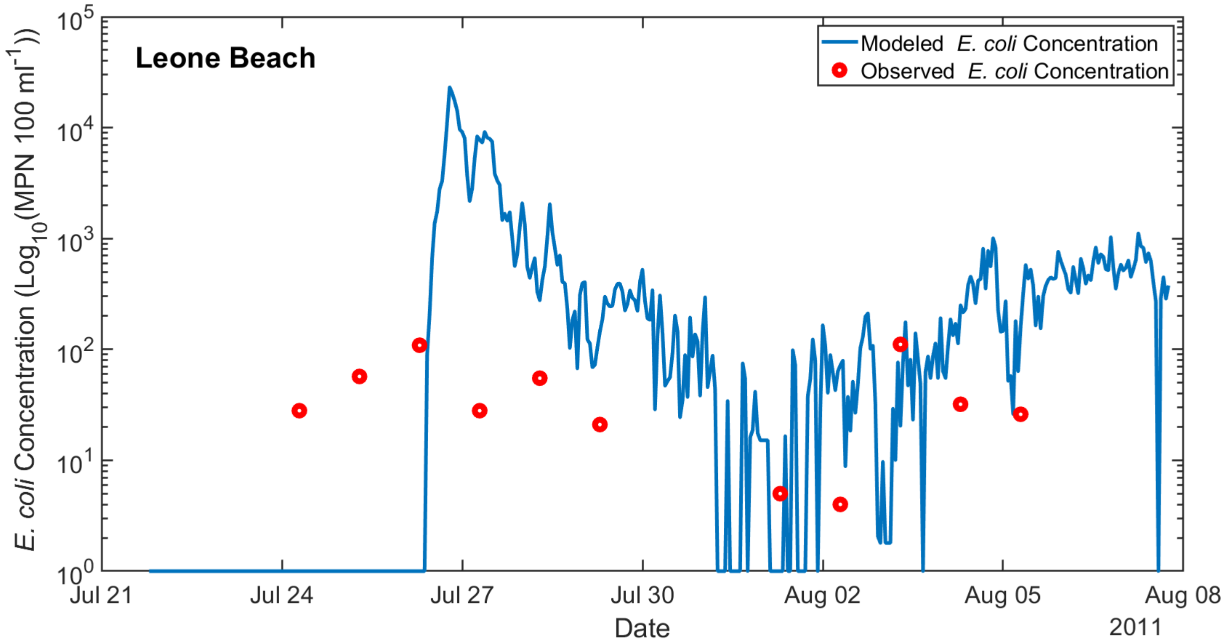

Figure D-2: Validation plot comparing modeled (blue line) and observed (red circles) E. coli concentrations during and after the July 2011 backflow event at Leone beach

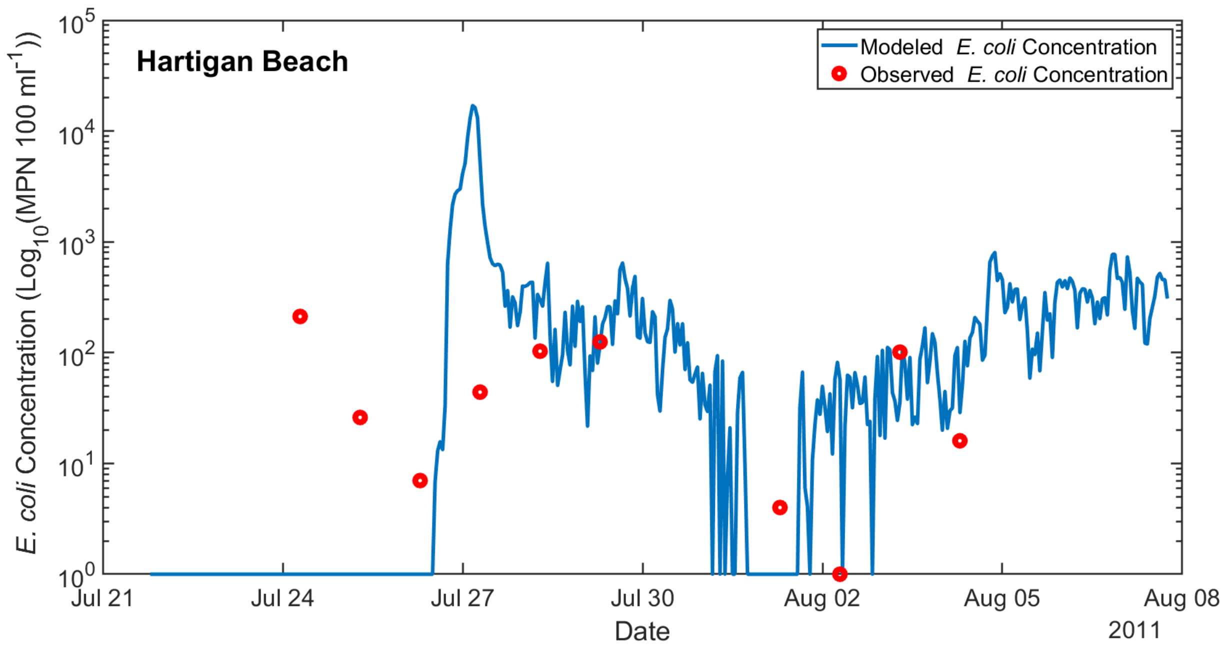

Figure D-3: Validation plot comparing modeled (blue line) and observed (red circles) E. coli concentrations during and after the July 2011 backflow event at Hartigan beach

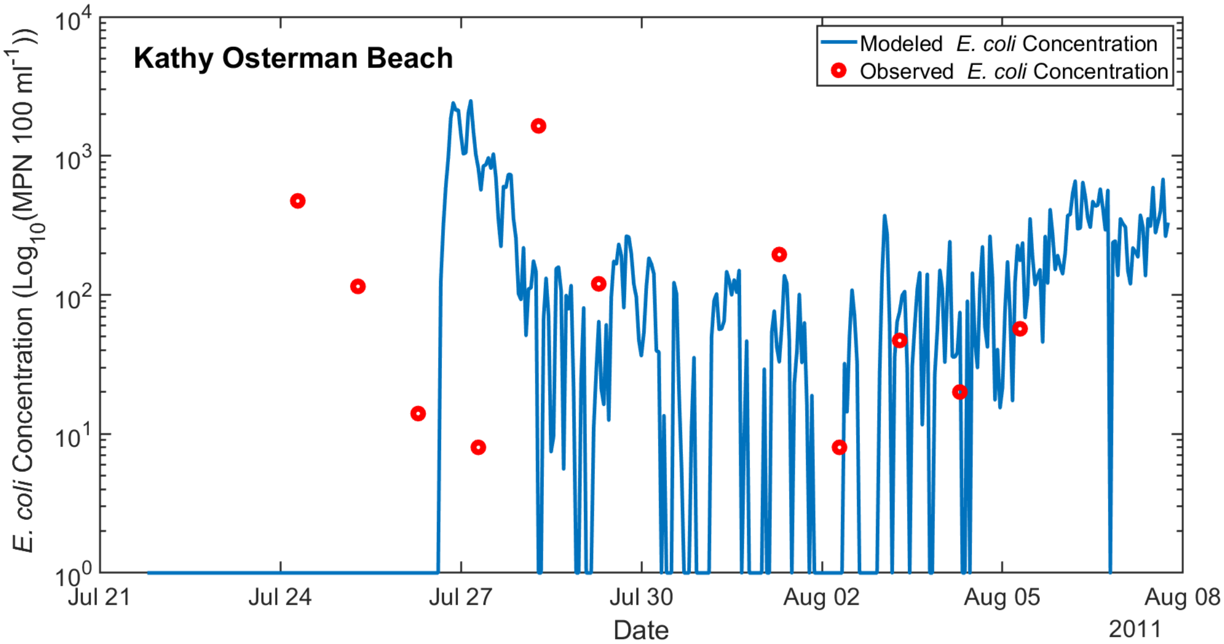

Figure D-4: Validation plot comparing modeled (blue line) and observed (red circles) E. coli concentrations during and after the July 2011 backflow event at Kathy Osterman beach

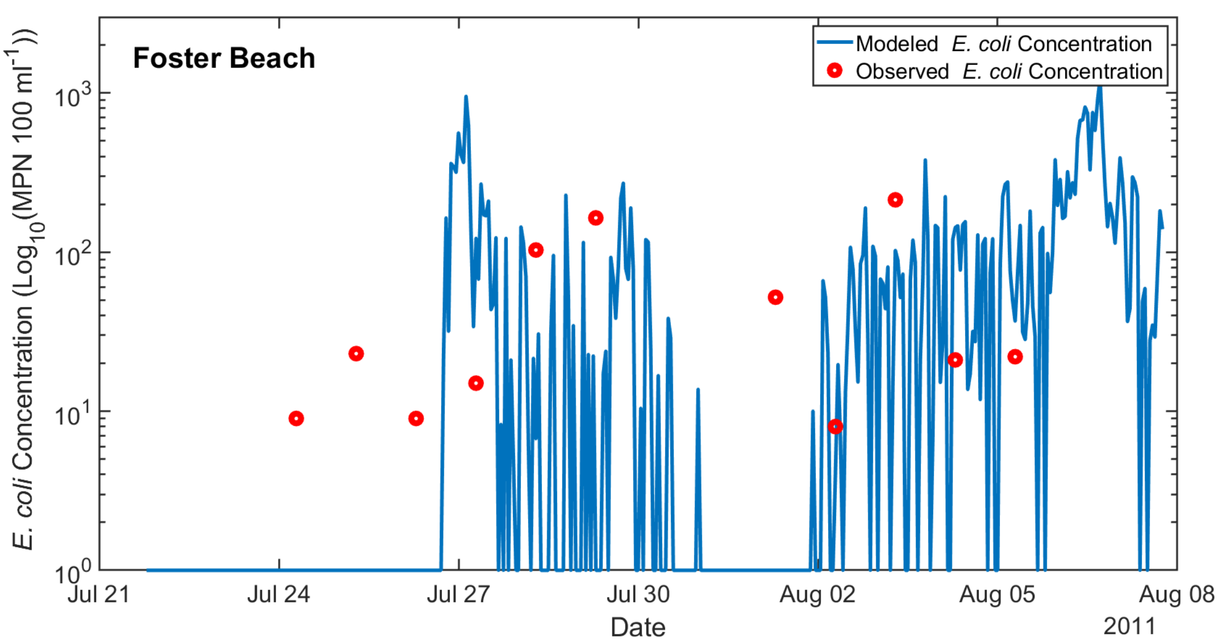

Figure D-5: Validation plot comparing modeled (blue line) and observed (red circles) E. coli concentrations during and after the July 2011 backflow event at Foster beach

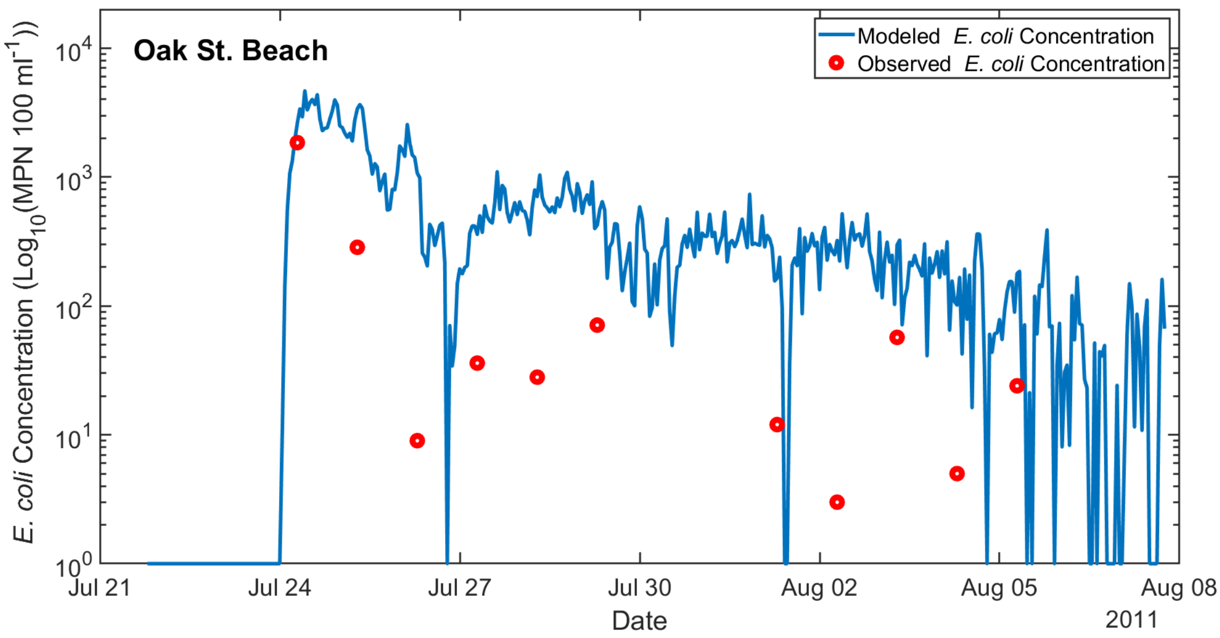

Figure D-6: Validation plot comparing modeled (blue line) and observed (red circles) E. coli concentrations during and after the July 2011 backflow event at Oak St. beach

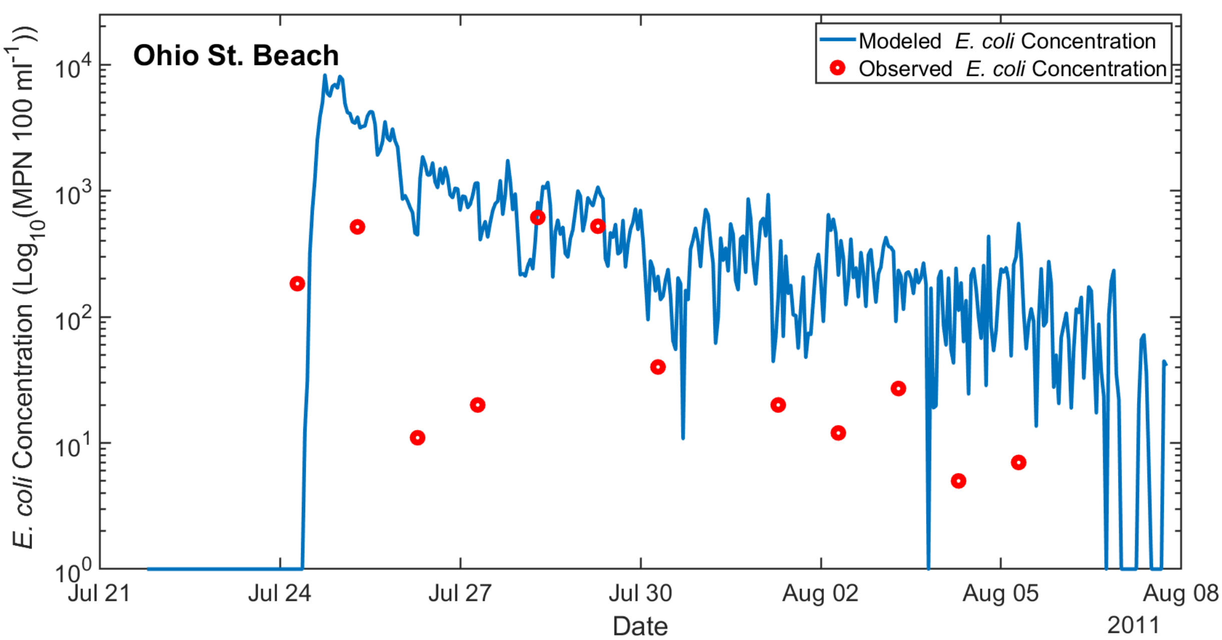

Figure D-7: Validation plot comparing modeled (blue line) and observed (red circles) E. coli concentrations during and after the July 2011 backflow event at Ohio St. beach

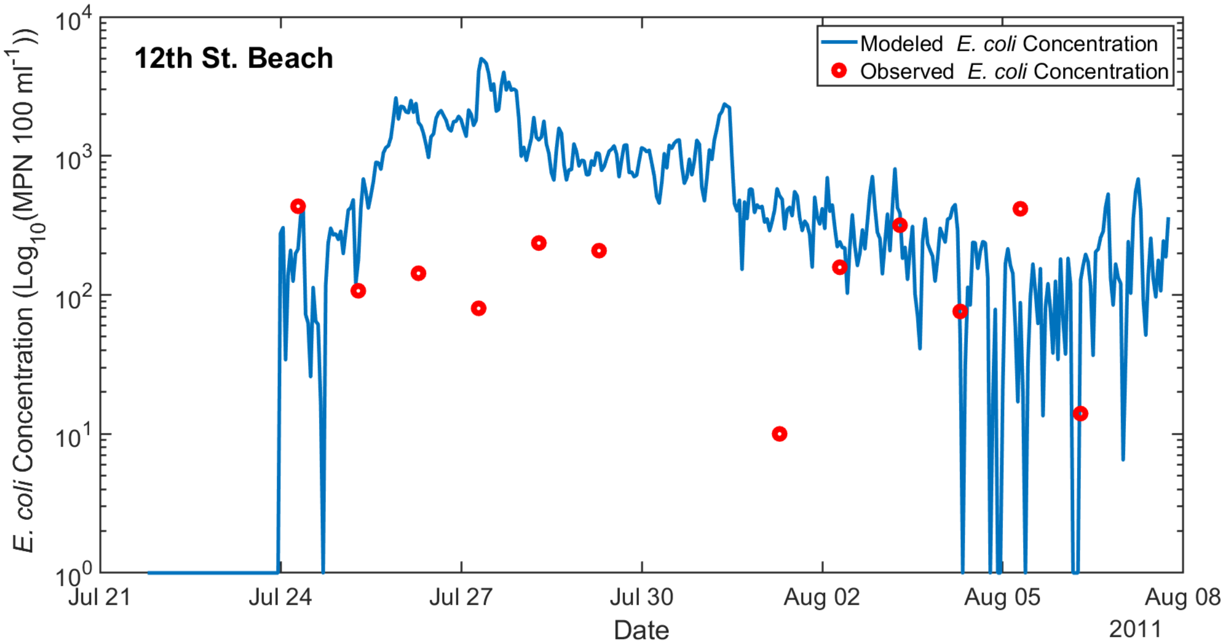

Figure D-8: Validation plot comparing modeled (blue line) and observed (red circles) E. coli concentrations during and after the July 2011 backflow event at 12th St. beach

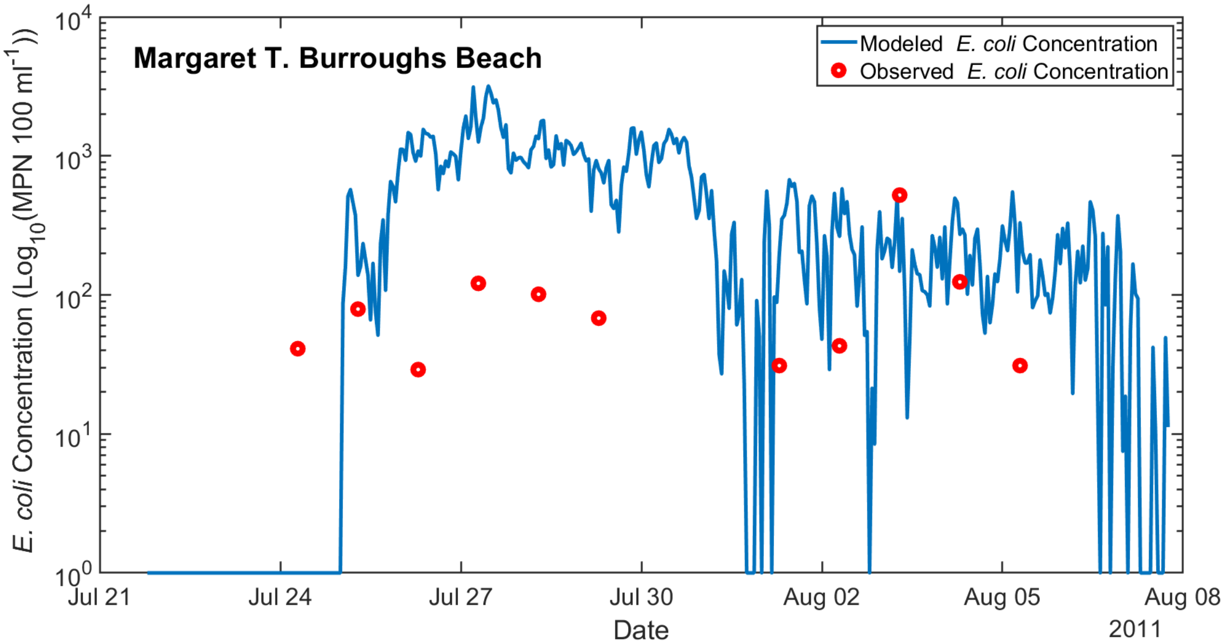

Figure D-9: Validation plot comparing modeled (blue line) and observed (red circles) E. coli concentrations during and after the July 2011 backflow event at Margaret T. Burroughs beach

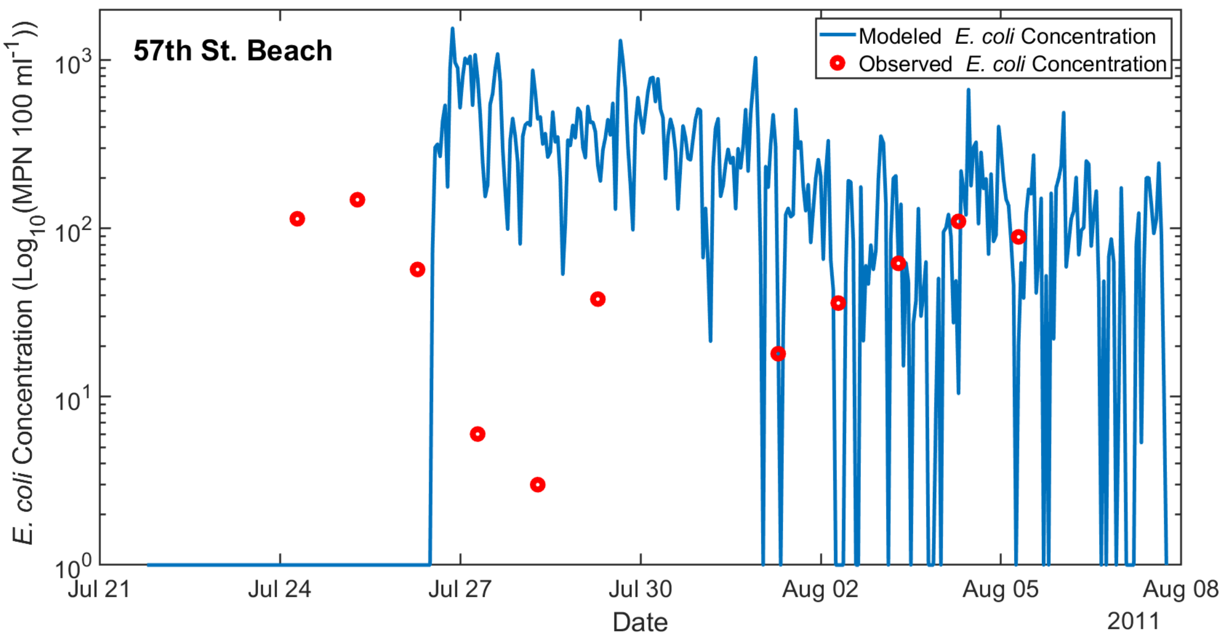

Figure D-10: Validation plot comparing modeled (blue line) and observed (red circles) E. coli concentrations during and after the July 2011 backflow event at 57th St. beach

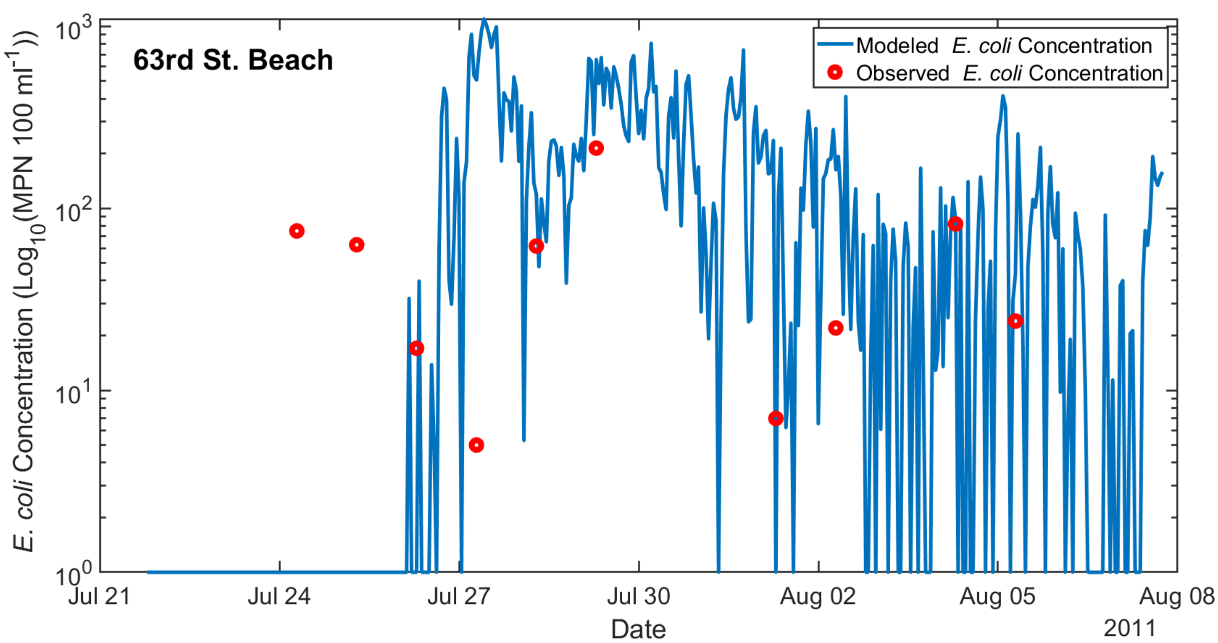

Figure D-11: Validation plot comparing modeled (blue line) and observed (red circles) E. coli concentrations during and after the July 2011 backflow event at 63rd St. beach

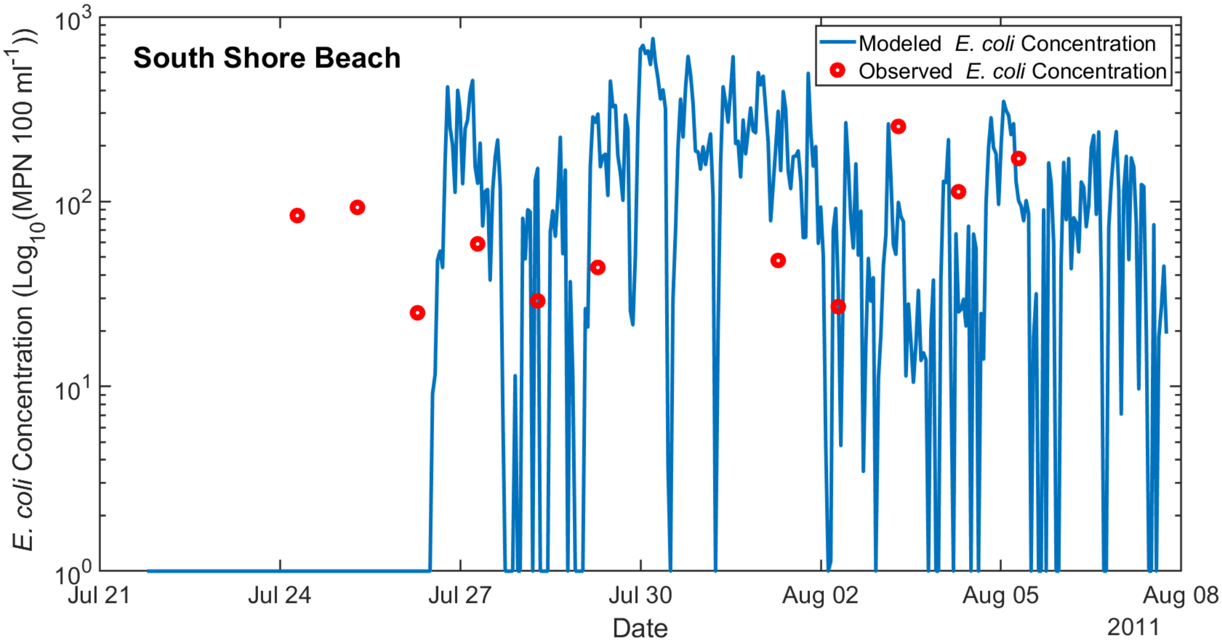

Figure D-12: Validation plot comparing modeled (blue line) and observed (red circles) E. coli concentrations during and after the July 2011 backflow event at South Shore beach

REFERENCES

REFERENCES

Abu-Bakar, A., Ahmadian, R., Falconer, R.A., 2017. Modelling the transport and decay processes of microbial tracers in a macro-tidal estuary. Water Res. 123, 802–824. https://doi.org/10.1016/j.watres.2017.07.007

Ackerman, D., Weisberg, S., 2003. Relationship between rainfall and beach bacterial concentrations on Santa Monica Bay beaches. J. Water Heal. 1, 85–89.

Allen, J., Newberger, P., Federiuk, J., 1995. Upwelling circulation on the Oregon continental shelf Part 1: Response to idealized forcing. J. Phys. Oceanogr. 25, 1843–1866.

Alm, E.W., Burke, J., Spain, A., 2003. Fecal indicator bacteria are abundant in wet sand at freshwater beaches. Water Res. 37, 3978–3982. https://doi.org/10.1016/s0043-1354(03)00301-4

Altman, D., Bland, J., 1994. Statistics Notes: Diagnostic tests 1: sensitivity and specificity. Br. Med. J. 308, 1552. https://doi.org/10.1136/bmj.308.6943.1552

Ambrose Jr., R., Wool, T., Martin, J., 1993. The water quality analysis simulation program, WASP5 Part A: Model Documentation. Athens, GA.

Anderson, E.J., Phanikumar, M.S., 2011. Surface storage dynamics in large rivers: Comparing three-dimensional particle transport, one-dimensional fractional derivative, and multirate transient storage models. Water Resour. Res. 47, 15. https://doi.org/10.1029/2010wr010228

Anderson, J.H., 1979. In vitro survival of human pathogenic fungi in Hawaiian beach sand. Sabouraudia 17, 13–22.

Angelescu, D.E., Huynh, V., Hausot, A., Yalkin, G., Plet, V., Mouchel, J.M., Guérin-Rechdaoui, S., Azimi, S., Rocher, V., 2019. Autonomous system for rapid field quantification of Escherichia coli in surface waters. J. Appl. Microbiol. 126, 332–343. https://doi.org/10.1111/jam.14066

ASCE, 2020. Reversal of the Chicago River [WWW Document]. URL https://www.asce.org/project/reversal-of-the-chicago-river/ (accessed 6.11.20).

Atwood, E.C., Falcieri, F.M., Piehl, S., Bochow, M., Matthies, M., Franke, J., Carniel, S., Sclavo, M., Laforsch, C., Siegert, F., 2019. Coastal accumulation of microplastic particles emitted from the Po River, Northern Italy: Comparing remote sensing and hydrodynamic modelling with in situ sample collections. Mar. Pollut. Bull. 138, 561–574. https://doi.org/10.1016/j.marpolbul.2018.11.045

Auer, M.T., Niehaus, S.L., 1993. Modeling fecal-coliform bacteria .1. Field and laboratory determination of loss kinetics. Water Res. 27, 693–701. https://doi.org/10.1016/0043-1354(93)90179-l

Barlage, M., Richards, P., Sousounis, P., Brenner, A., 2002. Impacts of climate change and land use change on runoff from a Great Lakes watershed. J. Great Lakes Res. 28, 568–582. https://doi.org/10.1016/S0380-1330(02)70606-0

Beaches Environmental Assessment and Coastal Health Act (BEACH Act), 2nd ed, 2000. , 33 USC 1251.

Bedri, Z., Bruen, M., Dowley, A., Masterson, B., 2011. A Three-Dimensional Hydro-Environmental Model of Dublin Bay. Environ. Model. Assess. 16, 369–384. https://doi.org/10.1007/s10666-011-9253-7

Bedri, Z., Corkery, A., O'Sullivan, J.J., Alvarez, M.X., Erichsen, A.C., Deering, L.A., Demeter, K., O'Hare, G.M.P., Meijer, W.G., Masterson, B., 2014. An integrated catchment-coastal modelling system for real-time water quality forecasts. Environ. Model. Softw. 61, 458–476. https://doi.org/10.1016/j.envsoft.2014.02.006

Beletsky, D., Schwab, D.J., 2001. Modeling circulation and thermal structure in Lake Michigan: Annual cycle and interannual variability. J. Geophys. Res. 106, 19745–19771. https://doi.org/10.1029/2000jc000691

Bernhard, A.E., Field, K.G., 2000. Identification of nonpoint sources of fecal pollution in coastal waters by using host-specific 16S ribosomal DNA genetic markers from fecal anaerobes. Appl. Environ. Microbiol. 66, 1587–1594.

Beversdorf, L.J., Bornstein-Forst, S.M., McLellan, S.L., 2007. The potential for beach sand to serve as a reservoir for Escherichia coli and the physical influences on cell die-off. J. Appl. Microbiol. 102, 1372–1381. https://doi.org/10.1111/j.1365-2672.2006.03177.x

Binding, C.E., Greenberg, T.A., Watson, S.B., Rastin, S., Gould, J., 2015. Long term water clarity changes in North America's Great Lakes from multi-sensor satellite observations. Limnol. Oceanogr. 16, 1976–1995. https://doi.org/10.1002/lno.10146

Blumberg, A.F., Mellor, G.L., 1987. A description of a three-dimensional coastal ocean model. Heaps, N. S. (Ed.). Coast. Estuar. Sci. 4. Three-Dimensional Coast. Ocean Model. Xi+208p. Am. Geophys. Union Washington, D.C., USA. Illus 1–16.

Boehm, A.B., Grant, S.B., Kim, J.H., Mowbray, S.L., McGee, C.D., Clark, C.D., Foley, D.M., Wellman, D.E., 2002. Decadal and shorter period variability of surf zone water quality at Huntington Beach, California. Environ. Sci. Technol. 36, 3885–3892.

Boehm, A.B., Yamahara, K.M., Love, D.C., Peterson, B.M., McNeill, K., Nelson, K.L., 2009. Covariation and photoinactivation of traditional, rapid, and novel indicator organisms and human viruses at a sewage-impacted marine beach. Environ. Sci. Technol. 43, 8046–8052.

Boehm, A.B., Yamahara, K.M., Sassoubre, L.M., 2014. Diversity and transport of microorganisms in intertidal sands of the California coast. Appl. Environ. Microbiol. 80, 3943–3951. https://doi.org/10.1128/aem.00513-14

Bouwer, L.M., 2019. Observed and Projected Impacts from Extreme Weather Events: Implications for Loss and Damage, in: Mechler, R., Bouwer, L., Schinko, T., Surminski, S., Linnerooth-Bayer, J. (Eds.), Loss and Damage from Climate Change. Springer, Cham, pp. 63–82. https://doi.org/https://doi.org/10.1007/978-3-319-72026-5_3

Boye, B.A., Falconer, R.A., Akande, K., 2015. Integrated water quality modelling: Application to the Ribble Basin, UK. J. Hydro-environment Res. 9, 187–199. https://doi.org/10.1016/j.jher.2014.07.002

Bravo, H.R., Mclellan, S.L., Klump, J.V., Hamidi, S.A., Talarczyk, D., 2017. Environmental Modelling & Software Modeling the fecal coliform footprint in a Lake Michigan urban coastal area. Environ. Model. Softw. 95, 401–419. https://doi.org/10.1016/j.envsoft.2017.06.011

Bredehoeft, J., Konikow, L., 1993. Ground-water models: Validate or invalidate. Ground Water 31, 178–179. https://doi.org/10.1111/j.1745-6584.1993.tb01808.x

Brito, D., Campuzano, F.J., Sobrinho, J., Fernandes, R., Neves, R., 2015. Integrating operational watershed and coastal models for the Iberian Coast: Watershed model implementation - A first approach. Estuar. Coast. Shelf Sci. 167, 138–146. https://doi.org/10.1016/j.ecss.2015.10.022

Brown, J.S., Stein, E.D., Ackerman, D., Dorsey, J.H., Lyon, J., Carter, P.M., 2013. Metals and bacteria partitioning to various size particles in Ballona creek storm water runoff. Environ. Toxicol. Chem. 32, 320–328. https://doi.org/10.1002/etc.2065

Brown, K.I., Boehm, A.B., 2016. Transport of fecal indicators from beach sand to the surf zone by recirculating seawater: Laboratory experiments and numerical modeling. Environ. Sci. Technol. 50, 12840–12847. https://doi.org/10.1021/acs.est.6b02534

Brownell, M.J., Harwood, V.J., Kurz, R.C., McQuaig, S.M., Lukasik, J., Scott, T.M., 2007. Confirmation of putative stormwater impact on water quality at a Florida beach by microbial source tracking methods and structure of indicator organism populations. Water Res. 41, 3747–3757.

Byappanahalli, M.N., Nevers, M.B., Whitman, R.L., Ge, Z.F., Shively, D., Spoljaric, A., Przybyla-Kelly, K., 2015. Wildlife, urban inputs, and landscape configuration are responsible for degraded swimming water quality at an embayed beach. J. Great Lakes Res. 41, 156–163. https://doi.org/10.1016/j.jglr.2014.11.027

Byrnes, J.E., Reed, D.C., Cardinale, B.J., Cavanaugh, K.C., Holbrook, S.J., Schmitt, R.J., 2011. Climate-driven increases in storm frequency simplify kelp forest food webs. Glob. Chang. Biol. 17, 2513–2524. https://doi.org/10.1111/j.1365-2486.2011.02409.x

Cabelli, V.J., 1977. Clostridium Perfringens as a Water Quality Indicator, in: Hoadley, A.W., Dutka, B.J. (Eds.), Bacterial Indicators/Health Hazards Associated with Water. ASTM International, West Conshohocken, PA, pp. 65–79.

Canada, S.D.F., 2011. Swim Guide [WWW Document]. Swim Guide. URL https://www.theswimguide.org/ (accessed 8.6.20).

Canale, R.P., Auer, M.T., Owens, E.M., Heidtke, T.M., Effler, S.W., 1993. Modeling fecal-coliform bacteria .2. Model development and application. Water Res. 27, 703–714. https://doi.org/10.1016/0043-1354(93)90180-p

Carlucci, A.F., Pramer, D., 1960. An evaluation of factors affecting the survival of Escherichia coli in sea water .2. Salinity, pH, and nutrients. Appl. Microbiol. 8, 247–250.

Chapra, S.C., 2008. Surface Water Quality Modeling. Waveland Press, Inc., Long Grove, IL.

Chatzichristos, C., Sagen, J., Huseby, O., Muller, J., 2000. Advanced numerical modelling for tracer flow, in: Proceedings of the TraM 2000 Conference at Liege, Belgium. pp. 17–23.

Chen, C., Beardsley, R.C., Cowles, G., 2006. An unstructured-grid finite-volume coastal ocean model (FVCOM) system. Oceanography 19, 78–89.

Chen, C.S., Liu, H.D., Beardsley, R.C., 2003. An unstructured grid, finite-volume, three-dimensional, primitive equations ocean model: Application to coastal ocean and estuaries. J. Atmos. Ocean. Technol. 20, 159–186. https://doi.org/10.1175/1520-0426(2003)020<0159:augfvt>2.0.co;2

Childers, D.L., Cadenasso, M.L., Morgan Grove, J., Marshall, V., McGrath, B., Pickett, S.T.A., 2015. An ecology for cities: A transformational nexus of design and ecology to advance climate change resilience and urban sustainability. Sustain. 7, 3774–3791. https://doi.org/10.3390/su7043774

Cho, K.H., Cha, S.M., Kang, J.H., Lee, S.W., Park, Y., Kim, J.W., Kim, J.H., 2010. Meteorological effects on the levels of fecal indicator bacteria in an urban stream: A modeling approach. Water Res. 44, 2189–2202. https://doi.org/10.1016/j.watres.2009.12.051

Choi, B.J., Wilkin, J.L., 2007. The effect of wind on the dispersal of the Hudson River plume. J. Phys. Oceanogr. 37, 1878–1897. https://doi.org/10.1175/JPO3081.1

City of Chicago, 2014. City of Chicago: green stormwater infrastructure strategy. City Chicago 48. https://doi.org/10.2308/accr-50153

Coffey, R., Paul, M.J., Stamp, J., Hamilton, A., Johnson, T., 2018. A review of water quality responses to air temperature and precipitation changes 2: Nutrients, algal blooms, sediment, pathogens. J. Am. Water Resour. Assoc. https://doi.org/10.1111/1752-1688.12711

Colford, J.M., Wade, T.J., Schiff, K.C., Wright, C.C., Griffith, J.F., Sandhu, S.K., Burns, S., Sobsey, M., Lovelace, G., Weisberg, S.B., 2007. Water quality indicators and the risk of illness at beaches with nonpoint sources of fecal contamination. Epidemiology 18, 27–35. https://doi.org/10.1097/01.ede.0000249425.32990.b9

Connolly, J.P., Blumberg, A.F., Quadrini, J.D., 1999. Modeling fate of pathogenic organisms in coastal waters of Oahu, Hawaii. J. Environ. Eng. 125, 398–406. https://doi.org/10.1061/(asce)0733-9372(1999)125:5(398)

Converse, R.R., Kinzelman, J.L., Sams, E.A., Hudgens, E., Dufour, A.P., Ryu, H., Santo-Domingo, J.W., Kelty, C.A., Shanks, O.C., Siefring, S.D., Haugland, R.A., Wade, T.J., 2012. Dramatic improvements in beach water quality following gull removal. Environ. Sci. Technol. 46, 10206–10213. https://doi.org/10.1021/es302306b

Corsi, S.R., Borchardt, M.A., Carvin, R.B., Burch, T.R., Spencer, S.K., Lutz, M.A., McDermott, C.M., Busse, K.M., Kleinheinz, G.T., Feng, X.P., Zhu, J., 2016. Human and Bovine Viruses and Bacteria at Three Great Lakes Beaches: Environmental Variable Associations and Health Risk. Environ. Sci. Technol. 50, 987–995. https://doi.org/10.1021/acs.est.5b04372

CPD, 2020. Beaches [WWW Document]. URL https://www.chicagoparkdistrict.com/beaches (accessed 6.11.20).

Crimaldi, J.P., Koseff, J.R., Monismith, S.G., 2006. A mixing-length formulation for the turbulent Prandtl number in wall-bounded flows with bed roughness and elevated scalar sources. Phys. Fluids 18. https://doi.org/10.1063/1.2227005

Curriero, F.C., Patz, J.A., Rose, J.B., Lele, S., 2001. The association between extreme precipitation and waterborne disease outbreaks in the United States, 1948-1994. Am. J. Public Health 91, 1194–1199. https://doi.org/10.2105/ajph.91.8.1194

da Costa Andrade, V., Del Busso Zampieri, B., Ballesteros, E., Bartelochi Pinto, A., Fernandes Cardoso de Oliveira, A., 2015. Densities and antimicrobial resistance of Escherichia coli isolated from marine waters and beach sands. Environ. Monit. Assess. 187. https://doi.org/10.1007/s10661-015-4573-8

de Brauwere, A., De Brye, B., Servais, P., Passerat, J., Deleersnijder, E., 2011. Modelling Escherichia coli concentrations in the tidal Scheldt river and estuary. Water Res. 45, 2724–2738.

DeFlorio-Barker, S., Wade, T.J., Turyk, M., Dorevitch, S., 2016. Water recreation and illness severity. J. Water Health 14, 713–726. https://doi.org/10.2166/wh.2016.002

Delpla, I., Rodriguez, M., 2014. Effects of Future Climate and Land Use Scenarios on Riverine Source Water Quality. Sci. Total Environ. 493, 1014–1024. https://doi.org/10.1016/j.scitotenv.2014.06.087

Donzis, D.A., Aditya, K., Sreenivasan, K.R., Yeung, P.K., 2014. The turbulent schmidt number. J. Fluids Eng. Trans. ASME 136, 1–5. https://doi.org/10.1115/1.4026619

Dorevitch, S., Pratap, P., Wroblewski, M., Hryhorczuk, D.O., Li, H., Liu, L.C., Scheff, P.A., 2012. Health Risks of Limited-Contact Water Recreation. Environ. Health Perspect. 120, 192–197. https://doi.org/10.1289/ehp.1103934

Dorfman, M., Haren, A., 2014. Testing the waters: a guide to water quality at vacation beaches. Natural Resources Defense Council.

Duncker, J.J., Johnson, K.K., 2016. Hydrology of and Current Monitoring Issues for the Chicago Area Waterway System, Northeastern Illinois. Reston, VA.

Dvorak, A.C., Solo-Gabriele, H.M., Galletti, A., Benzecry, B., Malone, H., Boguszewski, V., Bird, J., 2018. Possible impacts of sea level rise on disease transmission and potential adaptation strategies, a review. J. Environ. Manage. 217, 951–968. https://doi.org/10.1016/j.jenvman.2018.03.102

Dwight, R., Semenza, J., Baker, D., Olson, B., 2002. Association of urban runoff with coastal water quality in Orange County, California. Water Environ. Res. 74, 82–90. https://doi.org/10.2175/106143002X139776

Eadie, B.J., Schwab, D.J., Assel, R.A., Hawley, N., Lansing, M.B., Miller, G.S., Morehead, N.R., Robbins, J.A., Van Hoof, P.L., Leshkevich, G.A., Johengen, T.H., Lavrentyev, P., Holland, R.E., 1996. Development of recurrent coastal plume in Lake Michigan observed for first time. Eos (Washington. DC). 77, 337–338. https://doi.org/10.1029/96EO00234

EGLE, 2016. Michigan Beaches.

Elliott, Z.A., Venayagamoorthy, S.K., 2011. Evaluation of turbulent Prandtl (Schmidt) number parameterizations for stably stratified environmental flows. Dyn. Atmos. Ocean. 51, 137–150. https://doi.org/10.1016/j.dynatmoce.2011.02.003

Eregno, F.E., Tryland, I., Tjomsland, T., Kempa, M., Heistad, A., 2018. Hydrodynamic modelling of recreational water quality using Escherichia coli as an indicator of microbial contamination. J. Hydrol. 561, 179–186. https://doi.org/10.1016/j.jhydrol.2018.04.006

ESRL, N., 2020. NOAA Solar Calculator [WWW Document]. Glob. Monit. Lab. URL https://www.esrl.noaa.gov/gmd/grad/solcalc/ (accessed 9.18.20).

Evison, L.M., 1988. Comparative studies on the survival of indicator organisms and pathogens in fresh and sea-water. Water Sci. Technol. 20, 309–315.

Fahnenstiel, G., Nalepa, T., Pothoven, S., Carrick, H., Scavia, D., 2010. Lake Michigan lower food web: Long-term observations and Dreissena impact. J. Great Lakes Res. 36, 1–4. https://doi.org/10.1016/j.jglr.2010.05.009

Fahnenstiel, G., Pothoven, S., Vanderploeg, H., Klarer, D., Nalepa, T., Scavia, D., 2010. Recent changes in primary production and phytoplankton in the offshore region of southeastern Lake Michigan. J. Great Lakes Res. 36, 20–29. https://doi.org/10.1016/j.jglr.2010.03.009

Fairall, C.W., Bradley, E.F., Hare, J.E., Grachev, A.A., Edson, J.B., 2003. Bulk parameterization of air-sea fluxes: Updates and verification for the COARE algorithm. J. Clim. 16, 571–591. https://doi.org/10.1175/1520-0442(2003)016<0571:BPOASF>2.0.CO;2

Fairall, C.W., Bradley, E.F., Rogers, D.P., Edson, J.B., Young, G.S., 1996. Bulk parameterization of air-sea fluxes for Tropical Ocean Global Atmosphere Coupled Ocean Atmosphere Response Experiment. J. Geophys. Res. 101, 3747–3764. https://doi.org/10.1029/95jc03205

Federigi, I., Verani, M., Donzelli, G., Cioni, L., Carducci, A., 2019. The application of quantitative microbial risk assessment to natural recreational waters: A review. Mar. Pollut. Bull. https://doi.org/10.1016/j.marpolbul.2019.04.073

Feng, Z., Reniers, A., Haus, B.K., Solo-Gabriele, H.M., 2013. Modeling sediment-related enterococci loading, transport and inactivation at an embayed, non-point source beach. Water Resour. Res. 49, 1–20. https://doi.org/10.1029/2012WR012432

Feng, Z.X., Reniers, A., Haus, B.K., Solo-Gabriele, H.M., Wang, J.D., Fleming, L.E., 2015. A predictive model for microbial counts on beaches where intertidal sand is the primary source. Mar. Pollut. Bull. 94, 37–47. https://doi.org/10.1016/j.marpolbul.2015.03.019

Fewtrell, L., Kay, D., 2015. Recreational Water and Infection: A Review of Recent Findings. Curr. Environ. Heal. reports 2, 85–94. https://doi.org/10.1007/s40572-014-0036-6

Fleisher, J.M., Fleming, L.E., Solo-Gabriele, H.M., Kish, J.K., Sinigalliano, C.D., Plano, L., Elmir, S.M., Wang, J.D., Withum, K., Shibata, T., 2010. The BEACHES Study: health effects and exposures from non-point source microbial contaminants in subtropical recreational marine waters. Int. J. Epidemiol. dyq084.

Francy, D.S., Darner, R.A., 2007. Nowcasting beach advisories at Ohio Lake Erie beaches. U. S. Geological Survey.

Francy, D.S., Bertke, E.E., Darner, R.A., 2009. Testing and refining the Ohio nowcast at two Lake Erie beaches-2008. U. S. Geological Survey.

Francy, D.S., Brady, A.M., Carvin, R.B., Corsi, S.R., Fuller, L.M., Harrison, J.H., Hayhurst, B.A., Lant, J., Nevers, M.B., Terrio, P.J., Zimmerman, T.M., 2013. Developing and implementing the use of predictive models for estimating water quality at Great Lakes beaches. https://doi.org/10.3133/sir20135166

Francy, D.S., Stelzer, E.A., Duris, J.W., Brady, A.M.G., Harrison, J.H., Johnson, H.E., Ware, M.W., 2013. Predictive Models for Escherichia coli Concentrations at Inland Lake Beaches and Relationship of Model Variables to Pathogen Detection. Appl. Environ. Microbiol. 79, 1676–1688. https://doi.org/10.1128/aem.02995-12

Froelich, B., Bowen, J., Gonzalez, R., Snedeker, A., Noble, R., 2013. Mechanistic and statistical models of total Vibrio abundance in the Neuse River Estuary. Water Res. 47, 5783–5793. https://doi.org/10.1016/j.watres.2013.06.050

Fry, L.M., Hunter, T.S., Phanikumar, M.S., Fortin, V., Gronewold, A.D., 2013. Identifying streamgage networks for maximizing the effectiveness of regional water balance modeling. Water Resour. Res. 49, 2689–2700. https://doi.org/10.1002/wrcr.20233

Galperin, B., Kantha, L., Hassid, S., Rosati, A., 1988. A quasi-equilibrium turbulent energy model for geophysical flows. J. Atmos. Sci. 45, 55–62.

Gao, G.H., Falconer, R.A., Lin, B.L., 2015. Modelling the fate and transport of faecal bacteria in estuarine and coastal waters. Mar. Pollut. Bull. 100, 162–168. https://doi.org/10.1016/j.marpolbul.2015.09.011

Gao, G.H., Falconer, R.A., Lin, B.L., 2011. Numerical modelling of sediment-bacteria interaction processes in surface waters. Water Res. 45, 1951–1960. https://doi.org/10.1016/j.watres.2010.12.030

Garcia-Alba, J., Barcena, J., Ugarteburu, C., Garcia, A., 2019. Artificial neural networks as emulators of process-based models to analyse bathing water quality in estuaries. Water Res. 150, 283–295. https://doi.org/10.1016/j.watres.2018.11.063

Garcia-Armisen, T., Servais, P., 2007. Respective contributions of point and non-point sources of E-coli and enterococci in a large urbanized watershed (the Seine river, France). J. Environ. Manage. 82, 512–518. https://doi.org/10.1016/j.jenvman.2006.01.011

Gasper, R., Blohm, A., Ruth, M., 2011. Social and economic impacts of climate change on the urban environment. Curr. Opin. Environ. Sustain. 3, 150–157. https://doi.org/10.1016/j.cosust.2010.12.009

Ge, Z., Nevers, M.B., Schwab, D.J., Whitman, R.L., 2010. Coastal loading and transport of Escherichia coli at an embayed beach in Lake Michigan. Environ. Sci. Technol. 44, 6731–6737. https://doi.org/https://doi.org/10.1021/es100797r

Ge, Z.F., Whitman, R.L., Nevers, M.B., Phanikumar, M.S., 2012a. Wave-induced mass transport affects daily Escherichia coli fluctuations in nearshore water. Environ. Sci. Technol. 46, 2204–2211. https://doi.org/10.1021/es203847n

Ge, Z.F., Whitman, R.L., Nevers, M.B., Phanikumar, M.S., Byappanahalli, M.N., 2012b. Nearshore hydrodynamics as loading and forcing factors for Escherichia coli contamination at an embayed beach. Limnol. Oceanogr. 57, 362–381. https://doi.org/10.4319/lo.2012.57.1.0362

Gerba, C.P., 2005. Survival of viruses in the marine environment, in: Belkin, S., Colwell, R.R. (Eds.), Oceans and Health: Pathogens in the Marine Environment. Springer, New York, NY, pp. 133–142.

GLOS, NASA, MTRI, 2020. Satellite-Derived Great Lakes Remote Sensing [WWW Document]. URL https://greatlakesremotesensing.org/ (accessed 4.10.20).

Goodman, L., Levine, E.R., 2003. On the use of the turbulent kinetic energy and scalar variance budgets to obtain directly eddy viscosity and diffusivity from AUV turbulence measurements. J. Atmos. Ocean. Technol. 143–155.

Goonetilleke, A., Thomas, E., Ginn, S., Gilbert, D., 2005. Understanding the role of land use in urban stormwater quality management. J. Environ. Manage. 74, 31–42. https://doi.org/10.1016/j.jenvman.2004.08.006

Graf, W.H., Cellino, M., 2002. Suspension flows in open channels; experimental study. J. Hydraul. Res. 40, 435–447. https://doi.org/10.1080/00221680209499886

Graham, K.E., Prussin, A.J., Marr, L.C., Sassoubre, L.M., Boehm, A.B., 2018. Microbial community structure of sea spray aerosols at three California beaches. Fems Microbiol. Ecol. 94, 10. https://doi.org/10.1093/femsec/fiy005

Grant, S.B., Sanders, B.F., 2010. Beach boundary layer: A framework for addressing recreational water quality impairment at enclosed beaches. Environ. Sci. Technol. 44, 8804–8813.

Gräwe, U., 2011. Implementation of high-order particle-tracking schemes in a water column model. Ocean Model. 36, 80–89. https://doi.org/10.1016/j.ocemod.2010.10.002Griffith, J.F., Weisberg, S.B., 2011. Challenges in implementing new technology for beach water quality monitoring: lessons from a California demonstration project. Mar. Technol. Soc. J. 45, 65–73.

Gualtieri, C., Angeloudis, A., Bombardelli, F., Jha, S., Stoesser, T., 2017. On the values for the turbulent schmidt number in environmental flows. Fluids 2. https://doi.org/10.3390/fluids2020017

Hamrick, J., 1992. A three-dimensional environmental fluid dynamics computer code: Theoretical and computational aspects.

Hanes, N.B., Fragala, R., 1967. Effect of seawater concentration on survival of fecal indicator bacteria. J. Water Pollut. Control Fed. 39, 97–104.

Hansen, B., 2009. The Reversal of The Chicago River: Flushing the System. Civ. Eng. 79, 40–43. https://doi.org/10.1061/ciegag.0000533

Harwood, V.J., Staley, C., Badgley, B.D., Borges, K., Korajkic, A., 2014. Microbial source tracking markers for detection of fecal contamination in environmental waters: relationships between pathogens and human health outcomes. FEMS Microbiol. Rev. 38, 1–40.

He, L.M., He, Z.L., 2008. Water quality prediction of marine recreational beaches receiving watershed baseflow and stormwater runoff in southern California, USA. Water Res. 42, 2563–2573. https://doi.org/10.1016/j.watres.2008.01.002

Heaney, C.D., Exum, N.G., Dufour, A.P., Brenner, K.P., Haugland, R.A., Chern, E., Schwab, K.J., Love, D.C., Serre, M.L., Noble, R., Wade, T.J., 2014. Water quality, weather and environmental factors associated with fecal indicator organism density in beach sand at two recreational marine beaches. Sci. Total Environ. 497, 440–447. https://doi.org/10.1016/j.scitotenv.2014.07.113

Heaney, C.D., Sams, E., Wing, S., Marshall, S., Brenner, K., Dufour, A.P., Wade, T.J., 2009. Contact with beach sand among beachgoers and risk of illness. Am. J. Epidemiol. 170, 164–

172. https://doi.org/10.1093/aje/kwp152

Hill, L., 2019. The Chicago River: A Natural and Unnatural History. Southern Illinois University Press, Carbondale, IL, p. 302.

Hipsey, M.R., Antenucci, J.P., Brookes D., J., 2008. A generic, process-based model of microbial pollution in aquatic systems. Water Resour. Res. 44, 1–26. https://doi.org/10.1029/2007WR006395

Hipsey, M.R., Brookes, J.D., Regel, R.H., Antenucci, J.P., Burch, M.D., 2006. In situ evidence for the association of total coliforms and Escherichia coli with suspended inorganic particles in an Australian reservoir. Water. Air. Soil Pollut. 170, 191–209.

Ho, L.C., Litton, R.M., Grant, S.B., 2011. Anthropogenic Currents and Shoreline Water Quality in Avalon Bay, California. Environ. Sci. Technol. 45, 2079–2085. https://doi.org/10.1021/es103904n

Huang, C., Kuczynski, A., Auer, M.T., O'Donnell, D., Xue, P., 2019. Management transition to the Great Lakes nearshore: Insights from hydrodynamic modeling. J. Mar. Sci. Eng. 2019.

Huynh, V., Hausot, A., Angelescu, D.E., 2016. An autonomous field sensor for Total Coliform and *E. coli* monitoring at remote sites, in: Oceans 2016 MTS/IEEE Monterey. IEEE, Monterey, CA USA, pp. 1–5. https://doi.org/10.1109/OCEANS.2016.7761360

IDEM, 2016. Indiana Beach Guard.

IDPH, 2018. Illinois Beaches.

IPCC, 2014. Climate Change 2014 Synthesis Report, Climate Change Assessment Reports. Intergovernmental Panel on Climate Change.

Ishii, S., Hansen, D.L., Hicks, R.E., Sadowsky, M.J., 2007. Beach sand and sediments are temporal sinks and sources of Escherichia coli in Lake Superior. Environ. Sci. Technol. 41, 2203–2209. https://doi.org/10.1021/es0623156

Jabareen, Y., 2013. Planning the resilient city: Concepts and strategies for coping with climate change and environmental risk. Cities 31, 220–229. https://doi.org/10.1016/j.cities.2012.05.004

Jameel, Y., Stein, S., Grimm, E., Roswell, C., Wilson, A.E., Troy, C., Hook, T.O., Bowen, G.J., 2018. Physicochemical characteristics of a southern Lake Michigan river plume. J. Great Lakes Res. 44, 209–218. https://doi.org/10.1016/j.jglr.2018.01.003

Jamieson, R., Gordon, R., Joy, D., Lee, H., 2004. Assessing microbial pollution of rural surface waters - A review of current watershed scale modeling approaches. Agric. Water Manag. 70, 1–17. https://doi.org/10.1016/j.agwat.2004.05.006

Jennings, W.C., Cunniff, S., Lewis, K., Deres, H., Reineman, D.R., Davis, J., Boehm, A.B.,

2020. Participatory science for coastal water quality: Freshwater plume mapping and volunteer retention in a randomized informational intervention. Environ. Sci. Process. Impacts 22, 918–929. https://doi.org/10.1039/c9em00571d

Ji, R.B., Davis, C., Chen, C.S., Beardsley, R., 2008. Influence of local and external processes on the annual nitrogen cycle and primary productivity on Georges Bank: A 3-D biological-physical modeling study. J. Mar. Syst. 73, 31–47. https://doi.org/10.1016/j.jmarsys.2007.08.002

Jin, G., Englande, A., Liu, A., 2003. A preliminary study on coastal water quality monitoring and modeling. J. Environ. Sci. Heal. 38, 493–509.

Johnson, D., Enriquez, C., Pepper, I., Davis, T., Gerba, C., Rose, J., 1997. Survival of Giardia, Cryptosporidium, poliovirus and Salmonella in marine waters. Water Sci. Technol. 35, 261–268.

Jones, S.E., Lennon, J.T., 2015. A test of the subsidy-stability hypothesis: the effects of terrestrial carbon in aquatic ecosystems. Ecology 96, 1550–1560. https://doi.org/10.1890/14-1783.1

Kashefipour, S.M., Lin, B., Falconer, R.A., 2006. Modelling the fate of faecal indicators in a coastal basin. Water Res. 40, 1413–1425. https://doi.org/10.1016/j.watres.2005.12.046

Kaspar, C., Tamplin, M., 1993. Effects of temperature and salinity on the survival of Vibrio vulnificus in seawater and shellfish. Appl. Environ. Microbiol. 59, 2425–2429.

Kastner, S.E., Horner-Devine, A.R., Thomson, J., 2018. The Influence of Wind and Waves on Spreading and Mixing in the Fraser River Plume. J. Geophys. Res. Ocean. 123, 6818–6840. https://doi.org/10.1029/2018JC013765

Kays, W.M., 1994. Turbulent Prandtl Number - Where Are We? J. Heat Transfer 116, 284–295.

Kim, S.Y., Terrill, E.J., Cornuelle, B.D., 2009. Assessing coastal plumes in a region of multiple discharges: The U.S.-Mexico border. Environ. Sci. Technol. 43, 7450–7457. https://doi.org/10.1021/es900775p

Kinzelman, J.L., 2009. The economic impact of improved Great Lakes water quality.

Klein, Y., Osleeb, J., Viola, M., 2004. Tourism-generated earnings in the coastal zone: A regional analysis. J. Coast. Res. 20, 1080–1088. https://doi.org/10.2112/003-0018.1

Kocsis, L., Herman, P., Eke, A., 2006. The modified Beer-Lambert law revisited. Phys. Med. Biol. 51, N91–N98. https://doi.org/10.1088/0031-9155/51/5/n02

Kundu, P., Cohen, I., Dowling, D., 2016. Fluid Mechanics, 6th ed. Academic Press, Elsevier, Amsterdam. https://doi.org/10.1016/B978-0-12-405935-1.12001-5

Launder, B.E., 1989. Second-moment closure : present and future ? Int. J. Heat Fluid Flow 10, 282–300.

Lavender, J.S., Kinzelman, J.L., 2009. A cross comparison of QPCR to agar-based or defined substrate test methods for the determination of Escherichia coli and enterococci in municipal water quality monitoring programs. Water Res. 43, 4967–4979.

Lee, S., Park, M.S., Lim, Y.W., 2016. Diversity of marine-derived Aspergillus from tidal mudflats and sea sand in Korea. Mycobiology 44, 237–247. https://doi.org/10.5941/myco.2016.44.4.237

Legates, D.R., McCabe, G.J., 1999. Evaluating the use of "goodness-of-fit" measures in hydrologic and hydroclimatic model validation. Water Resour. Res. 35, 233–241. https://doi.org/10.1029/1998WR900018

Leggett, C., Scherer, N., Curry, M., Bailey, R., 2014. Assessing the economic benefits of reductions in marine debris: a pilot study of beach recreation in Orange County, California. NOAA Mar. Debris Progr. Ind. Econ. Inc. 45.

Lesser, G.R., Roelvink, J.A., van Kester, J.A.T.M., Stelling, G.S., 2004. Development and validation of a three-dimensional morphological model. Coast. Eng. 51, 883–915. https://doi.org/10.1016/j.coastaleng.2004.07.014

Li, G., Gregory, J., 1991. Flocculation and sedimentation of high-turbidity waters. Water Res. 25, 1137–1143.

Li, H., Beck, T., Moritz, H., Groth, K., Puckette, T., Marsh, J., Sanchez, A., 2019. Sediment tracer tracking and numerical modeling at Coos Bay inlet, Oregon. J. Coast. Res. 35, 4–25. https://doi.org/10.2112/JCOASTRES-D-17-00218.1

Liang, Z., He, Z., Zhou, X., Powell, C.A., Yang, Y., He, L.M., Stoffella, P.J., 2013. Impact of mixed land-use practices on the microbial water quality in a subtropical coastal watershed. Sci. Total Environ. 449, 426–433. https://doi.org/10.1016/j.scitotenv.2013.01.087

Lin, L., Deng, Z.Q., Gang, D.D., 2009. Nonpoint Source Pollution. Water Environ. Res. 81, 1996–2018. https://doi.org/10.2175/106143009x12445568400610

Liu, L., 2018. Application of a hydrodynamic and water quality model for inland surface water systems, in: Applications in Water Systems Management and Modeling. pp. 87–109. https://doi.org/10.5772/intechopen.74914

Liu, L., Phanikumar, M.S., Molloy, S.L., Whitman, R.L., Shively, D.A., Nevers, M.B., Schwab, D.J., Rose, J.B., 2006. Modeling the transport and inactivation of *E. coli* and enterococci in the near-shore region of Lake Michigan. Environ. Sci. Technol. 40, 5022–5028. https://doi.org/10.1021/es060438k

Liu, L.B., Fu, X.D., Wang, G.Q., 2014. Parametric Study of Fate and Transport Model of *E. coli* in the Nearshore Region of Southern Lake Michigan. J. Environ. Eng. 140, 11. https://doi.org/10.1061/(asce)ee.1943-7870.0000745

Liu, W.C., Chan, W.T., Young, C.C., 2015. Modeling fecal coliform contamination in a tidal Danshuei River estuarine system. Sci. Total Environ. 502, 632–640. https://doi.org/10.1016/j.scitotenv.2014.09.065

Liu, W.C., Huang, W.C., 2012. Modeling the transport and distribution of fecal coliform in a tidal estuary. Sci. Total Environ. 431, 1–8. https://doi.org/10.1016/j.scitotenv.2012.05.016

Loong, T., 2003. Understanding sensitivity and specificity with the right side of the brain. Br. Med. J. 327, 716–719. https://doi.org/10.1136/bmj.327.7417.716

Lušić, D.V., Kranjčević, L., Maćešić, S., Lušić, D., Jozić, S., Linšak, Ž., Bilajac, L., Grbčić, L., Bilajac, N., 2017. Temporal variations analyses and predictive modeling of microbiological seawater quality. Water Res. 119, 160–170. https://doi.org/10.1016/j.watres.2017.04.046

Madani, M., Seth, R., Leon, L.F., Valipour, R., Mccrimmon, C., 2020. Three dimensional modelling to assess contributions of major tributaries to fecal microbial pollution of lake St. Clair and Sandpoint Beach. J. Great Lakes Res. 46, 159–179. https://doi.org/10.1016/j.jglr.2019.12.005

Malhotra, A., Kang, S., 1984. Turbulent Prandtl number in circular pipes. Int. J. Heat Mass Transf. 27, 2158–2161.

Mancini, J.L., 1978. Numerical estimates of coliform mortality-rates under various conditions. J. Water Pollut. Control Fed. 50, 2477–2484.

Marshall, T.P., 2002. Tornado damage survey at Moore, Oklahoma. Weather Forecast. 17, 582–598. https://doi.org/10.1175/1520-0434(2002)017<0582:TDSAMO>2.0.CO;2

Masoner, J.R., Kolpin, D.W., Cozzarelli, I.M., Barber, L.B., Burden, D.S., Foreman, W.T., Forshay, K.J., Furlong, E.T., Groves, J.F., Hladik, M.L., Hopton, M.E., Jaeschke, J.B., Keefe, S.H., Krabbenhoft, D.P., Lowrance, R., Romanok, K.M., Rus, D.L., Selbig, W.R., Williams, B.H., Bradley, P.M., 2019. Urban Stormwater: An Overlooked Pathway of Extensive Mixed Contaminants to Surface and Groundwaters in the United States. Environ. Sci. Technol. 53, 10070–10081. https://doi.org/10.1021/acs.est.9b02867

McCambridge, J., McMeekin, T.A., 1981. Effect of solar radiation and predacious microorganisms on survival of fecal and other bacteria. Appl. Environ. Microbiol. 41, 1083–1087.

McCarthy, D.T., Hathaway, J.M., Hunt, W.F., Deletic, A., 2012. Intra-event variability of Escherichia coli and total suspended solids in urban stormwater runoff. Water Res. 46, 6661–6670. https://doi.org/10.1016/j.watres.2012.01.006

McCorquodale, J.A., Georgiou, I., Carnelos, S., Englande, A.J., 2004. Modeling coliforms in storm water plumes. J. Environ. Eng. Sci. 3, 419–431. https://doi.org/10.1139/s03-055

McLellan, S.L., Hollis, E.J., Depas, M.M., Van Dyke, M., Harris, J., Scopel, C.O., 2007.

Distribution and fate of Escherichia coli in Lake Michigan following contamination with urban stormwater and combined sewer overflows. J. Great Lakes Res. 33, 566–580. https://doi.org/10.3394/0380-1330(2007)33[566:dafoec]2.0.co;2

Mellor, G., Yamada, T., 1982. Development of a turbulence closure model for geophysical fluid problem. Rev. Geophys. Sp. Phys. 20, 851–875.

Mendes, R., Vaz, N., Fernández-Nóvoa, D., Da Silva, J.C.B., DeCastro, M., Gómez-Gesteira, M., Dias, J.M., 2014. Observation of a turbid plume using MODIS imagery: The case of Douro estuary (Portugal). Remote Sens. Environ. 154, 127–138. https://doi.org/10.1016/j.rse.2014.08.003

Mika, K.B., Imamura, G., Chang, C., Conway, V., Fernandez, G., Griffith, J.F., Kampalath, R.A., Lee, C.M., Lin, C.C., Moreno, R., Thompson, S., Whitman, R.L., Jay, J.A., 2009. Pilot- and bench-scale testing of faecal indicator bacteria survival in marine beach sand near point sources. J. Appl. Microbiol. 107, 72–84. https://doi.org/10.1111/j.1365-2672.2009.04197.x

Mohammed, H., Tveten, A., Seidu, R., 2019. Modelling the impact of climate change on flow and E . coli concentration in the catchment of an ungauged drinking water source in Norway. J. Hydrol. 573, 676–687. https://doi.org/10.1016/j.jhydrol.2019.04.021

Morgan, B.J., Stocker, M.D., Valdes-Abellan, J., Kim, M.S., Pachepsky, Y., 2020. Drone-based imaging to assess the microbial water quality in an irrigation pond: A pilot study. Sci. Total Environ. 716, 135757. https://doi.org/10.1016/j.scitotenv.2019.135757

Moriasi, D., Arnold, J., Van Liew, M., Bingner, R., Harmel, R., Veith, T., 2007. Model evaluation guidelines for systematic quantification of accuracy in watershed simulations. Trans. ASABE 50, 885–900.

Mortimer, C., 1974. Lake Hydrodynamics. Mitteilungen Int. Vereingung fuer Theor. und Angew. Limnol. 20, 124–197.

Muench, R., Padman, L., Gordon, A., Orsi, A., 2009. A dense water outflow from the Ross Sea, Antarctica: Mixing and the contribution of tides. J. Mar. Syst. 77, 369–387. https://doi.org/10.1016/j.jmarsys.2008.11.003

MWRD, 2020. TARP Status Report as of June 30, 2020, Protecting Our Water Environment. Chicago, IL. https://doi.org/10.1177/009102609602500405

MWRD, 2019. Collection System Operation and Maintenance Manual. Chicago, IL.

MWRD, 2011. Microbiological Report of Backflow Samples in 2010. Chicago, IL.

MWRD, n.d. About: Our History [WWW Document]. Dist. to MWRD A Hist. Prot. our water Environ. URL https://mwrd.org/our-history (accessed 5.21.20).

Nagano, Y., Kim, C., 1988. A Two-Equation Model for Heat Transport in Wall Turbulent Shear

Flows. J. Heat Transfer 110, 583–589. https://doi.org/10.1115/1.3250532

NASA Goddard Space Flight Center, Ocean Ecology Laboratory, Ocean Biology Processing Group, 2008. Moderate Resolution Imaging Spectroradiometer (MODIS)-Terra Ocean Color Data.

Nash, J., Sutcliffe, J., 1970. River flow forecasting through conceptual models. 1: Discussion of principles. J. Hydrol. 10, 282–290.

National Geophysical Data Center, 1996. Bathymetry of Lake Michigan. https://doi.org/10.7289/V5B85627

Nekouee, N., Hamidi, S.A., Roberts, P.J.W., Schwab, D.J., 2015. A coupled empirical-numerical model for a buoyant river plume in Lake Michigan. Water Air Soil Pollut. 226, 15. https://doi.org/10.1007/s11270-015-2676-z

Nerem, R., Beckley, B., Fasullo, J., Hamlington, B., Masters, D., Mitchum, G., 2018. Climate-change-driven accelerated sea-level rise in the altimeter era. Proc. Natl. Acad. Sci. U. S. A. 115, 2022–2025. https://doi.org/10.1073/pnas.1717312115

Nevers, M., Byappanahalli, M., Nakatsu, C., Kinzelman, J., Phanikumar, M., Shively, D., Spoljaric, A., 2020. Interaction of bacterial communities and indicators of water quality in shoreline sand, sediment, and water of Lake Michigan. Water Res. 178. https://doi.org/10.1016/j.watres.2020.115671

Nevers, M.B., Byappanahalli, M.N., Shively, D., Buszka, P.M., Jackson, P.R., Phanikumar, M.S., 2018. Identifying and Eliminating Sources of Recreational Water Quality Degradation along an Urban Coast. J. Environ. Qual. 47, 1042–1050. https://doi.org/10.2134/jeq2017.11.0461

Nevers, M.B., Whitman, R.L., 2011. Efficacy of monitoring and empirical predictive modeling at improving public health protection at Chicago beaches. Water Res. 45, 1659–1668.

Nevers, M.B., Whitman, R.L., 2005. Nowcast modeling of Escherichia coli concentrations at multiple urban beaches of southern Lake Michigan. Water Res. 39, 5250–5260.

Nezlin, N.P., DiGiacomo, P.M., 2005. Satellite ocean color observations of stormwater runoff plumes along the San Pedro Shelf (southern California) during 1997-2003. Cont. Shelf Res. 25, 1692–1711. https://doi.org/10.1016/j.csr.2005.05.001

Nezlin, N.P., DiGiacomo, P.M., Stein, E.D., Ackerman, D., 2005. Stormwater runoff plumes observed by SeaWiFS radiometer in the Southern California Bight. Remote Sens. Environ. 98, 494–510. https://doi.org/10.1016/j.rse.2005.08.008

Nguyen, T.D., Hawley, N., Phanikumar, M.S., 2017. Ice cover, winter circulation, and exchange in Saginaw Bay and Lake Huron. Limnol. Oceanogr. 62, 376–393.

Nguyen, T.D., Thupaki, P., Anderson, E.J., Phanikumar, M.S., 2014. Summer circulation and exchange in the Saginaw Bay-Lake Huron system. J. Geophys. Res. 119, 2713–2734. https://doi.org/10.1002/2014jc009828

Niu, J., Phanikumar, M.S., 2015. Modeling watershed-scale solute transport using an integrated, process-based hydrologic model with applications to bacterial fate and transport. J. Hydrol. 529, 35–48. https://doi.org/10.1016/j.jhydrol.2015.07.013

NOAA, 2020a. About Our Great Lakes: Lake by Lake Profiles [WWW Document]. URL https://www.glerl.noaa.gov/education/ourlakes/lakes.html (accessed 8.6.20).

NOAA, 2020b. ERDDAP [WWW Document]. Coast Watch. URL https://coastwatch.glerl.noaa.gov/erddap/search/index.html?page=1&itemsPerPage=1000&searchFor=LM (accessed 4.10.20).

NOAA, 2020c. Nine Dangers at the Beach [WWW Document]. URL https://oceanservice.noaa.gov/hazards/beach-dangers/ (accessed 8.6.20).

NOAA, 2018a. National Climatic Data Center.

NOAA, 2018b. National Data Buoy Center.

NOAA National Weather Service, 2020. Event Summaries [WWW Document]. NWS Chicago Sci. Past Events Page A Libr. local past Weather water events Sci. Stud. URL https://www.weather.gov/lot/events (accessed 10.28.20).

NOAA National Weather Service, 2011. July 23, 2011: Wettest Day on Record for Chicago Marks a Historically Wet End to July [WWW Document]. URL https://www.weather.gov/lot/2011Jul23_rainfall (accessed 9.9.20).

Noh, Y., Kang, Y.J., Matsuura, T., Iizuka, S., 2005. Effect of the Prandtl number in the parameterization of vertical mixing in an OGCM of the tropical Pacific. Geophys. Res. Lett. 32, 1–4. https://doi.org/10.1029/2005GL024540

ODH, 2020. BeachGuard [WWW Document]. Ohio Beach Guard. URL https://odh.ohio.gov/wps/portal/gov/odh/know-our-programs/bathing-beach-monitoring/BeachGuard/BeachGuard (accessed 8.6.20).

Otero, P., Ruiz-Villarreal, M., Peliz, A., 2008. Variability of river plumes off Northwest Iberia in response to wind events. J. Mar. Syst. 72, 238–255. https://doi.org/10.1016/j.jmarsys.2007.05.016

Oudin, L., Andréassian, V., Mathevet, T., Perrin, C., Michel, C., 2006. Dynamic averaging of rainfall-runoff model simulations from complementary model parameterizations. Water Resour. Res. 42, 1–10. https://doi.org/10.1029/2005WR004636

Pachauri, R.K., Allen, M.R., Barros, V.R., Broome, J., Cramer, W., Christ, R., Church, J.A., Clarke, L., Dahe, Q., Dasgupta, P., Dubash, N.K., Edenhofer, O., Elgizouli, I., Field, C.B., Forster, R., Friedlingstein, P., Fuglestvedt, J., Gomex-Echeverri, L., Hallegatte, S., Hegerl, G., Howden, M., Jiang, K., Jimenez Cisneroz, B., Kattsov, V., Lee, H., Mach, K.J., Marotzke, J., Mastrandrea, M.D., Meyer, L., Minx, J., Mulugetta, Y., O'Brien, K., Oppenheimer, M., Pereira, J.J., Pichs-Madruga, R., Plattner, G.K., Portner, H.O., Power, S.B., Preston, B., Ravindranath, N.H., Reisinger, A., Riahi, K., Rusticucci, M., Scholes, R., Seyboth, K., Sokona, Y., Stavins, R., Stocker, T.F., Tschakert, P., van Vuuren, D., van Ypserle, J.P., 2014. Climate Change 2014: Synthesis Report. IPCC, Geneva, Switzerland.

Packett, R., Dougall, C., Rohde, K., Noble, R., 2009. Agricultural lands are hot-spots for annual runoff polluting the southern Great Barrier Reef lagoon. Mar. Pollut. Bull. 58, 976–986. https://doi.org/10.1016/j.marpolbul.2009.02.017

Padgett, J., DesRoches, R., Nielson, B., Yashinsky, M., Kwon, O.-S., Burdette, N., Tavera, E., 2008. Bridge Reliability Assessment Based on Monitoring. J. Bridg. Eng. 13, 6–14. https://doi.org/10.1061/(ASCE)1084-0702(2008)13

Pakulski, J.D., Benner, R., Whitledge, T., Amon, R., Eadie, B., Cifuentes, L., Ammerman, J., Stockwell, D., 2000. Microbial metabolism and nutrient cycling in the Mississippi and Atchafalaya River plumes. Estuar. Coast. Shelf Sci. 50, 173–184. https://doi.org/10.1006/ecss.1999.0561

Patz, J.A., Vavrus, S.J., Uejio, C.K., McLellan, S.L., 2008. Climate change and waterborne disease risk in the Great Lakes region of the US. Am. J. Prev. Med. 35, 451–458. https://doi.org/10.1016/j.amepre.2008.08.026

Paule-Mercado, M.A., Ventura, J.S., Memon, S.A., Jahng, D., Kang, J.H., Lee, C.H., 2016. Monitoring and predicting the fecal indicator bacteria concentrations from agricultural, mixed land use and urban wstormwater runoff. Sci. Total Environ. 550, 1171–1181. https://doi.org/10.1016/j.scitotenv.2016.01.026

Pistrika, A.K., Jonkman, S.N., 2010. Damage to residential buildings due to flooding of New Orleans after hurricane Katrina. Nat. Hazards 54, 413–434. https://doi.org/10.1007/s11069-009-9476-y

Qi, J., Chen, C., Beardsley, R.C., Perrie, W., Cowles, G.W., Lai, Z., 2009. An unstructured-grid finite-volume surface wave model (FVCOM-SWAVE): Implementation, validations and applications. Ocean Model. 28, 153–166. https://doi.org/10.1016/j.ocemod.2009.01.007

Ramirez, D., Gelsey, K., 2021. Exploring How Antecedent Precipitation Amount and the Effects of Covid-19 Affect Stormwater Runoff Quality Along Urban Gradients. REU Final Reports 22.

Rauen, W.B., Angeloudis, A., Falconer, R.A., 2012. Appraisal of chlorine contact tank modelling practices. Water Res. 46, 5834–5847. https://doi.org/10.1016/j.watres.2012.08.013

Reder, K., Florke, M., Alcamo, J., 2015. Modeling historical fecal coliform loadings to large European rivers and resulting in-stream concentrations. Environ. Model. Softw. 63, 251–263. https://doi.org/10.1016/j.envsoft.2014.10.001

Rehmann, C.R., Soupir, M.L., 2009. Importance of interactions between the water column and the sediment for microbial concentrations in streams. Water Res. 43, 4579–4589.

Rhodes, M.W., Kator, H.I., 1990. Effects of sunlight and autochthonous microbiota on Escherichia coli survival in an estuarine environment. Curr. Microbiol. 21, 65–73. https://doi.org/10.1007/bf02090102

Ritter, A., Munoz-Carpena, R., 2013. Performance evaluation of hydrological models: Statistical significance for reducing subjectivity in goodness-of-fit assessment. J. Hydrol. 480, 33–45. https://doi.org/10.1016/j.hydrol.2012.12.004

Rodrigues, M., Oliveira, A., Guerreiro, M., Fortunato, A.B., Menaia, J., David, L.M., Cravo, A., 2011. Modeling fecal contamination in the Aljezur coastal stream (Portugal). Ocean Dyn. 61, 841–856. https://doi.org/10.1007/s10236-011-0392-9

Rodriguez, R., 2011. Storm Dumps Heavy Rain on Chicago, O’Hare and Other Roads Forced to Close [WWW Document]. NBC5 Chicago. URL https://www.nbcchicago.com/news/local/flash-floods/1906697/ (accessed 9.9.20).

Rousar, D.C., 1973. Seasonal and spatial changes in primary production and nutrients in Lake Michigan. Water, Air, Soil Pollut. 2, 497–514. https://doi.org/10.1007/BF00585093

Rowe, M.D., Anderson, E.J., Beletsky, D., Stow, C.A., Moegling, S.D., Chaffin, J.D., May, J.C., Collingsworth, P.D., Jabbari, A., Ackerman, J.D., 2019. Coastal Upwelling Influences Hypoxia Spatial Patterns and Nearshore Dynamics in Lake Erie. J. Geophys. Res. Ocean. 124, 6154–6175. https://doi.org/10.1029/2019JC015192

Rowe, M.D., Anderson, E.J., Wynne, T.T., Stumpf, R.P., Fanslow, D.L., Kijanka, K., Vanderploeg, H.A., Strickler, J.R., Davis, T.W., 2016. Vertical distribution of buoyant Microcystis blooms in a Lagrangian particle tracking model for short-term forecasts in Lake Erie. J. Geophys. Res. 121, 5296–5314. https://doi.org/10.1002/2016jc011720

Rowe, M.D., Anderson, E.J., Wynne, T.T., Stumpf, R.P., Fanslow, D.L., Kijanka, K., Vanderploeg, H.A., Strickler, J.R., Davis, T.W., 2016. Vertical distribution of buoyant Microcystis blooms in a Lagrangian particle tracking model for short-term forecasts in Lake Erie. J. Geophys. Res. 121, 5296–5314. https://doi.org/10.1002/2016jc011720

Sabino, R., Verissimo, C., Cunha, M.A., Wergikoski, B., Ferreira, F.C., Rodrigues, R., Parada, H., Falcão, L., Rosado, L., Pinheiro, C., Paixão, E., Brandão, J., 2011. Pathogenic fungi: An unacknowledged risk at coastal resorts? New insights on microbiological sand quality in Portugal. Mar. Pollut. Bull. 62, 1506–1511. https://doi.org/10.1016/j.marpolbul.2011.04.008

Safaie, A., Wendzel, A., Ge, Z.F., Nevers, M.B., Whitman, R.L., Corsi, S.R., Phanikumar, M.S., 2016. Comparative evaluation of statistical and mechanistic models of Escherichia coli at beaches in southern Lake Michigan. Environ. Sci. Technol. 50, 2442–2449. https://doi.org/10.1021/acs.est.5b05378

Sanders, B.F., Arega, F., Sutula, M., 2005. Modeling the dry-weather tidal cycling of fecal indicator bacteria in surface waters of an intertidal wetland. Water Res. 39, 3394–3408. https://doi.org/10.1016/j.watres.2005.06.004

Schang, C., Lintern, A., Cook, P.L.M., Osborne, C., McKinley, A., Schmidt, J., Coleman, R., Rooney, G., Henry, R., Deletic, A., McCarthy, D., 2016. Presence and survival of culturable Campylobacter spp. and Escherichia coli in a temperate urban estuary. Sci. Total Environ. 569, 1201–1211. https://doi.org/10.1016/j.scitotenv.2016.06.195

Schimmelpfennig, S., Kirillin, G., Engelhardt, C., Nützmann, G., 2012. Effects of wind-driven circulation on river intrusion in Lake Tegel: Modeling study with projection on transport of pollutants. Environ. Fluid Mech. 12, 321–339. https://doi.org/10.1007/s10652-012-9236-5

Schmidt, N., Thibault, D., Galgani, F., Paluselli, A., Sempéré, R., 2018. Occurrence of microplastics in surface waters of the Gulf of Lion (NW Mediterranean Sea). Prog. Oceanogr. 163, 214–220. https://doi.org/10.1016/j.pocean.2017.11.010

Scully, M.E., Friedrichs, C., Brubaker, J., Scully, E., Friedrichs, C., 2015. Control of Estuarine Stratification and Mixing by Wind-induced of the Estuarine Density Field Straining. Estuaries 28, 321–326.

Servais, P., Billen, G., Goncalves, A., Garcia-Armisen, T., 2007a. Modelling microbiological water quality in the Seine river drainage network: Past, present and future situations. Hydrol. Earth Syst. Sci. 11, 1581–1592.

Servais, P., Garcia-Armisen, T., George, I., Billen, G., 2007b. Fecal bacteria in the rivers of the Seine drainage network (France): sources, fate and modelling. Sci. Total Environ. 375, 152–167.

Shaikh, S., 2012. The value of beach visits and the effect of swim bans in Chicago, in: Delivering Healthy Water Workshop. University of Stirling, Scotland, UK.

Shively, D.A., Nevers, M.B., Breitenbach, C., Phanikumar, M.S., Przybyla-kelly, K., Spoljaric, A.M., Whitman, R.L., 2016. Prototypic automated continuous recreational water quality monitoring of nine Chicago beaches. J. Environ. Manage. 166, 285–293. https://doi.org/10.1016/j.jenvman.2015.10.011

Silva, M.R., Bravo, H.R., Cherkauer, D., Val Klump, J., Kean, W., McLellan, S.L., 2014. Effect of hydrological and geophysical factors on formation of standing water and FIB reservoirs at a Lake Michigan beach. J. Great Lakes Res. 40, 778–789. https://doi.org/https://doi.org/10.1016/j.jglr.2014.06.003

Sinton, L.W., Finlay, R.K., Lynch, P.A., 1999. Sunlight inactivation of fecal bacteriophages and bacteria in sewage- polluted seawater. Appl. Environ. Microbiol. 65, 3605–3613.

Sinton, L.W., Hall, C.H., Lynch, P.A., Davies-Colley, R.J., 2002. Sunlight inactivation of fecal indicator bacteria and bacteriophages from waste stabilization pond effluent in fresh and saline waters. Appl. Environ. Microbiol. 68, 1122–1131.

Smagorinsky, J., 1963. General circulation experiments with the primitive equations, I. The basic experiment. Mon. Weather Rev. 91, 99–164.

Smith, P., Carroll, C., Wilkins, B., Johnson, P., Gabhainn, S., Smith, L.P., 1999. The effect of wind speed and direction on the distribution of sewage-associated bacteria. Lett. Appl. Microbiol. 28, 184–188.

Sokolova, E., Pettersson, T., Bergstedt, O., Hermansson, M., 2013. Hydrodynamic modeling of the microbial water quality in a drinking water source as input for risk reduction management. J. Hydrol. 497, 15–23. https://doi.org/10.1016/j.hydrol.2013.05.044

Solic, M., Krstulovic, N., 1992. Separate and combined effects of solar radiation, temperature, salinity, and pH on the survival of faecal coliforms in seawater. Mar. Pollut. Bull. 24, 411–416.

Solo-Gabriele, H.M., Harwood, V.J., Kay, D., Fujioka, R.S., Sadowsky, M.J., Whitman, R.L., Wither, A., Caniça, M., Carvalho da Fonseca, R., Duarte, A., 2015. Beach sand and the potential for infectious disease transmission: Observations and recommendations. J. Mar. Biol. Assoc. United Kingdom 1–20.

Son, S., Wang, M., 2019. VIIRS-Derived water turbidity in the Great Lakes. Remote Sens. 11, 1–13. https://doi.org/10.3390/rs11121448

Song, X., Liu, Z., Zhao, Y., 2004. Cloud detection and analysis of MODIS image, in: 2004 IEEE International Geoscience and Remote Sensing Symposium. pp. 2764–2767. https://doi.org/10.1109/IGARSS.2004.1369875

Staley, Z.R., Chuong, J.D., Hill, S.J., Grabuski, J., Shokralla, S., Hajibabaei, M., Edge, T.A., 2018. Fecal source tracking and eDNA profiling in an urban creek following an extreme rain event. Sci. Rep. 8, 1–12. https://doi.org/10.1038/s41598-018-32680-z

Suh, S.W., 2006. A hybrid approach to particle tracking and Eulerian-Lagrangian models in the simulation of coastal dispersion. Environ. Model. Softw. 21, 234–242. https://doi.org/10.1016/j.envsoft.2004.04.015

Thomann, R. V, Mueller, J.A., 1987. Principles of Surface Water Quality Modeling and Control. Harper & Row, New York, NY.

Thomas, M.K., Charron, D.F., Waltner-Toews, D., Schuster, C., Maarouf, A.R., Holt, J.D., 2006. A role of high impact weather events in waterborne disease outbreaks in Canada, 1975-2001. Int. J. Environ. Health Res. 16, 167–180. https://doi.org/10.1080/09603120600641326

Thomas, A.C., Weatherbee, R.A., 2006. Satellite-measured temporal variability of the Columbia River plume. Remote Sens. Environ. 100, 167–178. https://doi.org/10.1016/j.rse.2005.10.018

Thupaki, P., Phanikumar, M.S., Beletsky, D., Schwab, D.J., Nevers, M.B., Whitman, R.L., 2010.

Budget analysis of Escherichia coli at a southern Lake Michigan beach. Environ. Sci. Technol. 44, 1010–1016. https://doi.org/10.1021/es902232a

Thupaki, P., Phanikumar, M.S., Schwab, D.J., Nevers, M.B., Whitman, R.L., 2013. Evaluating the role of sediment-bacteria interactions on Escherichia coli concentrations at beaches in southern Lake Michigan. J. Geophys. Res. 118, 7049–7065. https://doi.org/10.1002/2013jc008919

Tilburg, C.E., Jordan, L.M., Carlson, A.E., Zeeman, S.I., Yund, P.O., 2015. The effects of precipitation, river discharge, land use and coastal circulation on water quality in coastal Maine. R. Soc. Open Sci. 2, 18. https://doi.org/10.1098/rsos.140429

Tong, S.T.Y., Chen, W., 2002. Modeling the relationship between land use and surface water quality. J. Environ. Manage. 66, 377–393. https://doi.org/10.1006/jema.2002.0593

Topalcengiz, Z., Strawn, L.K., Danyluk, M.D., 2017. Microbial quality of agricultural water in Central Florida. PLoS One 12, 1–18. https://doi.org/10.1371/journal.pone.0174889

Turgeon, P., Michel, P., Levallois, P., Chevalier, P., Daignault, D., Crago, B., Irwin, R., McEwen, S., Neumann, N., Louie, M., 2012. Antimicrobial-resistant Escherichia coli in public beach waters in Quebec. Can. J. Infect. Dis. Med. Microbiol. 23, 20–25.

USACE, 2014. The GLMRIS Project, Appendix E: Hydrologic and Hydraulic Analyses.

USACE, 1996. Chicago Underflow Plan, McCook Reservoir Special Re-Evaluation Report, Environmental Impact Statement. Chicago, IL.

USEPA, 2019. Physical Features of the Great Lakes [WWW Document]. Phys. Featur. Gt. Lakes. URL https://www.epa.gov/greatlakes/physical-features-great-lakes (accessed 5.18.20).

USEPA, 2018. 2017 Five-Year Review of the 2012 Recreational Water Quality Criteria. Washington, DC.

USEPA, 2014a. Method 1603: Escherichia coli (*E. coli*) in Water by Membrane Filtration Using Modified membrane-Thermotolerant Escherichia coli Agar (Modified mTEC). Washington, DC.

USEPA, 2014b. National Beach Guidance and Required Performance Criteria for Grants, 2014 Edition, Epa-823-B-14-001. Washington D.C.

USEPA, 2013. Method 1609: Enterococci in Water by TaqMan Quantitative Polymerase Chain Reaction (qPCR) with Internal Aplification Control (IAC) Assay. Washington, DC.

USEPA, 2012. Recreational Water Quality Criteria. Washington, DC.

USEPA, 2010. Sampling and Consideration of Variability (Temporal and Spatial) for Monitoring Recreational Waters.

US Census Bureau, 2019. QuickFacts: Chicago City, Illinois [WWW Document]. QuickFacts. URL: https://www.census.gov/quickfacts/fact/table/chicagocityillinois,US/PST045219 (accessed 5.21.20).

Vanderploeg, H.A., Johengen, T.H., Lavrentyev, P.J., Chen, C., Lang, G.A., Agy, M.A., Bundy, M.H., Cavaletto, J.F., Eadie, B.J., Liebig, J.R., Miller, G.S., Ruberg, S.A., McCormick, M.J., 2007. Anatomy of the recurrent coastal sediment plume in Lake Michigan and its impacts on light climate, nutrients, and plankton. J. Geophys. Res. Ocean. 112, 1–23. https://doi.org/10.1029/2004JC002379

Van Wageningen-Kessels, F., Leclercq, L., Daamen, W., Hoogendoorn, S.P., 2016. The Lagrangian coordinate system and what it means for two-dimensional crowd flow models. Phys. A Stat. Mech. its Appl. 443, 272–285. https://doi.org/10.1016/j.physa.2015.09.048

Vermote, E., 2015. MOD09A1 MODIS/Terra Surface Reflectance 8-Day L3 Global 500 SIN Grid V006. https://doi.org/10.5067/MODIS/MOD09A1.006

Viau, E.J., Goodwin, K.D., Yamahara, K.M., Layton, B.A., Sassoubre, L.M., Burns, S.L., Tong, H.I., Wong, S.H.C., Lu, Y.A., Boehm, A.B., 2011. Bacterial pathogens in Hawaiian coastal streams - Associations with fecal indicators, land cover, and water quality. Water Res. 45, 3279–3290. https://doi.org/10.1016/j.watres.2011.03.033

Visser, A.W., 1997. Using random walk models to simulate the vertical distribution of particles in a turbulent water column. Mar. Ecol. Prog. Ser. 158, 275–281. https://doi.org/10.3354/meps158275

Vogel, L.J., O'Carroll, D.M., Edge, T.A., Robinson, C.E., 2016. Release of Escherichia coli from foreshore sand and pore water during intensified wave conditions at a recreational beach. Environ. Sci. Technol. 50, 5676–5684. https://doi.org/10.1021/acs.est.6b00707

WDNR, 2000. Wisconsin Beach Health.

Wade, T.J., Calderon, R.L., Brenner, K.P., Sams, E., Beach, M., Haugland, R., Wymer, L., Dufour, A.P., 2008. High sensitivity of children to swimming-associated gastrointestinal illness - Results using a rapid assay of recreational water quality. Epidemiology 19, 375–383. https://doi.org/10.1097/EDE.0b013e318169cc87

Walters, S.P., Thebo, A.L., Boehm, A.B., 2011. Impact of urbanization and agriculture on the occurrence of bacterial pathogens and stx genes in coastal waterbodies of central California. Water Res. 45, 1752–1762. https://doi.org/10.1016/j.watres.2010.11.032

Weiskerger, C.J., Brandao, J., Ahmed, W., Aslan, A., Avolio, L., Badgley, B.D., Boehm, A.B., Edge, T.A., Fleisher, J.M., Heaney, C.D., Jordao, L., Kinzelman, J.L., Klaus, J.S., Kleinheinz, G.T., Merilainen, P., Nshimyimana, J.P., Phanikumar, M.S., Piggot, A.M., Pitkanen, T., Robinson, C., Sadowsky, M.J., Staley, C., Staley, Z.R., Symonds, E.M., Vogel, L.J., Yamahara, K.M., Whitman, R.L., Solo-Gabriele, H.M., Harwood, V.J., 2019. Impacts of a changing earth on microbial dynamics and human health risks in the continuum between beach water and sand. Water Res. 162, 456–470.

https://doi.org/10.1016/j.watres.2019.07.006

Weiskerger, C.J., Rowe, M.D., Stow, C.A., Stuart, D., Johengen, T., 2018. Application of the Beer-Lambert Model to Attenuation of Photosynthetically Active Radiation in a Shallow, Eutrophic Lake. Water Resour. Res. 54, 8952–8962. https://doi.org/10.1029/2018wr023024

Weiskerger, C.J., Whitman, R.L., 2018. Monitoring *E. coli* in a changing beachscape. Sci. Total Environ. 619, 1236–1246. https://doi.org/10.1016/j.scitotenv.2017.11.167

Weiskerger, C.J., Phanikumar, M.S., 2020. Numerical modeling of microbial fate and transport in natural waters: Review and implications for normal and extreme storm events. Water (Switzerland) 12. https://doi.org/10.3390/W12071876

Whitman, R.L., Harwood, V.J., Edge, T.A., Nevers, M.B., Byappanahalli, M., Vijayavel, K., Brandão, J., Sadowsky, M.J., Alm, E.W., Crowe, A., Ferguson, D., Ge, Z.F., Halliday, E., Kinzelman, J., Kleinheinz, G., Przybyla-Kelly, K., Staley, C., Staley, Z., Solo-Gabriele, H.M., 2014. Microbes in beach sands: integrating environment, ecology and public health. Rev. Environ. Sci. Bio-Technology 13, 329–368. https://doi.org/10.1007/s11157-014-9340-8

Whitman, R.L., Przybyla-Kelly, K., Shively, D.A., Nevers, M.B., Byappanahalli, M.N., 2008. Sunlight, season, snowmelt, storm, and source affect *E. coli* populations in an artificially ponded stream. Sci. Total Environ. 390, 448–455. https://doi.org/10.1016/j.scitotenv.2007.10.014

Whitman, R.L., Nevers, M.B., 2004. Escherichia coli sampling reliability at a frequently closed Chicago beach: Monitoring and management implications. Environ. Sci. Technol. 38, 4241–4246. https://doi.org/10.1021/es034978i

Whitman, R.L., Nevers, M.B., Korinek, G.C., Byappanahalli, M.N., 2004. Solar and temporal effects on Escherichia coli concentration at a Lake Michigan swimming beach. Appl. Environ. Microbiol. 70, 4276–4285. https://doi.org/10.1128/aem.70.7.4276-4285.2004

Wilkinson, R.J., McKergow, L.A., Davies-Colley, R.J., Ballantine, D.J., Young, R.G., 2011. Modelling storm-event *E. coli* pulses from the Motueka and Sherry Rivers in the South Island, New Zealand. New Zeal. J. Mar. Freshw. Res. 45, 369–393. https://doi.org/10.1080/00288330.2011.592839

Willmott, C., Roberson, S., Matsuura, K., 2012. A refined index of model performance. Int. J. Climatol. 32, 2088–2094.

Wong, M., Kumar, L., Jenkins, T.M., Xagoraraki, I., Phanikumar, M.S., Rose, J.B., 2009. Evaluation of public health risks at recreational beaches in Lake Michigan via detection of enteric viruses and a human-specific bacteriological marker. Water Res. 43, 1137–1149. https://doi.org/10.1016/j.watres.2008.11.051

Wong, S.H.C., Monismith, S.G., Boehm, A.B., 2013. Simple estimate of entrainment rate of pollutants from a coastal discharge into the surf zone. Environ. Sci. Technol. 47, 11554–11561. https://doi.org/10.1021/es402492f

Wu, M.Z., O'Carroll, D.M., Vogel, L.J., Robinson, C.E., 2017. Effect of low energy waves on the accumulation and transport of fecal indicator bacteria in sand and pore water at freshwater beaches. Environ. Sci. Technol. 51, 2786–2794. https://doi.org/10.1021/acs.est.6b05985

Xu, K., Valeo, C., He, J., Xu, Z., 2019. Climate and Land Use Influences on Bacteria Levels in Stormwater. Water 11, 1–25. https://doi.org/10.3390/w22233451

Xue, P., Schwab, D.J., Zhou, X., Huang, C., Kibler, R., Ye, X., 2018. A hybrid Lagrangian-Eulerian particle model for ecosystem simulation. J. Mar. Sci. Eng. 6. https://doi.org/10.3390/jmse6040109

Yamahara, K.M., Layton, B.A., Santoro, A.E., Boehm, A.B., 2007. Beach sands along the California coast are diffuse sources of fecal bacteria to coastal waters. Environ. Sci. Technol. 41, 4515–4521. https://doi.org/10.1021/es062822n

Ye, X., Anderson, E.J., Chu, P.Y., Huang, C., Xue, P., 2019. Impact of Water Mixing and Ice Formation on the Warming of Lake Superior: A Model-guided Mechanism Study. Limnol. Oceanogr. 64, 558–574. https://doi.org/10.1002/lno.11059

Yousef, F., Schuchman, R., Sayers, M., Fahnenstiel, G., Henareh, A., 2017. Water clarity in the upper Great Lakes: Tracking changes between 1998-2012. J. Great Lakes Res. 43, 239–247. https://doi.org/10.1016/j.jglr.2016.12.002

Zhang, J., Qiu, H., Li, X., Niu, J., Nevers, M.B., Hu, X., Phanikumar, M.S., 2018. Real-Time Nowcasting of Microbiological Water Quality at Recreational Beaches : A Wavelet and Artificial Neural Network- Based Hybrid Modeling Approach. Environ. Sci. Technol. 52, 8446–8455. https://doi.org/10.1021/acs.est.8b01022

Zhang, Z., Chen, Q., 2007. Comparison of the Eulerian and Lagrangian methods for predicting particle transport in enclosed spaces. Atmos. Environ. 41, 5236–5248. https://doi.org/10.1016/j.atmosenv.2006.05.086

Zhang, Z., Deng, Z., Rusch, K.A., 2012. Development of predictive models for determining enterococci levels at Gulf Coast beaches. Water Res. 46, 465–474.

Zhang, Z., Deng, Z., Rusch, K.A., Walker, N.D., 2015. Modeling system for predicting enterococci levels at Holly Beach. Mar. Environ. Res. 109, 140–147. https://doi.org/10.1016/j.marenvres.2015.07.003

Zhu, X.F., Wang, J.D., Solo-Gabriele, H.M., Fleming, L.E., 2011. A water quality modeling study of non-point sources at recreational marine beaches. Water Res. 45, 2985–2995. https://doi.org/10.1016/j.watres.2011.03.015